Directing structure through chirality

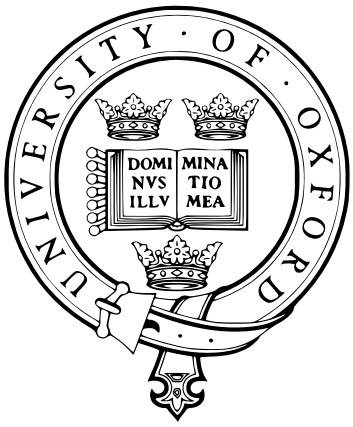

Maxime Maximilien Claude Tortora
The Queen's College
University of Oxford

A thesis submitted for the degree of
Doctor of Philosophy
Trinity 2019

Acknowledgements

The successful completion of this thesis would not have been possible without the helpful contribution of many others, both academic and otherwise, and I must apologise in advance to all those whose names won't appear here for lack of space or mindfulness: to all of you, thank you! I nonetheless ought to start with my supervisor Jon Doye, whose continued support led me through the good times and the bad over the course of my DPhil, and enabled me to bring this challenging endeavour to fruition. I am deeply indebted to Daniel Tracey, Domen Prešern, John Schreck, Dennis Palagin, Garima Mishra and all the intermittent (and not so intermittent) members of the Doye/Louis lab for countless enlightening and entertaining conversations, which helped make the long office days fly by.

The entire DiStruc team also deserves a great deal of credit for making these last few years so memorable and enjoyable, from the sunny beaches of Crete to the snowy German countryside: Dirk Aarts, Pavlik Lettinga, Irini Hatzimichali, Pavlina Schmitz, Louis Cortès, Luuk Metselaar, Marie Föllmer, Shari Finner and all the others, I cannot thank you enough for all your hard work and constant good humour. I am highly grateful to Éric Grelet for hosting me in his lab and sharing his fascination with chiral liquid crystals, and Andrii Repula and Hanna Anop for bearing with my utter lack of experimental skills and showing me around the premises.

I must finally thank all my friends and family, both in and beyond Oxford, for carrying me so enthusiastically through my time in England. First, my parents Catherine and Jean-Jacques, my brother Sam and my grand-parents Jacqueline and Constant for their heartfelt encouragements and unwavering faith in my abilities. Then, Jon Mannouch, Dom Fijan, Lucy Auton, Mark Forshaw and James Lamb for welcoming me into their home and tolerating my unreasonable love of curry. And, of course, Caroline for her endless patience and spectacular pasta recipes based exclusively on water (diluted to taste).

Abstract

Chirality — or the absence of mirror symmetry — is a fundamental physical property that permeates geometrical structures in nature, from the double-helical shape of DNA to the macroscopic anatomy of entire organisms. However, the specific mechanisms underpinning the propagation of chirality across such wide differences in length-scales often remain poorly understood. In this thesis, we explore the quantitative link between molecular and supramolecular chirality in liquid crystal phases of elongated polymers, which are ubiquitously observed in both biological and artificial colloidal solutions. We investigate the self-assembling behaviour of such systems through the combination of detailed numerical simulations and classical density functional theory in the Onsager formalism. The quantitative accuracy of the latter and of its various extensions is thoroughly assessed in the case of both rigid and flexible particle models, and rigorous first-principle derivations of its underlying mathematical framework are systematically provided. An original virial integration scheme based on hierarchical bounding volumes is also introduced to accelerate non-bonded interaction energy computations by several orders of magnitude for complex, highly-anisotropic molecular systems. These developments allow us to tackle the cholesteric assembly of DNA origamis using a structurally- and mechanically-realistic representation of the particles, and enable us to provide theoretical evidence of a novel mechanism of chirality amplification in liquid crystals, whereby phase chirality is governed by fluctuation-stabilised helical deformations in the conformations of their constituent molecules. Our results compare favourably to recent experimental measurements and demonstrate the influence of intra-molecular mechanics on chiral supramolecular order, with potential implications for a broad class of experimentally-relevant colloidal systems.

Contents

x

List of Figures

List of Abbreviations

BP . . . . . Base pair

BSC . . . . . Bounding sphero-cylinder

BVH . . . . . Bounding volume hierarchy

CIP . . . . . Cahn-Ingold-Prelog

CPU . . . . . Central processing unit

CS . . . . . Carnahan-Starling

DCF . . . . . Direct correlation function

DFT . . . . . Density functional theory

DH . . . . . Debye-Hückel

EOS . . . . . Equation of state

FENE . . . . . Finitely extensible nonlinear elastic

FMT . . . . . Fundamental measure theory

FY . . . . . Fynewever-Yethiraj

GPU . . . . . Graphical processing unit

HB . . . . . Helix bundle

HKM . . . . . Hohenberg-Kohn-Mermin

HSC . . . . . Hard sphero-cylinder

HTC . . . . . Hard twisted cuboid

HTP . . . . . Hard triangular prism

I/C . . . . . Isotropic/cholesteric

I/N . . . . . Isotropic/nematic

KG . . . . . Kremer-Grest

KS . . . . . Khokhlov-Semenov

LC . . . . . Liquid crystal

LCD . . . . . Liquid crystal display

LCHS . . . . . Linear chain of hard spheres

LCLC . . . . . Lyotropic cholesteric liquid crystal

MC . . . . . Monte Carlo

MD . . . . . Molecular dynamics

MPL . . . . . Modified Parsons-Lee

OBB . . . . . Oriented bounding box

ODF . . . . . Orientation distribution function

OF . . . . . Oseen-Frank

OP . . . . . Order parameter

OZ . . . . . Ornstein-Zernike

PCA . . . . . Principal component analysis

PL . . . . . Parsons-Lee

PMF . . . . . Potential of mean force

PW . . . . . Pynn-Wulf

SVD . . . . . Singular value decomposition

TCF . . . . . Total correlation function

TEM . . . . . Transmission electron microscopy

UCA . . . . . Unconfined chain approximation

WCA . . . . . Weeks-Chandler-Andersen

Chirality has become arguably the most important and complex topic of research in liquid crystals today.

— John William Goodby, FRS [1]

1 Introduction

Contents

1.1 Liquid crystals and colloidal self-assembly

Colloidal suspensions, from the Greek κωλλα (glue) [2], correspond to systems of insoluble particles with typical dimensions ranging from 1 nm to 1 µm, often metonymically referred to as *colloids*, dispersed in a (usually liquid) solvent [3]. Common examples include biological fluids (e.g., blood and milk) and fast-moving consumer goods (from shaving cream to mayonnaise), along with an impressive variety of industrial products and processes — ranging from paints and lubricants to the making of paper and rubber.

Beyond these numerous occurrences and their considerable intrinsic applications, colloids have garnered increasing interest in recent years from the perspective of

materials science, motivated by rapid experimental progress in the synthesis of micro- and nano-particles with complex shapes and tunable interactions [4]. In this context, the appeal of colloidal suspensions lies in the ability of the dispersed particles to arrange themselves into organised arrays based on their molecular morphology and assembly environment, in the absence of external human intervention. This fascinating phenomenon is commonly referred to as *colloidal self-assembly*, reflecting both the spontaneous character of the formation of such aggregates and the weak magnitude of the forces involved in their stabilisation — typically of the order of the solvent thermal energy [5].

The versatility of this ordering process and the relative simplicity of its experimental implementation have been exploited in a multitude of technological applications, such as the production of nano-structured solids for heterogeneous catalysis and of semiconductor superlattices for quantum dot solar cells [6]. More generally, colloidal self-assembly constitutes a remarkable illustration of the so-called *bottom-up* fabrication paradigm, which aims to achieve arbitrary target structures through the sole rational design of their elementary microscopic "building blocks", and could thus provide a potential cost-effective and scalable alternative to the current standard *top-down* techniques for nanoscale patterning — in which a bulk material is instead gradually processed down to the desired shape [7].

Therefore, considerable efforts have been dedicated to the elucidation of the physical and chemical principles governing the relationship between molecular properties and macroscopic organisation in colloid-based nanomaterials. In many cases, the transition from an amorphous fluid to a fully-crystalline solid was found to involve a surprisingly-complex succession of partially-ordered phases, collectively known as *liquid crystals* (LCs) [8]. The intermediary nature of the structural and mechanical characteristics of LCs, lying in-between those of the liquid and solid states of matter, motivates their broad classification under the term of *mesophases* — while LC-forming molecules are commonly referred to as *mesogens* — and has progressively established LCs as a major research area in their own right over the last decades.

1.1.1 Mesophase ordering and macroscopic organisation

The hallmark characteristic of LCs lies in the singular coexistence of long-ranged order and fluidity, which often leads to unusual combinations of physical properties — such as their ability to exhibit an elastic response to macroscopic deformations while retaining a liquid-like mesogen motion within their organised structures [9]. LC phases typically arise from a specific set of morphological and chemical features displayed by their constituent particles, the most notable of which being shape anisotropy. In other words, such particles are usually elongated along one or more directions, and therefore generally possess both a long and a short axis — respectively defined as the directions of maximum and minimum extent of their molecular backbone.

A remarkable consequence of this microscopic anisotropy is the wealth of symmetry-breaking transitions involved in LC phase-ordering kinetics, as not only the positions, but also the orientations of the molecules may display long-ranged correlations [9]. Therefore, LCs are characterised by a degree of orientational order, potentially associated with a form of positional organisation — leading to a considerable variety of macroscopic arrangements [10]. Instances of LC structures formed by colloidal systems abound in nature, spanning the formation of phospholipid bilayers in cell plasma membranes [11], the arrangements of F-actin filaments in the cytoplasm [12] and of haemoglobin chains in sickle-cell anaemic blood [13].

A unifying feature of these colloidal (or *lyotropic*) LCs lies in their strong dependence on concentration, with the shift from a disordered *isotropic* dispersion to a partially-ordered state being typically observed upon increasing the particle density beyond a certain critical, system-specific threshold [14]. This behaviour sets lyotropics apart from the *thermotropic* class of LCs, whose macroscopic structure is instead largely determined by temperature following the familiar pattern of common phase transitions. Interestingly, the relative insensitivity of lyotropic LCs to temperature constitutes a signature of the predominant role of entropy in their thermodynamic stability, and provided the first historical challenge to

our naive perception of entropy as a mere measure of microscopic "disorder", as discussed further in Section 1.1.2.

The simplest example of lyotropic LC assembly is the so-called *uniaxial nematic phase*, in which one of the molecular axes points on average in a particular direction called the *nematic director*, denoted by $\mathbf{n}$, while retaining fluid-like positional disorder. The resulting phases may then be qualified as *prolate* or *oblate*, respectively referring to the local orientational order of the particle long or short axes. This structural anisotropy bestows upon nematic LCs a strong optical birefringence [15], much like regular uniaxial crystals, along with unique electrical [16] and rheological [17] properties. In the absence of external aligning forces, the director generally fluctuates throughout the sample, and is therefore usually referred to as a *director field* $\mathbf{n}(\mathbf{r})$, with $\mathbf{r}$ the spatial coordinate vector. Less commonly, both the long and short mesogen axes may simultaneously display long-ranged correlations, thus instigating the *biaxial* class of nematic LCs, whose local structure may be generally described in terms of a full orthonormal director triad $\left[\mathbf{l}(\mathbf{r}) \;\; \mathbf{m}(\mathbf{r}) \;\; \mathbf{n}(\mathbf{r})\right]$ [18].

Further increases in particle concentration typically lead to the incremental stabilisation of positionally-ordered phases, broadly categorised in terms of the dimensionality of their lattice structure. The so-called *smectic* state refers to molecular arrangements characterised by a 1D periodicity along a fixed direction in space, with an extensive letter-based nomenclature (smectic A to H) describing the potential symmetries of the mesogen distribution within each layer [10]. In the case of amphiphilic molecules, comprising both hydrophilic (polar) and hydrophobic regions, each of these individual sheets instead takes the form of a bilayer, in which all particle polar groups lie on the outer surface to shield the hydrophobic sections from the aqueous solvent — thus giving rise to the *lamellar* phase. *Columnar* assemblies represent the next level of positional organisation, in which mesogens spontaneously form an array of cylindrical aggregates disposed in a (usually rectangular or hexagonal) lattice-like 2D pattern. The high thermal stability of these various structures, combined with their facile manipulation through the use of external

fields and controlled confinement conditions, renders them suitable for a wealth of potential applications, ranging from drug delivery and nano-templating to the synthesis of defect-free macroscopic crystals for organic electronics and energy conversion purposes [19, 20].

In this thesis, we largely restrict our focus to the case of prolate nematic LCs, typically formed by systems of *calamitic* (i.e., rod-like) particles, which arguably constitute the most common and iconic contemporary example of LC order. Such phases play a central role in a number of biological and industrial processes, such as the spinning of spider silk and high-performance fibres (e.g., Kevlar® and Twaron®) [21], but also provide the basis for the ubiquitous liquid crystal display (LCD) technology in modern electronic devices, as discussed in Section 1.2.1. More specifically, we shall pay particular interest to an important instance of spatial modulation of the nematic director known as the *cholesteric* structure, which will be thoroughly introduced in Section 1.2. However, it is worth first taking the time to briefly recall the general theoretical considerations pertaining to the investigation of self-assembly in colloidal suspensions.

1.1.2 Modelling the self-assembly of lyotropic LCs

Let us consider a closed system of colloidal particles dispersed in a solvent with fixed volume V in the *canonical ensemble*, in which the sample may freely exchange energy with a surrounding heat bath at fixed temperature T. The second law of thermodynamics states that the spontaneous evolution of the system tends to minimise its Helmholtz free energy $\mathscr{F}$,[1]

$$\mathscr{F} = E - TS. \tag{1.1}$$

In Eq. (1.1), E denotes the total internal energy, which arises from the kinetic energy and mutual interactions of the solvent and colloidal particles, and S is the Gibbs entropy,

$$S = -k_b \sum_i \Pi_i \log \Pi_i, \tag{1.2}$$

[1] Note that $\mathscr{F}$ is sometimes also referred to as the *intrinsic* Helmholtz free energy, reflecting the assumed absence of external forces acting on the sample in the formulation of Eq. (1.1).

with k_b the Boltzmann constant, and Π_i the probability to find the solvent-colloid mixture in any given *microstate* i — generally defined by the specification of the detailed positions, orientations, linear and angular momenta of each of its constituent molecules.

The statistical account of entropy underlying Eq. (1.2) is often explained in terms of the characteristic Brownian motion observed in typical colloidal systems, in which the configurations and velocities of the colloids fluctuate randomly on a sub-microsecond basis due to their continual collisions with the much-smaller solvent molecules. As a result of these fast stochastic dynamics, ensembles of colloidal particles are in principle able to explore the full extent of their accessible microstates over experimentally-relevant time-scales,[2] with the frequency of occupation of each microstate i providing a possible measure of the probability Π_i. Note that this simplified picture neglects the explicit contributions of the solvent to the total entropy S in Eq. (1.2), and therefore relegates the influence of solvent effects in Eq. (1.1) to the internal energy E. In this level of approximation, a common approach is to treat the solvent molecules *implicitly* by incorporating solvent-mediated forces into an "effective" colloid-colloid interaction potential, so that the equilibrium macroscopic properties of the sample may be fully determined from the distribution $\{\Pi_i\}$ of colloid microstates associated with the global minimum of $\mathscr{F}$ [23, 24].

Despite the remarkable successes of this simple thermodynamic description for the prediction of the phase diagrams of various colloidal systems [25], the intuitive interpretation of its implications has long been a matter of scientific debate, with a particularly enduring controversy surrounding the role of entropy on phase ordering. Indeed, it easy to show that for a given total number W of distinct accessible microstates, Eq. (1.2) admits a strict global maximum in the case of the uniform distribution $\Pi_i = 1/W$, in which all microstates are equiprobable, associated with an entropy $S_{\max}$ of the famous Boltzmann form [26],

$$S_{\max} = k_b \log W. \tag{1.3}$$

[2] This postulate, known as the *ergodic hypothesis*, constitutes a fundamental assumption of statistical mechanics. Its validity and potential shortcomings have been the subject of a considerable body of research; see, e.g., Ref. [22] for a brief historical overview.

This observation seemingly leads to the conclusion that the minimisation of the entropic contribution $-TS$ in Eq. (1.1) tends to drive our sample towards a macroscopic state in which its constituent colloids are equally likely to adopt any possible set of microscopic positions and orientations — and thus promotes maximal molecular "disorder". Early statistical physicists were therefore drawn to the notion that a spontaneous increase in the degree of visible order of a closed system inevitably stems from a decrease in its internal energy E, in order to offset the ensuing loss of entropy in the total free energy $\mathscr{F}$ [27, 28].

However, this consensus started to erode with the landmark simulation study of Alder and Wainwright [29], corroborated experimentally by Pusey and van Megen nearly 30 years later [30], which provided unequivocal evidence that systems of spherical colloids interacting through (nearly-)pure steric repulsion — colloquially known as "hard spheres" — undergo a crystalline transition at sufficiently high concentrations. This result is somewhat surprising, as the internal energy of such particles is by definition entirely of kinetic origin, and therefore independent of density. Hence, Eq. (1.1) implies that their observed freezing transition must necessarily be attributed to an increase in entropy, in apparent contradiction with the previous discussion.

This paradox may be resolved by remarking that while S is maximised by a uniform microstate distribution at fixed W, the extremal entropy $S_{\max}$ in Eq. (1.3) is an increasing function of W. Thus, an alternative means of increasing the entropy S of an arbitrary sample is to simply increase its number W of accessible microstates. It follows that the entropic loss arising from a shift of the distribution $\{\Pi_i\}$ away from uniformity may be potentially mitigated if the corresponding change in macroscopic state is accompanied by an increase in W. In the case of a classical colloidal system, in which all molecular degrees of freedom are continuous, W may be more rigorously described in terms of an accessible volume in the so-called *phase space*, which represents all possible colloid configurations and momenta. Therefore, a concise reformulation of the previous statement is that a spontaneous deviation

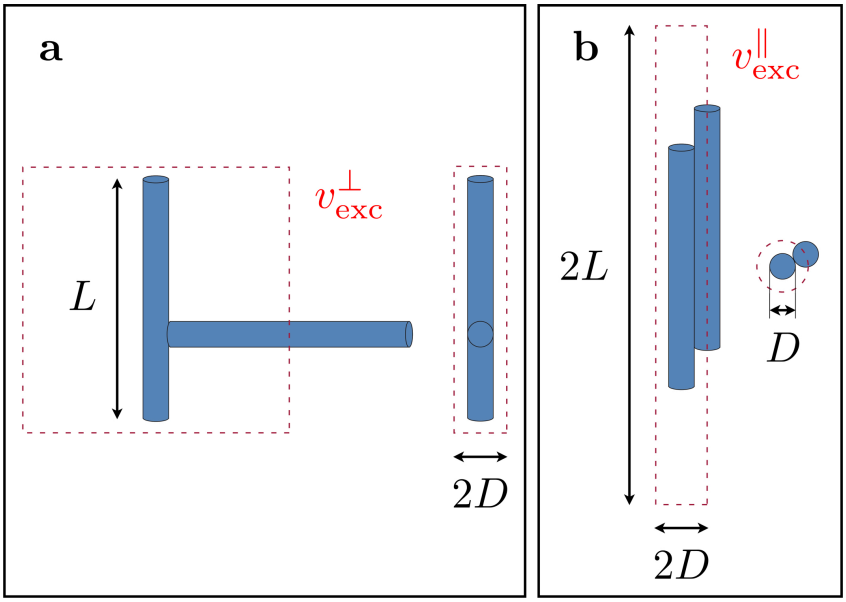

Figure 1.1: Entropic forces and orientational order in hard-rod colloids. a) Side and top views of two perpendicular cylindrical rods with identical diameter D and length L at close contact. The presence of the first rod prevents the centre of mass of the second rod from penetrating a finite geometric volume $v_{\mathrm{exc}}^{\perp}$, delimited by the red dashed lines. b) Same as a) in the case of two parallel rods, represented with their corresponding mutual excluded volume $v_{\mathrm{exc}}^{\parallel}$. Adapted with permission from Ref. [28].

from a uniform particle distribution may be entropically favourable, provided that it results in a large-enough increase in the volume of the available phase space.

An instructive illustration of this general tradeoff mechanism for our purposes is the case of colloidal hard rods. Such systems typically exhibit a fully-disordered isotropic phase at low concentrations, in which rod positions and orientations are uniformly distributed throughout the sample. However, steric interactions imply that each individual rod is associated with a finite volume v_{exc} that is inaccessible to any other particle in the sample. As depicted in Figure 1.1 for a pair of cylinders with diameter D and length L, v_{exc} usually depends on the relative orientations of vicinal molecules; in the limit of high particle aspect ratios ($L \gg D$), v_{exc} is minimal when the rods lie parallel to one another ($v_{\mathrm{exc}}^{\parallel} \simeq 2\pi L D^2$) and maximal if they are perpendicular ($v_{\mathrm{exc}}^{\perp} \simeq 2L^2 D$). Therefore, elongated calamitic mesogens may generally increase the volume of their accessible phase space by collectively aligning along a local arbitrary direction.

This effect only becomes statistically significant when the excluded volume $\overline{v}_{\rm exc}$ averaged over all possible relative molecular orientations is of comparable order of magnitude to the typical mean volume $v_{\rm free}$ available to the centre of mass of each particle. Denoting by N the fixed number of colloids in the sample, we obtain

$$v_{\rm free} \simeq \frac{V}{N} \equiv \frac{v}{\eta} \propto \frac{LD^2}{\eta},$$
$$\overline{v}_{\rm exc} \propto v_{\rm exc}^{\perp} \propto L^2 D,$$

where we introduced the particle volume fraction $\eta \equiv Nv/V$, with $v = \pi LD^2/4$ the physical rod volume, and used $v_{\rm exc}^{\perp} \gg v_{\rm exc}^{\parallel}$ for $L \gg D$. Thus, we crudely expect the system to undergo a spontaneous transition from a disordered isotropic state to an orientationally-ordered prolate nematic phase around a rough critical volume fraction η_c such that

$$\overline{v}_{\rm exc} \propto v_{\rm free} \implies \eta_c \propto \frac{D}{L}.$$

The first quantitative theoretical account of this phenomenon was provided in Onsager's seminal 1949 paper [31], which remarkably predates the numerical findings of Alder and Wainwright by nearly 10 years [29]. In this original approach, which prefigures the modern formulation of classical density functional theory (DFT), the previous discussion of relative isotropic/nematic (I/N) stability is equivalently rephrased in terms of the competition between *rotational entropy*, which promotes a uniform distribution of rod orientations, and a so-called *packing entropy*,[3] which favours the minimisation of the excluded volume per particle arising from mutual interactions. Furthermore, Onsager was able to show that the I/N transition is of the *first order*, and therefore generally occurs through the nucleation and growth of an ordered region within the disordered phase, and vice versa — similarly to the familiar freezing/melting process of common substances.

Ever since its first inception, the Onsager theory has played a continuous and fundamental role in the evolution of our understanding of lyotropic LCs, and provides

[3] Note that this packing entropic contribution is often inaccurately interpreted as an effect of *translational entropy* in this context [27, 28]. However, due to the absence of positional order in the nematic phase, it will be shown in Chapter 2 that translational entropy is actually unaffected by the onset of nematic order in the Onsager theory, and therefore plays no role in the I/N transition.

the basis for many of the results presented in this thesis; its formal mathematical framework will be introduced in detail in Chapter 2.

1.2 Introduction to lyotropic cholesteric LCs

For now, it is worth remarking that virtually all experimentally-relevant mesogens invariably deviate from the simple cylindrical shape originally considered by Onsager, and assumed in our previous qualitative treatment of nematic ordering. For instance, many common molecules do not possess an axis of continuous rotational symmetry, or lack an internal symmetry plane. A prominent consequence of their nontrivial atomic arrangements is expressed in the concept of *molecular chirality*, as originally articulated in the famous words of Lord Kelvin [32]:

> *I call any geometrical figure or group of points "chiral", and say it has chirality, if its image in a plane mirror, ideally realized, cannot be brought to coincide with itself.*

This absence of mirror symmetry is epitomised by the human hand, which provides the etymological basis of Kelvin's terminology (Greek: χειρ, hand). In keeping with this anatomical analogy, chiral compounds are often associated with a left or right *handedness*, so as to distinguish their structure from that of their mirror reflection. This somewhat-arbitrary nomenclature is usually fixed by international chemical conventions; in the case of organic molecules, the standardised protocol for the attribution of molecular handedness is provided by the so-called Cahn-Ingold-Prelog (CIP) priority rules [33].

The experimental discovery of molecular chirality in 1848 by Pasteur [34], who was able to isolate the left-handed form of sodium ammonium tartrate from its right-handed *enantiomer*,[4] constitutes a major milestone in the history of modern chemistry. The subtle chiral structure of a given compound is now universally recognised to have a profound effect on its chemical functions. For example, the right-handed form of limonene (R-limonene) is responsible for the fragrance of oranges, and acts as a popular flavouring agent in food manufacturing — while its

[4] In chemistry, *enantiomers* refer to the pair formed of a chiral molecule and its mirror image.

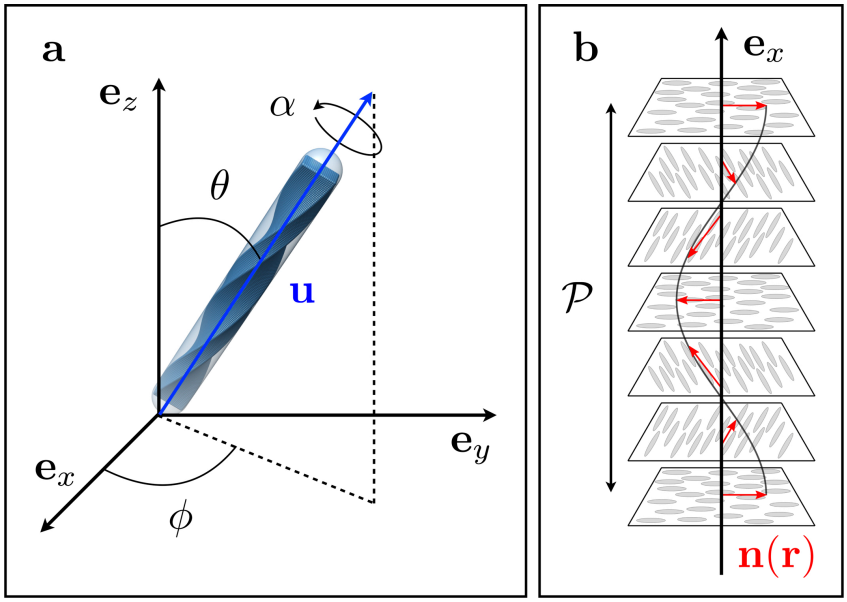

Figure 1.2: Cholesteric structure and angular parametrisation. a) Example of a calamitic chiral mesogen with long axis $\mathbf{u}$. b) Sketch of a right-handed prolate cholesteric phase of axis $\mathbf{e}_x$, director field $\mathbf{n}$ and pitch $\mathcal{P}$.

left-handed enantiomer (L-limonene) possesses a strong turpentine scent, and is mostly employed as an industrial solvent. More dramatically, L-methamphetamine is commonly used as a mild active ingredient in over-the-counter nasal decongestants, while its mirror image (R-methamphetamine, commonly referred to as "crystal meth") is a potent psychotropic drug. The control and analysis of molecular chirality is therefore of fundamental importance for chemical design and synthesis, especially in the context of pharmacology, and constitutes a focal point of the field of *stereochemistry* [35].

In LC assemblies, the presence of molecular chirality in some or all of the constituent mesogens generally results in a spontaneous breaking of the mirror symmetry of the mesophases formed. The most frequent manifestation of this macroscopic chirality in the case of nematic systems lies in the stabilisation of a helical modulation of the director field about a local normal axis, which is typically uniform throughout the sample in the absence of physical boundaries (Figure 1.2) [9]. The equilibrium bulk structure of such arrangements, known as *cholesteric phases*, may thus be described in terms of a single length-scale $\mathcal{P}$, termed the *cholesteric pitch*, corresponding to the spatial period of their uniform director rotation.

The helical symmetry of the cholesteric phase allows for the simple determination of its handedness using the so-called *right-hand rule*: a helix is qualified as right-handed (resp. left-handed) if, when viewed along the direction of its helical axis, a clockwise screwing motion drives it away from (resp. towards) the observer (Figure 1.2b). Note that this definition of handedness is independent of the perspective of the viewer, as chirality is an intrinsic property of the object considered; a right-handed helix may only be made to appear left-handed when visualised through a mirror. In the case of cholesterics, the handedness of the phase may be conveniently represented by the sign of the pitch $\mathcal{P}$, with the common convention that $\mathcal{P} > 0$ (resp. $\mathcal{P} < 0$) corresponds to a right-handed (resp. left-handed) macroscopic arrangement.

1.2.1 Biological relevance and applications

Lyotropic LCs play an essential role in biology, in which their combination of macroscopic order and molecular mobility is indispensable to many of the basic functions of living organisms [36]. This natural ubiquity, combined with the chiral character of most common biomolecules, leads to the recurring appearance of lyotropic cholesteric LC (LCLC) structures throughout the plant and animal kingdoms (Figure 1.3) [37]. However, the earliest observation of a cholesteric phase was initially reported by Friedrich Reinitzer in a thermotropic system in 1888 [38], in a study generally hailed as the first experimental description of LC organisation [39].

Reinitzer, a botanist, noticed that cholesteryl benzoate crystals extracted from carrot roots displayed two apparent "melting points" — a first at about 145 °C, at which the solid turned into a cloudy liquid with iridescent hues, and a second at around 178 °C, at which the liquid suddenly cleared up to become fully transparent. The observed iridescence of the intermediary phase was later recognised as an effect of selective light reflection within the liquid, and interpreted as evidence of its underlying spatial periodicity (see below); its macroscopic arrangement was finally elucidated in full by Georges Friedel, who christened it as "cholesteric" in 1922 [43].

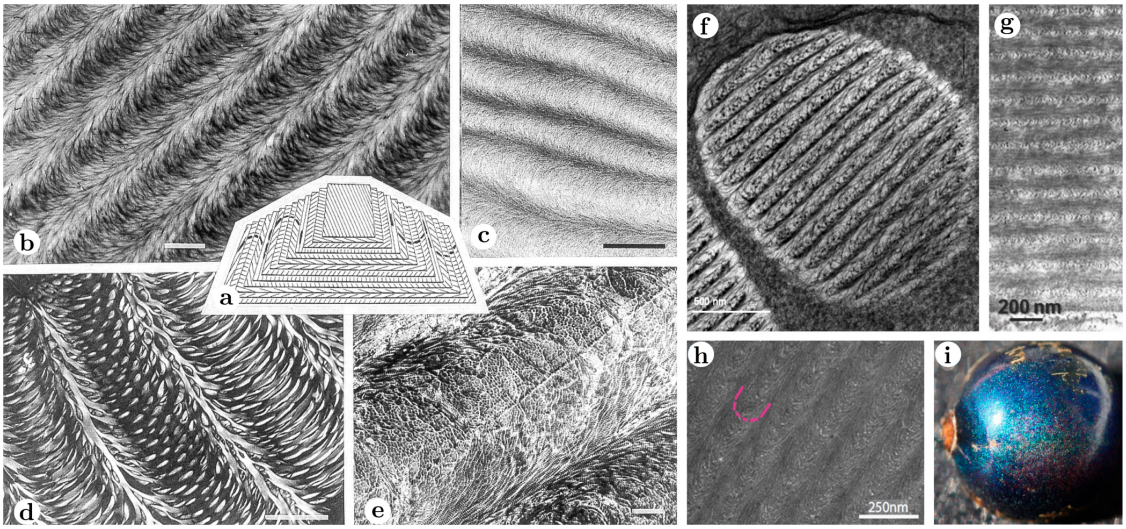

Figure 1.3: LCLC organisation in living matter. a) The "twisted plywood" model, interpreting the characteristic periodic arced patterns commonly observed in biological samples as oblique slices of an underlying cholesteric structure [40]. b) Transmission electron microscopy (TEM) view of the chitin-protein matrix in a decalcified crab cuticle (scale: 2 µm). c) TEM view of plant cell walls in the skin of a pear (scale: 0.5 µm). d) Collagen network in the dermal scutes of a fish, visualised in polarised light microscopy (scale: 40 µm). e) TEM view of collagen fibrils in decalcified human compact bone osteon (scale: 1 µm). f) TEM view of a *P. micans* dinoflagellate chromosome (scale: 0.5 µm). g) TEM cross-sectional view of plant cell walls in a *D. nodosa* leaf (scale: 0.2 µm). h) TEM cross-sectional view of the epicarp of *P. condensata* (scale: 0.25 µm). i) Matching photograph of a *P. condensata* fruit, exhibiting the strong iridescence typical of structural colouration (fruit diameter: 5 mm). Adapted with permission from Refs. [37], [41] and [42].

The remarkable *reflective* optical properties of cholesterics, pivotal to their original historical identification, stem from the fact that typical cholesteric pitches usually range from a few hundred nanometers to a few microns, and are thus generally comparable to the wavelengths of visible light (∼400 nm to ∼800 nm). As depicted in Figures 1.2b and 1.4a, the structure of *apolar* cholesteric LCs — in which the directions of local alignment $\mathbf{n}$ and $-\mathbf{n}$ are equivalent — may be schematically represented as a succession of parallel "cholesteric planes", separated by a distance $\mathcal{P}/2$ along the cholesteric axis. Therefore, the constructive interference of the light waves scattered (elastically) by the different planes imposes that the difference in optical path lengths between consecutive reflections is commensurate with the wavelength λ of the incident light [44]. This condition yields the so-called

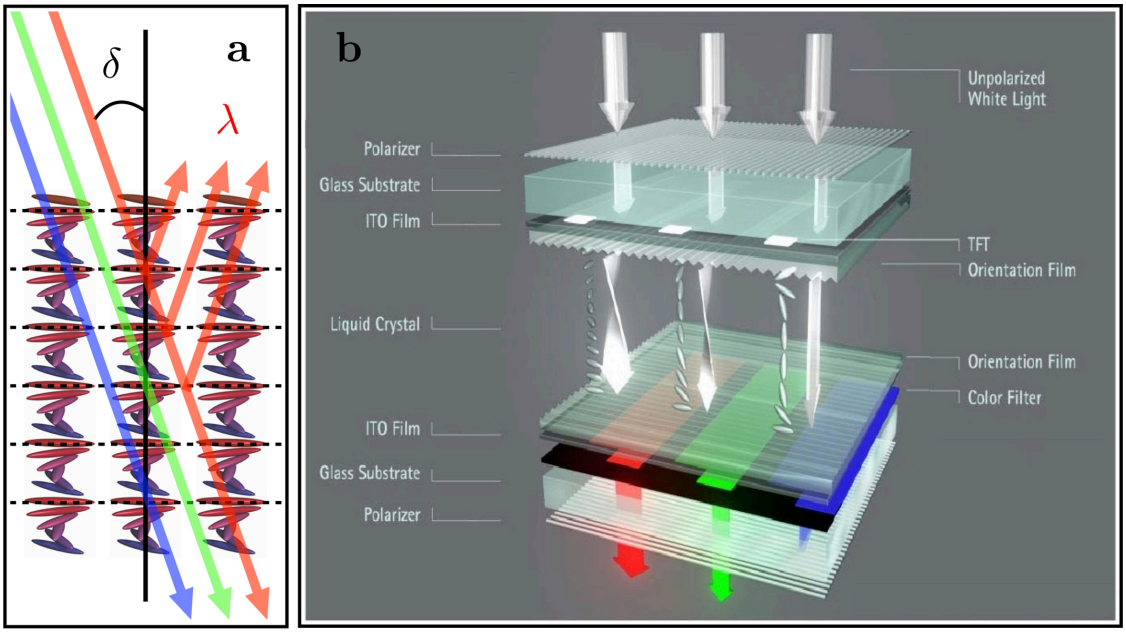

Figure 1.4: Bragg reflection and light transmission in cholesterics. a) Illustration of Bragg reflection in a cholesteric structure. Destructive interferences between the scattered light waves result in the selective reflection of wavelengths λ depending on the viewing angle δ (Eq. (1.4)). b) Working principle of a twisted nematic cell. A layer of chiral nematic LC is confined between two crossed polarisers. In the absence of external fields, the twist of the phase rotates the direction of polarisation of the incident light by 90° as it traverses the sample, allowing it to be transmitted through the device. This twist may be gradually eliminated by the application of an electric field of increasing voltage, which progressively inhibits the transmission of light through the crossed polarisers.

Bragg law, relating λ and $\mathcal{P}$ to the angle of incidence δ,

$$m\lambda = \overline{n} \times \mathcal{P} \cos\delta, \tag{1.4}$$

with $\overline{n}$ the average refractive index of the phase and m a positive integer. Hence, when λ and $\mathcal{P}$ are of comparable magnitude and respectively in and near the visible light range, Eq. (1.4) gives rise to the angle-dependent selective reflection characteristic of iridescence, which provides the *structural colouration* of cholesteric materials.

Conversely, a notable *transmissive* property of cholesterics is their strong optical rotatory power, as the combination of helical twist and local nematic birefringence leads to the periodic rotation of the plane of polarisation of incident light waves as they propagate through the sample [44]. The most prominent application of this phenomenon may be found in the *twisted nematic cell*, which single-handedly triggered the advent of modern LCDs [39]. Such devices mostly consist in a thin

layer of chiral nematic LC, which may be conceptually visualised as a cholesteric sample of thickness $\mathcal{P}/4$, enclosed within a crossed-polariser setup (Figure 1.4b). The twist of the phase may be suppressed by the application of a uniform electric field through the so-called Fréedericksz effect, in which the coupling between field lines and induced molecular dipoles acts as an effective aligning torque on the mesogens [16]. Individual pixels may thus be reversibly switched from a bright to a dark state by varying the field voltage between 0 and a finite critical threshold [9].

While this early LCD design, now largely phased out [39], originally made use of thermotropic chiral LC materials, the abundant biological occurrences of their lyotropic counterparts have inspired an increasing variety of biomimetic applications in recent years, and motivated further investigations of the functions of LCLC order *in vivo*. The extraordinary resistance of the crustacean exoskeleton has been attributed to the mineralised cholesteric patterns formed by its constituent chitin fibres (Figure 1.3b), which allows for an optimal dissipation of kinetic energy during impact events, and has been suggested for the fabrication of advanced structural armour [45]. The cholesteric arrangement of collagen fibrils in human compact bone osteon (Figure 1.3e) could be reasonably surmised to serve a similar purpose. The striking colours of the *P. condensata* fruit (Figure 1.3i) are the most brilliant of any known land-based organism [46], and arise from the selective reflection of light by multiple cholesteric cellulose domains in its epicarp (Figure 1.3h). This bright colouration facilitates their detection by seed-dispersing animals, and has been exploited in the production of chiral reflectors [47]. The singular metallic hues of several beetle species ("jewel beetles") also result from the LCLC arrangement of their chitin-based cuticles, which plays a central role in both their thermoregulation and sexual selection [37], and has motivated the development of cholesteric films with broadband reflective properties for energy efficiency applications [48].

Although far from exhaustive [37,48–50], the diversity of the list above would suggest the emergence of LCLC order in biology to proceed from a set of convergent evolutionary mechanisms. However, *in vitro* studies revealed a surprisingly-strong

dependence of cholesteric assembly on both particle structure and assembly conditions, and evidenced the striking complexity of the general rules governing LCLC organisation. For instance, the change of a single amino-acid in the coat proteins of filamentous *fd* viruses suffices to switch their spontaneous cholesteric twist from left- to right-handed, and to induce a five-fold relative variation in the magnitude of their corresponding pitches [51]. Puzzlingly, this macroscopic twist was found to persist even when the viruses are coated with a polymer layer thick enough to screen their electrostatic interactions entirely [52]. Tobacco mosaic and Pf1 viruses, though morphologically similar to *fd*, do surprisingly not display any measurable phase chirality — presumably because their cholesteric pitch is too large to be observed experimentally [53, 54]. Short DNA oligomers have been shown to form both left- and right-handed LCLC phases, based on their length and detailed sequence [55]. More generally, the high sensitivity of cholesteric pitches to changes in particle concentration and solvent conditions — such as temperature, pH and ionic strength — has been extensively documented in a range of synthetic and bio-colloidal polymer systems (see, e.g., Refs. [56–62]), and has been exploited in the design of physical [63] and chemical [64] sensors.

Despite their singularly-long history and rich array of applications, the intricacy of the experimental phase behaviour of LCLCs has so far largely eluded attempts to resolve its microscopic underpinnings. As a result, the mechanisms of *chirality amplification* — referring to the hierarchical transfer of chirality from individual molecular units to higher-order assemblies — have remained poorly understood in cholesterics; their elucidation constitutes a long-standing challenge of soft-condensed matter theory, as discussed in the next paragraphs.

1.2.2 Theoretical challenges

The remarkable simplicity of cholesteric structures implies that their macroscopic chirality is entirely described by the sign and magnitude of the cholesteric pitch, which may in principle be obtained from a straightforward experimental analysis of their distinctive fingerprint-like texture (Figure 1.3). However, a fundamental

difficulty in microscopic theories of cholesteric order is that the underlying molecular chirality of their constituent mesogens is often much more ambiguous to quantify. For instance, while CIP rules lead to an identification of chirality based solely on the mass distribution of individual molecules, it is easy to see that other factors such as their distribution of charges may play an equally-significant role in determining the chiral inter-particle interactions underpinning their cholesteric assembly. In general, it may be shown that molecular chirality is characterised by an infinite set of pseudoscalar parameters [65], although this rather unwieldy description is of limited practical use for the prediction of the cholesteric pitch of any given mesogen model [66]. Therefore, molecular chirality is usually treated as a purely "binary" quantity, characterised only by its presence or its absence, which largely precludes a general discussion of the quantitative link between molecular and phase chirality in broad, system-independent terms.

More concretely, the macroscopic twist of (prolate) LCLCs is governed by the competition between the propensity of calamitic mesogens to locally align, following the arguments of Section 1.1.2, and the geometric frustration arising from the incompatibility of their molecular chirality with uniform orientational order. The delicate interplay of these two contributions is hard to capture accurately in experimentally-realistic systems, due to both the variety of microscopic interactions involved and the wide differences in the typical length- and time-scales associated with molecular and phase chirality. The former difficulty, which reflects the complex dependence of the cholesteric pitch on multiple physico-chemical factors, largely restricts the practical relevance of simple analytical models to purely qualitative discussions — while the latter generally limits the applicability of atomistic computational approaches to highly-idealised mesogen descriptions, for the reasons outlined below.

In this thesis, we mostly focus on LCLC systems in the canonical ensemble, using an implicit treatment of the solvent molecules (see Section 1.1.2). Standard molecular simulation techniques for the study of such colloidal dispersions can be broadly classified into molecular dynamics (MD) and Monte-Carlo (MC) methods.

In this context, the MD approach generally amounts to integrating the Newton equations of motion of the mesogens in the so-called Langevin formalism, in which effective colloid-colloid interactions are supplemented with damping and stochastic noise terms to approximate the role of the solvent as a thermal reservoir. These viscous and random forces are usually linked by fluctuation-dissipation relations, ensuring that the particles evolve towards a stationary state with fixed temperature T. Conversely, MC simulations directly sample the microstate distribution $\{\Pi_i\}$ describing the thermodynamic equilibrium of the system in the chosen ensemble (Eqs. (1.1) and (1.2)), based on an *ad hoc* set of stochastic trial moves for the colloids at every simulation step — such as that prescribed by the popular *Metropolis algorithm* [67]. Plenty of excellent introductions to MC and MD have been presented in the literature, and we refer the interested reader to, e.g., Refs. [68] and [69], along with the references provided in the relevant sections of this thesis, for more detailed discussions.

Although MC and MD lead in principle to equivalent statistical descriptions of equilibrium thermodynamics, the two approaches possess their own respective strengths and shortcomings. For instance, MD generally provides a physically-reasonable representation of the colloid dynamics, albeit with no account of hydrodynamic effects in the absence of explicit solvent interactions, and is well-suited for parallel calculations on distributed super-computing platforms. The latter advantage is particularly valuable due to the high numerical cost of LCLC simulations, as the large magnitude of the cholesteric pitch relative to typical particle dimensions requires the use of large sample sizes for the reliable determination of cholesteric properties in the case of experimentally-realistic mesogens. However, real LCLCs are often characterised by slow equilibration kinetics, with most experimental systems requiring several hours to several days to attain their full equilibrium state [54–62]. Such time-scales are far beyond the grasp of current computational capabilities [70], and may likely confine the reasonable reach of MD methods to strongly coarse-grained molecular models in this context [71, 72].

By contrast, the irrelevance of the molecular equations of motion in the MC framework potentially allows for a much faster equilibration, as the use of fairly large and possibly unphysical particle moves does usually not affect the convergence or numerical stability of MC simulations [69]. Furthermore, the energy-based formalism of MC obviates the calculation of inter-molecular forces, and therefore allows for the treatment of non-differentiable interaction potentials — such as in the case of pure hard-body repulsion. However, the sequential nature of general-purpose MC algorithms renders them difficult to parallelise, and thus often impractical for the study of large samples [73] — which may largely restrict their applicability to simplified LCLC systems with unrealistically-short cholesteric pitches [74].

Other limitations shared by MC and MD descriptions of LCLCs include the unsuitability of standard periodic boundary conditions, commonly employed to emulate bulk phases in simulations of finite-size samples, as the intrinsic periodicity of cholesteric structures would require the system dimensions to be commensurate with their *a priori* unknown cholesteric pitch to avoid spurious distortion effects [75]. Several workarounds have been proposed, usually based on the use of hard confining walls normal to the cholesteric axis [72,74] or on the study of the thermodynamic response of the sample to artificial under- and over-twisted boundary conditions [75–81]. While the latter approach could potentially alleviate some of the previous restrictions, it only provides for an indirect measurement of the cholesteric pitch through the introduction of additional analytical assumptions [75,76], and further investigations of its quantitative accuracy would be desirable. Finally, both MC and MD are generally unable to efficiently handle highly-anisotropic molecules, as small fluctuations in their orientations may lead to large displacements of the particle extremities — and thus require the use of either very short MD integration timesteps to prevent unphysical particle overlaps, or very small MC rotational trial moves to avoid systematic rejection.

This last restriction is also problematic, as many common experimental LCLC mesogens, such as filamentous viruses and cellulose nanocrystals, are characterised by high molecular aspect ratios. Such systems, however, conveniently fall within

the scope of the Onsager theory, which is asymptotically exact in the limit of large particle anisotropy (see Chapter 2). Furthermore, the Onsager DFT may be readily extended to the description of cholesteric phases by introducing macroscopic chirality *perturbatively*, as first proposed by Straley [82], and by thus exploiting the separation of length-scales between molecular dimensions and equilibrium cholesteric pitch (see Chapter 3). Therefore, DFT is naturally well-suited to the experimentally-relevant regime of high particle aspect ratios and long cholesteric pitches, which is not easily accessible in molecular simulations.

However, most DFT investigations of cholesteric organisation to date have been limited by analytical constraints to highly simplified particle models, and further had to resort to a number of *ad hoc* approximations for the tractable inclusion of chiral contributions in the virial formalism of the Onsager theory [83–91]. Some attempts to tackle more realistic systems — including both steric and soft repulsion — represented significant steps forward, but were still hindered by a cumbersome mathematical procedure and multiple simplifying assumptions [92–94]. A notable development was recently achieved though the introduction of a general and accurate numerical framework capable of handling arbitrarily complex particle shapes and interaction potentials [95,96], although the non-perturbative treatment of phase chirality employed in this approach renders its computational costs largely prohibitive in the case of experimentally-relevant systems.

1.3 Thesis outline

In this thesis, we aim to make progress towards an efficient, comprehensive and quantitatively-reliable molecular theory of cholesteric order in LCLC assemblies of arbitrary particles. Our method, based on the combination of an accurate numerical implementation of the Onsager-Straley DFT with high-performance virial integration techniques and single-molecule simulations, may be conveniently applied to a wide variety of mesogen models, both rigid and flexible. Its ability to take into account the full details of their microscopic Hamiltonian representation allows for the straightforward application of theory and simulations to identical

particle descriptions — and thus lends itself to a thorough examination of the different physical assumptions underpinning the DFT framework, and of their potential shortcomings in the case of cholesteric phases. The practical significance of our approach is illustrated through its application to experimental systems of DNA origamis, which enables us to evidence a novel general paradigm of chirality amplification in LCLCs driven by conformational statistics, rather than ground-state structure or specific inter-molecular interactions.

The thesis is organised as follows. We provide in Chapter 2 a thorough first-principle introduction to the Onsager DFT, and discuss its extensions to cholesteric (and, more generally, non-uniform nematic) phases in Chapter 3. We describe in Chapter 4 an original computational scheme to considerably accelerate inter-molecular energy evaluations for highly-anisotropic particles in the context of the Onsager-Straley theory, and dedicate Chapter 5 to the incorporation of mesogen flexibility into our hybrid numerical and theoretical framework. We finally present the results of the application of our approach to experimentally-relevant DNA origami assemblies in Chapter 6, and recapitulate in Chapter 7 the main conclusions of the previous chapters, along with some prospective directions for future research.

The main results of this thesis have been reported in a number of peer-reviewed publications. The discussions of Chapters 2 and 3 form the basis of Ref. [97]; the methods introduced in Chapters 4 and 5 have been outlined in Refs. [98] and [99], respectively; the findings of the case study of Chapter 6 will be further presented in the forthcoming Ref. [100].

2

Classical DFT for uniaxial nematic LCs

Contents

The prediction of the observable properties of experimental systems from the nanoscale features of their molecular constituents constitutes the overarching goal of statistical mechanics. However, the prohibitive number of microscopic degrees of freedom associated with most macroscopic structures often renders this task rather daunting, even when their description is restricted to a purely classical treatment. Classical density functional theory (DFT) provides a particularly powerful theoretical tool to circumvent some of these difficulties by coarse-graining discrete microscopic variables into a continuous density field — while retaining the salient details of the underlying molecular interaction potentials. In this chapter, we formally introduce

the fundamental equations of DFT in the context of the Onsager theory, which underpins much of this thesis, before detailing their first application to the case of uniform uniaxial nematic phases. Some comparisons with the results of numerical simulations are finally presented for a few simple model systems, in order to illustrate the relative strengths and shortcomings of the theory in light of the various physical assumptions involved in its derivation.

2.1 The Onsager free energy functional

2.1.1 Ideal and excess free energies

As in Section 1.1.2, we consider a closed classical system of N arbitrarily-shaped particles, assumed to be infinitely rigid and indistinguishable, confined in a large finite volume V. The microscopic configuration of the system is generally determined by the specification of the centre-of-mass position vector $\mathbf{r}_i \in V$ and orientation matrix $\mathcal{R}_i \in SO(3)$ of each constituent particle $i \in [\![1, N]\!]$, where $SO(3)$ denotes the 3D rotation group. As detailed in Appendix A, we here choose to parametrise $\mathcal{R}_i$ in terms of the Euler angle triad $(\alpha_i, \theta_i, \phi_i)$ in the z-y-z convention (c.f. Figure 1.2a), and use the shorthand

$$\oint d\mathcal{R}_i \cdot \equiv \int_0^{2\pi} d\alpha_i \int_0^{2\pi} d\phi_i \int_0^{\pi} d\theta_i \sin\theta_i \cdot$$

for all integrals involving angular degrees of freedom.

Let us denote by m and $\mathcal{I}$ the mass and inertia tensor of the particles, respectively. In the absence of applied external fields, the so-called *intrinsic Hamiltonian* $\mathscr{H}_N$ of the system reads as

$$\mathscr{H}_N = \sum_{i=1}^{N} \left(\frac{1}{2m} \mathbf{p}_i^2 + \frac{1}{2} \boldsymbol{\ell}_i^{\mathsf{T}} \cdot \mathcal{I}^{-1} \cdot \boldsymbol{\ell}_i \right) + U_N\Big(\{\mathbf{r}_i\}_{i \in [\![1,N]\!]}, \{\mathcal{R}_i\}_{i \in [\![1,N]\!]} \Big), \tag{2.1}$$

with $\mathbf{p}_i$ and $\boldsymbol{\ell}_i$ the respective linear and angular momenta of particle i, $\mathcal{I}^{-1}$ the matrix inverse of $\mathcal{I}$ and U_N the total potential energy, which generally depends on all molecular positional and orientational degrees of freedom $\{\mathbf{r}_i\}$ and $\{\mathcal{R}_i\}$. Assuming the system to be in thermal equilibrium with a surrounding heat bath at given temperature T, the probability Π_N to find the N particles in a given

microstate $(\{\mathbf{p}_i\},\{\boldsymbol{\ell}_i\},\{\mathbf{r}_i\},\{\mathcal{R}_i\})$ is proportional to the Boltzmann weight associated with Eq. (2.1),

$$\Pi_N\Big(\{\mathbf{p}_i\},\{\boldsymbol{\ell}_i\},\{\mathbf{r}_i\},\{\mathcal{R}_i\}\Big) = \frac{1}{Z_N}\exp\Big[-\beta\mathscr{H}_N\Big(\{\mathbf{p}_i\},\{\boldsymbol{\ell}_i\},\{\mathbf{r}_i\},\{\mathcal{R}_i\}\Big)\Big], \tag{2.2}$$

where $\beta \equiv 1/k_bT$, and the normalisation factor Z_N is known as the *canonical partition function*,[1]

$$Z_N \equiv \frac{1}{h^{6N}N!}\int_{-\infty}^{+\infty} d\{\mathbf{p}_i\}\int_{-\infty}^{+\infty} d\{\boldsymbol{\ell}_i\}\int_{V^N} d\{\mathbf{r}_i\}\oint d\{\mathcal{R}_i\}\, e^{-\beta\mathscr{H}_N}. \tag{2.3}$$

In Eq. (2.3), h denotes the Planck constant, and we introduced the shorthand $d\{\mathcal{X}_i\} \equiv d\mathcal{X}_1\ldots d\mathcal{X}_N$ for all molecular degrees of freedom $\mathcal{X}_i$.

The total entropy S of the system may then be readily obtained from the distribution Π_N through the continuum (Shannon) form of Eq. (1.2) [26],

$$S = -k_b\Big\langle \log\Pi_N\Big\rangle_N, \tag{2.4}$$

with $\langle\cdot\rangle_N$ the *canonical average*,

$$\Big\langle\,\cdot\,\Big\rangle_N \equiv \frac{1}{h^{6N}N!}\int_{-\infty}^{+\infty} d\{\mathbf{p}_i\}\int_{-\infty}^{+\infty} d\{\boldsymbol{\ell}_i\}\int_{V^N} d\{\mathbf{r}_i\}\oint d\{\mathcal{R}_i\}\,\Pi_N\;\cdot\;. \tag{2.5}$$

Eqs. (2.2)–(2.5) directly lead to

$$k_b\log Z_N = S - \frac{1}{T}\Big\langle\mathscr{H}_N\Big\rangle_N \equiv S - \frac{E}{T},$$

where we invoked the first law of thermodynamics to substitute the equilibrium internal energy E for the Boltzmann-averaged intrinsic Hamiltonian $\langle\mathscr{H}_N\rangle_N$. Therefore, it follows from Eq. (1.1) that the intrinsic Helmholtz free energy $\mathscr{F}$ of the equilibrated system is fully determined by the canonical partition function Z_N,

$$\mathscr{F} = E - TS = -k_bT\log Z_N. \tag{2.6}$$

Let us attempt to work out a closed-form expression for $\mathscr{F}$ using Eq. (2.6). The decoupling of kinetic momenta and configurational degrees of freedom in Eq. (2.1) enables us to factorise their respective contributions to the integral in Eq. (2.3),

$$Z_N = Z_N^{\mathrm{id}}\times Q_N. \tag{2.7}$$

[1] Note that the volume V and temperature T of the sample are also held fixed in the canonical ensemble, but are here omitted from the relevant subscripts for readability.

In Eq. (2.7), Z_N^{id} denotes the "ideal" partition function in the absence of molecular interactions, which may be computed analytically as a generalised Gaussian integral,

$$\begin{aligned} Z_N^{\mathrm{id}} &\equiv \frac{(8\pi^2 V)^N}{h^{6N} N!} \int_{-\infty}^{+\infty} d\{\mathbf{p}_i\} \int_{-\infty}^{+\infty} d\{\boldsymbol{\ell}_i\} \, \exp\left\{ -\beta \sum_{i=1}^{N} \left(\frac{1}{2m} \mathbf{p}_i^2 + \frac{1}{2} \boldsymbol{\ell}_i^{\mathsf{T}} \cdot \mathcal{I}^{-1} \cdot \boldsymbol{\ell}_i \right) \right\} \\ &= \frac{(8\pi^2 V)^N}{h^{6N} N!} \left(\sqrt{2\pi m k_b T} \right)^{3N} \times \left(\sqrt{(2\pi k_b T)^3 \det \mathcal{I}} \right)^N, \end{aligned}$$

and Q_N is the so-called *configurational integral*,

$$Q_N \equiv \frac{1}{(8\pi^2 V)^N} \int_{V^N} d\{\mathbf{r}_i\} \oint d\{\mathcal{R}_i\} \, \exp\Big[-\beta U_N\big(\{\mathbf{r}_i\}, \{\mathcal{R}_i\}\big) \Big]. \tag{2.8}$$

Thus,

$$Z_N^{\mathrm{id}} = \frac{1}{N!} \left(\frac{V}{\lambda_{\mathrm{dB}}^3} \sqrt{\pi \left(\frac{T}{\Theta_r} \right)^3} \right)^N, \tag{2.9}$$

with λ_{dB} the thermal de Broglie wavelength and Θ_r the rotational temperature,

$$\begin{aligned} \lambda_{\mathrm{dB}} &\equiv \frac{h}{\sqrt{2\pi m k_b T}}, \\ \Theta_r &\equiv \frac{h^2}{8\pi^2 k_b \sqrt[3]{\det \mathcal{I}}}. \end{aligned}$$

Introducing the thermal length-scale

$$\lambda \equiv \lambda_{\mathrm{dB}} \sqrt{4\pi \frac{\Theta_r}{T}},$$

Eq. (2.9) may be compactly recast as

$$Z_N^{\mathrm{id}} = \frac{1}{N!} \left(\frac{8\pi^2 V}{\lambda^3} \right)^N. \tag{2.10}$$

Hence, Eqs. (2.6) and (2.7) yield the Helmholtz free energy in the general form

$$\mathscr{F} = \mathscr{F}_{\mathrm{id}} + \mathscr{F}_{\mathrm{ex}}, \tag{2.11}$$

where $\mathscr{F}_{\mathrm{id}}$ is the free energy of an ideal gas of non-interacting particles,

$$\mathscr{F}_{\mathrm{id}} \equiv -k_b T \log Z_N^{\mathrm{id}} = k_b T \left(\log N! + N \log \frac{\lambda^3}{8\pi^2 V} \right), \tag{2.12}$$

and $\mathscr{F}_{\mathrm{ex}}$ is the so-called *excess free energy* of the system, which takes into account all inter-molecular interactions,

$$\mathscr{F}_{\mathrm{ex}} \equiv -k_b T \log Q_N. \tag{2.13}$$

In the van Hove thermodynamic limit, in which $N \to \infty$ and $V \to \infty$ at fixed number density $\rho = N/(8\pi^2 V)$, one may invoke the Stirling approximation,

$$\log N! = N \log N - N + \mathcal{O}(\log N),$$

which leads to a simple expression for the Helmholtz free energy of an ideal anisotropic fluid with homogeneous density ρ,[2]

$$\beta \mathscr{F}_{\rm id} = N \Big\{ \log \big(\rho \lambda^3 \big) - 1 \Big\} + \mathcal{O}(\log N). \tag{2.14}$$

In the case of a non-homogeneous system, the density ρ generally takes the form of a position- and orientation-dependent field, which may be locally averaged over a mesoscopic volume $d\mathbf{r}$ and solid angle $d\mathcal{R}$. In this framework, the number $\delta^2 N(\mathbf{r}, \mathcal{R})$ of particles with centre-of-mass position $\mathbf{r}$ and orientation $\mathcal{R}$ within the elementary volume $d\mathbf{r} \times d\mathcal{R}$ reads as

$$\delta^2 N(\mathbf{r}, \mathcal{R}) = \rho(\mathbf{r}, \mathcal{R}) d\mathbf{r} d\mathcal{R}. \tag{2.15}$$

Let us assume $\rho(\mathbf{r}, \mathcal{R})$ to be a smooth, slowly-varying function of $\mathbf{r}$ and $\mathcal{R}$, so that the quantities $d\mathbf{r}$ and $d\mathcal{R}$ in Eq. (2.15) may be chosen to be large enough for the inequality

$$\delta^2 N(\mathbf{r}, \mathcal{R}) \gg \log \delta^2 N(\mathbf{r}, \mathcal{R})$$

to hold at all points $(\mathbf{r}, \mathcal{R})$ of the mesoscopic configurational space. Eq. (2.14) then yields the ideal free energy $\delta^2 \mathscr{F}_{\rm id}$ of the elementary volume $d\mathbf{r} \times d\mathcal{R}$, to leading order in $\log \delta^2 N(\mathbf{r}, \mathcal{R})$,

$$\beta \delta^2 \mathscr{F}_{\rm id}(\mathbf{r}, \mathcal{R}) = \delta^2 N(\mathbf{r}, \mathcal{R}) \Big\{ \log \rho(\mathbf{r}, \mathcal{R}) \lambda^3 - 1 \Big\}. \tag{2.16}$$

Using the extensivity of the Helmholtz free energy, the ideal free energy $\mathscr{F}_{\rm id}$ of the full non-uniform system may be readily obtained from Eqs. (2.15) and (2.16),

$$\begin{aligned} \beta \mathscr{F}_{\rm id} &= \beta \int_{\mathbf{r} \in V} \int_{\mathcal{R} \in SO(3)} \delta^2 \mathscr{F}_{\rm id}(\mathbf{r}, \mathcal{R}) \\ &= \int_V d\mathbf{r} \oint d\mathcal{R}\, \rho(\mathbf{r}, \mathcal{R}) \Big\{ \log \big[\rho(\mathbf{r}, \mathcal{R}) \lambda^3 \big] - 1 \Big\}. \end{aligned} \tag{2.17}$$

[2] In this thesis, we use the word *homogeneous* to refer to macroscopic systems which are both uniform and isotropic — i.e., whose physical properties are position- and orientation-independent.

Eq. (2.17) thus provides a generalised expression for $\mathscr{F}_{\rm id} = \mathscr{F}_{\rm id}[\rho]$ in the form of a *functional* of the mesoscopically-averaged density distribution $\rho(\mathbf{r}, \mathcal{R})$, which fully characterises the macroscopic structure of the fluid.[3] In this context, the determination of the total Helmholtz free energy $\mathscr{F}[\rho]$ of an arbitrary system reduces to the derivation of its excess free energy functional $\mathscr{F}_{\rm ex}[\rho]$.

Unfortunately, the coupling between configurational degrees of freedom introduced by the interaction potential U_N generally renders the underlying integral Q_N intractable by analytical methods — a limitation which provided the early motivation for the development of computational approaches in molecular physics [67]. In the following two sections, we present two different approaches to the celebrated Onsager approximation for $\mathscr{F}_{\rm ex}$ — first by performing the "brute-force" virial expansion of Q_N, as in Onsager's original paper, then by exploiting the general link between excess free energies and inter-particle correlations in the formalism of DFT.

2.1.2 Excess free energy from the virial expansion

To proceed, it is necessary to simplify the dependence of the potential energy U_N on the configurational degrees of freedom. The simplest such approximation consists in assuming U_N to be pairwise-additive,

$$U_N\Big(\{\mathbf{r}_i\}, \{\mathcal{R}_i\}\Big) = \sum_{i<j} u(\mathbf{r}_i, \mathbf{r}_j, \mathcal{R}_i, \mathcal{R}_j). \tag{2.18}$$

Note that while Eq. (2.18) is ubiquitously used in statistical mechanics as a means to offset some of the analytical and computational difficulties of the treatment of many-body problems, it should generally not be expected to yield an accurate representation of inter-molecular energies, as the presence of additional particles in the vicinity of particles i and j generally affects their pair interaction potential u due to polarisation effects [102]. However, the pairwise additive approximation is asymptotically exact in the regime of low particle densities, on which the Onsager

[3] Note that the equilibrium density distribution of an ideal gas in the absence of external fields is, of course, necessarily homogeneous. Therefore, the quantity $\mathscr{F}_{\rm id}[\rho]$ for an arbitrary distribution ρ does generally not correspond to the equilibrium free energy involved in standard thermodynamic identities, and is sometimes referred to as a *generalised* free energy [101].

theory is largely focused, and Eq. (2.18) is thus assumed to hold without loss of generality for our purposes. Eq. (2.8) may then be recast in the compact form

$$Q_N = \left\langle \prod_{i<j} \exp\Big\{ -\beta u(\mathbf{r}_i, \mathbf{r}_j, \mathcal{R}_i, \mathcal{R}_j)\Big\} \right\rangle, \tag{2.19}$$

where we introduced the *configurational average* $\langle\cdot\rangle$,

$$\Big\langle \cdot \Big\rangle \equiv \frac{1}{(8\pi^2 V)^N} \int_{V^N} d\{\mathbf{r}_i\} \oint d\{\mathcal{R}_i\} \ \cdot \ . \tag{2.20}$$

A convenient auxiliary quantity for the calculation of Q_N is known as the Mayer f-function,

$$f(\mathbf{r}_i, \mathbf{r}_j, \mathcal{R}_i, \mathcal{R}_j) = \exp\Big\{ -\beta u(\mathbf{r}_i, \mathbf{r}_j, \mathcal{R}_i, \mathcal{R}_j)\Big\} - 1. \tag{2.21}$$

Using Eq. (2.21), the factorial in Eq. (2.19) may be expanded in powers of f,

$$Q_N = 1 + \sum_{i<j} \langle f_{ij}\rangle + \sum_{\{(i,j),(k,l)\}} \sum \langle f_{ij} f_{kl}\rangle + \cdots + \langle \prod_{i<j} f_{ij}\rangle, \tag{2.22}$$

where $f_{ij} \equiv f(\mathbf{r}_i, \mathbf{r}_j, \mathcal{R}_i, \mathcal{R}_j)$, and the m-th sum in Eq. (2.22) runs over the set of $\binom{N(N-1)/2}{m}$ distinct indices $\{(i_1, j_1), \ldots, (i_m, j_m)\}$ such that $i_n < j_n$ for $n \in [\![1, m]\!]$. A convenient graphical representation of this expansion may be provided in the form of Feynman diagrams, in which each factor f_{ij}, accounting for the pair interaction between two distinct particles i and j, may be depicted by a line joining two vertices i and j. The first two sums in Eq. (2.22) may then be equivalently written as

$$\sum_{i<j} \langle f_{ij}\rangle = \quad i \bullet\!\!-\!\!-\!\!\bullet\, j \ , \tag{2.23}$$

$$\sum_{\{(i,j),(k,l)\}} \sum \langle f_{ij} f_{kl}\rangle = \sum_{i<j} \sum_{i<k} \langle f_{ij} f_{ik}\rangle + \sum_{i<j} \sum_{j<k} \langle f_{ij} f_{jk}\rangle + \sum_{i<k} \sum_{j<k} \langle f_{ik} f_{jk}\rangle + \sum_{\substack{\{(i,j),(k,l)\}\\ i,j\notin(k,l)}} \sum \langle f_{ij} f_{kl}\rangle$$

$$= \quad i \bullet\!\!-\!\!-\!\!\bullet\, j \quad i \\ \quad\quad\quad\quad k \bullet \quad + \quad i \bullet\!\!-\!\!-\!\!\bullet\, j \quad i \\ \quad\quad\quad\quad k \bullet \quad + \quad i \bullet\!\!-\!\!-\!\!\bullet\, j \quad i \\ \quad\quad\quad\quad k \bullet \quad + \quad i \bullet\!\!-\!\!-\!\!\bullet\, j \quad , \\ \quad\quad\quad\quad k \bullet\!\!-\!\!-\!\!\bullet\, l \tag{2.24}$$

where we have abstracted summation and averaging symbols from the diagrammatic representation. Due to the indistinguishability of the particles, it is evident that

the first three diagrams in Eq. (2.24) are equivalent, and may thus be subsumed into a single contribution. It follows from this discussion that Eq. (2.22) may be represented as a sum over all topologically-distinct diagrams obtained by linking together all possible subsets (or "clusters") of the N particles,

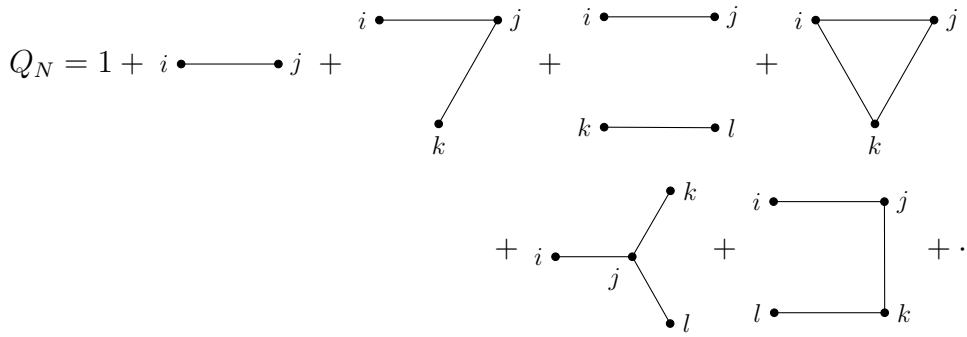

(2.25)

It is proven in Appendix B that this diagrammatic expansion may be recast in the compact form

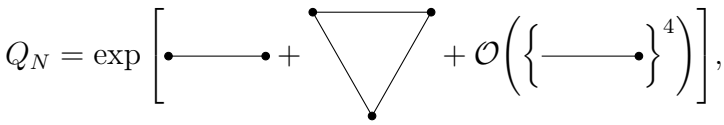

(2.26)

where the Landau $\mathcal{O}$ symbol denotes contributions arising from mutual correlations between 4 or more particles, and

$$= \sum_{i<j} \frac{1}{(8\pi^2 V)^2} \iint_{V^2} d\mathbf{r}_i d\mathbf{r}_j \oiint d\mathcal{R}_i d\mathcal{R}_j \, f_{ij} \tag{2.27}$$

$$= \binom{N}{2} \frac{1}{8\pi^2 V} \times \beta_1, \tag{2.28}$$

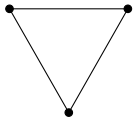

$$= \sum_{i<j<k} \frac{1}{(8\pi^2 V)^3} \int_{V^3} d\mathbf{r}_i d\mathbf{r}_j d\mathbf{r}_k \oint d\mathcal{R}_i d\mathcal{R}_j d\mathcal{R}_k \, f_{ij} f_{ik} f_{jk} \tag{2.29}$$

$$= \binom{N}{3} \frac{2}{(8\pi^2 V)^2} \times \beta_2, \tag{2.30}$$

with β_1 and β_2 the first two *irreducible cluster integrals* [103],

$$\beta_1 \equiv \frac{1}{8\pi^2 V} \iint_{V^2} d\mathbf{r}_1 d\mathbf{r}_2 \oiint d\mathcal{R}_1 d\mathcal{R}_2 \, f_{12}, \tag{2.31}$$

$$\beta_2 \equiv \frac{1}{2} \frac{1}{8\pi^2 V} \int_{V^3} d\mathbf{r}_1 d\mathbf{r}_2 d\mathbf{r}_3 \oint d\mathcal{R}_1 d\mathcal{R}_2 d\mathcal{R}_3 \, f_{12} f_{13} f_{23}, \tag{2.32}$$

which provide the first two terms of the virial equation of state (EOS) of classical liquids. In the case of calamitic particles with aspect ratio L/D interacting through pure steric repulsion, it was shown by Onsager [31] that elementary geometric considerations lead to the scaling relationship

$$\frac{\beta_2}{(\beta_1)^2} = \mathcal{O}\left(\frac{D}{L}\log\frac{L}{D}\right) \xrightarrow[\frac{L}{D}\to\infty]{} 0. \tag{2.33}$$

It follows from Eqs. (2.26)–(2.33) that many-body contributions to the configurational integral Q_N vanish at all densities ρ for "needle-like" particles with high shape anisotropy ($D/L \to 0$), provided that $\rho\beta_1$ remains finite [104]. In this case, Eqs. (2.13), (2.26) and (2.27) yield the excess free energy in the explicit form

$$-\beta\mathscr{F}_{\rm ex} = \bullet\!\!-\!\!\!-\!\!\bullet = \frac{1}{2}\sum_{i\neq j}\frac{1}{(8\pi^2 V)^2}\iint_{V^2} d\mathbf{r}_i d\mathbf{r}_j \oiint d\mathcal{R}_i d\mathcal{R}_j\, f(\mathbf{r}_i,\mathbf{r}_j,\mathcal{R}_i,\mathcal{R}_j). \tag{2.34}$$

As in Section 2.1.1, we now wish to express the excess free energy $\mathscr{F}_{\rm ex}$ in the form of a functional of some continuous density field $\rho(\mathbf{r},\mathcal{R})$, into which the microscopic degrees of freedom in Eq. (2.34) may be coarse-grained. Let us recast Eq. (2.34) in the equivalent form

$$-\beta\mathscr{F}_{\rm ex} = \frac{1}{2}\iint_{V^2} d\mathbf{r}d\mathbf{r}' \oiint d\mathcal{R}d\mathcal{R}' \left\langle f(\mathbf{r},\mathbf{r}',\mathcal{R},\mathcal{R}')\sum_{i\neq j}\rho_i(\mathbf{r},\mathcal{R})\rho_j(\mathbf{r}',\mathcal{R}')\right\rangle, \tag{2.35}$$

where $\langle\cdot\rangle$ is the configurational average (Eq. (2.20)), and

$$\rho_i(\mathbf{r},\mathcal{R}) \equiv \delta(\mathbf{r}-\mathbf{r}_i)\delta(\mathcal{R}-\mathcal{R}_i), \tag{2.36}$$

with δ the Dirac distribution. We now introduce the microscopic density operator ρ_m,

$$\rho_m(\mathbf{r},\mathcal{R}) \equiv \sum_{i=1}^{N}\rho_i(\mathbf{r},\mathcal{R}). \tag{2.37}$$

Using the basic properties of the δ-function, it is easy to show that

$$\left\langle \rho_m(\mathbf{r},\mathcal{R})\rho_m(\mathbf{r}',\mathcal{R}')\right\rangle = \left\langle \sum_{i\neq j}\rho_i(\mathbf{r},\mathcal{R})\rho_j(\mathbf{r}',\mathcal{R}')\right\rangle + N\delta(\mathbf{r}-\mathbf{r}')\delta(\mathcal{R}-\mathcal{R}'), \tag{2.38}$$

where the diagonal term on the right-hand side simply yields an irrelevant additive constant after integration over $(\mathbf{r},\mathbf{r}',\mathcal{R},\mathcal{R}')$ in the excess free energy (Eq. (2.35)).

Let us further invoke the mean-field approximation to assimilate the discrete microscopic density profile ρ_m to the mesoscopically-averaged density distribution ρ of Section 2.1.1,

$$\rho_m(\mathbf{r},\mathcal{R}) \cong \rho(\mathbf{r},\mathcal{R}). \tag{2.39}$$

Eqs. (2.35), (2.38) and (2.39) finally yield the Onsager excess free energy functional,

$$\mathscr{F}_{\text{ex}}[\rho] = -\frac{k_bT}{2}\iint_{V^2} d\mathbf{r}d\mathbf{r}' \oiint d\mathcal{R}d\mathcal{R}'\,\rho(\mathbf{r},\mathcal{R})\rho(\mathbf{r}',\mathcal{R}')f(\mathbf{r},\mathbf{r}',\mathcal{R},\mathcal{R}'), \tag{2.40}$$

where the configurational average vanishes due to the assumed independence of the mean-field density ρ from the microscopic degrees of freedom $\{\mathbf{r}_i\}$ and $\{\mathcal{R}_i\}$.

2.1.3 Excess free energy from the Ornstein-Zernike equation

A quicker, albeit less physically-instructive derivation of Eq. (2.40) may be obtained in the context of the density functional theory (DFT) of classical fluids [105]. In this section, we now proceed to provide a brief outline of this equivalent approach, as the formalism introduced in its derivation will find further use in the rest of this thesis. Let $\mathscr{F}[\rho]$ be the intrinsic Helmholtz free energy functional to be determined. Using Eq. (2.11), $\mathscr{F}[\rho]$ may be generically decomposed into ideal (non-interacting) and excess (interacting) contributions,

$$\mathscr{F}[\rho] = \mathscr{F}_{\text{id}}[\rho] + \mathscr{F}_{\text{ex}}[\rho], \tag{2.41}$$

where $\mathscr{F}_{\text{id}}[\rho]$ is given by Eq. (2.17) and $\mathscr{F}_{\text{ex}}[\rho]$ is an *a priori* unknown functional, whose existence and uniqueness are guaranteed by the Hohenberg-Kohn-Mermin (HKM) theorem [106, 107]. The so-called *variational principle* imposes that the equilibrium density $\rho_{\text{eq}}(\mathbf{r},\mathcal{R})$ describing the quiescent structure of the system constitutes a global minimum of the Helmholtz free energy $\mathscr{F}[\rho]$,[4] which implies that

$$\left.\frac{\delta\mathscr{F}}{\delta\rho}\right|_{\rho=\rho_{\text{eq}}} = \mu_N, \tag{2.42}$$

[4]Note that this general result, sometimes referred to as the second HKM theorem, is closely related to the second law of thermodynamics; a concise formal proof is provided in Ref. [108] in the formalism of classical DFT.

with μ_N a constant Lagrange multiplier, commensurate with a chemical potential, to be chosen so as to enforce the canonical fixed-density constraint,

$$\int_V d\mathbf{r} \oint d\mathcal{R}\, \rho(\mathbf{r}, \mathcal{R}) = N. \tag{2.43}$$

The functional differentiation of Eq. (2.17) leads to

$$\frac{\delta \mathscr{F}_{\text{id}}[\rho]}{\delta \rho(\mathbf{r}, \mathcal{R})} = k_b T \log\left\{\rho(\mathbf{r}, \mathcal{R})\lambda^3\right\}. \tag{2.44}$$

Let us define

$$c^{(1)}\Big(\mathbf{r}, \mathcal{R}; [\rho]\Big) \equiv -\beta \frac{\delta \mathscr{F}_{\text{ex}}[\rho]}{\delta \rho(\mathbf{r}, \mathcal{R})}. \tag{2.45}$$

It follows from Eqs. (2.41)–(2.45) that

$$\rho_{\text{eq}}(\mathbf{r}, \mathcal{R}) = \frac{1}{\lambda^3} \exp\left\{c^{(1)}\Big(\mathbf{r}, \mathcal{R}; [\rho_{\text{eq}}]\Big) + \beta\mu_N\right\}, \tag{2.46}$$

which yields a self-consistent relation between excess free energy and equilibrium density distribution. Hence, the equilibrium density profile ρ_{eq} may be fully characterised by the functional determination of $c^{(1)}$.

Let us further differentiate Eq. (2.45),

$$\frac{\delta c^{(1)}\Big(\mathbf{r}, \mathcal{R}; [\rho]\Big)}{\delta \rho(\mathbf{r}', \mathcal{R}')} = -\beta \frac{\delta^2 \mathscr{F}_{\text{ex}}[\rho]}{\delta \rho(\mathbf{r}, \mathcal{R}) \delta \rho(\mathbf{r}', \mathcal{R}')} \equiv c^{(2)}\Big(\mathbf{r}, \mathbf{r}', \mathcal{R}, \mathcal{R}'; [\rho]\Big). \tag{2.47}$$

It is shown in Appendix C that $c^{(2)}_{\text{eq}} \equiv c^{(2)}[\rho_{\text{eq}}]$ satisfies the general integral relation

$$\begin{aligned} h^{(2)}_{\text{eq}}(\mathbf{r}_1, \mathbf{r}_2, \mathcal{R}_1, \mathcal{R}_2) &= c^{(2)}_{\text{eq}}(\mathbf{r}_1, \mathbf{r}_2, \mathcal{R}_1, \mathcal{R}_2) \\ &+ \int_V d\mathbf{r}_3 \oint d\mathcal{R}_3\, \rho_{\text{eq}}(\mathbf{r}_3, \mathcal{R}_3) h^{(2)}_{\text{eq}}(\mathbf{r}_1, \mathbf{r}_3, \mathcal{R}_1, \mathcal{R}_3) c^{(2)}_{\text{eq}}(\mathbf{r}_3, \mathbf{r}_2, \mathcal{R}_3, \mathcal{R}_2), \end{aligned} \tag{2.48}$$

known as the Ornstein-Zernike (OZ) equation. In Eq. (2.48), $h^{(2)}_{\text{eq}}$ is the so-called *total correlation function* (TCF),

$$h^{(2)}_{\text{eq}}(\mathbf{r}_1, \mathbf{r}_2, \mathcal{R}_1, \mathcal{R}_2) \equiv \frac{\rho^{(2)}_{\text{eq}}(\mathbf{r}_1, \mathbf{r}_2, \mathcal{R}_1, \mathcal{R}_2)}{\rho_{\text{eq}}(\mathbf{r}_1, \mathcal{R}_1)\rho_{\text{eq}}(\mathbf{r}_2, \mathcal{R}_2)} - 1, \tag{2.49}$$

where $\rho^{(2)}_{\text{eq}}(\mathbf{r}_1, \mathbf{r}_2, \mathcal{R}_1, \mathcal{R}_2)$ is the two-particle density, which quantifies the probability of finding two particles with respective positions $\mathbf{r}_1$, $\mathbf{r}_2$ and orientations $\mathcal{R}_1$, $\mathcal{R}_2$

in the equilibrated system. At large separation distances $\|\mathbf{r}_1 - \mathbf{r}_2\|$, one expects the density fluctuations at points $\mathbf{r}_1$ and $\mathbf{r}_2$ to decorrelate,

$$\rho_{\text{eq}}^{(2)}(\mathbf{r}_1, \mathbf{r}_2, \mathcal{R}_1, \mathcal{R}_2) \xrightarrow[\|\mathbf{r}_1 - \mathbf{r}_2\| \to \infty]{} \rho_{\text{eq}}(\mathbf{r}_1, \mathcal{R}_1)\rho_{\text{eq}}(\mathbf{r}_2, \mathcal{R}_2),$$

so that $h_{\text{eq}}^{(2)}$ vanishes. Hence, $h_{\text{eq}}^{(2)}(\mathbf{1}, \mathbf{2}) \equiv h_{\text{eq}}^{(2)}(\mathbf{r}_1, \mathbf{r}_2, \mathcal{R}_1, \mathcal{R}_2)$ constitutes a measure of the net impact of the presence of a particle 1 at position $\mathbf{r}_1$ with orientation $\mathcal{R}_1$ on that of a second particle 2 at position $\mathbf{r}_2$ with orientation $\mathcal{R}_2$. In this context, the OZ equation (Eq. (2.48)) may be interpreted as the mathematical statement of the fact that the "total" correlation $h_{\text{eq}}^{(2)}(\mathbf{1}, \mathbf{2})$ between a pair of particles 1 and 2 may be decomposed into a "direct" component $c_{\text{eq}}^{(2)}(\mathbf{1}, \mathbf{2})$ arising from their unmediated interaction, and an "indirect" component stemming from mutual interactions involving any number of intermediary particles [108]. For this reason, $c_{\text{eq}}^{(2)}$ is referred to as the *direct pair correlation function* (DCF), from which the equilibrium structure and thermodynamics of the system may be determined using Eqs. (2.41)–(2.47).

Eqs. (2.46) and (2.48) thus provide a system of two coupled integro-differential equations relating three unknown functions ρ_{eq}, $h_{\text{eq}}^{(2)}$ and $c_{\text{eq}}^{(2)}$. For their resolution, it is therefore necessary to introduce an additional equation, known as the *closure relation*, to further constrain these three quantities. In the regime of low-particle concentrations, a particularly simple closure relation may be obtained by remarking that in the absence of influence from other surrounding particles, the probability of finding any two particles in a given microscopic state $\{\mathbf{r}_1, \mathbf{r}_2, \mathcal{R}_1, \mathcal{R}_2\}$ is commensurate with the Boltzmann weight of their two-body interaction potential $U_2(\mathbf{r}_1, \mathbf{r}_2, \mathcal{R}_1, \mathcal{R}_2)$. More formally, it is shown in Appendix C that in the thermodynamic limit, in which the canonical quantities $h_{\text{eq}}^{(2)}$ and ρ_{eq} may be assimilated to their grand-canonical counterparts, the asymptotic behaviour of the TCF $h_{\text{eq}}^{(2)}$ reads as

$$h_{\text{eq}}^{(2)}(\mathbf{r}, \mathbf{r}', \mathcal{R}, \mathcal{R}') \xrightarrow[\frac{N}{V} \to 0]{} \exp\Big\{ - \beta U_2(\mathbf{r}, \mathbf{r}', \mathcal{R}, \mathcal{R}') \Big\} - 1. \tag{2.50}$$

Assuming the full potential U_N to be pairwise additive, it follows from Eq. (2.48) that

$$c_{\text{eq}}^{(2)}(\mathbf{r}, \mathbf{r}', \mathcal{R}, \mathcal{R}') \xrightarrow[\frac{N}{V} \to 0]{} f(\mathbf{r}, \mathbf{r}', \mathcal{R}, \mathcal{R}'), \tag{2.51}$$

where we substituted u for U_2, with f the Mayer function of Section 2.1.2 (Eq. (2.21)). Note that in deriving Eq. (2.51), we have somewhat naively neglected the "indirect" integral contribution in the right-hand side of Eq. (2.48) in the low-density limit, as is commonly performed [104,108]. While this approximation should obviously hold in the case of homogeneous fluids, it is hard to justify *a priori* for systems of highly-anisotropic particles, in which $\rho_{\text{eq}}(\mathbf{r}_3, \mathcal{R}_3)$ may take sizeable values over a small fraction of configurational space even in the regime of vanishing particle densities ($N/V \to 0$). These issues will be discussed further in Section 2.3.1.

For now, let us consider a family of density functions parametrised by a scalar $\gamma \in [0,1]$,

$$\rho_\gamma(\mathbf{r}, \mathcal{R}) = \gamma \rho(\mathbf{r}, \mathcal{R}). \tag{2.52}$$

Assuming the arbitrary density distribution $\rho(\mathbf{r}, \mathcal{R})$ to be dilute and weakly non-homogeneous, we may thus write

$$c^{(2)}\Big(\mathbf{r}, \mathbf{r}', \mathcal{R}, \mathcal{R}'; [\rho_\gamma]\Big) \simeq f(\mathbf{r}, \mathbf{r}', \mathcal{R}, \mathcal{R}') \quad \forall \gamma \in [0,1]. \tag{2.53}$$

The functional integration of Eq. (2.47) along the compression path in Eq. (2.52) yields [105]

$$c^{(1)}\Big(\mathbf{r}, \mathcal{R}; [\rho]\Big) = \int_0^1 d\gamma \int_V d\mathbf{r}' \oint d\mathcal{R}' \, \frac{\partial \rho_\gamma(\mathbf{r}', \mathcal{R}')}{\partial \gamma} c^{(2)}\Big(\mathbf{r}, \mathbf{r}', \mathcal{R}, \mathcal{R}'; [\rho_\gamma]\Big) \tag{2.54}$$

$$= \int_V d\mathbf{r}' \oint d\mathcal{R}' \, \rho(\mathbf{r}', \mathcal{R}') f(\mathbf{r}, \mathbf{r}', \mathcal{R}, \mathcal{R}'), \tag{2.55}$$

where we used $c^{(1)}[\rho = 0] = 0$, as particle interactions do not affect the equilibrium density profile in the limit of vanishing concentrations (Eq. (2.46)). Finally, integrating Eq. (2.45) along the same path, we recover the Onsager excess free energy functional (Eq. (2.40)),

$$\mathscr{F}_{\text{ex}}[\rho] = -\frac{k_b T}{2} \iint_{V^2} d\mathbf{r} d\mathbf{r}' \oiint d\mathcal{R} d\mathcal{R}' \, \rho(\mathbf{r}, \mathcal{R}) \rho(\mathbf{r}', \mathcal{R}') f(\mathbf{r}, \mathbf{r}', \mathcal{R}, \mathcal{R}'),$$

and the equilibrium density distribution may be determined self-consistently by plugging Eq. (2.55) into Eq. (2.46),

$$\rho_{\text{eq}}(\mathbf{r}, \mathcal{R}) = \frac{e^{\beta \mu_N}}{\lambda^3} \exp\left\{ \int_V d\mathbf{r}' \oint d\mathcal{R}' \, \rho_{\text{eq}}(\mathbf{r}', \mathcal{R}') f(\mathbf{r}, \mathbf{r}', \mathcal{R}, \mathcal{R}') \right\}. \tag{2.56}$$

It is interesting to note that while the approaches of Secs. 2.1.2 and 2.1.3 obviously lead to identical results, the physical assumptions underlying both derivations are subtly different and somewhat complementary. For instance, in the (Onsager) cluster expansion route, we exploited the large aspect ratio of the particles, but made no significant assumptions as to the structure or density of the fluid — while in the DFT calculation, we restricted our study to the dilute, weakly non-homogeneous regime without regard to the particle shape. Furthermore, the pairwise additive approximation (Eq. (2.18)) plays a central role in the former derivation — while it is largely unnecessary in the latter, which may instead be directly formulated in terms of the two-body potential U_2 in the grand-canonical ensemble (Eq. (2.50)). Such distinctions are worth keeping in mind for the extension of the theory to more general particle models, as discussed in Section 2.2.2.

2.2 Application to uniform nematic phases

2.2.1 Uniaxial nematic symmetries

In the rest of this chapter, we restrict our study to the case of prolate uniaxial nematic phases, which are typically formed by systems of rod-like particles bearing cylindrical symmetry about their long axis $\mathbf{u}$. The orientation of such molecules may be entirely prescribed by the respective polar and azimuthal angles θ and ϕ, parametrising the direction of the normalised vector $\mathbf{u}$. Analogously, prolate uniaxial phases are characterised by the absence of long-ranged correlations in the internal rotational degree of freedom α of their constituent particles, so that the macroscopic structure of the phase is fully captured by the density field

$$\rho(\mathbf{r}, \mathcal{R}) = \rho(\mathbf{r}, \mathbf{u}), \tag{2.57}$$

which quantifies the spatial distribution of the molecular long axes $\mathbf{u}$. In the case of a uniform director field $\mathbf{n}(\mathbf{r}) = \mathbf{n}_0$, the combination of phase translational invariance and rotational symmetry about $\mathbf{n}_0$ further imposes

$$\rho(\mathbf{r}, \mathbf{u}) = \overline{\rho}\psi(\mathbf{u} \cdot \mathbf{n}_0), \tag{2.58}$$

with $\overline{\rho} \equiv N/V$ the uniform angle-integrated density and $\psi(\mathbf{u}\cdot\mathbf{n}_0)$ the so-called *orientation distribution function* (ODF), which describes the probability of finding a particle with its long axis borne by $\mathbf{u}$ with respect to the uniform director $\mathbf{n}_0$. With this convention, the fixed-density constraint (Eq. (2.43)) simply reads as

$$2\pi \oint_{\mathcal{S}} d\mathbf{u}\, \psi(\mathbf{u}\cdot\mathbf{n}_0) = 1, \tag{2.59}$$

where we used Eq. (A.5). Plugging this density ansatz into Eqs. (2.17) and (2.40) yields the ideal and excess Helmholtz free energy functionals of the system in the form

$$\frac{\beta\mathscr{F}_{\mathrm{id}}[\psi]}{V} = \overline{\rho}\Big\{\log\left(\overline{\rho}\lambda^3\right) - 1\Big\} + \overline{\rho}\oint d\mathcal{R}\, \psi(\mathbf{u}\cdot\mathbf{n}_0)\log\psi(\mathbf{u}\cdot\mathbf{n}_0), \tag{2.60}$$

$$\frac{\beta\mathscr{F}_{\mathrm{ex}}[\psi]}{V} = -\frac{\overline{\rho}^2}{2V}\iint_V d\mathbf{r}_1 d\mathbf{r}_2 \oiint d\mathcal{R}_1 d\mathcal{R}_2\, \psi(\mathbf{u}_1\cdot\mathbf{n}_0)\psi(\mathbf{u}_2\cdot\mathbf{n}_0) f(\mathbf{r}_1,\mathbf{r}_2,\mathcal{R}_1,\mathcal{R}_2). \tag{2.61}$$

One recognises in the first term of Eq. (2.60) the free energy of the homogeneous ideal gas (Eq. (2.14)), which can in this context be interpreted as the translational entropy of the system — while the second term is commensurate with the so-called *Shannon entropy* of the ODF [26], and may thus be assimilated to the total rotational entropy. The excess component of the free energy (Eq. (2.61)), commonly referred to as the packing entropy in the case of hard particle interactions, is then generally minimised by ODFs representing ideal crystalline orientational arrangements. Its quadratic dependence in the density $\overline{\rho}$ in the second-virial approximation gradually outweighs the linear scaling of the rotational entropy with increasing particle concentrations, and thus progressively stabilises a nematic phase in the framework of the Onsager theory.

In the following, let us use the homogeneity of space to write

$$f(\mathbf{r}_1,\mathbf{r}_2,\mathcal{R}_1,\mathcal{R}_2) = f(\mathbf{r}_{12},\mathcal{R}_{12}),$$

where $\mathbf{r}_{12} \equiv \mathbf{r}_2 - \mathbf{r}_1$ is the centre-of-mass separation vector and $\mathcal{R}_{12} \equiv \mathcal{R}_1^{\mathsf{T}}\cdot\mathcal{R}_2$ is the relative orientation of particle 2 projected in the molecular frame of particle 1. Assuming the particles to bear uniaxial symmetry yields the further simplification

$$f(\mathbf{r}_{12},\mathcal{R}_{12}) = f(\mathbf{r}_{12},\mathbf{u}_1\cdot\mathbf{u}_2),$$

where the scalar product may be evaluated using Eq. (A.6),

$$\mathbf{u}_1 \cdot \mathbf{u}_2 = \sin\theta_1 \sin\theta_2 \cos(\phi_2 - \phi_1) + \cos\theta_1 \cos\theta_2.$$

Let us choose the laboratory frame to be such that $\mathbf{e}_z \equiv \mathbf{n}_0$, so that macroscopic order may be fully described in terms of the polar angle θ of the particles,

$$\psi(\mathbf{u} \cdot \mathbf{n}_0) = \psi(\cos\theta). \tag{2.62}$$

Without loss of generality, one may then choose the laboratory axis $\mathbf{e}_x$ to be such that the molecular axis $\mathbf{u}_1$ is coplanar with $\mathbf{e}_x$ and $\mathbf{e}_z$, so that $\phi_1 = 0$. Thus,

$$f(\mathbf{r}_{12}, \mathcal{R}_{12}) = f(\mathbf{r}_{12}, \theta_1, \theta_2, \phi_2), \tag{2.63}$$

and plugging Eqs. (2.62) and (2.63) into Eq. (2.56) yields the self-consistent equation

$$\psi_{\text{eq}}(\cos\theta) = \frac{e^{\beta\mu_N}}{\overline{\rho}\lambda^3} \exp\left\{2\pi\overline{\rho} \int_0^\pi \sin\theta' d\theta' \, \psi_{\text{eq}}(\cos\theta') \int_V d\mathbf{r} \int_0^{2\pi} d\phi' \, f(\mathbf{r}, \theta, \theta', \phi')\right\}, \tag{2.64}$$

which fully determines the equilibrium structure of a uniaxial nematic LC at given particle density $\overline{\rho}$.

However, this original form of the Onsager DFT is restricted by the approximations of Sections 2.1.2 and 2.1.3 to the regime of either large particle anisotropy or high particle dilution, and is therefore of limited practical use. We hence devote the next section to a brief overview of subsequent attempts to extend this framework to a wider class of experimentally-realistic mesogens and thermodynamic conditions.

2.2.2 Generalisation to finite mesogen anisotropy

In the context of Section 2.1.2, the main difficulty involved in the description of finite-sized colloids lies in the need to include higher-order terms in the cluster expansion of the configurational integral (Eq. (2.26)), due to the rapid increase of their relative magnitudes with decreasing molecular aspect ratios [109]. The second-virial approach of the Onsager theory has thus been found to be quantitatively inaccurate in the case of rod-like particles with aspect ratios as high as 100 [110]. Therefore, several studies have chosen to explicitly include the third-order virial contribution

(Eq. (2.30)) in the excess free energy functional, with some encouraging success being reported in the case of phases with biaxial symmetries [111,112]. However, the quick escalation of computational complexity with increasing truncation order [113] severely restricts the number of terms that may be tractably included in the expansion of Eq. (2.26), and thus largely prevents the systematic application of such approaches. Furthermore, evidence of the decreased radius of convergence of the virial series in the case of moderate-to-high mesogen anisotropy [114] may paradoxically limit their numerical stability range to regions of lower density, and even prevent the prediction of a stable nematic phase altogether for aspect ratios as low as 10 as one pushes the expansion beyond the third order in $\overline{\rho}$ [115].

Conversely, in the formalism of DFT, the larger particle densities associated with the onset of LC order renders the high-dilution approximation (Eq. (2.53)) increasingly inadequate for the treatment of molecular systems with lower aspect ratios. In the general case, an exact expression for the excess free energy may be obtained from Eqs. (2.47) and (2.54) by double functional integration,

$$\frac{\beta\mathscr{F}_{\mathrm{ex}}[\psi]}{V} = -\frac{\overline{\rho}^2}{2V}\iint_V d\mathbf{r}_1 d\mathbf{r}_2 \oiint d\mathcal{R}_1 d\mathcal{R}_2\, \psi(\mathbf{u}_1\cdot\mathbf{n}_0)\psi(\mathbf{u}_2\cdot\mathbf{n}_0)\overline{c^{(2)}}\Big(\mathbf{r}_{12},\mathcal{R}_1,\mathcal{R}_2;[\overline{\rho}\psi]\Big), \tag{2.65}$$

with $\overline{c^{(2)}}$ the DCF integrated along the compression path of Eq. (2.52),

$$\overline{c^{(2)}}\Big(\mathbf{r}_{12},\mathcal{R}_1,\mathcal{R}_2;[\overline{\rho}\psi]\Big) = 2\int_0^1 d\gamma \int_0^\gamma d\gamma'\, c^{(2)}\Big(\mathbf{r}_{12},\mathcal{R}_1,\mathcal{R}_2;[\gamma'\times\overline{\rho}\psi]\Big). \tag{2.66}$$

Note that in the low-density limit, plugging Eq. (2.53) into Eq. (2.66) yields the density-functional equivalent of the second-virial approximation,

$$\overline{c^{(2)}}\Big(\mathbf{r}_{12},\mathcal{R}_1,\mathcal{R}_2;[\overline{\rho}\psi]\Big) \simeq f(\mathbf{r}_{12},\mathcal{R}_1,\mathcal{R}_2), \tag{2.67}$$

which reduces Eq. (2.65) to the Onsager excess free energy of Section 2.1.3. However, in the general case, the accurate determination of $\mathscr{F}_{\mathrm{ex}}$ — or, equivalently, of $\overline{c^{(2)}}$ — from Eqs. (2.65) and (2.66) requires a more realistic account of the density dependence of the DCF $c^{(2)}$.

While good approximations for the DCF of so-called *simple fluids*, characterised by radially-symmetric pair molecular interactions, have been obtained by directly

solving the OZ equation using various closure relations [116,117], the additional orientational degrees of freedom render this process mostly intractable when particle anisotropy is introduced [104]. A number of recent efforts to derive closed-form expressions for the excess free energy and associated DCF of anisotropic systems have thus resorted to first-principle geometric considerations instead, on the basis of Rosenfeld's original fundamental measure theory (FMT) for hard spheres [118]. Although FMT presumably provides a good description of the DCF spatial-orientational coupling, such approaches are unfortunately limited by construction to convex particle models [119] and are not naturally suited for the treatment of soft interaction potentials [120].

Another class of approaches revolve around the derivation of *ad hoc* approximate expressions for these quantities by remapping either the relevant DCF or excess free energy to those of the well-characterised hard-sphere fluid [104]. A significant number of such methods rely on the so-called *decoupling approximation*, in which inter-particle correlations are accounted for via simplified ansätze of the form

$$c^{(2)}(\mathbf{r}_{12},\mathcal{R}_1,\mathcal{R}_2;[\overline{\rho}\psi]) = c^{(2)}_{\text{ref}}\left\{\frac{\|\mathbf{r}_{12}\|}{\sigma(\mathbf{u}_{12},\mathcal{R}_1,\mathcal{R}_2)};\overline{\rho}\right\}, \tag{2.68}$$

irrespective of ψ, with $\mathbf{u}_{12}\equiv\mathbf{r}_{12}/\|\mathbf{r}_{12}\|$. $c^{(2)}_{\text{ref}}$ then corresponds to a heuristic DCF inferred from that of a reference hard-sphere system at the same density $\overline{\rho}$, either explicitly through the use of a closure relation as first proposed by Pynn [121] and Wulf [122], or implicitly from the corresponding EOS as suggested independently by Parsons [123] and Lee [124]. In this framework, particle anisotropy is introduced solely through the orientation-dependent distance of closest approach between two particles $\sigma(\mathbf{u}_{12},\mathcal{R}_1,\mathcal{R}_2)$, defined as the centre-of-mass separation distance at which their respective molecular surfaces are tangent.[5] In the limit of pure steric interactions, it is shown in Appendix D that Eqs. (2.65) and (2.66) then lead to effective expressions for $\overline{c^{(2)}}$ of the general form

$$\overline{c^{(2)}}(\mathbf{r}_{12},\mathcal{R}_1,\mathcal{R}_2;[\overline{\rho}\psi]) = G_{\text{ref}}(\overline{\rho}v_{\text{ref}})\times f(\mathbf{r}_{12},\mathcal{R}_1,\mathcal{R}_2), \tag{2.69}$$

[5]Note that the uniqueness of $\sigma(\mathbf{u}_{12},\mathcal{R}_1,\mathcal{R}_2)$ is generally only guaranteed in the case of convex particles as a direct corollary of the so-called *separating axis theorem* [125]. The application of the decoupling approximation to systems of non-convex molecules will be discussed in more detail in Section 3.3.2.

with v_{ref} the molecular volume of the reference hard-sphere fluid, which may *a priori* differ from that of the anisotropic particles considered, as discussed in Section 3.3.2. In the general case, the effective volume fraction η_{ref} of the reference system is thus linked to that of the physical system with molecular volume v at identical number density $\overline{\rho}$ through the relation

$$\eta_{\text{ref}} \equiv \overline{\rho} v_{\text{ref}} = \eta \times \frac{v_{\text{ref}}}{v}.$$

The density-dependent prefactor G_{ref} is then related to the isothermal compressibility of the chosen reference framework — namely, the Percus-Yevick DCF [116,126] in the Pynn-Wulf (PW) approximation, and the Carnahan-Starling (CS) EOS [127] in the Parsons-Lee (PL) approach. The respective corresponding expressions for G_{ref} read as [104]

$$G_{\text{PW}}(\eta) = \frac{3/4 - 3\eta/8}{(1-\eta)^2} - \frac{\log(1-\eta)}{4\eta}, \tag{2.70}$$

$$G_{\text{PL}}(\eta) = \frac{1 - 3\eta/4}{(1-\eta)^2} \tag{2.71}$$

which both trivially satisfy

$$G_{\text{ref}}(\eta) \xrightarrow[\eta \to 0]{} 1.$$

Hence, Eqs. (2.70) and (2.71) simply reduce to the second-virial approximation (Eq. (2.67)) in the limit of high particle dilution. The equilibrium ODF ψ_{eq} may then be obtained by direct functional minimisation of Eqs. (2.60) and (2.65) with respect to ψ at fixed density $\overline{\rho}$,

$$\psi_{\text{eq}}(\cos\theta) = \frac{e^{\beta\mu_{\overline{\rho}}}}{\overline{\rho}\lambda^3} \exp\left\{ \frac{\overline{\rho} G_{\text{ref}}(\eta_{\text{ref}})}{4\pi^2} \int_0^\pi \sin\theta' d\theta' \, \psi_{\text{eq}}(\cos\theta') \kappa(\theta, \theta') \right\}, \tag{2.72}$$

with κ the generalised excluded volume kernel,

$$\kappa(\theta, \theta') = \int_V d\mathbf{r} \iint_0^{2\pi} d\alpha d\alpha' \iint_0^{2\pi} d\phi d\phi' \, f(\mathbf{r}, \mathcal{R}, \mathcal{R}'). \tag{2.73}$$

Following the previous discussions, it is easy to verify that Eqs. (2.72) and (2.73) reduce to Eq. (2.64) for systems of highly-dilute uniaxial calamitic particles.

A detailed derivation of the PL theory (Eq. (2.71)) from Eqs. (2.66) and (2.68) is provided in Appendix D, using the DFT formalism of Section 2.1.3. In this case, it is shown that the functional minimisation of $\mathscr{F}[\psi]$ leads to the introduction of a prefactor $G_{\mathrm{PL}}^{(1)}$ in the self-consistent Eq. (2.72) that differs from the correction G_{PL} appearing in the excess free energy,

$$G_{\mathrm{PL}}^{(1)}(\eta) = \frac{1}{8\eta}\left\{\frac{3-\eta}{(1-\eta)^3} - 3\right\}. \tag{2.74}$$

This discrepancy stems from the fact that we here made use of a decoupling approximation for the DCF (Eq. (2.68)), while the original treatment of Parsons [123] is instead formulated in terms of the TCF (Eq. (2.49)). While there is no *a priori* reason to privilege one approach over the other, it will be shown in Section 2.3.2 that the original PL prefactor (Eq. (2.71)) yields better agreement with numerical simulations in the case of uniaxial molecules — whereas the use of Eq. (2.74) in Eq. (2.72) leads to significant gains in accuracy for the prediction of the isotropic/nematic (I/N) transition of hard faceted particles (see Section 3.3.2). Unless otherwise stated, we mostly restrict ourselves throughout this thesis to the "standard" form of the PL theory, due to both its relative simplicity and well-documented success in describing the nematic behaviour of a wide range of hard [128, 129] and soft [130] particle models.

2.3 Comparison with numerical simulations

An iconic model system for the comparison of theoretical predictions with molecular simulations in entropy-driven mesophases is the so-called hard sphero-cylinder (HSC) model, consisting of a hard cylindrical body of radius R and axial length L tipped with two hemispherical caps at each of its end extremities (Figure 2.1). Such particles constitute a basic example of a *sphere-swept volume*, which may in this case be equivalently obtained by rolling a sphere of radius R along a straight line of length L. Therefore, the detection of hard overlaps between HSCs effectively reduces to the determination of the minimal distance separating their respective cylindrical centrelines, which may be expediently performed by elementary geometric

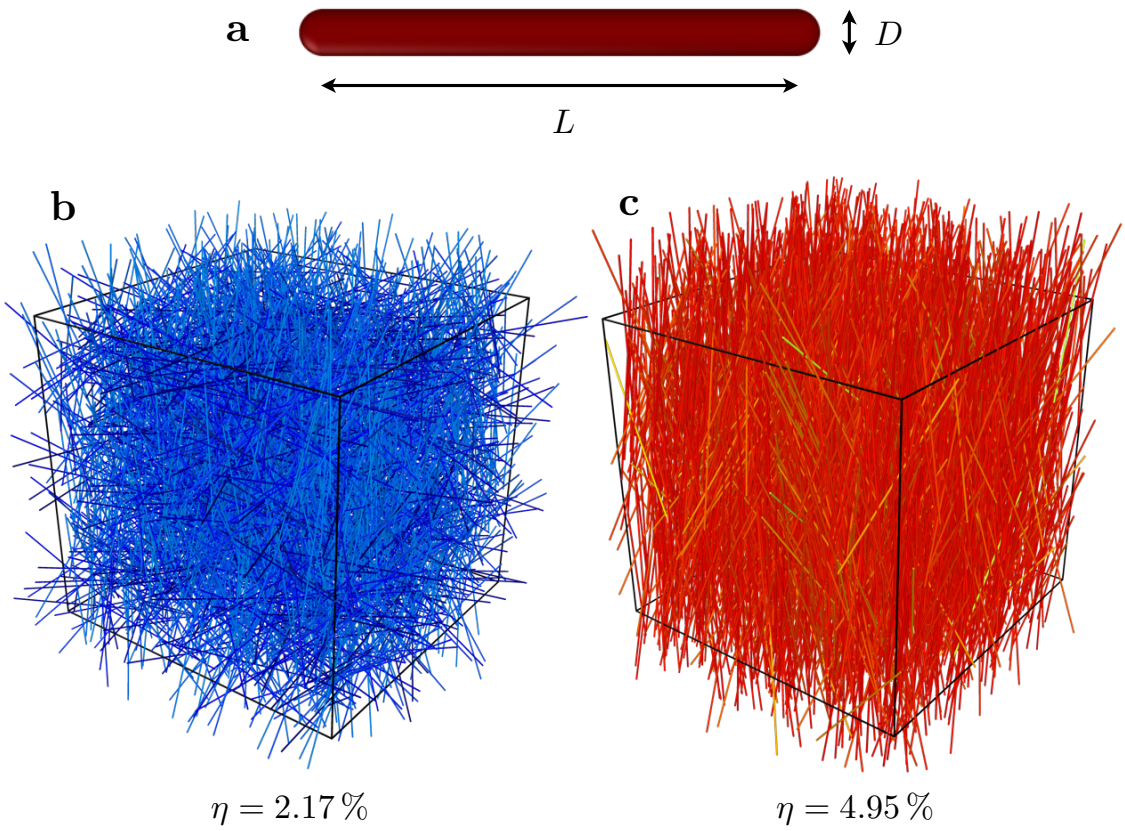

Figure 2.1: HSC geometry and I/N phase ordering transition. a) The HSC particle model. b) Snapshot of an equilibrated NPT-MC simulation of $N = 3600$ HSCs with aspect ratio $L/D = 100$, taken at volume fraction $\eta = 2.17\,\%$. Particles are coloured according to the projection of their long axis on the nematic director $\mathbf{n}_0$ rescaled by the order parameter $S^{(2)}$, obtained from the ensemble-averaged $\mathcal{Q}$ tensor (see Section 2.3.2). c) Same as b) at $\eta = 4.95\,\%$.

algorithms [131]. This numerical convenience, combined with the demonstrated ability of HSCs to stabilise the full range of uniaxial phases exhibited by anisotropic experimental colloids [132, 133], has rendered HSCs a mainstay of computational studies of lyotropic LCs in a variety of contexts [109, 134–138]. In this section, we compare the theoretical predictions of the Onsager and Parsons-Lee approaches with the results of numerical simulations in the isotropic and nematic phase of HSCs, in terms of both microscopic correlation functions and macroscopic thermodynamic quantities.

2.3.1 Correlation functions

Let us now drop the overbar notation from the angle-integrated number density $\overline{\rho} \equiv N/V$, along with the superscripts from the DCF $c^{(2)} \equiv c$ and TCF $h^{(2)} \equiv h$, when no confusion can arise. In light of the previous sections, it is apparent that the accuracy of the Onsager treatment of nematic LCs is contingent on that of the underlying DCF for systems of arbitrarily-anisotropic particles. However, the numerical determination of the DCF in anisotropic fluids is often rendered cumbersome by broken rotational invariance, which leads to an additional dependence of c on up to 8 angular degrees of freedom to quantify the relative position and absolute orientations of the particles. It is thus generally convenient to expand c in a complete basis of rotational invariants, which may for instance be chosen in the form of spherical harmonics in the case of uniaxial particles parametrised by their molecular axis $\mathbf{u}$,

$$c\Big(\mathbf{r}_{12},\mathbf{u}_1,\mathbf{u}_2;[\rho\psi]\Big) = \sum_{l_1,m_1}\sum_{l_2,m_2}\sum_{l,m} c_{l_1m_1l_2m_2lm}\Big(r;[\rho\psi]\Big)\, Y_{l_1m_1}(\mathbf{u}_1)Y_{l_2m_2}(\mathbf{u}_2)Y_{lm}(\mathbf{u}_{12}), \tag{2.75}$$

where we used the notations of Section 2.2.2, along with the shorthand

$$\sum_{l,m}\cdot \equiv \sum_{l=0}^{l_{\max}}\sum_{m=-l}^{l}\cdot\,,$$

with $l_{\max}$ an arbitrarily-high numerical truncation order. Using the orthonormality of spherical harmonics, Eq. (2.75) may be immediately inverted to yield

$$c_{l_1m_1l_2m_2lm}\Big(r;[\rho\psi]\Big) = \oint_{\mathcal{S}} d\mathbf{u}_1 d\mathbf{u}_2 d\mathbf{u}_{12}\, c\Big(\mathbf{r}_{12},\mathbf{u}_1,\mathbf{u}_2;[\rho\psi]\Big)\, Y^*_{l_1m_1}(\mathbf{u}_1)Y^*_{l_2m_2}(\mathbf{u}_2)Y^*_{lm}(\mathbf{u}_{12}),$$

where Y^*_{lm} is the complex conjugate of Y_{lm}. Note that in the case of an isotropic system, phase symmetry imposes that the DCF must remain invariant under any simultaneous rotation of its three arguments $\mathbf{r}_{12},\mathbf{u}_1,\mathbf{u}_2$, so that Eq. (2.75) may be considerably simplified by expressing c in a local frame whose polar axis is borne by the centre-of-mass separation vector $\mathbf{r}_{12}$,

$$c_{\text{iso}}(r,\mathbf{u}_1,\mathbf{u}_2;\rho) = \sum_{l_1,m_1}\sum_{l_2,m_2} c_{l_1l_2m_1}(r;\rho)\, Y_{l_1m_1}(\mathbf{u}_1)Y_{l_2m_2}(\mathbf{u}_2)\delta_{m_1\underline{m_2}}, \tag{2.76}$$

with δ the Kronecker delta and $\underline{m} \equiv -m$, where the selection rule $m_1 + m_2 = 0$ is imposed by the cylindrical invariance of the system about $\mathbf{u}_{12}$. However, in the

presence of long-ranged orientational order, the functional dependence of c on the ODF ψ introduces an additional dependence of the DCF on the local nematic director $\mathbf{n}_0$, so that the full fixed-frame expansion (Eq. (2.75)) must generally be used.

In this case, the steep increase in the number of coefficients $c_{l_1m_1l_2m_2lm}$ with increasing truncation order $l_{\max}$ restricts the applicability of such methods to molecular systems for which the harmonic series of Eq. (2.75) is rapidly convergent. This limitation unfortunately excludes both highly-anisotropic particle models and steeply-repulsive interaction potentials [139], for which the approximations of the previous theories are expected to work best, and illustrates the general difficulties involved in the accurate formulation of DFT and molecular simulations in terms of identical particle models. As such, numerical measurements of the DCF of anisotropic fluids have, to our knowledge, only been performed in the isotropic phase of HSCs with moderate aspect ratios [140] and in both the isotropic and nematic phase of very short ellipsoids [141–145]. To assess the validity of the Onsager theory in a context where it may be reasonably applied, we shall here focus on the former system.

In the fixed laboratory frame, the isotropic expansion Eq. (2.76) may be recast in the form [140]

$$c_{\text{iso}}(\mathbf{r}_{12},\mathbf{u}_1,\mathbf{u}_2;\rho) = \sum_{l_1,m_1}\sum_{l_2,m_2}\sum_{l,m} c_{l_1l_2l}(r;\rho)\,\mathscr{C}^{m_1m_2m}_{l_1l_2l} Y_{l_1m_1}(\mathbf{u}_1)Y_{l_2m_2}(\mathbf{u}_2)Y^*_{lm}(\mathbf{u}_{12}),$$

with $\mathscr{C}$ the Clebsch-Gordan coefficients, and where the fixed-frame components $c_{l_1l_2l}$ are related to their molecular-frame counterparts $c_{l_1l_2m}$ through [139]

$$c_{l_1l_2l}(r;\rho) = \sqrt{\frac{4\pi}{2l+1}}\sum_m c_{l_1l_2m}(r;\rho)\mathscr{C}^{mm0}_{l_1l_2l}. \tag{2.77}$$

We reproduce in Figure 2.2 the radial dependence of some selected $c_{l_1l_2l}$ coefficients as reported in Ref. [140] for HSCs with aspect ratio $L/D = 10$, obtained by numerical resolution of the OZ equation with $l_{\max} = 10$. These results are matched against the corresponding Onsager second-virial DCF c_{O},

$$c_{\text{O}}(\mathbf{r}_{12},\mathbf{u}_1,\mathbf{u}_2) = f(\mathbf{r}_{12},\mathbf{u}_1,\mathbf{u}_2) = \begin{cases} -1 & \text{if } 1\cap 2 \neq \varnothing \\ 0 & \text{if } 1\cap 2 = \varnothing \end{cases}, \tag{2.78}$$

where the set intersection sign denotes the potential overlap region of two HSCs. The projection coefficients $c_{l_1 l_2 m}$ were evaluated through the numerical inversion of Eq. (2.76) in the molecular frame,

$$c_{l_1 l_2 m}(r) = 4\pi^4 \Big\langle \sin\theta_1 \sin\theta_2 \, c_{\mathrm{O}}(r_{12}, \mathbf{u}_1, \mathbf{u}_2) Y_{l_1 \underline{m}}(\mathbf{u}_1) Y_{l_2 m}(\mathbf{u}_2) \Big\rangle_r , \tag{2.79}$$

where the radial average $\langle \cdot \rangle_r$ was performed stochastically over all particle pairs with centre-of-mass vector $\mathbf{r}_{12}$ borne by $\mathbf{e}_z$ with norm $\|\mathbf{r}_{12}\| \in [r, r + \delta r]$. Molecular axes $\mathbf{u}_i$ were drawn uniformly in Euler angle space as described in Appendix A, and HSC overlap queries (Eq. (2.78)) were performed using the algorithm of Vega and Lago [131]. The bin width was set to $\delta r = 0.075\, D$, and 10^9 random pair configurations such that $r_{12} \in [0, L + D]$ were used. Expansion coefficient were finally projected onto the space-fixed frame using Eq. (2.77).

To further compare theoretical predictions with numerical results, it is worth recalling that the decoupling approximation (Eq. (2.68)) does not necessarily provide an explicit expression for the DCF c, but instead generally yields an *effective* expression for the density-integrated DCF $\bar{c}$ appearing in the excess free energy. A useful approximation may therefore be borrowed from the DFT of simple fluids by invoking linear response theory in the limit of weakly non-uniform systems, which in our notation reads as [146, 147]

$$c\Big(\mathbf{r}_{12}, \mathcal{R}_1, \mathcal{R}_2; [\rho\psi]\Big) \simeq \bar{c}\Big(\mathbf{r}_{12}, \mathcal{R}_1, \mathcal{R}_2; [\rho\psi]\Big), \tag{2.80}$$

so that Eqs. (2.80) and (2.69) yield the decoupled DCFs as simple rescaled versions of the Onsager DCF c_{O}, with prefactors given by Eqs. (2.70) and (2.71). In this context, it is interesting to note that a different corrective prefactor G_{L} was also derived for the DCF by Lee [148], which may be recovered by directly plugging Eqs. (2.68) and (2.80) into Eq. (D.2), and substituting from Eqs. (D.18) and (D.19),

$$c_{\mathrm{L}}\Big(\mathbf{r}_{12}, \mathbf{u}_1, \mathbf{u}_2; [\rho\psi]\Big) = \frac{1 - \eta_{\mathrm{ref}}/4}{(1 - \eta_{\mathrm{ref}})^4} \times c_{\mathrm{O}}(\mathbf{r}_{12}, \mathbf{u}_1, \mathbf{u}_2) \equiv G_{\mathrm{L}}(\eta_{\mathrm{ref}}) \times c_{\mathrm{O}}(\mathbf{r}_{12}, \mathbf{u}_1, \mathbf{u}_2). \tag{2.81}$$

While the validity of the assumptions underlying Eq. (2.80), which in our case amount to treating the nematic phase as a weakly-disturbed isotropic liquid, is

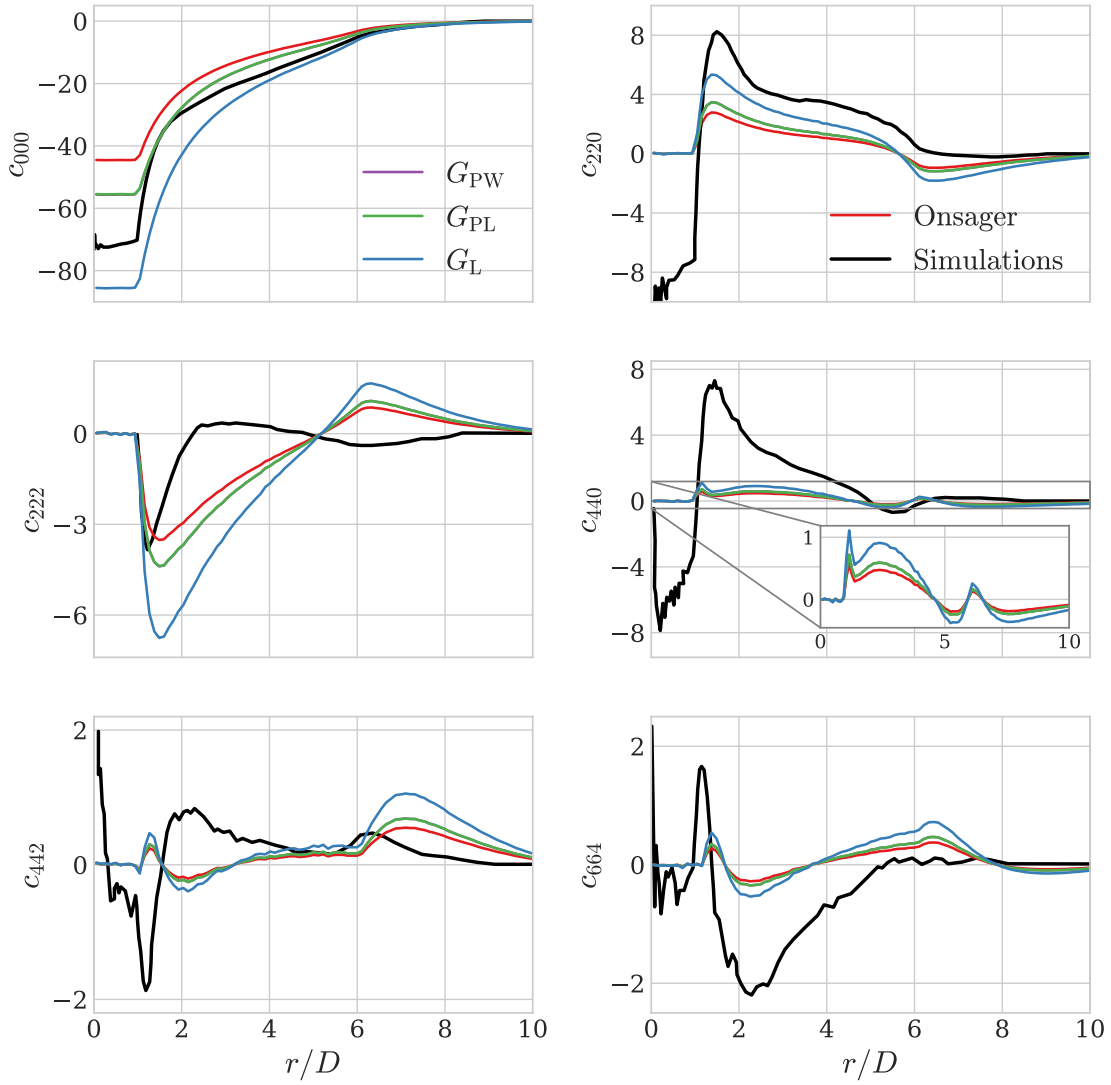

Figure 2.2: DCF isotropic expansion coefficients $c_{l_1 l_2 l}$ as a function of scaled radial separation distance r/D for HSCs with aspect ratio $L/D = 10$. Black lines denote the simulation results of Ref. [140] at volume fraction $\eta = 15.92\,\%$, in the stable isotropic regime [109]. Coloured lines represent the predictions of the Onsager theory (Eqs. (2.78) and (2.79)) and of the various decoupling approximations based on Eqs. (2.69) and (2.80) at $\eta_{\mathrm{ref}} = 15.92\,\%$, as described in the text. Note that the results of the PW and PL approaches (Eqs. (2.70) and (2.71)) are virtually identical at that density.

clearly questionable, this relation provides a simple and direct way to check the effective correlations derived from the previous theories against the numerical DCFs obtained from simulations in the vicinity of the I/N transition. The results of the three rescaled approaches are reproduced in Figure 2.2 by assimilating the reference volume v_{ref} to the molecular volume v of the physical system, so that $\eta_{\mathrm{ref}} = \eta$.

It is apparent from Figure 2.2 that coefficients of the type $c_{l_1 l_2 0}$ are reasonably-well captured by the rescaled theories outside of the hard overlap region ($r/D < 1$), although no single corrective prefactor systematically yields the best results for all expansion coefficients. For instance, near-quantitative agreement with simulations is achieved by the PL and PW approximations for the position-position correlation function c_{000}, while the G_{L} prefactor (Eq. (2.81)) seemingly provides the best numerical accuracy for c_{220}. Furthermore, all approaches are found to significantly underestimate the short-ranged structure of the higher-order coefficient c_{440}, although its predicted variations are qualitatively consistent with simulation results (see inset). However, it is evident that the radial dependence of the $c_{l_1 l_2 l}$ can generally not be correctly described by a simple rescaling of the Onsager DCF c_{O} for $l > 0$. This discrepancy may be easily understood as a consequence of the decoupling approximation, as such coefficients describe the angular correlations between the relative position vector $\mathbf{r}_{12}$ and the orientations $\mathbf{u}_i$ of the particles, which are effectively neglected through the use of the ansatz in Eq. (2.68). The analysis of these expansion coefficients for different particle aspect ratios L/D and volume fractions η would thus provide a direct numerical test of the convergence of the DCF towards c_{O}, although such studies may be similarly hindered by the high truncation orders required in the corresponding harmonic series (Eq. (2.76)). A potential workaround, as previously suggested to circumvent similar issues [149], would be to instead resort to the expansion of an auxiliary function $y(\mathbf{r}_{12}, \mathbf{u}_1, \mathbf{u}_2; \rho)$, related to c through

$$c(\mathbf{r}_{12}, \mathbf{u}_1, \mathbf{u}_2; \rho) = e^{-\beta u(\mathbf{r}_{12}, \mathbf{u}_1, \mathbf{u}_2)} \sum_{l_1, m_1} \sum_{l_2, m_2} y_{l_1 l_2 m_1}(r; \rho)\, Y_{l_1 m_1}(\mathbf{u}_1) Y_{l_2 m_2}(\mathbf{u}_2) \delta_{m_1 \underline{m_2}} - 1,$$

in which the sharp angular variations of c at small separation distance r are effectively subdued by the Boltzmann weight in y to ensure rapid convergence. The feasibility

of this alternative expansion in the context of the OZ equation would deserve to be investigated further, and could provide an interesting avenue for future research.

The effects of nematic order on local particle correlations may be more simply probed by comparing the numerically-determined TCF h with the low-density ansatz in Eq. (2.50), which may be readily obtained from molecular simulations using Eq. (2.49) from the expansion coefficients of the the pair correlation function $\rho^{(2)}$ in a space-fixed frame [149],

$$\rho^{(2)}_{l_1 m_1 l_2 m_2 l m}(r) = 4\pi\rho^2 g(r)\Big\langle Y^*_{l_1 m_1}(\mathbf{u}_1) Y^*_{l_2 m_2}(\mathbf{u}_2) Y^*_{lm}(\mathbf{u}_{12})\Big\rangle_r, \tag{2.82}$$

where $g(r)$ is the simulated radial distribution function. In Eq. (2.82), the radial average is now performed over all pairs of molecules with separation vector $\mathbf{r}_{12}$ such that $\|\mathbf{r}_{12}\| \in [r, r+\delta r]$ within the simulation box, regardless of orientation. Setting the laboratory polar axis $\mathbf{e}_z$ to the uniform director $\mathbf{n}_0$, the harmonic expansion of the nematic density field Eq. (2.58) reads as

$$\rho(\mathbf{u}) = \rho \sum_l \psi_l \, Y_{l0}(\mathbf{u}), \tag{2.83}$$

$$\psi_l = \oint_{\mathcal{S}} d\mathbf{u}\, \psi(\mathbf{u}\cdot\mathbf{n}_0) Y_{l0}(\mathbf{u}) \equiv \frac{1}{2\pi}\Big\langle Y_{l0}(\mathbf{u})\Big\rangle_\psi, \tag{2.84}$$

where we used the cylindrical invariance of the uniaxial phase about $\mathbf{n}_0$ to prune the azimuthal coefficients $\{Y_{lm}\}_{m\neq 0}$ from the density expansion, and introduced the *ensemble average* $\langle\cdot\rangle_\psi$ (sometimes referred to as the *thermodynamic average*),

$$\Big\langle \cdot \Big\rangle_\psi \equiv 2\pi \oint_{\mathcal{S}} d\mathbf{u}\, \psi(\mathbf{u}\cdot\mathbf{n}_0) \;\cdot\; . \tag{2.85}$$

Using the statistical definition of the equilibrium density distribution (Eq. (C.5)), it is easy to show that the ensemble average $\langle\cdot\rangle_{\psi^{(\rho)}_{\mathrm{eq}}}$ respective to the equilibrium ODF $\psi^{(\rho)}_{\mathrm{eq}}$ is equivalent to the canonical average $\langle\cdot\rangle_N$ of Eq. (2.5) at any given particle concentration $\rho = N/V$ and temperature T, provided that the density ansatz in Eq. (2.58) holds.

The expansion coefficients of h may then be obtained from the harmonic projection of Eq. (2.49) [142],

$$\rho^{(2)}_{l_1m_1l_2m_2lm}(r) = \rho^2\sqrt{4\pi}\delta_{m_10}\delta_{m_20}\delta_{l0}\delta_{m0}\psi_{l_1}\psi_{l_2} + \rho^2 \sum_{\substack{l_1',l_1'' \\ l_2',l_2''}} \mathscr{G}^{m_1m_10}_{l_1l_1'l_1''}\mathscr{G}^{m_2m_20}_{l_2l_2'l_2''}\,\psi_{l_1''}\psi_{l_2''} \times h_{l_1'm_1l_2'm_2lm}(r), \quad (2.86)$$

where $\mathscr{G}$ denotes the so-called Gaunt coefficients, determined through the application of the Wigner-Eckart theorem [150],

$$\mathscr{G}^{mm'm''}_{ll'l''} \equiv \oint_{\mathcal{S}} d\mathbf{u}\, Y^*_{lm}(\mathbf{u})Y_{l'm'}(\mathbf{u})Y_{l''m''}(\mathbf{u}) = \sqrt{\frac{(2l'+1)(2l''+1)}{4\pi(2l+1)}}\mathscr{C}^{000}_{l''l'l}\mathscr{C}^{m''m'm}_{l''l'l}.$$

Ensemble averages in Eqs. (2.82) and (2.84) were performed using 2000 independent box configurations of $N = 3600$ HSCs obtained through equilibrated NPT-MC simulations using simple isotropic volume deformations from a close-packed initial state, and the nematic director $\mathbf{n}_0$ was determined as the eigenvector associated with the largest eigenvalue of the ensemble-averaged $\mathcal{Q}$ tensor of each configuration [9],

$$\mathcal{Q}_{mn} = \left\langle \frac{3u_mu_n - \delta_{mn}}{2} \right\rangle_{\psi}, \quad (2.87)$$

where $u_m \equiv \mathbf{u}\cdot\mathbf{e}_m$ for $m \in \{x,y,z\}$. Simulations were run using the HPMC integrator [73], provided as part of the HooMD-blue numerical package [151,152], starting from a dense crystalline initial configuration. Bin widths were set to $\delta r = 0.075\,D$, and all harmonic expansions were truncated at order $l_{\max} = 12$.

We report in Figure 2.3 the simulated radial dependence of a few selected TCF expansion coefficients at various volume fractions, obtained by numerical inversion of Eq. (2.86), along with their theoretical low-density asymptotic behaviour from Eq. (2.50). It is interesting to note that the low-density ansatz in Eq. (2.50) is in surprisingly good quantitative agreement with simulations in the isotropic phase up to the isotropic binodal, although it leads to increasing underestimations of the radially-averaged coefficients $h_{l_1m_1l_2m_200}$ at short separation distances with increasing packing fractions. However, the short-ranged structure of all expansion coefficients is found to change drastically upon the onset of orientational order,

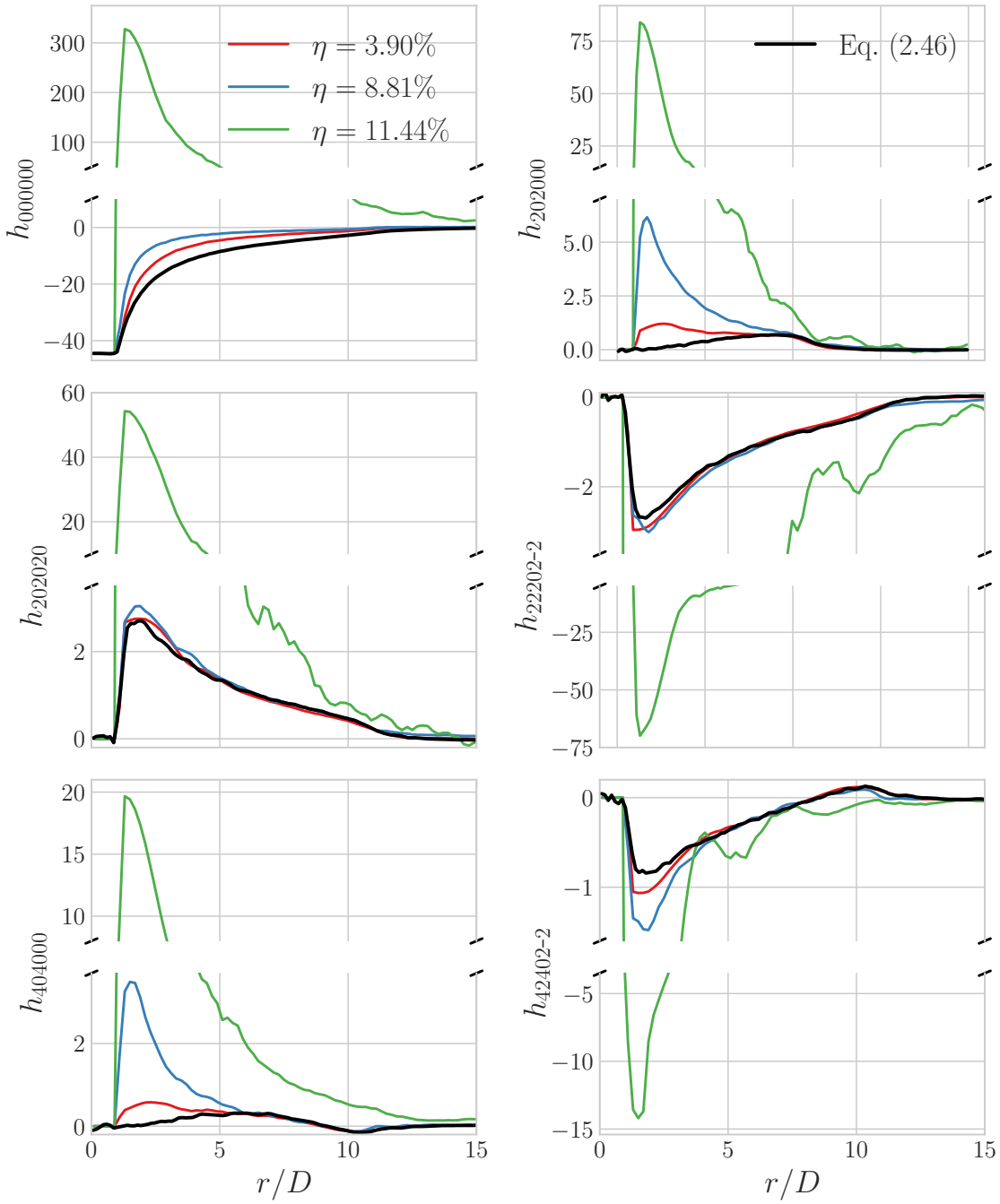

Figure 2.3: TCF nematic expansion coefficients $h_{l_1 m_1 l_2 m_2 l m}$ as a function of scaled radial separation distance r/D for HSCs with aspect ratio $L/D = 20$. Coloured lines denote the results of NPT-MC simulations obtained from Eqs. (2.82)–(2.86) in the stable isotropic phase ($\eta = 3.90\,\%$), and near the isotropic and nematic binodal points ($\eta = 8.81\,\%$ and $11.44\,\%$, respectively). Black lines represent the expansion coefficients of the low-density ansatz in Eq. (2.50), computed using a similar numerical procedure to Eq. (2.79).

which points to the general inadequacy of Eq. (2.50) in the nematic phase, regardless of particle density. This observation mirrors simulation results for fluids of short ellipsoids [144], and suggests that the rigorous justification of the validity of the Onsager DCF c_{O} in orientationally-ordered systems lies in the geometric argument of Eq. (2.33), rather than in the low-density expansion of the TCF and related quantities, as proposed by previous authors [104, 123].

2.3.2 Osmotic pressure and order parameters

We finally turn our focus to larger length-scales, and assess the ability of the Onsager DFT to correctly reproduce some of the other macroscopic observables that directly arise from the nematic free energy functional $\mathscr{F}[\psi]$ at thermodynamic equilibrium – namely, the osmotic pressure and the order parameters quantifying the degree of orientational order. In the following, we restrict our study to systems described by the decoupling ansatz in Eq. (2.69), and introduce the shorthand

$$\mathscr{X}(\rho) \equiv \mathscr{X}\left[\psi_{\mathrm{eq}}^{(\rho)}\right]$$

for all functionals $\mathscr{X}$ of the equilibrium nematic density distribution ψ_{eq} at fixed number density ρ (Eq. (2.72)). The osmotic pressure P and chemical potential μ of the system may be readily obtained from Eqs. (2.60), (2.61) and (2.69) through standard thermodynamic identities in the canonical ensemble,

$$\beta P(\rho) = -\left.\frac{\partial \mathscr{F}}{\partial V}\right|_{N,T} = \rho + \rho^2 b_2 \Big\{ G_{\mathrm{ref}}(\eta_{\mathrm{ref}}) + \eta_{\mathrm{ref}} G'_{\mathrm{ref}}(\eta_{\mathrm{ref}}) \Big\}, \tag{2.88}$$

$$\beta\mu(\rho) = \left.\frac{\partial \mathscr{F}}{\partial N}\right|_{V,T} = \log\left(\rho\lambda^3\right) - \Sigma + \rho b_2 \Big\{ 2G_{\mathrm{ref}}(\eta_{\mathrm{ref}}) + \eta_{\mathrm{ref}} G'_{\mathrm{ref}}(\eta_{\mathrm{ref}}) \Big\}, \tag{2.89}$$

with $\mathscr{F}$ the total Helmholtz free energy, Σ the rotational entropy per particle and b_2 the angle-averaged second-virial coefficient,

$$\Sigma(\rho) = -4\pi^2 \int_0^\pi \sin\theta d\theta \log\left\{\psi_{\mathrm{eq}}^{(\rho)}(\cos\theta)\right\} \psi_{\mathrm{eq}}^{(\rho)}(\cos\theta), \tag{2.90}$$

$$b_2(\rho) = \frac{1}{2}\int_0^\pi \sin\theta d\theta \int_0^\pi \sin\theta' d\theta' \, \kappa(\theta,\theta') \psi_{\mathrm{eq}}^{(\rho)}(\cos\theta) \psi_{\mathrm{eq}}^{(\rho)}(\cos\theta').$$

The mechanical and thermodynamical equilibria of a biphasic system comprised of an isotropic and a nematic fraction respectively require the osmotic pressures

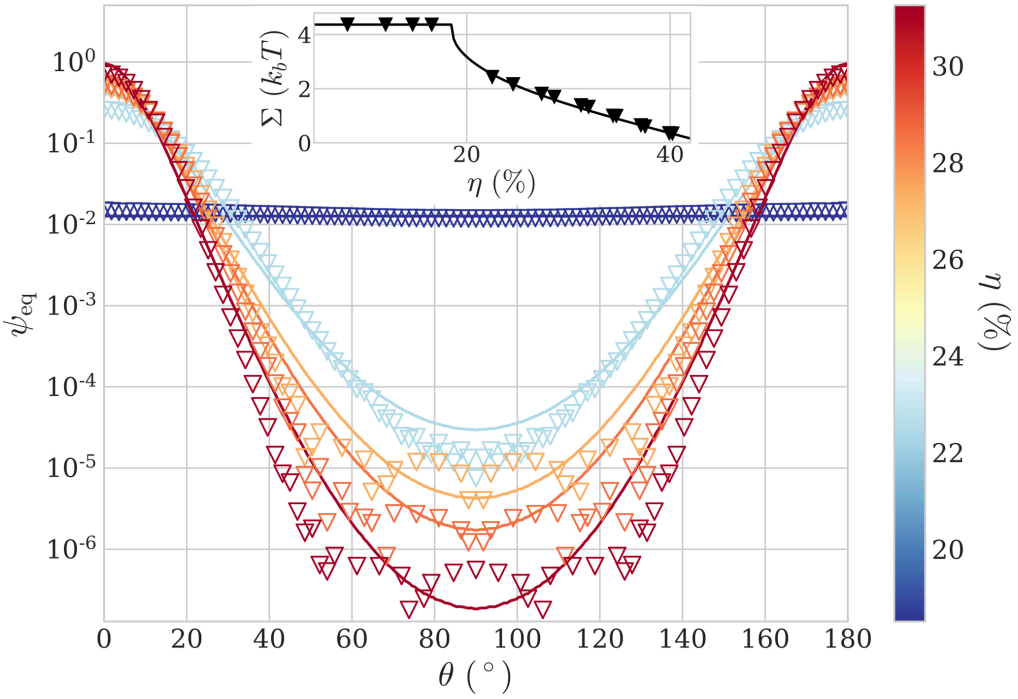

Figure 2.4: Equilibrium ODF $\psi_{\rm eq}$ as a function of polar angle $\theta \equiv \arccos(\mathbf{u}\cdot\mathbf{n}_0)$ and volume fraction η for HSCs with aspect ratio $L/D = 15$. Solid lines denote the DFT predictions of Section 2.2.2 in the PL approximation (Eqs. (2.71)–(2.73)). Symbols represent the results of NPT-MC simulations, using 2000 independent box configurations of $N = 3600$ particles for the evaluation of the ensemble-averaged expansion coefficients $\{\psi_l\}$ up to truncation order $l_{\rm max} = 40$ (Eqs. (2.83) and (2.84)). Inset: associated rotational entropy per particle Σ (Eq. (2.90)) as a function of η.

and chemical potentials of the two phases to be equal. The so-called *binodal concentrations* delimiting the ranges of isotropic and nematic stability can thus be obtained by equating Eqs. (2.88) and (2.89) in the two phases, and solving the resulting set of coupled coexistence equations via a relaxed multivariate Newton-Raphson scheme [153], using the uniform limit of the ODF in the isotropic phase,

$$\psi_{\rm iso}(\mathbf{u}) = \frac{1}{8\pi^2}. \tag{2.91}$$

We reproduce in Figure 2.4 the angular and density dependence of the equilibrium ODF $\psi_{\rm eq}$ for HSCs with aspect ratios $L/D = 15$. We note that the overall level of agreement observed between DFT and simulation results is excellent, although the quantitative comparison between the two is somewhat hindered at higher concentrations by the sharp peaks of the function about $\theta = 0$ and π, describing the increasing head-tail-symmetric alignment of the molecules about the nematic

director $\mathbf{n}_0$. A simpler approach to visualise the angular variations of the ODF, and thus the global equilibrium structure of the single-phase fluid, is to instead resort to a set of scalar *order parameters* (OPs), from which the basic symmetries of the system may be more easily grasped. In light of the discussions of Section 2.3.1, a natural starting point lies in the decomposition of ψ_{eq} in a basis of rotational invariants, whose expansion coefficients are simply given by Eq. (2.84) in the case of a uniaxial phase, and from which the full ODF may be readily reconstructed using Eq. (2.83). For the purposes of normalisation, let us define

$$S^{(l)}(\rho) = \sqrt{\frac{16\pi^3}{2l+1}}\psi_l(\rho) = \sqrt{\frac{4\pi}{2l+1}}\left\langle Y_{l0}(\mathbf{u})\right\rangle_{\psi_{\mathrm{eq}}^{(\rho)}},$$

where we used Eq. (2.84). Thus,

$$S^{(l)}(\rho) = 2\pi \oint_{\mathcal{S}} d\mathbf{u}\, \psi_{\mathrm{eq}}^{(\rho)}(\mathbf{u}\cdot\mathbf{n}_0) P_l(\mathbf{u}\cdot\mathbf{n}_0), \tag{2.92}$$

where we substituted Eq. (2.85) for the ensemble average, and introduced the Legendre polynomials P_l. It follows from the orthogonality of the P_l that in the isotropic phase, $S^{(l)}$ satisfies for all $l > 0$,

$$S_{\mathrm{iso}}^{(l)} = \frac{1}{4\pi}\oint_{\mathcal{S}} d\mathbf{u}\, P_l(\mathbf{u}\cdot\mathbf{e}_z) = 0,$$

where we used Eq. (2.91), while in the fully-ordered crystalline phase,

$$\psi(\mathbf{u}\cdot\mathbf{n}_0) \longrightarrow \psi_{\mathrm{cr}}(\mathbf{u}\cdot\mathbf{n}_0) = \frac{\delta(1-|\mathbf{u}\cdot\mathbf{n}_0|)}{8\pi^2},$$
$$S^{(l)} \longrightarrow S_{\mathrm{cr}}^{(l)} = \frac{P_l(1)+P_l(-1)}{2} = \begin{cases} 1 & \text{if } l \text{ is even} \\ 0 & \text{if } l \text{ is odd} \end{cases}.$$

More generally, it is easy to show that in the case of apolar phases, for which $\mathbf{n}_0$ and $-\mathbf{n}_0$ are equivalent, the parity properties of Legendre polynomials impose that $S^{(l)} = 0$ for all odd integers l. In formal terms, the set of scalars $\{S^{(2l)}\}_{l>0}$ may thus fully quantify orientational order in macroscopic systems possessing $C_{\infty h}$ point-group symmetry, and are referred to as the *uniaxial nematic order parameters*. In particular, for $l = 1$, it is straightforward to show that $S^{(2)}$ corresponds to the largest eigenvalue of the ensemble-averaged Q tensor (Eq. (2.87)) [9], which provides a convenient route for its determination from numerical simulations.

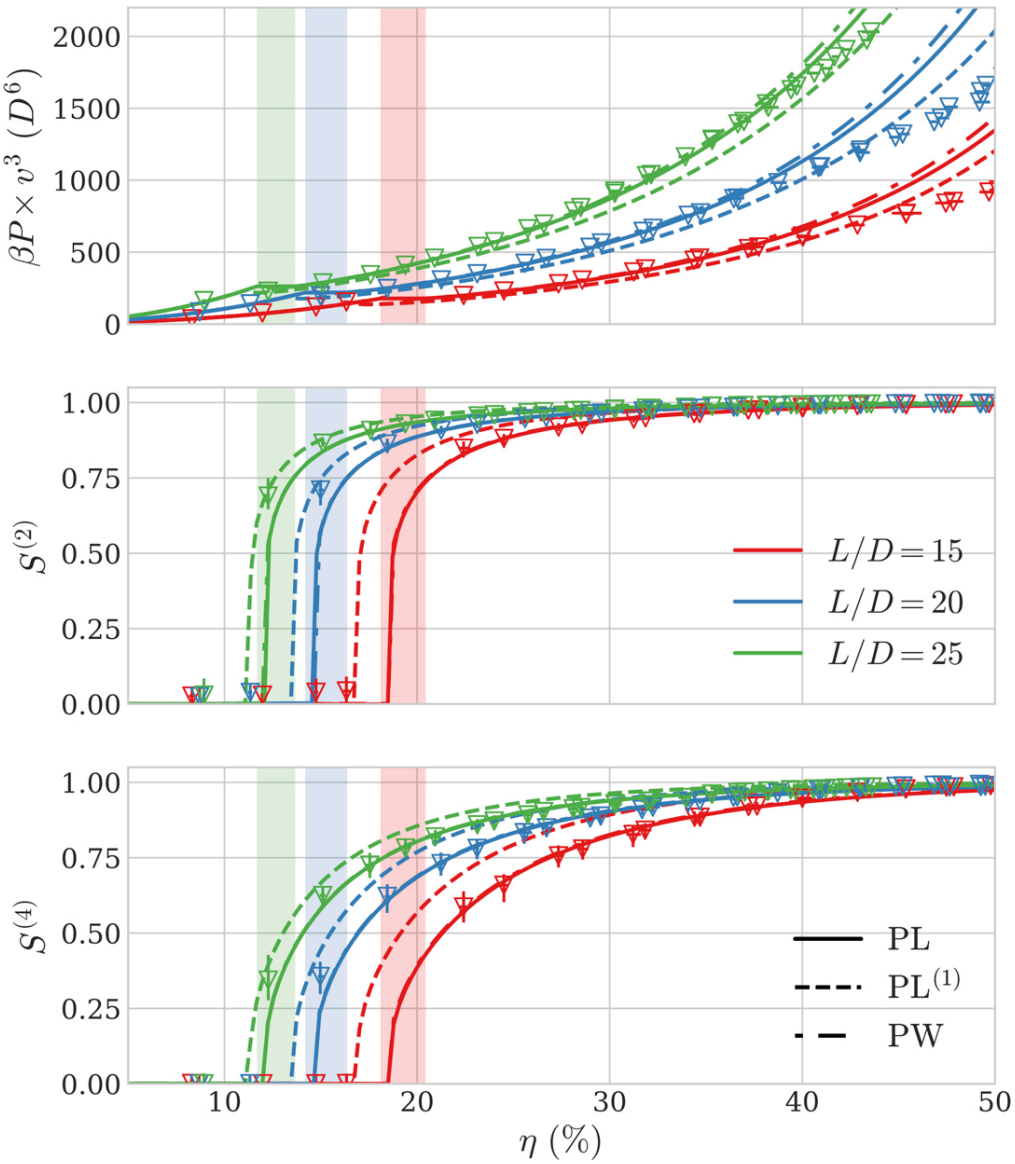

Figure 2.5: Osmotic pressure P and nematic OPs $S^{(2)}$, $S^{(4)}$ as a function of particle volume fraction η for HSCs with aspect ratios $L/D \in [15, 25]$. Solid lines denote the predictions of the various theories of Section 2.2.2 and symbols represent the results of NPT-MC simulations performed as in Section 2.3.1, with error bars obtained over 2000 independent box configurations of $N = 3600$ particles. Coloured areas delimit the ranges of I/N coexistence as computed from Eqs. (2.88) and (2.89) using the standard PL corrective prefactor (Eq. (2.71)). The discontinuity of the nematic OPs mark the location of the nematic spinodal point, as discussed in Section 3.3.1.

We reproduce in Figure 2.5 the density dependence of the osmotic pressure and the first two nematic OPs for HSCs of various aspect ratios. The predictions of the three rescaled theories of Eqs. (2.70), (2.71) and (2.74), obtained using the computational procedure detailed in Section 3.3.1, are found to be very similar, with relative numerical dispersions of under 10 % being reported over most of the concentration range for all systems. Their results are further found to gradually reduce to a single master curve with increasing aspect ratios, illustrating the convergence of all three approaches towards the Onsager theory as $L/D \to \infty$. The predictions of the PL and and PW theories are found to be largely identical in all cases, and in excellent quantitative agreement with simulations results up to volume fractions $\eta \simeq 40\,\%$. These discrepancies are consistent with the approximations of the theories, and may be further imputed to the gradual stabilisation of positionally-ordered phases in the higher-density range, for which the symmetry assumptions underlying the decoupling approximation fail (c.f. Appendix D).

2.4 Conclusion

In this chapter, we have proposed a thorough reexamination of the Onsager theory, in the formalism of both virial expansions and classical DFT. This analysis reveals that the validity of the second-virial free-energy functional in the uniaxial nematic phase of highly-anisotropic mesogens may not be rigorously justified by a naive low-density expansion of the OZ equation, and highlights the enduring relevance of Onsager's seminal geometric arguments. The extension of the theory to the treatment of finite-sized particles is also presented in detail, and the application of the decoupling approximation to the DCF in the PL framework is shown to lead to the introduction of a novel correction prefactor $G_{\mathrm{PL}}^{(1)}$ (Eq. (2.74)), whose quantitative accuracy will be further investigated in Section 3.3.2. More broadly, the microscopic correlation functions emphasised throughout this chapter will be seen to play a fundamental role in the molecular theory of LC elasticities, which underpins our description of cholesteric order, and which will be extensively discussed in Chapter 3.

3

Perturbative density functional methods for LCLCs

Contents

In Chapter 2, we have derived a microscopic theory of uniaxial nematic LCs in the limiting case of a uniform nematic director — i.e., assuming the average direction of local molecular alignment to be identical at all points in space. Real nematic phases, however, generally display a position-dependent director field $\mathbf{n}(\mathbf{r})$, giving rise to the eponymous "thread-like" textures typically observed in experimental systems (Greek: νημα, thread). Cholesteric phases, characterised by the periodic rotation of $\mathbf{n}$ about a fixed normal axis (Figure 1.2b), constitute a particularly

notable illustration of these spatial variations in the context of this thesis. To extend our microscopic description to cholesterics, it is therefore necessary to introduce director modulations into the previous theoretical framework, which provides the main motivation for the current chapter.

3.1 The Oseen-Frank free energy

In statistical field theories, the spatial fluctuations of macroscopic phases are commonly described through the construction of an effective phenomenological Hamiltonian consistent with the physical symmetries of the system, from which the structure of the underlying free energy landscape may be probed in the vicinity of the (generally uniform) ground state [154]. In this spirit, the Helmholtz free energy $\mathscr{F}$ of a uniaxial nematic phase characterised by an arbitrary director field $\mathbf{n}(\mathbf{r})$ may be sought in the form of a gradient expansion of $\mathbf{n}$ about that $\mathscr{F}_0$ of the phase with uniform director state $\mathbf{n}(\mathbf{r}) = \mathbf{n}_0$, as derived in Chapter 2. Assuming the spatial variations of $\mathbf{n}$ to be smooth, it is expedient to introduce a local frame $\mathcal{T}(\mathbf{r}) \equiv \left[\mathbf{e}'_x\ \mathbf{e}'_y\ \mathbf{e}'_z\right]$ such that $\mathbf{n}(\mathbf{r}) = \mathbf{e}'_z$, so that the director field $\mathbf{n}(\mathbf{r}')$ in the vicinity of $\mathbf{r}$ reads as

$$\mathbf{n}(\mathbf{r}') = \sqrt{1 - \|\mathbf{t}(\mathbf{r}')\|^2}\,\mathbf{e}'_z + \mathbf{t}(\mathbf{r}'),$$

with $\mathbf{t}(\mathbf{r}') \cdot \mathbf{e}'_z = 0$ and $\|\mathbf{t}(\mathbf{r}')\| \ll 1$. Thus,

$$\nabla\mathbf{n}(\mathbf{r}) = \nabla\mathbf{t}(\mathbf{r}) + \mathcal{O}\left(\|\mathbf{t}\|^2\right) \simeq \begin{bmatrix} \frac{\partial t_x}{\partial r_x} & \frac{\partial t_x}{\partial r_y} & \frac{\partial t_x}{\partial r_z} \\ \frac{\partial t_y}{\partial r_x} & \frac{\partial t_y}{\partial r_y} & \frac{\partial t_y}{\partial r_z} \\ 0 & 0 & 0 \end{bmatrix}_{\mathcal{T}(\mathbf{r})},$$

where $t_m \equiv \mathbf{t}(\mathbf{r}) \cdot \mathbf{e}'_m$ and $r_m \equiv \mathbf{r} \cdot \mathbf{e}'_m$ for $m \in \{x, y, z\}$. Denoting by s_i the 6 independent local curvature components of $\nabla\mathbf{n}(\mathbf{r})$, and using the extensivity of the free energy, we obtain

$$\mathscr{F} = \mathscr{F}_0 + \int_V d\mathbf{r}\, f_d(\mathbf{r}), \tag{3.1}$$

with $f_d(\mathbf{r})$ the local *distortion free energy density*, to quadratic order in the strains s_i,

$$f_d(\mathbf{r}) = \sum_{i=1}^{6} k_i s_i + \frac{1}{2}\sum_{i=1}^{6}\sum_{j=1}^{6} k_{ij} s_i s_j. \tag{3.2}$$

In the limit of weak curvature deformations, for which the gradient expansion in Eqs. (3.1) and (3.2) is well defined, uniaxial symmetry dictates that $f_d(\mathbf{r})$ must be locally invariant by rotation about $\mathbf{n}(\mathbf{r})$. Furthermore, we here restrict our study to the case of apolar LCs, for which the equivalence of $\mathbf{n}(\mathbf{r})$ and $-\mathbf{n}(\mathbf{r})$ imposes that f_d remains unchanged by the local frame transformation

$$\mathbf{n} \to -\mathbf{n}, \qquad \mathbf{e}'_x \to \mathbf{e}'_x, \qquad \mathbf{e}'_y \to -\mathbf{e}'_y, \qquad \mathbf{e}'_z \to -\mathbf{e}'_z.$$

Lengthy, but straightforward manipulations [155] demonstrate that the use of these two symmetry constraints reduces the 42 terms in the expansion of Eq. (3.2) down to just 5 independent contributions, which may be recast in the compact form

$$f_d(\mathbf{r}) = \frac{K_1}{2}\Big(\nabla\cdot\mathbf{n}\Big)^2 + \frac{K_2}{2}\Big(\mathbf{n}\cdot[\nabla\times\mathbf{n}]\Big)^2 + \frac{K_3}{2}\Big(\mathbf{n}\times[\nabla\times\mathbf{n}]\Big)^2 + k_t\Big(\mathbf{n}\cdot[\nabla\times\mathbf{n}]\Big) + K_{24}\Big(\nabla\cdot\Big\{\mathbf{n}(\nabla\cdot\mathbf{n}) + \mathbf{n}\times[\nabla\times\mathbf{n}]\Big\}\Big). \quad (3.3)$$

As will be shown in Section 3.2, the expansion coefficients K_i and k_t generally depend on the microscopic properties of the constituent particles and the degree of nematic order about the local director $\mathbf{n}(\mathbf{r})$. In the absence of topological defects or strong concentration gradients, the local distribution of molecules about $\mathbf{n}(\mathbf{r})$ is generally assumed to be independent of $\mathbf{r}$, so that all expansion coefficients in Eq. (3.3) may be taken to be spatially uniform. In this case, the term in K_{24}, known as the *saddle-splay* contribution, takes the form of a total differential, and it follows from the divergence theorem that

$$\int_V d\mathbf{r}\, K_{24}\Big(\nabla\cdot\Big\{\mathbf{n}(\nabla\cdot\mathbf{n}) + \mathbf{n}\times[\nabla\times\mathbf{n}]\Big\}\Big) = K_{24}\oiint_{\partial V} d\mathbf{S}\cdot\Big\{\mathbf{n}(\nabla\cdot\mathbf{n}) + \mathbf{n}\times[\nabla\times\mathbf{n}]\Big\},$$

where $d\mathbf{S}$ denotes the local surface normal to the closed boundary ∂V of the sample. Therefore, saddle-splay only provides a surface contribution to the total Helmholtz free energy $\mathscr{F}$ (Eq. (3.1)), and may be disregarded in the thermodynamic limit. Thus, Eqs. (3.1) and (3.3) yield the so-called *Oseen-Frank (OF) free energy*,

$$\mathscr{F} = \mathscr{F}_0 + \frac{1}{2}\int_V d\mathbf{r}\,\Big[K_1\Big(\nabla\cdot\mathbf{n}\Big)^2 + K_2\Big(\mathbf{n}\cdot[\nabla\times\mathbf{n}]\Big)^2 + K_3\Big(\mathbf{n}\times[\nabla\times\mathbf{n}]\Big)^2 + 2k_t\Big(\mathbf{n}\cdot[\nabla\times\mathbf{n}]\Big)\Big], \quad (3.4)$$

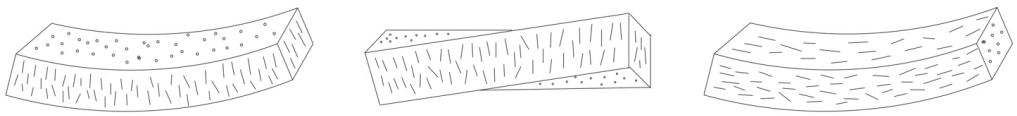

K_1 K_2 K_3

Figure 3.1: Illustration of the splay (left), twist (centre) and bend (right) curvature strains in nematic LCs. Adapted with permission from Ref. [156].

which provides a continuum-level description of a nematic LC with arbitrary director field $\mathbf{n}$. In this context, the thermodynamic stability of local nematic order with respect to director fluctuations imposes that $K_i > 0$, so that K_1, K_2 and K_3 may be interpreted as the respective elastic moduli associated with the three independent curvature deformations of uniaxial nematic LCs — namely, *splay*, *twist*, and *bend* (Figure 3.1). The first order term in k_t can further be shown to be non-zero only in the case of mirror-asymmetric particles, and is referred to as the *chiral strength*, which stabilises a finite director twist to accommodate the local molecular chirality.

Indeed, for a cholesteric phase of axis $\mathbf{e}_x$ and inverse pitch $q \equiv 2\pi/\mathcal{P}$, the helical modulation of the equilibrium director field is described by

$$\mathbf{n}(\mathbf{r}) = -\sin(qr_x)\,\mathbf{e}_y + \cos(qr_x)\,\mathbf{e}_z, \tag{3.5}$$

where we used the conventions of Figure 1.2b, choosing the laboratory frame such that $\mathbf{e}_z \equiv \mathbf{n}(\mathbf{0})$ and ensuring that $q > 0$ corresponds to a right-handed phase. Eq. (3.5) immediately leads to

$$\mathbf{n}\cdot[\nabla\times\mathbf{n}] = -q, \qquad \nabla\cdot\mathbf{n} = 0, \qquad \mathbf{n}\times[\nabla\times\mathbf{n}] = \mathbf{0},$$

so that Eq. (3.4) yields the Helmholtz free energy of the cholesteric phase in the form

$$\mathscr{F} = \mathscr{F}_0 + \frac{V}{2}(K_2\,q^2 - 2k_t\,q). \tag{3.6}$$

The equilibrium director configuration may thus be obtained by minimisation of Eq. (3.6) with respect to q,

$$\left.\frac{\partial\mathscr{F}}{\partial q}\right|_{N,V,T}(q = q_{\mathrm{eq}}) = 0 \quad\Longleftrightarrow\quad \mathcal{P}_{\mathrm{eq}}(\rho,T) = 2\pi\frac{K_2(\rho,T)}{k_t(\rho,T)}. \tag{3.7}$$

Therefore, the equilibrium pitch $\mathcal{P}_{\rm eq}$ of a cholesteric phase is driven by the competition between the chiral torque k_t, which promotes local director twist, and the twist elastic modulus K_2, which favours local alignment. The determination of $\mathcal{P}_{\rm eq}$ for a given molecular system thus reduces to the derivation of microscopic expressions for K_2 and k_t.

In light of the previous discussions, a convenient framework for the purposes of this calculation is provided by perturbation theory, through which the properties of weakly-modulated phases may be related to those of the uniform nematic LCs considered in Chapter 2 by exploiting the large gap in length-scales between director fluctuations and typical molecular sizes. We now respectively outline in Sections 3.2.1 and 3.2.2 the salient points of this approach in the case of uniaxial nematic and cholesteric phases.

3.2 Microscopic theory of LC elasticities

3.2.1 The Poniewierski-Stecki equations

The director field $\mathbf{n}(\mathbf{r})$ associated with an arbitrary density distribution $\rho(\mathbf{r},\mathcal{R})$ may be defined as the largest eigenvalue of the local angle-averaged $\mathcal{Q}$-tensor [9],

$$\mathcal{Q}_{mn}(\mathbf{r}) = \frac{V}{N}\oint d\mathcal{R}\,\rho(\mathbf{r},\mathcal{R})\frac{3u_m u_n - \delta_{mn}}{2},$$

where we used the notation of Section 2.3.1. This linear relationship implies that a small fluctuation $\delta\mathbf{n}(\mathbf{r})$ of the director about a given equilibrium configuration $\mathbf{n}(\mathbf{r})$ may be equivalently expressed in terms of an elementary perturbation $\delta\rho$ of the density field about $\rho_{\rm eq}$,

$$\delta\rho(\mathbf{r},\mathcal{R}) \equiv \rho(\mathbf{r},\mathcal{R}) - \rho_{\rm eq}(\mathbf{r},\mathcal{R}). \tag{3.8}$$

The corresponding variation $\delta\mathscr{F} \equiv \mathscr{F}[\rho] - \mathscr{F}[\rho_{\rm eq}]$ of the Helmholtz free energy may be obtained by functional Taylor expansion to second order in $\delta\rho$,

$$\delta\mathscr{F} = \frac{1}{2}\iint_V d\mathbf{r}_1 d\mathbf{r}_2 \oiint d\mathcal{R}_1 d\mathcal{R}_2 \left.\frac{\delta^2\mathscr{F}[\rho]}{\delta\rho(\mathbf{r}_1,\mathcal{R}_1)\delta\rho(\mathbf{r}_2,\mathcal{R}_2)}\right|_{\rho_{\rm eq}} \delta\rho(\mathbf{r}_1,\mathcal{R}_1)\delta\rho(\mathbf{r}_2,\mathcal{R}_2),$$

where the first-order term cancels out from the combination of Eq. (2.42) and the conservation of the total number of molecules in the system,

$$\int_V d\mathbf{r} \oint d\mathcal{R}\, \frac{\delta\mathscr{F}[\rho]}{\delta\rho(\mathbf{r},\mathcal{R})}\bigg|_{\rho_{\rm eq}} \delta\rho(\mathbf{r},\mathcal{R}) = \mu_N \int_V d\mathbf{r} \oint d\mathcal{R}\, \delta\rho(\mathbf{r},\mathcal{R}) = 0.$$

Differentiating Eq. (2.44), and using Eq. (2.47),

$$\delta\mathscr{F} = \frac{k_bT}{2} \iint_V d\mathbf{r}_1 d\mathbf{r}_2 \oiint d\mathcal{R}_1 d\mathcal{R}_2 \left\{ \frac{\delta(\mathbf{r}_{12})\delta(\mathcal{R}_2-\mathcal{R}_1)}{\rho_{\rm eq}(\mathbf{r}_1,\mathcal{R}_1)} - c\Big(\mathbf{r}_1,\mathbf{r}_2,\mathcal{R}_1,\mathcal{R}_2;[\rho_{\rm eq}]\Big)\right\} \times \delta\rho(\mathbf{r}_1,\mathcal{R}_1)\delta\rho(\mathbf{r}_2,\mathcal{R}_2), \quad (3.9)$$

which reveals the link between the DCF $c \equiv c^{(2)}$ and the local response of nematic LCs to elementary variations of the director field. Let us introduce the centre-of-mass position $\mathbf{R} \equiv (\mathbf{r}_1+\mathbf{r}_2)/2$ of an arbitrary pair of particles 1 and 2,

$$\mathbf{r}_{1,2} = \mathbf{R} \mp \mathbf{r}_{12}/2. \quad (3.10)$$

Using the change of variable in Eq. (3.10), with unit Jacobian determinant, the total Helmholtz free energy penalty $\delta\mathscr{F}$ (Eq. (3.9)) may then be recast in the form

$$\delta\mathscr{F} = \int_V d\mathbf{R}\, \delta f(\mathbf{R}), \quad (3.11)$$

with $\delta f(\mathbf{R})$ the free energy density of the deformation,

$$\delta f(\mathbf{R}) = \frac{k_bT}{2} \int_V d\mathbf{r}_{12} \oiint d\mathcal{R}_1 d\mathcal{R}_2 \left\{ \frac{\delta(\mathbf{r}_{12})\delta(\mathcal{R}_2-\mathcal{R}_1)}{\rho_{\rm eq}(\mathbf{R}-\mathbf{r}_{12}/2,\mathcal{R}_1)} - c\Big(\mathbf{r}_{12},\mathbf{R},\mathcal{R}_1,\mathcal{R}_2;[\rho_{\rm eq}]\Big)\right\} \times \delta\rho\left(\mathbf{R}-\frac{\mathbf{r}_{12}}{2},\mathcal{R}_1\right)\delta\rho\left(\mathbf{R}+\frac{\mathbf{r}_{12}}{2},\mathcal{R}_2\right), \quad (3.12)$$

which quantifies the thermodynamic penalty associated with a weak director fluctuation about the arbitrary equilibrium director configuration.

To identify δf with the OF expression (Eq. (3.4)), let us for now restrict ourselves to the case of a uniform equilibrium director field,

$$\mathbf{n}(\mathbf{R}) = \mathbf{n}(\mathbf{0}) \equiv \mathbf{n}_0,$$
$$\delta\mathscr{F} = \mathscr{F} - \mathscr{F}_0.$$

In this limit, the equilibrium density $\rho_{\rm eq}$ simply reduces to the uniform equilibrium ODF $\rho\psi_{\rm eq}$ of Section 2.2.1, while translational invariance eliminates the explicit

dependence of the DCF $c_0 \equiv c[\rho\psi_{\rm eq}]$ on $\mathbf{R}$. Substituting the Fourier-space representation of c_0 and $\delta\rho$ in Eq. (3.12) leads to, after rearrangements,

$$\delta f(\mathbf{R}) = \frac{k_b T}{2} \iint d\mathbf{k} d\mathbf{k}' \oiint d\mathcal{R}_1 d\mathcal{R}_2 \left\{ \frac{\delta(\mathcal{R}_2 - \mathcal{R}_1)}{\rho\psi_{\rm eq}(\mathbf{u}_1)} - \widehat{c_0}(\mathbf{k}, \mathcal{R}_1, \mathcal{R}_2) \right\} \times \widehat{\delta\rho}\left(\frac{\mathbf{k}'}{2} + \mathbf{k}, \mathcal{R}_1\right) \widehat{\delta\rho}\left(\frac{\mathbf{k}'}{2} - \mathbf{k}, \mathcal{R}_2\right) \exp(2i\pi\mathbf{k}' \cdot \mathbf{R}), \quad (3.13)$$

where $\widehat{\zeta}$ denotes the Fourier transform of any function ζ with respect to its first argument. It should be noted that the implicit use of periodic boundary conditions in the derivation of Eq. (3.13) is consistent with our neglect of surface elasticity terms in the OF free energy, as discussed in Ref. [157]. Furthermore, assuming the director distortion $\delta\mathbf{n}$ to be weak enough so as not to affect the local structure of the phase, we may obtain the density of the deformed phase by a simple local rotation of the equilibrium uniform distribution (Eq. (2.58)),

$$\rho(\mathbf{r}, \mathcal{R}) = \rho\psi_{\rm eq}\Big\{\mathbf{u} \cdot [\mathbf{n}_0 + \delta\mathbf{n}(\mathbf{r})]\Big\}, \quad (3.14)$$

so that Eq. (3.8) yields, to first order in $\delta\mathbf{n}$,

$$\delta\rho(\mathbf{r}, \mathcal{R}) = \rho\dot{\psi}_{\rm eq}(\mathbf{u} \cdot \mathbf{n}_0) \times \Big\{\mathbf{u} \cdot \delta\mathbf{n}(\mathbf{r})\Big\}.$$

Note that the use of the use of the ansatz in Eq. (3.14) effectively neglects the potential coupling between the local molecular density ρ and the spatial fluctuations of the director $\mathbf{n}$, which is expected to be appropriate for the twist deformations characteristic of cholesteric phases, but may require additional compressibility corrections in the general case of arbitrary director conformations — especially for the treatment of splay contributions [158]. The effects of these considerations remain largely unexplored [159] and would require further investigations, which lie beyond the scope of this chapter. Eq. (3.14) further reduces the orientational dependence of the density field to the single scalar $\mathbf{u} \cdot [\mathbf{n}_0 + \delta\mathbf{n}(\mathbf{r})]$ and thereby assumes that the non-uniform nematic phase retains local cylindrical invariance. This symmetry constraint therefore restricts its applicability to the description of systems in which the spatial variations of $\mathbf{n}$ occurring over molecular length-scales are vanishingly weak, consistently with the approximations of the OF theory.

Let us perform the Taylor expansion of $\widehat{c}_0$ to second order in $\mathbf{k}$,

$$\widehat{c}_0(\mathbf{k},\mathcal{R}_1,\mathcal{R}_2) = \widehat{c}_0(\mathbf{0},\mathcal{R}_1,\mathcal{R}_2) + \sum_m k_m \frac{\partial \widehat{c}_0(\mathbf{k},\mathcal{R}_1,\mathcal{R}_2)}{\partial k_m}\bigg|_{\mathbf{k}=\mathbf{0}} + \frac{1}{2}\sum_{m,n} k_m k_n \frac{\partial^2 \widehat{c}_0(\mathbf{k},\mathcal{R}_1,\mathcal{R}_2)}{\partial k_m \partial k_n}\bigg|_{\mathbf{k}=\mathbf{0}}. \quad (3.15)$$

It follows from particle-exchange symmetry that

$$\widehat{c}_0(\mathbf{k},\mathcal{R}_1,\mathcal{R}_2) = \widehat{c}_0(-\mathbf{k},\mathcal{R}_2,\mathcal{R}_1),$$

which imposes that all linear terms in $\mathbf{k}$ vanish from the corresponding expansion of δf (Eq. (3.13)). Furthermore, the $\mathbf{k}=\mathbf{0}$ contribution to Eq. (3.15) is analogous to the isothermal compressibility of simple fluids (Eq. (D.16)), and may be shown to exactly cancel out with the ideal gas contribution in Eq. (3.13) due to the invariance of the overall density ρ with respect to director fluctuations [142, 160]. Thus, Eqs. (3.11)–(3.15) lead to

$$\beta\delta\mathscr{F} = -\frac{\rho^2}{4}\sum_{m,n}\int d\mathbf{k} \oiint d\mathcal{R}_1 d\mathcal{R}_2\, \dot{\psi}_{\mathrm{eq}}(\mathbf{u}_1\cdot\mathbf{n}_0)\dot{\psi}_{\mathrm{eq}}(\mathbf{u}_2\cdot\mathbf{n}_0)\frac{\partial^2 \widehat{c}_0(\mathbf{k},\mathcal{R}_1,\mathcal{R}_2)}{\partial k_m \partial k_n}\bigg|_{\mathbf{k}=\mathbf{0}} \times k_m k_n \Big\{\mathbf{u}_1\cdot\widehat{\delta\mathbf{n}}(\mathbf{k})\Big\}\Big\{\mathbf{u}_2\cdot\widehat{\delta\mathbf{n}}(-\mathbf{k})\Big\}, \quad (3.16)$$

which may be compared with the reciprocal-space formulation of Eq. (3.4), assuming the perturbation $\delta\mathbf{n}(\mathbf{r})$ to be smooth,

$$\delta\mathscr{F} = \frac{k_b T}{2}\int d\mathbf{k}\left\{K_1\Big(\mathbf{k}\cdot\widehat{\delta\mathbf{n}}\Big)^2 + K_2\Big(\widehat{\delta\mathbf{n}}\cdot\Big[\mathbf{k}\times\widehat{\delta\mathbf{n}}\Big]\Big)^2 + K_3\Big(\widehat{\delta\mathbf{n}}\times\Big[\mathbf{k}\times\widehat{\delta\mathbf{n}}\Big]\Big)^2\right\}. \quad (3.17)$$

Setting $\mathbf{n_0} = \mathbf{e}_z$, a tedious but straightforward term-by-term comparison of Eqs. (3.16) and (3.17) [157] finally yields the so-called Poniewierski-Stecki relations [161],

$$\beta K_1[\psi_{\mathrm{eq}}] = \frac{\rho^2}{2}\int_V d\mathbf{r}_{12} \oiint d\mathcal{R}_1 d\mathcal{R}_2\, c\Big(\mathbf{r}_{12},\mathcal{R}_1,\mathcal{R}_2;[\rho\psi_{\mathrm{eq}}]\Big)\times r_x^2 u_{1x}u_{2x} \times \dot{\psi}_{\mathrm{eq}}(u_{1z})\dot{\psi}_{\mathrm{eq}}(u_{2z}), \quad (3.18)$$

$$\beta K_2[\psi_{\mathrm{eq}}] = \frac{\rho^2}{2}\int_V d\mathbf{r}_{12} \oiint d\mathcal{R}_1 d\mathcal{R}_2\, c\Big(\mathbf{r}_{12},\mathcal{R}_1,\mathcal{R}_2;[\rho\psi_{\mathrm{eq}}]\Big)\times r_x^2 u_{1y}u_{2y} \times \dot{\psi}_{\mathrm{eq}}(u_{1z})\dot{\psi}_{\mathrm{eq}}(u_{2z}), \quad (3.19)$$

$$\beta K_3[\psi_{\mathrm{eq}}] = \frac{\rho^2}{2}\int_V d\mathbf{r}_{12} \oiint d\mathcal{R}_1 d\mathcal{R}_2\, c\Big(\mathbf{r}_{12},\mathcal{R}_1,\mathcal{R}_2;[\rho\psi_{\mathrm{eq}}]\Big)\times r_z^2 u_{1x}u_{2x} \times \dot{\psi}_{\mathrm{eq}}(u_{1z})\dot{\psi}_{\mathrm{eq}}(u_{2z}), \quad (3.20)$$

with $r_n \equiv \mathbf{r}_{12}\cdot\mathbf{e}_n$ and $u_{im} \equiv \mathbf{u}_i\cdot\mathbf{e}_m$, and where we used the standard Fourier identity

$$\left.\frac{\partial^2\widehat{c}_0(\mathbf{k},\mathcal{R}_1,\mathcal{R}_2)}{\partial k_m\partial k_n}\right|_{\mathbf{k}=\mathbf{0}} = -\int_V d\mathbf{r}_{12}\, c_0(\mathbf{r}_{12},\mathcal{R}_1,\mathcal{R}_2) r_m r_n.$$

3.2.2 Straley's approach

In the case where the equilibrium director configuration is cholesteric rather than uniform — i.e., where $k_t \neq 0$ — a more convenient starting point for the derivation of Eqs. (3.18)–(3.20) is provided by Eq. (2.65). By analogy with Eq. (3.14), let us now postulate that the density distribution ρ of the weakly-modulated phase may be written as a generalised form of Eq. (2.58) [162],

$$\rho(\mathbf{r},\mathcal{R}) = \rho\psi\Big\{\mathbf{u}\cdot\mathbf{n}(\mathbf{r})\Big\} \equiv \rho\psi_{(\mathbf{r})}(\mathbf{u}). \tag{3.21}$$

Using the density ansatz in Eq. (3.21), the double functional integration of Eq. (2.47) along the compression path of Eq. (2.52) yields the immediate generalisation of Eqs. (2.60) and (2.65) to the case of an arbitrary director field $\mathbf{n}(\mathbf{r})$,

$$\beta\mathscr{F}_{\rm id}[\psi] = \int_V d\mathbf{r} \oint d\mathcal{R}\, \rho\psi\Big\{\mathbf{u}\cdot\mathbf{n}(\mathbf{r})\Big\}\Big[\log\Big(\rho\lambda^3\psi\Big\{\mathbf{u}\cdot\mathbf{n}(\mathbf{r})\Big\}\Big) - 1\Big], \tag{3.22}$$

$$\beta\mathscr{F}_{\rm ex}[\psi] = -\frac{\rho^2}{2}\iint_V d\mathbf{r}_1 d\mathbf{r}_2 \oiint d\mathcal{R}_1 d\mathcal{R}_2\, \psi\Big\{\mathbf{u}_1\cdot\mathbf{n}(\mathbf{r}_1)\Big\}\psi\Big\{\mathbf{u}_2\cdot\mathbf{n}(\mathbf{r}_2)\Big\} \times \overline{c}\Big(\mathbf{r}_1,\mathbf{r}_2,\mathcal{R}_1,\mathcal{R}_2;[\rho\psi]\Big). \tag{3.23}$$

Let $\mathcal{T}(\mathbf{r})$ be a rotation matrix such that

$$\mathbf{n}(\mathbf{r}) = \mathcal{T}(\mathbf{r})\cdot\mathbf{n}_0. \tag{3.24}$$

Introducing the unit-Jacobian transformation $\mathcal{R}' \equiv \mathcal{T}(\mathbf{r})^{\mathsf{T}}\cdot\mathcal{R}$ in Eq. (3.22) leads to

$$\beta\mathscr{F}_{\rm id}[\psi] = \int_V d\mathbf{r} \oint d\mathcal{R}'\, \rho\psi(\mathbf{u}'\cdot\mathbf{n}_0)\Big\{\log[\rho\lambda^3\psi(\mathbf{u}'\cdot\mathbf{n}_0)] - 1\Big\},$$

which indicates that the ideal Helmholtz free energy functional is unaffected by director fluctuations.

Furthermore, it follows from the short-ranged character of the DCF that a pair of molecules 1 and 2 may physically contribute to the integral in Eq. (3.23) only if their centre-of-mass separation distance $\mathbf{r}_{12}$ is of the order of the typical

molecular dimensions. Using Eq. (3.10), we may thus write, in the limit of long-wavelength director distortions,

$$\mathbf{n}(\mathbf{r}_i) \simeq \mathbf{n}(\mathbf{R}) \mp \frac{\nabla\mathbf{n}(\mathbf{R})\cdot\mathbf{r}_{12}}{2} + \frac{\nabla^2\mathbf{n}(\mathbf{R}) : (\mathbf{r}_{12}\otimes\mathbf{r}_{12})}{8},$$

with $\otimes$ and $:$ the respective tensor and double dot products. In the case of the cholesteric modulation of Eq. (3.5), a local rotating frame $\mathcal{T}(\mathbf{R}) \equiv \left[\mathbf{e}'_x\ \mathbf{e}'_y\ \mathbf{e}'_z\right]$ satisfying Eq. (3.24) is given by

$$\mathcal{T}(\mathbf{R}) \equiv \begin{bmatrix} 1 & 0 & 0 \\ 0 & \cos(qR_x) & -\sin(qR_x) \\ 0 & \sin(qR_x) & \cos(qR_x) \end{bmatrix}.$$

It is straightforward to show that

$$\nabla\mathbf{n}(\mathbf{R}) = -q\,\mathbf{e}'_y\otimes\mathbf{e}'_x,$$
$$\nabla^2\mathbf{n}(\mathbf{R}) = -q^2\,\mathbf{e}'_z\otimes\mathbf{e}'_x\otimes\mathbf{e}'_x,$$

which directly lead to

$$\psi\Big\{\mathbf{u}_i\cdot\mathbf{n}(\mathbf{r}_i)\Big\} = \psi(u'_{iz}) \pm \frac{qu'_{iy}r'_x}{2}\dot{\psi}(u'_{iz}) - \frac{u'_{iz}}{2}\left\{\frac{qr'_x}{2}\right\}^2\dot{\psi}(u'_{iz}) + \frac{1}{2}\left\{\frac{qu'_{iy}r'_x}{2}\right\}^2\ddot{\psi}(u'_{iz}) + \mathcal{O}(q^3), \quad (3.25)$$

where primed quantities are expressed in the local frame $\mathcal{T}(\mathbf{R})$, with $u'_{ij} \equiv \mathbf{u}_i\cdot\mathbf{e}'_j$ and $r'_x \equiv \mathbf{r}_{12}\cdot\mathbf{e}'_x$.

Under the same assumption of weak local director gradients, we may further postulate that the effective DCF $\bar{c}$ may be written as a local functional of the density distribution $\psi_{(\mathbf{R})}$ at the particles centre of mass $\mathbf{R}$ (Eq. (3.21)),

$$\bar{c}\Big(\mathbf{r}_1,\mathbf{r}_2,\mathcal{R}_1,\mathcal{R}_2;[\rho\psi]\Big) \cong \bar{c}\Big(\mathbf{r}_{12},\mathbf{R},\mathcal{R}_1,\mathcal{R}_2;[\rho\psi_{(\mathbf{R})}]\Big) = \bar{c}\Big(\mathbf{r}'_{12},\mathcal{R}'_1,\mathcal{R}'_2;[\rho\psi_{(\mathbf{0})}]\Big), \quad (3.26)$$

where the last equality stems from the invariance of the bulk cholesteric phase by combined translation of vector $\mathbf{R}$ and rotation $\mathcal{T}(\mathbf{R})$. Plugging Eqs. (3.25) and (3.26) into Eq. (3.23) and using the change of variable in Eq. (3.10) yields the total Helmholtz free energy in the form

$$\mathscr{F}[\psi] = \mathscr{F}_0[\psi] + \int_V d\mathbf{R}\, f_d[\psi], \quad (3.27)$$

with $\mathscr{F}_0$ the Helmholtz free energy functional of the uniform nematic phase (Eqs. (2.41), (2.60) and (2.65)), and f_d the distortion free energy density functional,

$$f_d[\psi] = \frac{\rho^2}{2}\int_V d\mathbf{r}_{12} \oiint d\mathcal{R}_1 d\mathcal{R}_2\, \bar{c}\Big(\mathbf{r}_{12},\mathcal{R}_1,\mathcal{R}_2;[\rho\psi_{(\mathbf{0})}]\Big) \times\left\{2\psi(u_{1z})\dot{\psi}(u_{2z})\left(\frac{qu_{2y}r_x}{2}\right)+2\dot{\psi}(u_{1z})\dot{\psi}(u_{2z})\left(\frac{qu_{1y}r_x}{2}\right)\left(\frac{qu_{2y}r_x}{2}\right)\right\}, \quad (3.28)$$

where we dropped the prime notation from the dummy integration variables. Note that to derive Eq. (3.28), we made use of an integration by parts with respect to $\mathbf{R}$ for the second-order terms in Eq. (3.25).

Eq. (3.28) so far relies on the sole hypothesis that the spatial variations of the director field $\mathbf{n}$ are negligible at the molecular length-scale, so that the uses of the ansätze in Eqs. (3.21) and (3.26) and of the truncated gradient expansion of ψ (Eq. (3.25)) are both justifiable. In order to proceed, let us further assume that the local equilibrium distribution of molecular orientations about the spatially-modulated director is identical to that of the uniform system, i.e.,

$$\psi_{(\mathbf{0})}(\mathbf{u}) \equiv \psi(\mathbf{u}\cdot\mathbf{n}_0) \cong \psi_{\mathrm{eq}}(\mathbf{u}\cdot\mathbf{n}_0). \quad (3.29)$$

It is worth remarking that Eq. (3.29) is conceptually similar to Eq. (3.14), which was based on the fact that the equilibrium density distribution ρ_{eq} about which the free energy expansion in Eq. (3.9) is performed was taken to be uniform in Section 3.2.1, and which may be formally shown to be exact in the case of apolar uniaxial molecules [157]. This assumption is obviously unsuitable in the case of a cholesteric phase, and the validity of Eq. (3.29), which underpins the perturbative treatment of phase chirality as introduced by Straley [82], is thus hard to assess *a priori*. Its quantitative accuracy will be investigated in detail in Section 3.4.2.

Using Eqs. (3.27)–(3.29), it follows from the HKM theorem [106, 107] that $f_d[\psi=\psi_{\mathrm{eq}}]$ reduces to the elastic component of the equilibrium Helmholtz free energy density, to quadratic order in q,

$$f_d[\psi_{\mathrm{eq}}] = -k_t[\psi_{\mathrm{eq}}]\,q + K_2[\psi_{\mathrm{eq}}]\,\frac{q^2}{2}, \quad (3.30)$$

which by term-to-term comparison with Eq. (3.3) finally yields

$$\beta k_t[\psi_{\rm eq}] = -\frac{\rho^2}{2}\int_V d\mathbf{r}_{12}\oiint d\mathcal{R}_1 d\mathcal{R}_2\, \overline{c}\Big(\mathbf{r}_{12},\mathcal{R}_1,\mathcal{R}_2;[\rho\psi_{\rm eq}]\Big)\times r_x u_{2y} \times \psi_{\rm eq}(\cos\theta_1)\dot{\psi}_{\rm eq}(\cos\theta_2), \tag{3.31}$$

$$\beta K_2[\psi_{\rm eq}] = \frac{\rho^2}{2}\int_V d\mathbf{r}_{12}\oiint d\mathcal{R}_1 d\mathcal{R}_2\, \overline{c}\Big(\mathbf{r}_{12},\mathcal{R}_1,\mathcal{R}_2;[\rho\psi_{\rm eq}]\Big)\times r_x^2 u_{1y}u_{2y} \times \dot{\psi}_{\rm eq}(\cos\theta_1)\dot{\psi}_{\rm eq}(\cos\theta_2), \tag{3.32}$$

where $\cos\theta_i \equiv u_{iz}$. The combined use of Eqs. (3.28) and (3.29) for the different nematic deformation modes similarly leads to microscopic expressions for K_1 and K_3 [162],

$$\beta K_1[\psi_{\rm eq}] = \frac{\rho^2}{2}\int_V d\mathbf{r}_{12}\oiint d\mathcal{R}_1 d\mathcal{R}_2\, \overline{c}\Big(\mathbf{r}_{12},\mathcal{R}_1,\mathcal{R}_2;[\rho\psi_{\rm eq}]\Big)\times r_x^2 u_{1x}u_{2x} \times \dot{\psi}_{\rm eq}(\cos\theta_1)\dot{\psi}_{\rm eq}(\cos\theta_2), \tag{3.33}$$

$$\beta K_3[\psi_{\rm eq}] = \frac{\rho^2}{2}\int_V d\mathbf{r}_{12}\oiint d\mathcal{R}_1 d\mathcal{R}_2\, \overline{c}\Big(\mathbf{r}_{12},\mathcal{R}_1,\mathcal{R}_2;[\rho\psi_{\rm eq}]\Big)\times r_z^2 u_{1x}u_{2x} \times \dot{\psi}_{\rm eq}(\cos\theta_1)\dot{\psi}_{\rm eq}(\cos\theta_2), \tag{3.34}$$

from which one recovers Eqs. (3.18)–(3.20), provided that Eq. (2.80) holds,

$$c\Big(\mathbf{r}_{12},\mathcal{R}_1,\mathcal{R}_2;[\rho\psi_{\rm eq}]\Big) = \overline{c}\Big(\mathbf{r}_{12},\mathcal{R}_1,\mathcal{R}_2;[\rho\psi_{\rm eq}]\Big).$$

Interestingly, the corresponding expression for c in the PL approximation (Eqs. (2.69) and (2.71)) reduces to the first-order term of the DCF derived through different arguments by Somoza and Tarazona for the OF elastic moduli of HSCs [163], as will be discussed further in Section 3.4.1.

The previous discussions, combined with the theoretical framework of Chapter 2, therefore provide a full microscopic description of the equilibrium structure and properties of cholesteric LCs. However, the complex integral equations underlying this approach are generally intractable to analytical methods, and often need to be solved numerically to yield accurate quantitative results. Let us now outline the computational procedure employed throughout this thesis for their accurate resolution.

3.3 Numerical procedure

3.3.1 The DFT/MC hybrid algorithm

The numerical algorithm employed, inspired from Refs. [95] and [96], can be simply oultined as follows.

1. We numerically integrate the angle-dependent virial kernel $\kappa(\theta, \theta')$ (Eq. (2.73)) for the chosen particle model using a discrete grid for polar angles θ and θ'.
2. We plug κ into Eq. (2.72), which is solved self-consistently using a standard iterative scheme [164] (see below) to compute the equilibrium ODF ψ_{eq} at fixed number density ρ and temperature T.
3. $\psi_{\text{eq}}^{(\rho)}$ is then plugged into Eqs. (3.32)–(3.34) and (3.31) to work out $K_i(\rho, T)$ and $k_t(\rho, T)$ for $i \in [\![1, 3]\!]$ by further numerical integration.
4. The equilibrium pitch $\mathcal{P}_{\text{eq}}(\rho, T)$ of the system is finally given by Eq. (3.7).

The most computationally-intensive elements of this approach correspond to steps 1 and 3, in which functionals of the microscopic interaction potential have to be integrated over the two-particle excluded volume manifold for the chosen mesogen model. Due to the high dimensionality of this manifold, we chose to follow in the footsteps of Ref. [95] and compute these integrals by MC sampling. In the notation of Appendix A, we may thus write, for any function ζ,

$$\int_V d\mathbf{r}_{12} \oiint d\mathcal{R}_1 d\mathcal{R}_2 \, \zeta(\mathbf{r}_{12}, \mathcal{R}_1, \mathcal{R}_2) \simeq \frac{V_{\text{MC}}}{N_{\text{MC}}} \sum_{i=1}^{N_{\text{MC}}} \sin\theta_1^{(i)} \sin\theta_2^{(i)} \zeta\left(r_{x,y,z}^{(i)}, \alpha_{1,2}^{(i)}, \theta_{1,2}^{(i)}, \phi_{1,2}^{(i)}\right), \tag{3.35}$$

where $\mathcal{R}_j \equiv \mathcal{R}(\alpha_j, \theta_j, \phi_j)$ (Eq. (A.2)), and the (i) superscript denotes uncorrelated uniformly-distributed random variables such that

$$\begin{aligned} \alpha_{1,2}^{(i)} &\in [0, 2\pi], \\ \phi_{1,2}^{(i)} &\in [0, 2\pi], \\ \theta_{1,2}^{(i)} &\in [0, \pi], \\ r_{x,y,z}^{(i)} &\in [-L/2, L/2], \end{aligned}$$

where we assumed the sample to be confined in a cubic container of linear dimension $L \equiv \sqrt[3]{V}$. Note that all integrand functions $\zeta(\mathbf{r}_{12}, \mathcal{R}_1, \mathcal{R}_2)$ of interest in this

thesis typically vanish when the corresponding particles 1 and 2 are not physically interacting, so that the volume L^3 may be restricted to the smallest cubic box containing all possible interacting configurations of two particles. The total phase-space volume V_{MC} spanned by the nine variables then reads as

$$V_{\mathrm{MC}} = 16\pi^6 L^3.$$

It follows from the central limit theorem that the right-hand side of Eq. (3.35) converges with the number N_{MC} of function evaluations as $1/\sqrt{N_{\mathrm{MC}}}$, which is asymptotically faster than the respective $1/N_{\mathrm{MC}}^{2/9}$ and $1/N_{\mathrm{MC}}^{4/9}$ convergence rates of standard trapezoidal and Simpson quadrature rules in dimension 9 [165]. A further advantage of stochastic sampling lies in its trivial parallelisation, as the N_{MC} independent terms of the sum in Eq. (3.35) may be evaluated concurrently in a distributed-computing environment. The statistical errors of all relevant integral quantities are thus entirely controlled by N_{MC}, which can be tuned as required to achieve the desired numerical accuracy.

Given a numerically-determined kernel κ, a convenient algorithmic route for the determination of ψ_{eq} at fixed density ρ is described in Ref. [164]. In this framework, we define a sequence of function $\{\psi_n\}_{n\geq 0}$ through the recursive relation

$$\psi_{n+1}(\cos\theta) = \mathscr{G}\Big(\cos\theta; [\psi_n, \rho\kappa]\Big) \qquad \forall\theta \in [0,\pi], \tag{3.36}$$

where the functional $\mathscr{G}$ is given by the right-hand side of Eq. (2.72),

$$\mathscr{G}\Big(\cos\theta; [\psi, \rho\kappa]\Big) \equiv \frac{1}{Z[\psi,\rho\kappa]} \exp\left\{\frac{G_{\mathrm{ref}}(\eta_{\mathrm{ref}})}{4\pi^2}\int_0^\pi \sin\theta' d\theta'\, \psi(\cos\theta')\rho\kappa(\theta,\theta')\right\}, \tag{3.37}$$

with $Z[\psi,\rho\kappa]$ a Lagrange multiplier ensuring the normalisation of ψ_{n+1} (Eq. (2.59)),

$$Z[\psi,\rho\kappa] = 4\pi^2 \int_0^\pi \sin\theta d\theta\, \mathscr{G}\Big(\cos\theta; [\psi,\rho\kappa]\Big). \tag{3.38}$$

Let us define the so-called *uniform norm* $\|\psi\|_\infty$ of an arbitrary, real-valued continuous function $\psi : [-1,1] \to \mathbb{R}$,

$$\|\psi\|_\infty \equiv \max_{|x|\leq 1} |\psi(x)|.$$

It is verified in Ref. [164] that there exists a positive constant $L[\rho\kappa] < 1$ such that for any two functions ζ and ξ, $\mathscr{G}$ satisfies the Lipschitz condition,

$$\|\mathscr{G}[\zeta, \rho\kappa] - \mathscr{G}[\xi, \rho\kappa]\|_\infty \leq L[\rho\kappa]\|\zeta - \xi\|_\infty.$$

In this case, it is straightforward to show that for any two positive integers m and n,

$$\|\psi_{n+m} - \psi_n\|_\infty \leq \sum_{i=n+1}^{n+m} \|\psi_i - \psi_{i-1}\|_\infty \leq \frac{L^n}{1-L}\|\psi_1 - \psi_0\|_\infty \xrightarrow[n\to\infty]{m\to\infty} 0.$$

Thus, $\{\psi_n\}_{n\geq 0}$ constitutes a so-called *Cauchy sequence* [166], and it follows from the completeness of real numbers that $\{\psi_n\}$ converges uniformly to a function ψ, which is necessarily a solution of Eq. (2.72),

$$\psi(\cos\theta) = \mathscr{G}\Big(\cos\theta; [\psi, \rho\kappa]\Big).$$

Hence, $\psi = \psi_{\text{eq}}$ may be determined iteratively from Eqs. (3.36)–(3.38), starting from a given initial trial function ψ_0.

We here make use of a simple nematic ansatz for ψ_0,

$$\psi_0(\cos\theta) = \frac{\exp(\cos^2\theta - 1)}{4\pi^2 \displaystyle\int_{-1}^{1} d\cos\theta\, \exp(\cos^2\theta - 1)}.$$

It is proven in Ref. [164] that Eqs. (3.36)–(3.38) further lead to a monotonic decrease of the corresponding Helmholtz free energy $\mathscr{F}$ (Eqs. (2.60) and (2.65)),

$$\mathscr{F}[\psi_{n+1}] < \mathscr{F}[\psi_n],$$

so that the procedure always converges to a local free energy minimum $\mathscr{F}[\psi_{\text{eq}}]$ of the single-phase system described by the ODFs ψ_n. With this choice of ψ_0, the critical density ρ^* below which ψ_{eq} reduces to its isotropic form ψ_{iso} (Eq. (2.91)) therefore provides a simple numerical estimate of the nematic spinodal point [167]. Throughout this thesis, we employ a finite grid of fixed size $N_\theta = 250$ for polar angles θ, which we verified to yield negligible discretisation errors for all computed macroscopic quantities, and use the following convergence criterion for the determination of ψ_{eq},

$$\|\psi_{n+1} - \psi_n\|_\infty = \max_{j\in[\![1,N_\theta]\!]} |\psi_{n+1}(\cos\theta_j) - \psi_n(\cos\theta_j)| < 10^{-8},$$

where $\theta_j \equiv j\pi/(N_\theta + 1)$.

We remark that this numerical framework is particularly well-suited for the study of lyotropic LCs, as the kernel κ defined in Eq. (2.73) is generally independent of particle density. Therefore, the full concentration dependence of the ODF may be worked out from Eq. (2.72) with minimal numerical effort using a single computation of the underlying virial integral. Nevertheless, all of our previous discussions remain conceptually valid in the case of thermotropic LCs, and our method may therefore also be applied to the investigation of thermotropic self-assembly by evaluating the temperature dependence of κ. An important caveat however lies in the limited aspect ratios of most experimental thermotropic mesogens, which may require a more accurate description of inter-particle correlations beyond the decoupling approximation [168].

3.3.2 Molecular geometry and reference nematic state

Sections 3.1 and 3.2 thus yield a convenient common theoretical formalism in which uniform uniaxial nematic phases are simply assimilated to "degenerate" cholesteric phases with infinite helical pitch, and in which the reliable determination of equilibrium cholesteric structure is contingent on the accurate account of local uniaxial order [82]. It is therefore necessary to probe the ability of the methods introduced in Section 3.3.1 to correctly describe the local orientational organisation of chiral (or, more generally, non-uniaxial) particles. The ground-state LC assemblies of such systems can obviously not be generally expected to possess $C_{\infty h}$ symmetry, in contrast with the assumptions of Chapter 2. However, in the case of biaxial calamitic particles, it is important to distinguish between the deviations from local uniaxial symmetry arising from potential director spatial fluctuations, and the breaking of cylindrical invariance induced by the additional ordering of their short molecular axes in the normal plane to the local director [66].

While the former are likely to be inconsequential in the limit of long-wavelength deformations, as discussed in Section 3.2.1, the latter gives rise to the broad family of *biaxial nematic phases*, which have been the subject of intense experimental

and theoretical interest in recent years in both lyotropic [112,169–171] and thermotropic [18,172–176] systems. Such phases are nonetheless typically characterised by narrow ranges of thermodynamic stability, and are altogether absent from the phase diagram of a surprisingly-large variety of biaxial particles, in which they may be replaced by either positionally-ordered or uniaxial nematic regimes (see, e.g., Refs. [112] and [177]). In this thesis, we therefore assume the spatially-uniform reference nematic state described by $\mathscr{F}_0$ to be uniaxial regardless of molecular symmetries, although the potential implications of long-ranged biaxial correlations for the equilibrium cholesteric pitch will be discussed in Section 3.4.2.

In this context, an interesting first test system is provided by the coarse-grained helical particle model first introduced in Ref. [178], and subsequently studied extensively using both direct computer simulations [178,179] and different theoretical approaches [94–96,178]. Such particles are defined as chains of N_s fused hard spheres of radii σ placed along a helical backbone of microscopic pitch p, radius r and contour length l (Figure 3.2). Similarly to these previous investigations, we here restrict our study to particles with a right-handed symmetry, and use the shorthand $r_a p_b l_c$ to refer to helices with microscopic radius $r = a$, pitch $p = b$ and contour length $l = c$ in units of σ.

The uniaxial nematic assembly of such helices was numerically investigated in Ref. [178], in which the use of standard periodic conditions was found to effectively suppress long-wavelength director distortions within the simulation box. While reasonable agreement was reported therein in terms of their I/N transition densities, the comparison of simulation results with theoretical predictions revealed that the use of the PL approximation leads to significant underestimations of the osmotic pressure [178], which mirrors the conclusions of previous studies of the nematic assembly of non-convex particles [180]. A simple explanation for this discrepancy may be provided by invoking the concept of *effective molecular volume* [181], which we introduce below.

Let $\Gamma \equiv V \times SO(3)$ be the total configuration space accessible to the particles, and $(\mathscr{P}, \mathscr{P}') \in \Gamma^2$ an arbitrary pair of identical hard particles. The mathematical

definition of the excluded volume manifold Γ_{exc} which may not be penetrated by particle $\mathcal{P}'$ in any configuration due to the presence of $\mathcal{P}$ reads as

$$\Gamma_{\text{exc}} = \left\{ \mathbf{r} \in V \,\middle|\, \forall \mathcal{P}' \in \Gamma,\, \mathbf{r} \in \mathcal{P}' \implies \mathcal{P} \cap \mathcal{P}' \neq \varnothing \right\}. \tag{3.39}$$

The effective molecular volume v_{eff} of particle $\mathcal{P}$ is then defined as

$$v_{\text{eff}} \equiv \Lambda(\Gamma_{\text{exc}}), \tag{3.40}$$

with Λ the standard Lebesgue measure for subsets of $\mathbb{R}^3$. It is easy to show that v_{exc} satisfies $v_{\text{exc}} \geq v$, which reflects the smaller volume available to non-convex particles with respect to their convex counterparts at fixed density ρ, and therefore accounts for the higher osmotic pressures obtained in numerical simulations for the former systems. Varga and Szalai [182] thus proposed to assign this effective molecular volume to the volume of the reference hard-sphere particles,

$$v_{\text{ref}} = v_{\text{eff}}, \tag{3.41}$$

which together with Eqs. (2.69) and (2.71) yields the so-called modified Parsons-Lee (MPL) approximation for hard non-convex particles.

A general numerical scheme to compute this effective volume for arbitrary particle models may then be obtained by discretising V into a mesh of size $N_x \times N_y \times N_z$ and evaluating the excluded volume manifold Γ_{exc} by MC sampling, similarly to the integration procedure of Section 3.3.1. Assuming the first particle $\mathcal{P}$ to be fixed at the origin of the reference frame, this process amounts to generating a number N_{MC} of uncorrelated configurations for particle P' by drawing random centre-of-mass positions $\mathbf{r}' \in V$ and particle orientations $\mathcal{R}' \in SO(3)$, and checking $\mathcal{P}$ and $\mathcal{P}'$ for hard overlaps. In the absence of any such overlaps, all the mesh points contained within the generated configuration for particle $\mathcal{P}'$ are guaranteed to lie outside of the excluded volume manifold, and may therefore be pruned.

This algorithm thus enables one to efficiently obtain a discretised representation of Γ_{exc} for a wide range of particle models, with a numerical precision determined by both the chosen mesh resolution and the number of MC steps used. The corresponding reference volume v_{ref} may finally be determined from Eqs. (3.39)–(3.41) as the

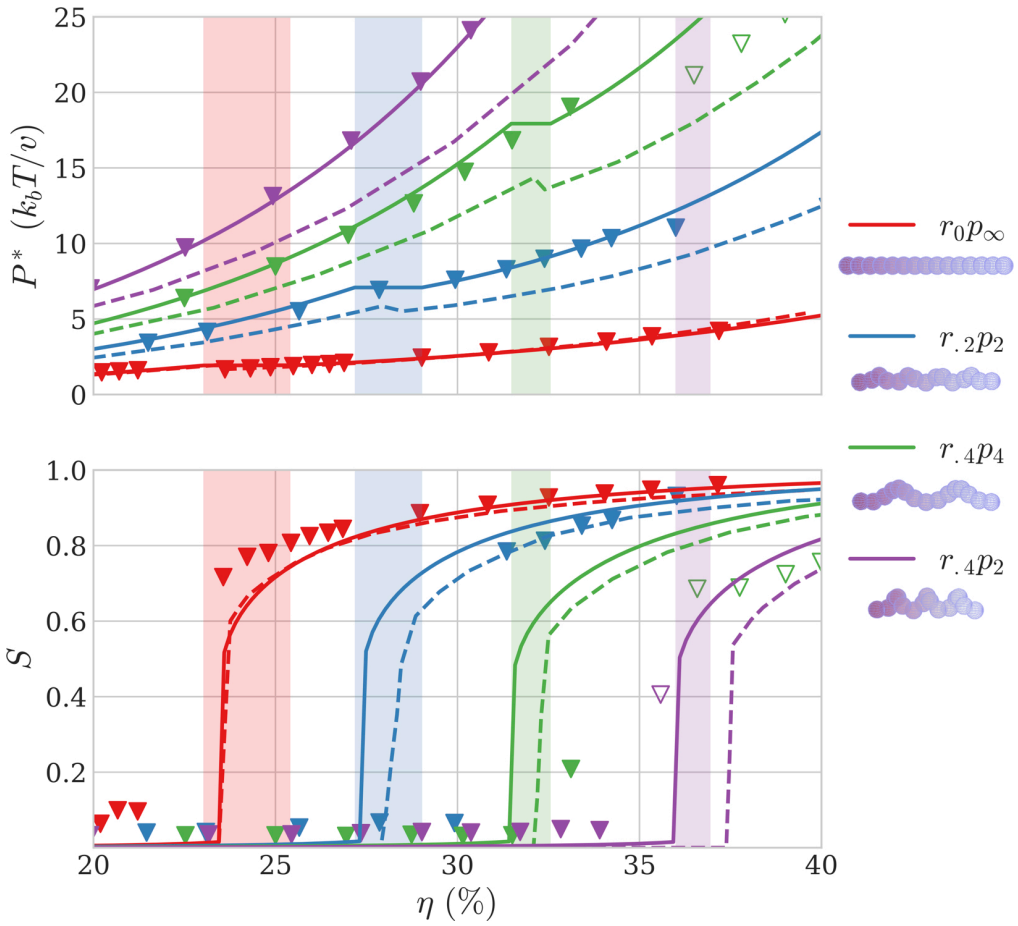

Figure 3.2: Nematic order parameter S and rescaled osmotic pressure $P^* = P \times [1 + 50r^2/(p\sigma)]$ as a function of particle volume fraction η for a selection of hard helices with $N_s = 15$ and $l = 10\,\sigma$. Solid lines correspond to the results the MPL approximation, while symbols and dashed lines represent the simulation and theory data reported in Ref. [178], respectively. Unfilled symbols denote metastable state points not fully characterised by simulations. The coloured areas delimit the ranges of I/N coexistence for the different particle models as computed using the MPL theory. All results were obtained by averaging over 32 independent runs using $N_{\mathrm{MC}} = 1 \times 10^{11}$ integration steps each, and numerical dispersion was found to be negligible at all densities.

sum of the volumes of all mesh points comprising Γ_{exc} at the end of the calculation. We here choose for V the minimal volume containing all possible overlapping configurations of two particles, prescribing the long axis of the reference particle $\mathcal{P}$ to $\mathbf{e}_z$. The mesh dimensions were then set to $N_x \times N_y \times N_z = 150 \times 150 \times 1500$ and a number $N_{\mathrm{MC}} = 1 \times 10^8$ of random sampling steps was used, yielding a statistical dispersion of less than 1% for all computed values of v_{ref} and ensuring a negligible dependence on varying mesh resolutions.

We reproduce in Figure 3.2 the osmotic pressure P (Eq. (2.88)) and first nematic

order parameter $S \equiv S^{(2)}$ (Eq. (2.92)) as a function of particle density for various hard helices, including the limiting case of an achiral linear chain of hard spheres (LCHS) for $r = 0$. We note that the pressures predicted by our approach are found to be in significantly better agreement with simulation data than those obtained by the theory of Ref. [178] in both the cholesteric and isotropic phases of all helices considered. This is because the effective molecular volumes v_{exc} of the particles was assumed in Ref. [178] to be given by those of the corresponding LCHS systems with equal contour lengths, for which analytical expressions have been derived [182]. This approximation therefore neglects the contributions of the non-linear molecular backbones to the overall shape non-convexity of the helices, and thus leads to sizeable underestimates of the associated osmotic pressures. Our results are however found to be virtually identical to those of Ref. [178] in the case of LCHSs, for which our numerical excluded volume converges to the analytical expression of Ref. [182].

Interestingly, we also remark that the quantitative agreement of the MPL theory with simulation results in terms of the nematic order parameter S is somewhat less convincing, and that the inclusion of the full molecular excluded volume does conversely not lead to systematic improvements for the prediction of the I/N coexistence range. This observation seemingly mirrors the findings of Ref. [182] for systems of long LCHSs; however, while the MPL treatment was in that case reported to lead to a significant overestimate of the nematic transition density, our results for $r_{.2}p_2$ helices rather underestimate this quantity with respect to the simulation data of Ref. [178]. This would appear to suggest that the influence of particle non-convexity on nematic self-assembly is highly non-trivial, and may be too subtle to be fully captured by the simple hard-sphere analogy of the PL approximation.

Further limitations of the PL theory have also been recently reported in the case of hard triangular prisms (HTPs), defined as impenetrable polyhedra of height h with equilateral triangular cross sections of edge length l and circumference $3l \equiv \pi w$ (Figure 3.3) [183]. Overlap queries between such particles may be efficiently performed using the RAPID library [184], which will be discussed in detail in Chapter 4. HTPs with aspect ratios $h/w \gtrsim 4$ were found to form stable uniaxial

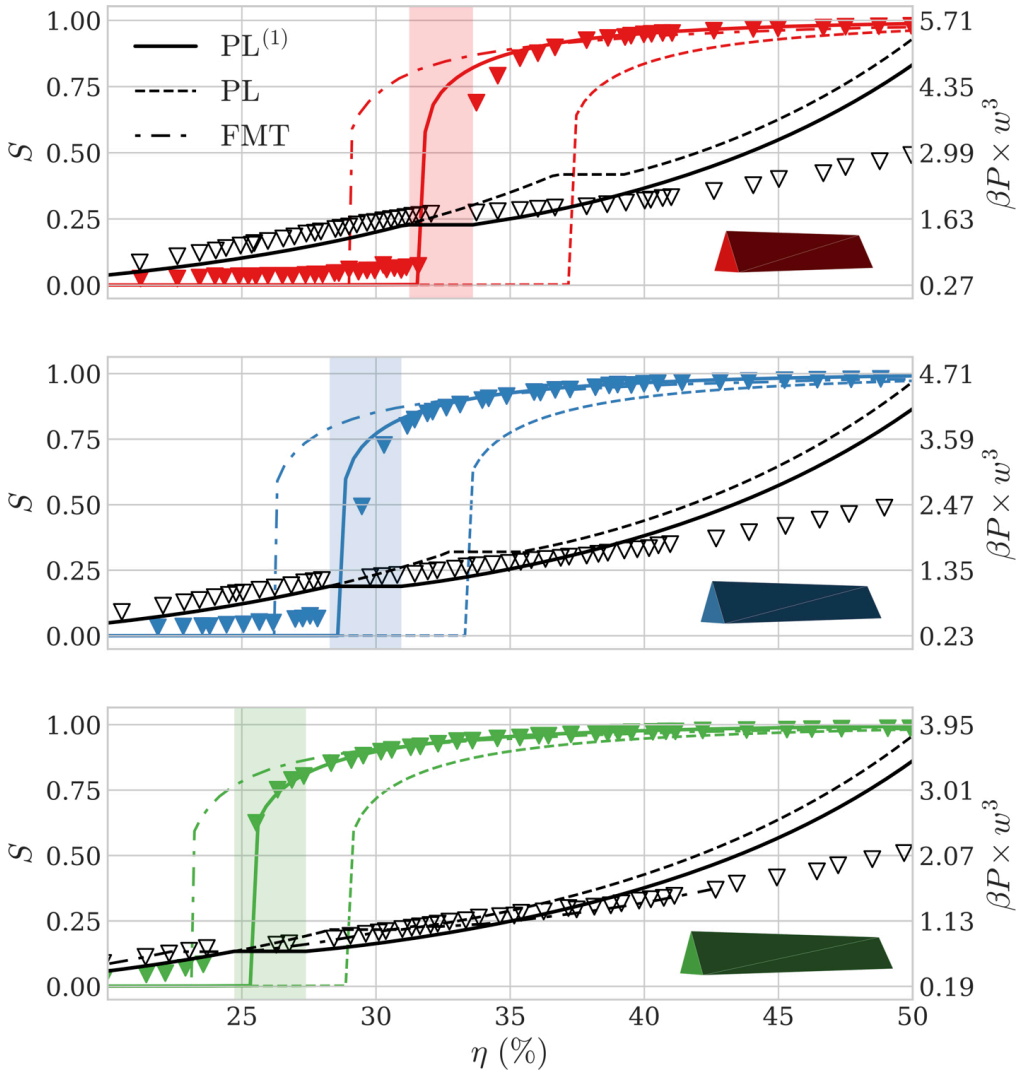

Figure 3.3: Osmotic pressure P (in black) and first nematic OP S as a function of particle volume fraction η for HTPs with aspect ratios $h/w = 4.3$ (top), 5 (centre) and 6 (bottom). Markers and dashed-dotted lines represent the simulation and FMT results of Ref. [183], respectively. Solid and dashed lines denote the results obtained using the $G_{\mathrm{PL}}^{(1)}$ (Eq. (2.74)) and G_{PL} (Eq. (2.71)) respective prefactors in Eq. (2.72), with $N_{\mathrm{MC}} = 5 \times 10^{11}$ integration steps. The coloured areas delimit the ranges of I/N coexistence for the different particle models as computed using $G_{\mathrm{PL}}^{(1)}$. Note that the prefactor G_{ref} appearing in the excess free energy (Eqs. (2.65) and (2.69)) is given by Eq. (2.71) in both cases, so the osmotic pressures predicted by the two approaches are identical in the isotropic phase.

nematic phases at densities significantly lower than their PL-predicted I/N transition concentrations [183]. Somewhat surprisingly, we here report in Figure 3.3 that the use of $G_{\mathrm{PL}}^{(1)}$ (Eq. (2.74)) leads to significantly better agreement with numerical simulations than both the standard PL theory and the FMT implemented in Ref. [183], with quantitative agreement being achieved in terms of the nematic order parameter S for the highest aspect ratio considered ($h/w = 6$), despite some underestimations of the corresponding osmotic pressure P in the nematic regime. The reasons for this improvement are not obvious, as the uses of G_{PL} and $G_{\mathrm{PL}}^{(1)}$ are *a priori* equally justifiable (c.f. Section 2.2.2). The comparison of the results of both approaches with numerical simulations for a greater range of particle models would be desirable for the further investigation of these effects, and for the potential derivation of a set of empirical rules guiding the choice of one prefactor over the other.

3.4 Application to simple model systems

3.4.1 The Oseen-Frank elastic moduli of HSCs

We now move on to the applications of our approach to the microscopic calculation of the OF elastic moduli of HSCs, following the procedure of Section 3.3.1. The determination of macroscopic curvature elasticities from direct molecular simulations is a notoriously challenging task, owing to the large length-scales of the associated nematic distortions in the weak deformation framework of the OF free energy (Eq. (3.4)). Therefore, their reliable measurement from the spatial fluctuations of the director field generally requires the use of very large simulation boxes and the careful extrapolation of the results on finite-sized systems to the regime of vanishing deformation wavenumbers. The methods of Section 3.2 may thus provide a general and efficient alternative to work out the OF elastic moduli of a wide variety of particle models, and to assess their sensitivity to microscopic mesogen structure and thermodynamic state.

However, a consequence of these computational difficulties is the scarcity of the available numerical data to which our results may be compared, as simulation measurements of the nematic elastic moduli have so far been limited to a few

state points in the phase diagram of highly simplified particle models [70]. We therefore only report in Figure 3.4 our results in the case of HSCs with aspect ratios $L/D \in [5, 20]$, for which simulation [71,185,186] and theoretical results from both FMT [187] and DFT [163] have been reported.

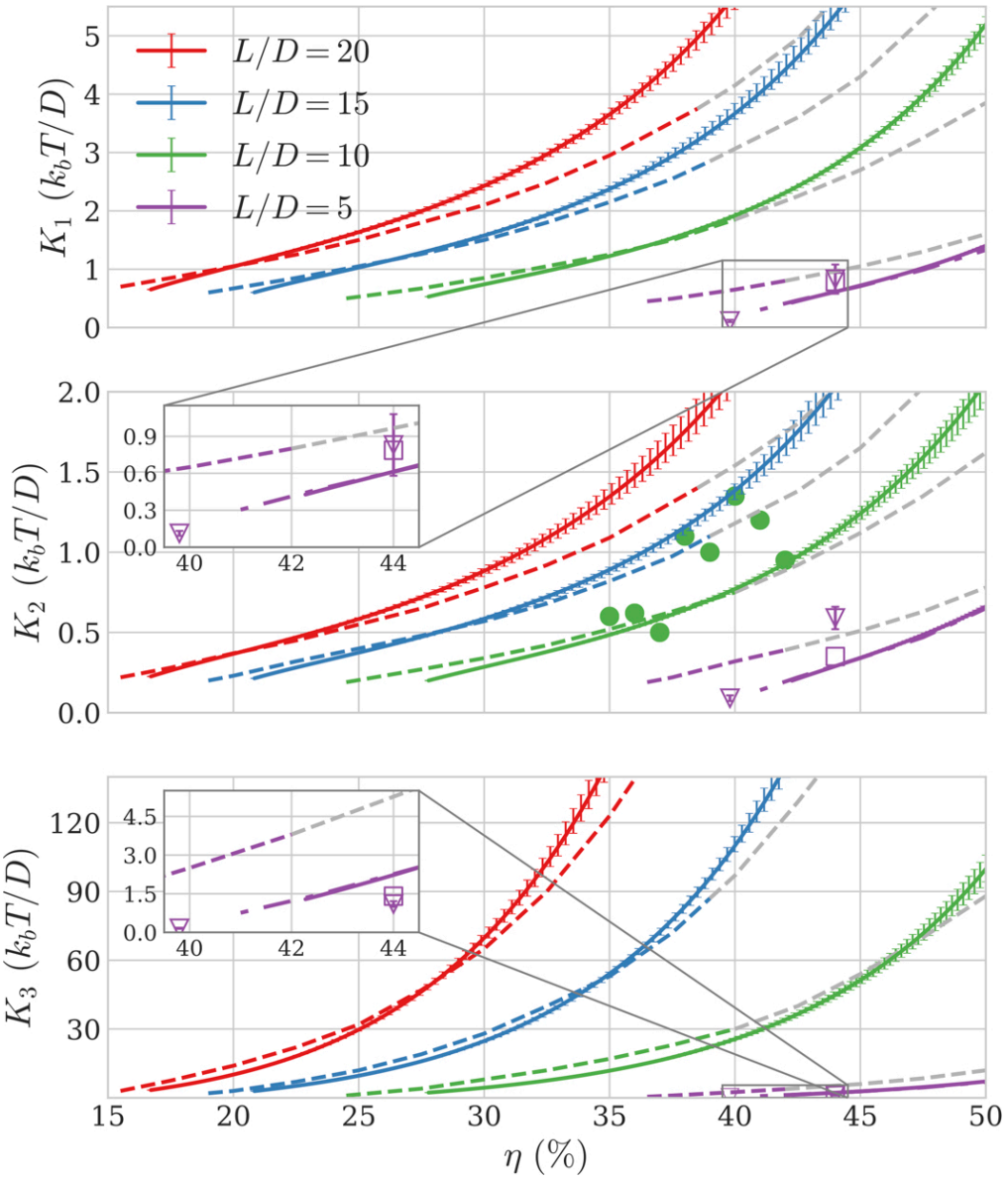

Figure 3.4: OF elastic moduli of HSCs with aspect ratios $L/D \in [5, 20]$. Solid lines correspond to the results of Eqs. (3.32)–(3.34) in the PL approximation, and dashed lines to those of the FMT of Ref. [187]. In the latter case, the greyed-out dashed lines denote state points lying outside of the predicted region of nematic stability. Dash-dotted lines represent the DFT results of Ref. [163] for $L/D = 5$. Square and triangular symbols respectively designate the simulation data of Refs. [185] and [186] for $L/D = 5$, and solid dots mark the simulated values of K_2 reported in Ref. [71] for $L/D = 10$. Error bars were obtained from 16 independent runs with $N_{\mathrm{MC}} = 1 \times 10^{10}$.

We note that our data obeys $K_3 > K_1 > K_2$ for all particles studied, as expected from general mean-field calculations for calamitic particles [188]. Furthermore, our results are found to be in reasonable quantitative agreement with the predictions of FMT, although increasing discrepancies are observed in the locations of the I-N transition with decreasing aspect ratios; both approaches are however in comparable agreement with the simulation values of Frenkel and Bolhuis [133] for all reported aspect ratios. While both methods provide a good match for the limited simulation data available for the OF elastic moduli, our method predicts a significantly stronger dependence of K_1 and K_2 on particle density than estimated by FMT; this deserves to be investigated further, and more extensive simulation studies involving a larger number of state points would therefore be very useful in enabling the assessment of the validity of the different theoretical descriptions [71].

We also remark that our results are virtually identical to those of Somoza and Tarazona [163], who made use of a more involved DFT approach based on a weighted-density approximation [189]. This is due to the fact that the full DCF obtained in Ref. [163] reduces to the effective expression of Eqs. (2.69), (2.71) and (2.80) in the functional subspace of Eq. (3.21),

$$c\Big(\mathbf{r}_{12}, \mathcal{R}_1, \mathcal{R}_2; [\rho\psi_0]\Big) = G_{\mathrm{PL}}(\eta) \times f(\mathbf{r}_{12}, \mathcal{R}_1, \mathcal{R}_2), \tag{3.42}$$

and therefore leads to an equivalent description of nematic director fluctuations in the framework of Section 3.2. We finally note for the sake of completeness that other results using different variants of DFT have been reported for these systems [148, 190], but are not reproduced here due to their wide dispersion. We further expect the results of FMT, which corresponds to the most sophisticated analytical effort to date in the microscopic description of hard-particle LCs [191], to provide the most reliable theoretical benchmark currently available for the validation of our approach in this case.

3.4.2 The cholesteric behaviour of HTPs and hard helices

We now compare the cholesteric pitches computed using our method against the results of numerical simulations in order to probe its reliability for the description of cholesteric order. A remarkably simple model system for this purpose may be obtained based on the HTPs of Section 3.3.2 by rotating one of the two triangular bases by an angle α about the long axis of the prisms [74]. The chirality of the twisted HTPs may be further tuned by considering isosceles, rather than equilateral triangular cross sections, which may be achieved by allowing the corresponding base angles γ to differ from $\pi/3$ [74]. In the following, we restrict our study to the case of right-handed HTPs with aspect ratios $h/w = 5$ which may be fully parametrised by the choice of α and γ, and use the shorthand $\alpha_a\gamma_b$ to denote HTPs with respective twist and base angles $\alpha = a$ and $\gamma = b$.

We reproduce in Figure 3.5 the juxtaposition of our pitch predictions and the simulation results of Ref. [74]. As reported in Section 3.3.2 for the nematic phase of untwisted HTPs, we find that the use of the standard PL prefactor in Eq. (2.72) leads to significant overestimations in the isotropic/cholesteric (I/C) transition density of their twisted counterparts. In contrast with Figure 3.3, these discrepancies however appear to persist to some extent with the use of $G^{(1)}_{\mathrm{PL}}$, which could potentially be attributed to the non-convexity of the twisted HTPs [74] following the previous discussions. The precise numerical determination of the I/C transition of twisted HTPs would be desirable for the thorough investigation of this effect.

As in Ref. [74], we further find that the absolute cholesteric pitches of all particles are sizeably overestimated by theory, although their predicted handedness, order of magnitude and concentration dependence are consistent with simulation results. This observation mirrors the conclusions of previous investigations of cholesteric assembly in systems of short ellipsoids with soft chiral interaction potentials [87], and could be partially attributed to the previous shortcomings of the PL approximation. A more serious potential source of error, as mentioned in Section 3.3.2, lies in the use of the uniaxial ansatz (Eq. (3.21)) for the cholesteric density field, which assumes a uniform distribution of particle angles α and ϕ within any mesoscopic

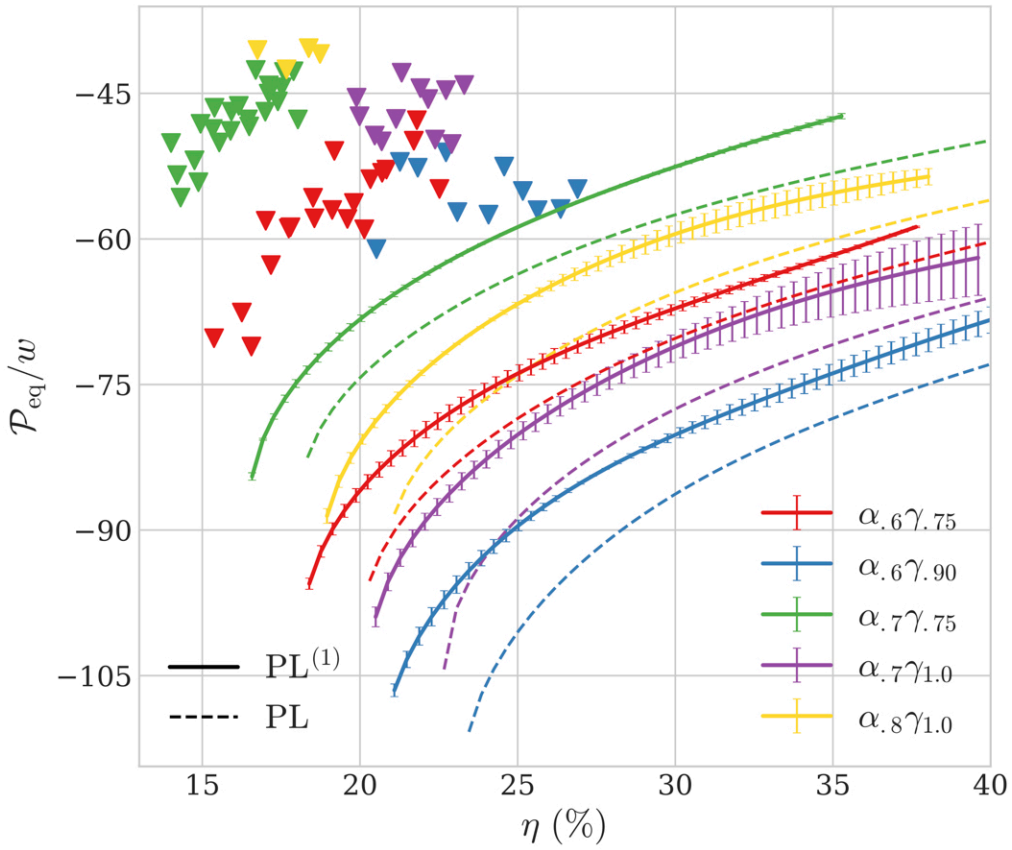

Figure 3.5: Equilibrium cholesteric pitch of right-handed twisted HTPs with $h/w = 5$ as a function of particle volume fraction η. Solid and dashed lines denote the results obtained using the respective $G_{\mathrm{PL}}^{(1)}$ and G_{PL} rescaling prefactors (c.f. Figure 3.3). The molecular volume v was computed through standard numerical formulae for orientable polyhedra [74]. Markers represent the simulation data of Ref. [74]. Error bars were obtained using 8 independent runs with $N_{\mathrm{MC}} = 1 \times 10^{10}$ each, and are only reported for the PL$^{(1)}$ results for readability.

sample of the system. This hypothesis thus precludes any long-range orientational order for the particle short axes and therefore dictates that phase chirality arises solely from the short-ranged correlations prescribed by the DCF (Eq. (3.42)). While consistent with the weak deformation framework of Section 3.2, this conjecture is hard to justify *a priori* for systems of chiral particles and may adversely affect the reliability of the theory for cholesteric phases, as discussed in the next paragraphs.

We finally compare our pitch predictions against those reported by previous microscopic theories [94, 96] in the case of the hard helix model descried in Section 3.3.2. We begin by assessing the dependence of the pitch on the inclusion of particle non-convexity in the MPL approximation by comparing in Figure 3.7

the results obtained using for v_{ref} both an analytical expression for the real particle volume v [178] and the effective molecular volume v_{exc} computed using the procedure of Section 3.3.1 for different hard helices.

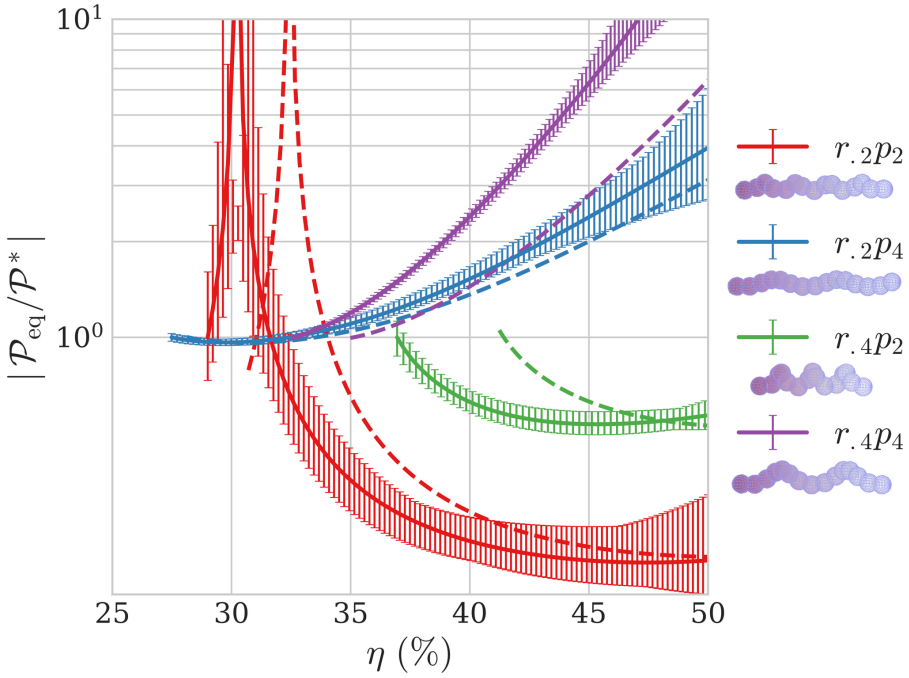

Figure 3.6: Influence of the MPL theory on the equilibrium pitch of hard helices with $N_s = 15$ and $l = 10\,\sigma$. $\mathcal{P}^*$ corresponds to the equilibrium pitch at the I/C transition as predicted by the MPL theory. Solid lines correspond to the results of our MPL approach, and dashed lines to those of the original PL approximation. Error bars were evaluated from 32 independent runs with $N_{\mathrm{MC}} = 5 \times 10^{10}$, and are only reported for the MPL results. Note that the diverging pitch for helices with $r = 0.2\,\sigma$ and $p = 2\,\sigma$ denotes a cholesteric inversion from left to right-handedness with increasing particle concentrations.

We note that the MPL theory does not qualitatively alter the cholesteric behaviour of the systems, and mostly shifts the density dependence of the pitch to lower particle concentrations owing to the smaller volume available to non-convex mesogens. We however emphasise that this effect may lead to significant differences in the handedness and magnitude of the predicted pitches at given particle density, contrary to the suggestion of Ref. [94]; this is due to the fact that the Parsons-Lee prefactor G_{PL} implicitly affects the equilibrium ODF (Eq. (2.72)) involved in the calculations of K_2 and k_t, even though its contribution to the effective DCF (Eq. (2.69)) explicitly cancels out at all densities in the ratio of these two quantities (Eq. (3.7)). In the following, we nonetheless restrict ourselves to the canonical

form of the PL theory as employed in Refs. [94], [95] and [96], for the consistent comparison of our predictions with the results of these studies.

Note that the approach implemented in Refs. [95] and [96] relies on the evaluation of the full chiral free energy landscape of the molecules using a finite grid of macroscopic pitches, and is independent of the perturbative framework introduced in Section 3.2.2. Therefore, the comparison of our predictions with the results of this full-functional description provides a direct test of the accuracy of the assumptions underlying Eq. (3.29), and of Straley's treatment of cholesteric order [82]. This comparison is summarised in Figure 3.7 summarises in terms of the equilibrium cholesteric wavenumber q_{eq} of hard helices with equal microscopic pitch and radius but different contour lengths, for which large equilibrium pitches $|\mathcal{P}_{\mathrm{eq}}| \gtrsim 500\,\sigma$ have been reported [96]. We obtain excellent agreement between the two methods throughout the whole cholesteric stability range of all particles studied, providing quantitative evidence of the validity of the perturbative treatment of chirality for these systems. We further note that the computational cost of our method is roughly two orders of magnitude lower than that of our implementation of Ref. [95], thanks to our use of the angle-dependent virial kernel (Eq. (2.73)) instead of its more expensive, pitch-dependent projections on a finite basis of Legendre polynomials.

We compare in Table 3.1 the predictions of our approach to those of Refs. [94] and [96] for a variety of helices at the onset of cholesteric stability. The macroscopic pitches computed by our method are found to be within 15% of those reported by Ref. [96] for all particles studied, with the larger relative discrepancies generally corresponding to the shorter pitches, i.e. the more strongly twisted phases. This observation is fully consistent with the limitations of our weak deformation framework, and is further discussed in the next paragraphs.

The correspondence between our results and those of Ref. [94] is somewhat more tenuous, especially for larger values of $\mathcal{P}_{\mathrm{eq}}$ — a fact all the more puzzling given that both our approaches are based on the same perturbative description of the cholesteric phase. These differences may most likely be attributed to finite-order truncation effects in the Wigner matrix expansions introduced in Refs. [92] and [94]

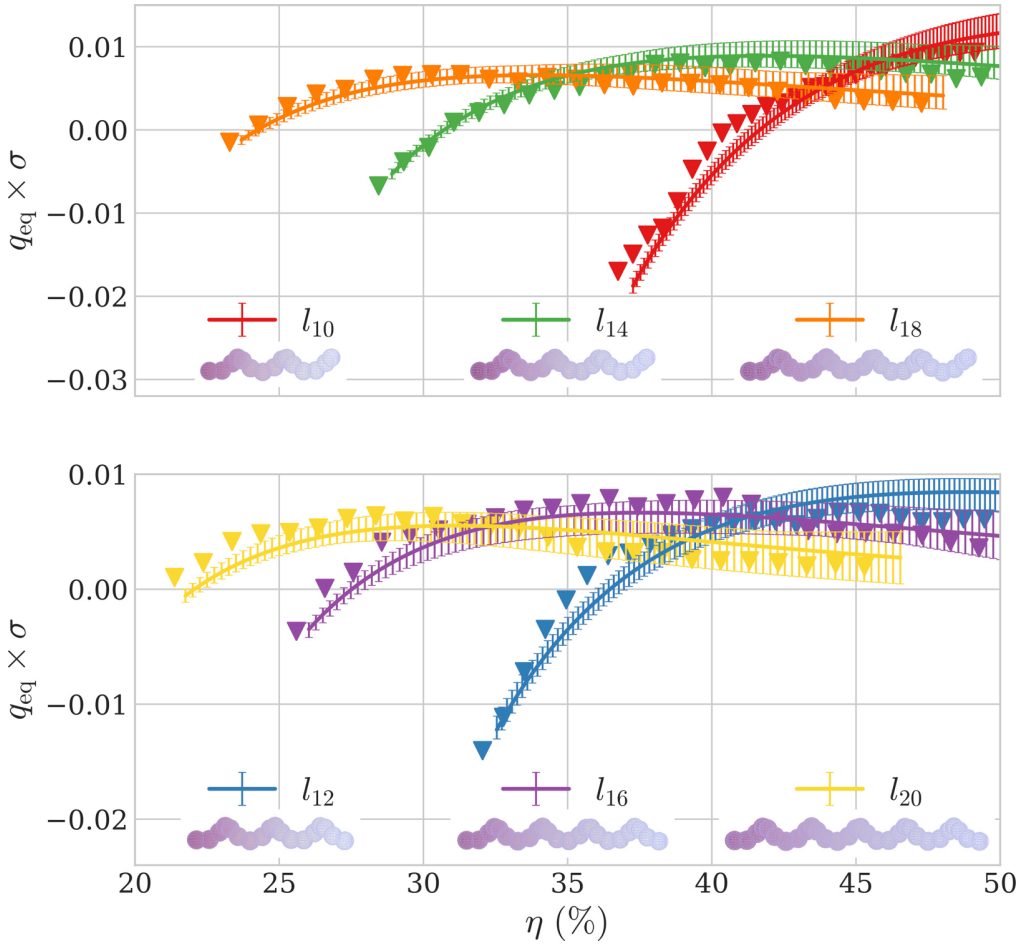

Figure 3.7: Equilibrium cholesteric wavenumber $q_{eq} = 2\pi/\mathcal{P}_{eq}$ for hard helices with $r = 0.4\,\sigma$, $p = 3\,\sigma$ and various contour lengths l and numbers of beads $N_s = 3l/(2\sigma)$. Solid lines represent the results of this work, and symbols those obtained using our own implementation of Ref. [95]. Error bars were computed from 32 independent runs with $N_{MC} = 5 \times 10^{10}$, and are only reported for the results of our method.

for the computation of K_2 and k_t, as small discrepancies in these two coefficients may lead to significant variations of the corresponding equilibrium pitch Eq. (3.7) in the weak chirality limit. We therefore expect our method, which allows for the calculation of all relevant quantities with a tuneable degree of precision and obviates further numerical approximations, to be more reliable in these cases.

We finally investigate the validity of our perturbative treatment in the limit of strong chirality in Figure 3.8 by focusing on systems for which the predicted cholesteric pitches are of the order of a few dozen particle diameters, corresponding to the shortest values reported in Ref. [96]. Quantitative agreement with the full-functional description of Ref. [95] is still found to be very satisfactory, which

Table 3.1: Comparison of this work, Ref. [94] and Ref. [96] for hard helices with $N_s = 15$ and $l = 10\,\sigma$ at the I/C transition. $|\Delta\mathcal{P}|/\mathcal{P}_{\mathrm{eq}}$ represents the relative difference between the equilibrium pitch predicted by our method and those reported in the references above, normalised by our value. Our results were obtained by averaging over 8 independent runs with $N_{\mathrm{MC}} = 5 \times 10^{11}$; numerical dispersion was found to be below 5% for all computed pitches, and smaller than the last significant digit for all other variables.

		$r_{.2}p_2$	$r_{.2}p_4$	$r_{.2}p_8$	$r_{.4}p_2$	$r_{.4}p_4$	$r_{.4}p_8$
η (%)	**here**	30.7	28.1	26.5	41.2	35.0	29.2
	Ref. [96]	30.0	27.4	25.8	40.3	34.0	28.2
S	**here**	0.704	0.684	0.696	0.629	0.632	0.621
	Ref. [96]	0.699	0.677	0.690	0.612	0.622	0.619
	Ref. [94]	0.64	0.66	0.68	0.60	0.61	0.61
$-10^4 \times k_t$ (k_bT/σ^2)	**here**	4.12	52.1	46.0	-11.6	130	139
	Ref. [96]	4.27	47.3	42.3	-10.7	110	115
	Ref. [94]	4.83	41.36	29.03	-3.83	98.35	110.13
K_2 (k_bT/σ)	**here**	0.201	0.197	0.207	0.170	0.167	0.181
	Ref. [96]	0.199	0.194	0.203	0.160	0.150	0.136
	Ref. [94]	0.154	0.177	0.184	0.153	0.152	0.159
$\mathcal{P}_{\mathrm{eq}}$ (σ)	**here**	-3065	-238	-283	921	-81	-82
	Ref. [96]	-2990	-260	-310	965	-93	-90
	Ref. [94]	-2008	-268	-399	2509	-97	-90
$\lvert\Delta\mathcal{P}\rvert/\mathcal{P}_{\mathrm{eq}}$ (%)	Ref. [96]	2.45	9.24	9.54	4.78	14.8	9.76
	Ref. [94]	34.5	12.6	41.0	172	19.8	9.76

indicates that the effects of the low-order q-expansion of the free energy (Eq. (3.6)) and of the change in local orientational order induced by the cholesteric twist are both of limited consequence for the systems studied.

We nevertheless note that the original framework of Ref. [95] also relies on the assumption of local phase uniaxiality (Eq. (3.21)), and therefore still qualifies as a weak-deformation account of cholesteric order. A theoretical route to incorporate the deviations from local cylindrical symmetry induced by macroscopic twist in the approach of Ref. [95] has subsequently been outlined by Allen [192], but has to our knowledge not yet been implemented in numerical studies. These effects are however only expected to be substantial in the limit of short pitches [193], and may therefore be of limited practical relevance for the study of most experimentally-realistic systems.

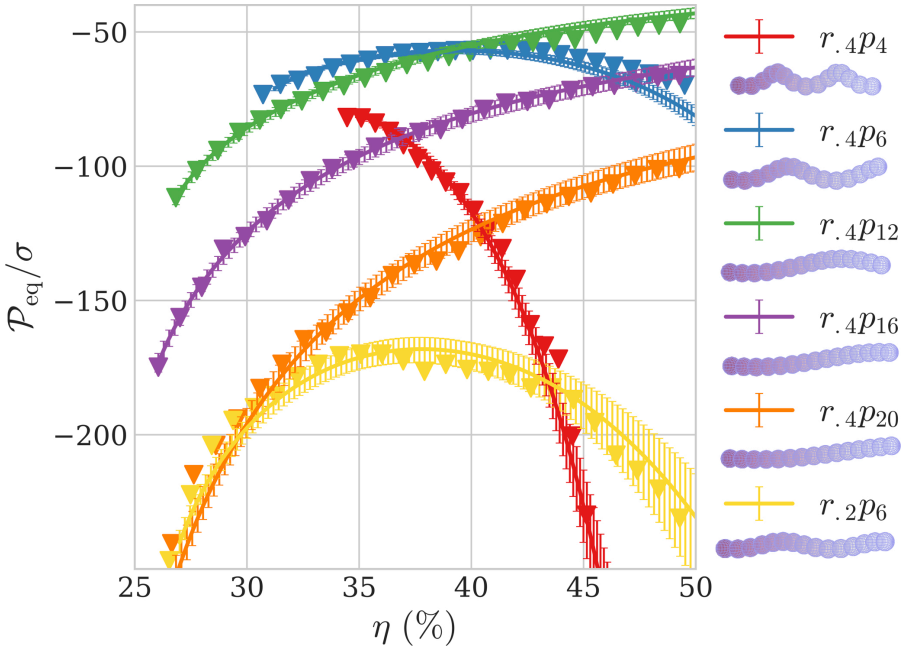

Figure 3.8: Equilibrium pitch in the limit of strong chirality for diverse hard helices with $N_s = 15$ and $l = 10\,\sigma$. Lines, symbols and error bars are defined as in Figure 3.7.

Conversely, it is well known that chiral mesogens are intrinsically biaxial, and that particle interactions at the microscale may thus give rise to an additional level of biaxial organisation in cholesterics beyond this simple phase-induced symmetry breaking [65, 66]. In this bottom-up picture, the cholesteric pitch of the system is also expected to be strongly contingent on its degree of local biaxial order, leading to a generally intricate causal relationship between phase chirality and biaxiality [194]. Consequently, the use of a uniaxial ansatz for the local description of a cholesteric LC may result in a significant overestimation of its equilibrium pitch, which could account for some of the discrepancies reported in Section 3.4.2. These limitations apply to all studies discussed in this section, and may therefore hamper the reliability of the methods described therein even in the limit of weak deformations. Extending the current density functional framework to explicitly include long-ranged biaxial correlations would allow for a direct and systematic investigation of the link between particle and phase biaxiality, and of its macroscopic effects on cholesteric behaviour.

3.5 Towards more realistic particle models

We finally remark that our method does not rely on any assumptions as to the nature of the microscopic interaction potential u in Eq. (2.21), and is therefore applicable to any short-ranged particle potential in the pairwise additive approximation. While the previous sections focused on the case of pure steric repulsion, more experimentally-realistic particle models are likely to involve additional contributions from electrostatic and/or dispersion interactions [195]. Following Ref. [91], we now consider a system of HSCs of length L and diameter D decorated with a helical charge distribution of microscopic pitch p located at their surface. To mimic a uniform linear distribution, we discretise the charges in a number N_p of identical interaction sites uniformly spread along the helical thread. The full pair interaction energy of two particles P_1 and P_2 then reads as

$$u(\mathbf{r}_{12}, \mathcal{R}_1, \mathcal{R}_2) = \begin{cases} +\infty & \text{if } P_1 \cap P_2 \neq \varnothing \\ \left(\dfrac{L}{N_p}\right)^2 \displaystyle\sum_{i,j=1}^{N_p} u_e(r_{ij}) & \text{if } P_1 \cap P_2 = \varnothing \end{cases}$$

where the set intersection sign denotes the potential overlap region of the HSCs, and u_e represents the electrostatic interaction potential per unit particle length [91]. r_{ij} then corresponds to the distance between interaction sites $i \in P_1$ and $j \in P_2$, which implicitly depends on the centre-of-mass separation vector $\mathbf{r}_{12}$ and respective orientations $\mathcal{R}_1, \mathcal{R}_2$ of the two particles. Following Ref. [91], we choose to account for electrostatic repulsion in the Debye-Hückel formalism, introducing a finite cutoff distance r_c for computational efficiency,

$$\beta u_e(r) = \begin{cases} u_0 \times \dfrac{\exp(-r/\lambda_D)}{r} & \text{if } r \leq r_c \\ 0 & \text{if } r > r_c \end{cases}$$

with λ_D the Debye length of the system. In the following, we set the cutoff length to $r_c = 10\,\lambda_D$ and number of patches to $N_p = 50$, which we verified to yield negligible truncation and discretisation effects for our results, and use $u_0 = 1/D^2$ for consistency with the values of Ref. [91].

Our numerical approach then enables us to directly investigate the validity of the framework of Ref. [91], in which a similar perturbative description was used, but where a number of approximations were introduced to work out the full pair interaction potential u and OF parameters K_2 and k_t semi-analytically for this particle model [90]. For consistency with the approach used therein, we now revert to the original form of the Onsager theory and thus set $G_{\mathrm{PL}} = 1$ for the rest of this section. The comparison of the equilibrium pitches predicted by our method to those reported in Ref. [91] is then summarised in Figure 3.9 for helical charge distributions with a variety of microscopic pitches.

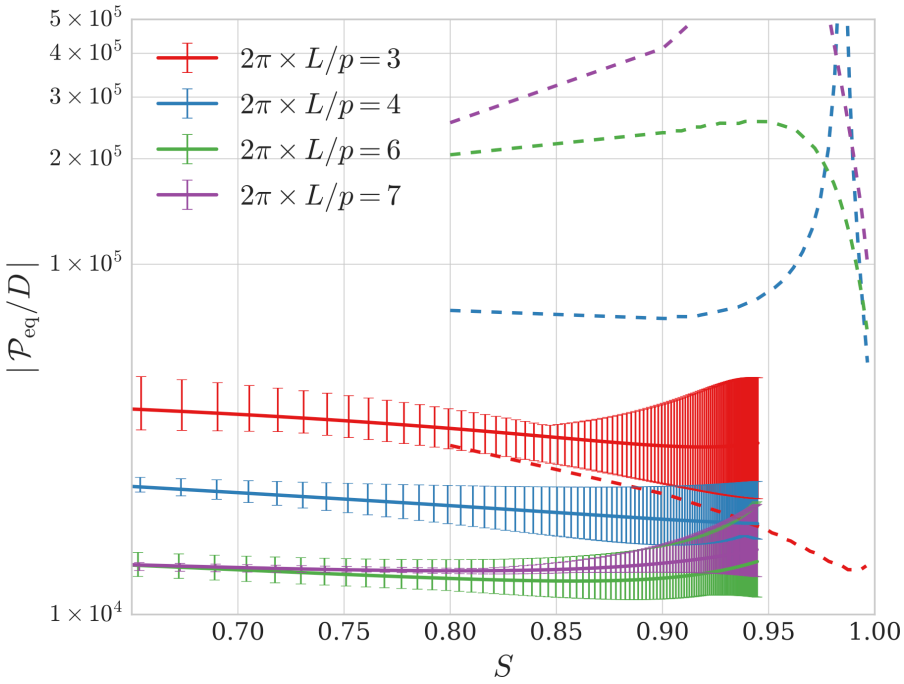

Figure 3.9: Absolute equilibrium pitch as a function of nematic order parameter for sphero-cylinders with aspect ratio $L/D = 50$, Debye length $\lambda_D = L/20$ and helical charge distributions of varying pitches p. Solid lines denote the results of this work, and dashed lines the data reported in Ref. [91]. All pitches predicted by our method are left-handed, while those of Ref. [91] are right-handed at lower densities with a potential handedness inversion at higher particle concentrations. Error bars were obtained from 8 independent runs with $N_{\mathrm{MC}} = 2.5 \times 10^{11}$.

We find no evidence of qualitative agreement in terms of either magnitude or handedness of the predicted pitches for any of the particles studied, despite the common use of the Onsager-Straley theoretical basis in both our approaches. Furthermore, we find that the inclusion of electrostatic repulsion moves the I/C

transition to lower volume fractions than in the case of purely steric interactions, with the onset of cholesteric order for all systems considered occurring at $\eta \simeq 2\%$ compared to the simulation value of $\eta \simeq 7\%$ obtained for HSCs with $L/D = 50$ [133]. This effect is consistent with theoretical results for uniformly-charged rods [196], but contrasts with the higher value $\eta \simeq 10\%$ reported in Ref. [91]. The origin of these discrepancies most likely lies in some of the simplifying assumptions introduced in Refs. [90] and [91] to obtain tractable expressions for all microscopic integrals of the form of Eqs. (2.73), (3.31) and (3.32). The magnitude of the resulting disparities illustrates the difficulty of deriving reliable analytical approximations in microscopic descriptions of the cholesteric phase, due to the strong dependence of such systems on the fine structural and thermodynamic properties of their constituent particles.

We also note that a number of simulation results on closely related systems have recently been reported [71,197,198]. However, the first of these studies [71] focused on fairly short sphero-cylinders in a regime of large Debye lengths, leading to effective particle aspect ratios too low to be accurately described by Onsager-like theories [196], while the other two [197,198] introduced an explicit dependence of the pair potential u on particle density, which as discussed in Section 3.3.1 would require significantly higher computational costs to be probed using our method. We nevertheless remark that Refs. [197] and [198] also found that the onset of cholesteric organisation was shifted to significantly lower volume fractions by the effects of electrostatic repulsion.

3.6 Conclusion

In this chapter, we have described a general density-functional method to systematically investigate the link between microscopic structure and macroscopic LC properties in cholesteric and uniaxial nematic phases. This multi-scale approach relies on a molecular description of local orientational order based on the Onsager-PL theory, combined with a continuum-level treatment of macroscopic spatial fluctuations through the microscopic theory of LC elasticities in the OF formalism. The use of numerical MC schemes to work out the underlying generalised virial

integrals greatly improves its applicability and reliability over that of previous analytical approaches, while the implementation of Straley's perturbative framework reduces its computational cost to a fraction of that of Refs. [95] and [96] for cholesteric systems. It further circumvents the need for the partial decomposition of the density field in a basis of rotational invariants (Eq. (2.83)), which greatly increases its tractability over that of previous numerical studies [92, 94–96].

The OF elastic moduli of HSCs computed using our model are found to be consistent with previous numerical and theoretical investigations, while our predictions for the cholesteric pitch of hard helices are in excellent quantitative agreement with the full-functional results of Ref. [96] for all systems studied. This latter observation confirms that the additional assumptions introduced by the perturbative description of phase chirality are not particularly limiting, and still work well down to surprisingly-short pitch lengths. We further reiterate that experimental lyotropic cholesterics typically have pitches that are very large compared to the particle diameters, and are therefore expected to be fully amenable to such a treatment.

However, we wish to highlight that there are a number of key approximations in most implementations of the DFT of cholesterics that we feel could potentially limit its quantitative accuracy, and need further consideration. Firstly, there are potential deficiencies in the PL rescaling in the case of strongly non-convex mesogens for the prediction of the onset of nematic order, which are not obviously improved upon by modifying the theory to account for the real effective molecular volume of the particles. This likely points to the need for a more sophisticated description of inter-particle correlations in these cases, following the considerations of Section 2.2.2. We note that an approach involving the explicit third-order virial contribution to the excess free energy was also implemented with some success for such systems, albeit under stringent symmetry assumptions [111]. It would be interesting to investigate whether its generalisation to configurations of freely-rotating particles may lead to significant improvements over the MPL approximation in our case.

Secondly, there is the assumption of local uniaxiality, and we wish to further emphasise the potential importance of long-ranged biaxial order in systems of chiral mesogens. Although the theory does not neglect biaxial correlations altogether, as sometimes erroneously suggested [65], it entirely relegates their effects to the short-ranged DCF arising from chiral inter-particle interactions, and does not account for their possible propagation over larger length-scales through the macroscopic density field. The angle dependence of our virial kernel κ (Eq. (2.73)) would provide a natural framework for the introduction of phase biaxiality, which may shed some light on the systematic underestimations of the cholesteric twist obtained by density functional methods in previous studies [74, 87].

The explicit inclusion of biaxial order would also represent a first step towards the description of more complex chiral nematic assemblies, such as the so-called twist-bend [199] and screw-like [179] nematic phases. However, recent studies suggest that the accurate treatment of the former may require a more involved account of the link between density field and director fluctuations beyond the simple PS ansatz (Eq. (3.14)) [200], while the coupling between orientational and translational degrees of freedom of the latter would call for further modifications of our symmetry assumptions [179]. Thus, in our opinion, significant efforts are still required to achieve a unified field-theoretical description of the chiral nematic state.

Hence, we stress that numerical simulations of simple cholesteric model systems along the lines of Refs. [71, 74, 198] are of particular importance to probe the quantitative validity of these different approximations. However, the degree of mutual consistency of the different numerical procedures employed in these previous studies for the determination of equilibrium cholesteric pitches remains largely unascertained, due to their focus on different particle models and parameter ranges. We therefore hope that the results of this chapter will stimulate further investigations of the respective reliabilities of these various methods, and help generate a reference set of data suitable for the thorough assessment of density-functional descriptions of the cholesteric phase.

4

Hierarchical bounding structures for efficient virial computations

Contents

The main performance bottleneck of the methods introduced in Chapters 2 and 3 lies in the calculation of the particle pair interaction energy u as part of the stochastic sampling of Eqs. (2.73) and (3.31)–(3.34). In common with most molecular modelling methods, the origin of this computational expense largely resides in the number of inter-atom[1] distances to be evaluated at every step for the computation of the various non-bonded interaction potentials comprising u. In the pairwise additive approximation, the naive time complexity of molecular

[1]Note that we here use the term *atoms* rather loosely to refer to the elementary building blocks comprising a single particle. As in the previous chapters, we further use the terms "particle" and "molecule" interchangeably to denote a full mesogenic compound.

simulations is indeed generally quadratic in the number of their constituent atoms, leading to rapidly-prohibitive numerical costs with increasing system sizes and particle complexity.

While the use of density-functional methods enables us to considerably alleviate this computational burden by providing a statistical-mechanical link between bulk equilibrium properties and pair molecular interactions, the high numerical accuracy required in the evaluation of Eqs. (3.31) and (3.32) for the reliable prediction of long cholesteric pitches (Eq. (3.7)) usually entails the use of a large number of MC steps to ensure the full convergence of these virial integrals. The corresponding number of pair interaction energies to be computed thus generally hinders the tractable treatment of experimentally-realistic systems, and one must therefore devise general numerical schemes capable of efficiently handling complex atomistic particle models in this context.

In this chapter, we detail the application of bounding volume hierarchies to accelerate second-virial evaluations for arbitrary particles interacting through hard and soft finite-ranged potentials. This procedure, based on the construction of neighbour lists through the combined use of recursive atom-decomposition techniques and binary overlap search schemes, is shown to scale sub-logarithmically with particle resolution in the case of molecular systems with high aspect ratios. We illustrate the method through the determination of the cholesteric behaviour of structurally-resolved, hard twisted cuboids (HTCs), and investigate the detailed influence of local surface structure on their chiral LC assembly.

4.1 Recursive acceleration structures for virial integration

A traditional approach to expedite potential energy calculations, as employed in most modern molecular simulation frameworks, is to exploit the locality of finite-ranged interaction potentials through the use of cell lists [68], which generally enable one to achieve a linear time complexity in the number of particles by restricting energy evaluation queries to pairs of neighbouring atoms. These methods usually

rely on the spatial partition of the simulation box into a grid of cells, into which the different constituent particles may be binned for the efficient determination of all atom pairs within the interaction cutoff range. However, the memory scaling of these simple acceleration structures with system volume, combined with their ineffective handling of anisotropic interaction potentials [201], render them ill-suited for the study of dilute suspensions of particles with high aspect ratios — as in the case of the colloidal LCs considered in this thesis.

Recent numerical studies [73, 202] have proposed to circumvent these issues through the construction of neighbour lists based on the partitioning of the particles themselves, rather than that of their total accessible volume. These algorithms, inspired by general considerations borrowed from the field of graphics rendering, instead resort to the use of recursive data structures known as bounding volume hierarchies (BVHs) to accelerate the binning of neighbouring atoms into simple geometric primitives. Their parallel implementation on graphical processing units (GPUs) was thus found to yield sizeable performance gains over standard grid-based methods in molecular dynamics simulations of non-uniform colloidal suspensions with high size polydispersity [202].

BVHs are commonly used in many computational geometry applications in which the rapid detection of potential collisions involving complex moving objects is critical; examples include motion planning in robotics [203], ray casting in real-time graphics rendering [204] and the physics engine of both video games [205] and computer-aided design platforms [206]. The popularity of BVHs stems from their ability to capture the geometric features of a wide variety of 3D objects at successive levels of spatial resolution, and hence quickly prune the sections of their structure contained in non-overlapping bounding volumes, as illustrated in Figures 4.1 and 4.2. Similar culling procedures have been successfully employed in recent years for the efficient implementation of neighbour search in systems of complex molecules, both rigid [207, 208] and flexible [209].

One of the challenges in designing effective BVHs lies in the choice of the elementary bounding volumes to be used, as their performance is generally contingent

on two antagonistic factors. Namely, (i) the bounding volumes should fit the chosen particle model as tightly as possible in order to minimise the number of distance queries to be performed at the end of the pruning process, and (ii) the computational cost of testing two bounding volumes for overlap should be minimal, so as to ensure the rapid traversal of the BVH [210]. Therefore, there exists no universal choice of a BVH yielding optimal performance in all situations, and one must rather tailor the selection of a geometric primitive to the particular system studied, keeping the two previous considerations in mind [211].

A good overall compromise between tightness and computational expense was achieved in Ref. [184] by introducing a culling hierarchy of orthorhombic boxes with variable axes for the efficient detection of intersections between sets of triangle meshes. While these oriented bounding boxes (OBBs) were found to be particularly well-suited for the case of complex particle models containing large numbers of topological features in close proximity, their efficiency unfortunately rapidly decreases with increasing inter-particle distance, as the relatively high cost of their overlap test progressively outweighs the benefits of their geometric tightness [184].

This limitation is particularly critical in the case of highly anisotropic particles, for which slight angular fluctuations may result in large separation distances between vast sections of the molecules even in the case of small inter-axis separation distances, as illustrated in Figure 4.3a. We therefore propose to combine this hierarchy of OBBs with preliminary overlap queries based on simple bounding sphero-cylinders (BSCs) for the efficient determination of neighbour lists in systems of complex particles with high aspect ratios interacting through arbitrary, finite-ranged atomistic potentials.

4.1.1 Construction of the BVH

For simplicity, let us consider a generic particle model comprised of N_a identical atoms, and index their positions by a $3 \times N_a$ coordinate matrix $\mathcal{M} = \{\mathbf{r}_i\}_{i \in [\![1, N_a]\!]}$ expressed in the fixed reference frame $\mathcal{R}_{\text{lab}} \equiv \left[\mathbf{e}_x \ \mathbf{e}_y \ \mathbf{e}_z\right]$. Our algorithm for the recursive construction of the BVH may then be summarised as follows.

1. We determine the molecular long and short axes $\mathbf{u}$ and $\mathbf{v}$ of the particle described by $\mathcal{M}$ through the procedure discussed in the next paragraph, and define its local Cartesian frame as $\mathcal{R} = \begin{bmatrix}\mathbf{v}\ \mathbf{w}\ \mathbf{u}\end{bmatrix}$, with $\mathbf{w} \equiv \mathbf{u} \times \mathbf{v}$.
2. We work out the smallest orthorhombic OBB aligned with $\mathcal{R}$ that encapsulates all the constituent atoms of $\mathcal{M}$.
3. We then split this OBB along the median plane of its long axis $\mathbf{u}$, and partition the atoms of $\mathcal{M}$ between the two resulting half-boxes; we denote the respective coordinate matrices of their enclosed atoms by $\mathcal{M}_1$ and $\mathcal{M}_2$.
4. We recursively iterate steps 1–3 on the subsystems respectively defined by $\mathcal{M}_1$ and $\mathcal{M}_2$, termed *child nodes* of our bounding hierarchy, until the total number of enclosed atoms at step 1 becomes smaller than an arbitrary number m — termed the *leaf parameter*.
5. The child nodes at the end of the final recursion step are then referred to as *leaf nodes*, and contain a number n_l of atoms such that $1 \leq n_l \leq m$ and

$$\sum_{\{l\}} n_l = N_a, \tag{4.1}$$

   where the sum runs over all the leaf nodes l of the hierarchy.
6. We finally append the tightest BSC of axis $\mathbf{u}$ enclosing the full particle to the first node of the hierarchy, termed the *root node* of the tree structure, as illustrated in Figure 4.3a.

In order to exploit the pipeline architecture of modern CPUs, atoms contained within the same leaf node are further allocated to contiguous memory locations to maximise the number of cache hits in the tree traversal procedure outlined in Section 4.1.2 [151].

This geometric construction largely revolves around the determination of the long and short axes $\mathbf{u}$ and $\mathbf{v}$ of the collections of atoms enclosed by the successive nodes, which define the orientations of their corresponding OBBs. A general mathematical method for the efficient calculation of such quantities is known as principal component analysis (PCA), commonly used in data processing applications to determine the directions of extremal statistical dispersion of high-dimensional sets of variables. In the framework of PCA, the long and short axes of a molecule defined

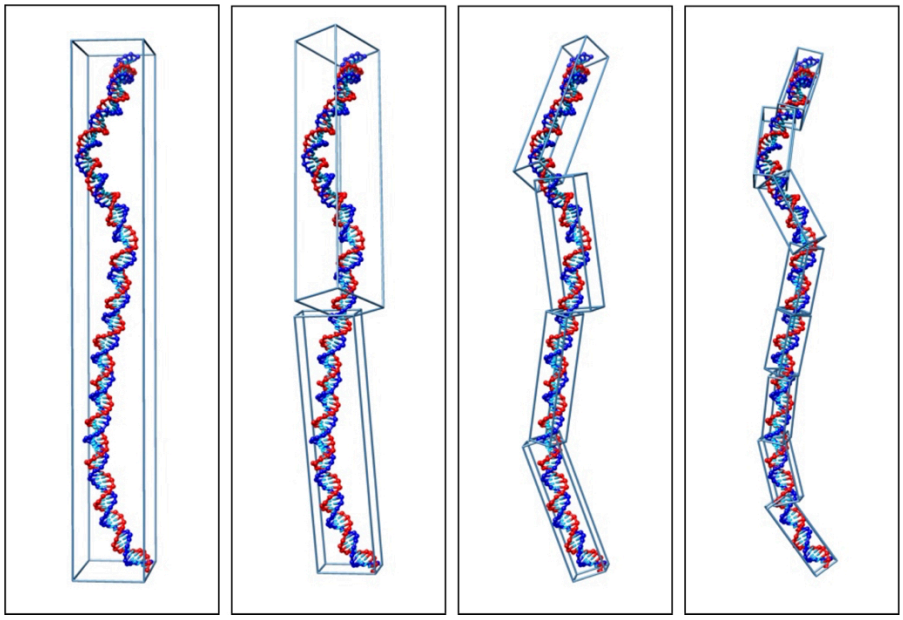

Figure 4.1: The first 15 nodes of the culling hierarchy for a 146 base-pair DNA duplex as described by the oxDNA coarse-grained model [212]. The different OBBs are computed using the recursive procedure of Section 4.1.1.

by a coordinate matrix $\mathcal{M}$ therefore correspond to the respective eigenvectors associated with the largest and smallest eigenvalues of the covariance matrix of $\mathcal{M}$. Assuming the particle centre of mass to be set to the origin of the reference frame, the covariance matrix may be assimilated to the gyration tensor $\mathcal{G}$ of the molecule,

$$\mathcal{G}_{mn} \equiv \frac{1}{N_a} \sum_{i=1}^{N_a} r_{im} r_{in} = \frac{1}{N_a} \left(\mathcal{M} \cdot \mathcal{M}^{\mathsf{T}} \right)_{mn}, \tag{4.2}$$

for $(m, n) \in \{x, y, z\}^2$, with $r_{im} \equiv \mathbf{r}_i \cdot \mathbf{e}_m$.

It is easy to prove that this definition for $\mathbf{u}$ is mathematically equivalent to that of Ref. [213] based on the principal axes of inertia, if one assumes all the atoms of the system to bear equal masses. However, a significant advantage of PCA over this previous description lies in its close association with the formalism of singular value decomposition (SVD), as the eigenvectors of $\mathcal{G}$ may by conveniently worked out as the left-singular vectors of $\mathcal{M}$ [214]. Therefore, SVD provides a direct numerical route for the evaluation of the local molecular axes as previously defined, and may be performed in $\mathcal{O}(N_a)$ operations for a matrix of size $3 \times N_a$ — while the computation and spectral decomposition of the inertia tensor would lead to a quadratic overall complexity in the number of enclosed atoms [215]. The

capabilities of PCA for the efficient fitting of tight bounding volumes have been well-documented in a variety of contexts [216], and enable our BVH to rapidly converge towards arbitrarily complex molecular shapes, as illustrated in Figure 4.1.

A considerable asset of this object-based acceleration structure is that it only needs to be constructed once per molecule in the case of rigid particle models, whose accessible configuration space may then be fully sampled by rigid-body rotations and translations of the nodes comprising their initial BVHs. Furthermore, the use of the so-called *median cut algorithm* [217] described in step 3 for the recursive partitioning of the hierarchy leads to the design of a *balanced binary tree* of bounding volumes, in which every non-leaf node is associated with two children nodes enclosing generally comparable numbers of atoms. Such structures have found widespread applications in many areas of computer science owing to their strong synergy with binary search methods, which generally allows for the efficient parsing of complex datasets in logarithmic time [218]. We now proceed to outline the practical implementation of such a scheme for the accelerated computation of inter-molecular interactions.

4.1.2 BVHs and binary neighbour search

Let us now consider a pair of arbitrary particles defined by coordinate matrices $\mathcal{M}_A$ and $\mathcal{M}_B$, interacting through a pairwise additive interatomic potential u_a with cutoff range r_c. We first construct the respective BVHs of $\mathcal{M}_A$ and $\mathcal{M}_B$ following the procedure of Section 4.1.1, and extend all the corresponding bounding volumes by a length r_c along the 3 directions of their local frames. A necessary condition for the existence of non-zero interactions between a given pair of atoms in that case lies in the intersection of all of their respective parent bounding volumes, as illustrated in Figure 4.2.

Based on this simple observation, an efficient neighbour search algorithm may be implemented as follows.

1. We test the BSCs of the root nodes of $\mathcal{M}_A$ and $\mathcal{M}_B$ for mutual overlaps, using the algorithms discussed in the next paragraph.
2. If they intersect, we check the corresponding OBBs for overlap.

3. If these OBBs intersect, we recursively iterate steps 2 and 3 by descending into the children of the node enclosing the largest number of atoms, until either two leaf nodes are reached or the corresponding OBBs are disjoint.
4. The full interaction energy u of the two molecules is finally given by

$$u = \sum_{\{l_A, l_B\}} \left(\sum_{i \in l_A} \sum_{j \in l_B} u_a(\mathbf{r}_i, \mathbf{r}_j) \right), \tag{4.3}$$

where the outer sum runs over all pairs of overlapping leaf nodes l_A and l_B reached at the end of the traversal process, and the two inner sums over the atoms they respectively enclose.

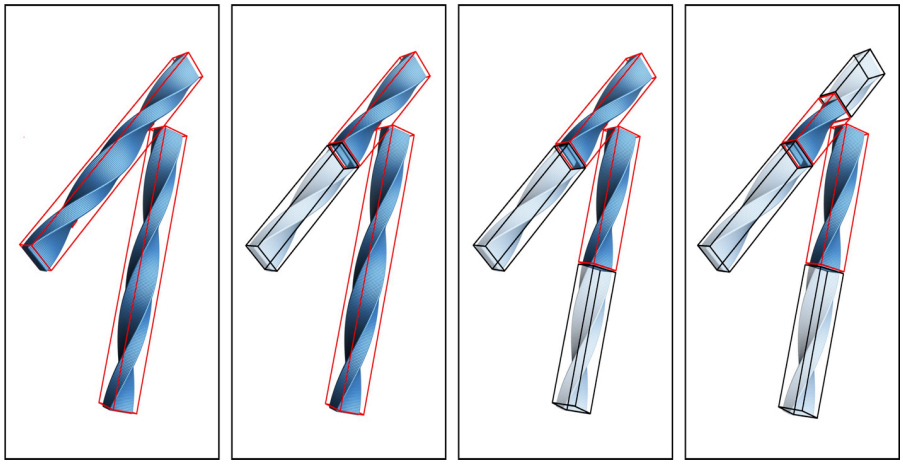

Figure 4.2: Schematic representation of the first 4 steps of the BVH-accelerated neighbour search for a pair of twisted cuboidal particles comprised of thousands of fused hard-spheres. Only opaque spheres need to be checked for overlap once the leaf nodes of the hierarchies have been reached.

The overlap tests involving BSCs may be efficiently performed using the approach of Vega and Lago [131], which amounts to determining the distance of minimum approach between the axes of their cylindrical backbones, while the intersection checks between OBBs can be expedited by invoking the separating axis theorem as described in Ref. [210]. Owing to the multiple early exit conditions of the latter test, the relative performance of these two algorithms may vary considerably from case to case; using our implementations, we found the average overlap query times to be roughly 40% faster for BSCs than those of the corresponding OBBs.

A further advantage of BSCs lies in their uniaxial symmetry, which obviates the computation of the full 3×3 orientation matrix $\mathcal{R}$ of the enclosed molecule (Eq. (A.2)). In the context of the MC integration of Eqs. (2.73) and (3.31)–(3.34), the interaction energy between an arbitrary pair of molecules may thus be efficiently determined by randomly generating their centre-of-mass separation vector $\mathbf{r}_{12} \in V$ and normalised main axes $\mathbf{u}_{1,2}$, and restricting the explicit evaluation of $\mathcal{R}_1$ and $\mathcal{R}_2$ to cases in which the corresponding BSCs overlap. The performance of the BVH may finally be optimised by fine-tuning the leaf parameter m, as illustrated in Figure 4.4; the optimal value for m typically depends on both molecular geometry and the complexity of the underlying inter-atomic potential [208], and generally needs to be determined empirically for the chosen particle model.

4.2 The cholesteric behaviour of HTCs

We now propose to illustrate the application of our method to systems of chiral cuboidal particles obtained by continuously twisting an orthorhombic solid of long axis $\mathbf{u}$ and short axes $\mathbf{v}$, $\mathbf{w}$ through an overall angle γ along $\mathbf{u}$, as depicted in Figure 4.3. The biaxiality and chirality of such mesogens may then be independently tuned by respectively varying their transverse cross section $L_\mathbf{v} \times L_\mathbf{w}$ and thread angle ν, defined in Figure 4.3b, related to the twist angle γ through

$$\tan \nu = \frac{2L_\mathbf{u}}{\gamma \sqrt{L_\mathbf{v}^2 + L_\mathbf{w}^2}}, \tag{4.4}$$

with $L_\mathbf{k}$ the extent of the cuboids along axis $\mathbf{k}$.

Similarly-shaped particles have been synthesised using the DNA origami technique [219], where low-aspect-ratio twisted cuboidal origamis have been concatenated to form long particles [220]. A particularly attractive feature of DNA origamis as potential mesogenic units lies in the ability to precisely control their molecular shape, twist and curvature [220], and thus to provide a route towards systematically exploring the link between microscopic features and phase organisation in LCs. Indeed, the Dogic group has recently probed the cholesteric behaviour of very

high-aspect ratio origamis consisting of 6 parallel double helices in an hexagonal arrangement with varying degrees of axial twist [221], as discussed in Chapter 6.

Furthermore, recent experimental evidence suggests that cellulose nanocrystals may naturally adopt configurations with a twisted cuboidal shape [222,223], which may in turn dictate their chiral nematic arrangement [224]. Therefore, the theoretical investigation of the cholesteric assembly of HTCs as a function of particle twist and biaxiality may provide a valuable starting point for the quantitative understanding of the emergence of chirality in such experimental systems.

4.2.1 Voxelisation and surface representations

Despite their conceptual simplicity, the numerical treatment of such particles presents a significant practical challenge owing to the difficulty of accurately describing their detailed structure in terms of simple geometric primitives. The precise representation of their twist-induced local curvature thus requires the decomposition of their surface into a discrete set of elementary points, termed *voxels*. In this framework, the simplest finite-element representation of a particle may be obtained by associating each voxel with a hard spherical shell of given radius σ, as illustrated in Figure 4.3b. Denoting by $N_{\mathbf{u}}$, $N_{\mathbf{v}}$ and $N_{\mathbf{w}}$ the respective numbers of voxels uniformly distributed along their 3 orthorhombic axes, the smallest possible shell radius $\sigma_{\min}$ is given by

$$\sigma_{\min} = \max_{\mathbf{k}\in\{\mathbf{u},\mathbf{v},\mathbf{w}\}} \frac{L_{\mathbf{k}}}{N_{\mathbf{k}} - 1}, \tag{4.5}$$

which ensures that no adjacent spheres are disjoint, and guarantees the integrity of the resulting surfaces.

Overlap queries between such fused hard-sphere models then simply reduce to checking their constituent voxels for intersection, and may thus be efficiently handled by the procedure of Section 4.1 using the simple hard-sphere limit for the interatomic potential u_a,

$$u_a(\mathbf{r}_i, \mathbf{r}_j) = \begin{cases} +\infty & \text{if } \|\mathbf{r}_i - \mathbf{r}_j\| \leq \sigma \\ 0 & \text{if } \|\mathbf{r}_i - \mathbf{r}_j\| > \sigma \end{cases}.$$

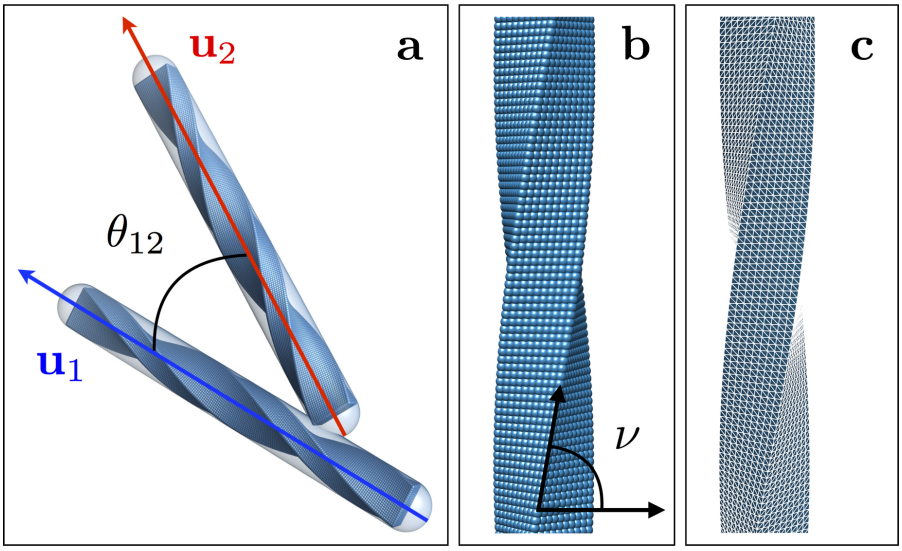

Figure 4.3: Particle long axes and local surface representations of HTCs. a) BSCs and inter-axis angle θ_{12} for a pair of calamitic HTCs. b) Rasterised model of HTCs; each voxel is represented as the centre of a hard sphere of radius σ. c) Tesselated mesh obtained by constrained Delaunay triangulation of the former.

In the following, we set $\sigma = 1.5\,\sigma_{\min}$ and use $N_{\mathbf{k}} = \xi L_{\mathbf{k}}$, with ξ the voxel density per unit length. The total number N_{vox} of voxels comprising a single particle is then

$$N_{\text{vox}} = 2 + \sum_{\mathbf{k}\neq\mathbf{l}} (N_{\mathbf{k}} - 1)(N_{\mathbf{l}} - 1), \tag{4.6}$$

where the sum runs over all distinct pairs of axes $\mathbf{k}, \mathbf{l} \in \{\mathbf{u}, \mathbf{v}, \mathbf{w}\}$.

A limitation of this rasterised representation however lies in the roughness of the resulting surfaces, which entails the use of a high voxel resolution to emulate a smooth particle texture. An alternative geometric description may be obtained by constrained Delaunay triangulation, which in our case simply amounts to allocating a unique hard triangle to each triplet of neighbouring voxels — imposing that each voxel is associated to a vertex shared between at most 6 distinct triangles, as depicted in Figure 4.3c. The number N_s of constituent simplices within the resulting mesh is then given by the so-called Euler-Poincaré formula with genus 0 [225],

$$N_s = 2N_{\text{vox}} - 4. \tag{4.7}$$

Owing to their ubiquity in computer graphics applications, multiple highly-efficient algorithms have been developed in recent years for the reliable detection

of overlaps between such triangle meshes. We here choose to make use of the well-established RAPID open-source library, based on the bounding tree hierarchy introduced in Ref. [184]. This numerical implementation constitutes one of the standard collision detection schemes used in a number of performance-critical applications [226], and provides a valuable benchmark for the assessment of the efficiency and accuracy of our approach.

We summarise in Figure 4.4 the average processing times of a single overlap test between pairs of HTCs with aspect ratios of 100 and various voxel resolutions using both our approach and the RAPID library, along with standard (st) and object-based (ob) variations of conventional grid acceleration structures. In the latter object-based case, we split the root OBBs of the two particles into two arrays of contiguous bounding boxes aligned with their respective molecular frames, into which constituent voxels may be binned. If the root OBBs intersect, we incrementally traverse the two grids and iterate over the voxels enclosed by each pair of overlapping boxes until a hard sphere collision is detected. We here set the number of boxes allocated along each particle axis $\mathbf{k}$ to $N_{\mathbf{k}}^b = N_{\mathbf{k}}/5$, which was found to yield optimal performance for the particles studied, with the corresponding box dimensions $L_{\mathbf{k}}^b$ related to those $L_{\mathbf{k}}$ of the root OBBs through

$$L_{\mathbf{k}}^b = L_{\mathbf{k}}/N_{\mathbf{k}}^b + \sigma \quad \forall \mathbf{k} \in \{\mathbf{u}, \mathbf{v}, \mathbf{w}\}.$$

The standard grid implementation is identical to that described in Ref. [208] using a cutoff distance of σ, and is conceptually equivalent to a traditional cell-list approach.

We note that the performance scaling of hierarchy-based methods is found to be sub-logarithmic in the number N_{vox} of elementary voxels per particle, with the average processing time of a pair configuration increasing by roughly 20% upon raising N_{vox} from 8 018 to 2 540 168, corresponding to a sixteenfold increase in voxel density from $\xi = 5$ to $\xi = 80$. Accordingly, the associated speedups relative to a naive quadratic implementation — in which every pair of constituent voxels needs to be checked for overlaps at each step — range from 6 to 11 orders of magnitude for these systems, with our approach for $m = 10$ yielding an increase

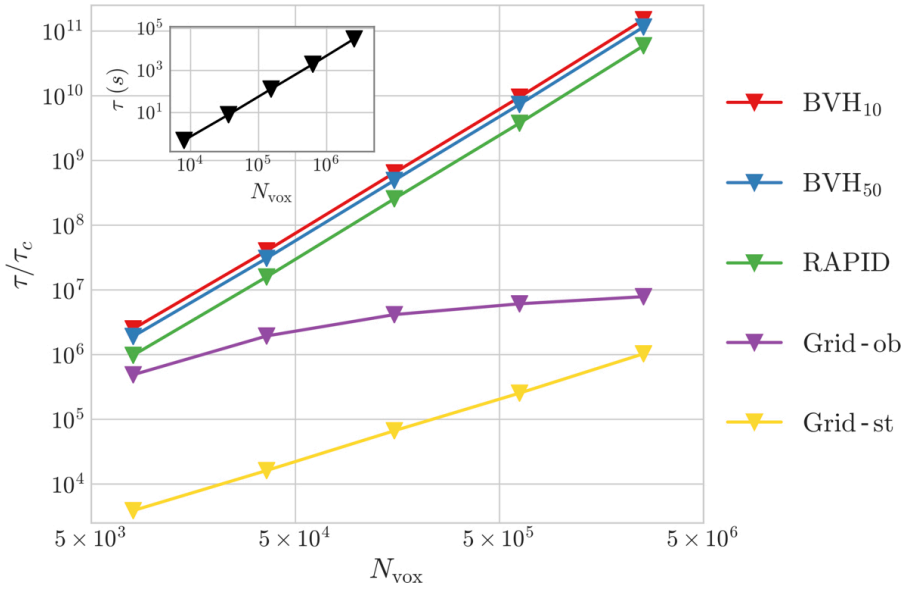

Figure 4.4: Relative speedups of the different neighbour search algorithms for HTCs with $L_u = 100$, $L_v = L_w = 1$, $\nu = 80°$ and variable numbers of voxels. τ represents the average time of a naive overlap query between a single pair of particles, plotted in the inset, and τ_c describes the corresponding numerical costs of the different culling structures described in the text. BVH_m denotes the performance of our bounding volume hierarchy using a given value of leaf parameter m (c.f. Section 4.1.2.) All measured times were averaged over 10^2 to 10^5 randomly generated configurations on an Intel® Core™ i5-4690 CPU.

in performance upwards of 250% over RAPID on all tests. This difference may be attributed both to the comparatively lower cost of overlap queries between spherical primitives and to our additional use of BSCs to efficiently prune non-overlapping configurations, as described in Section 4.1. Benchmarking tests further indicate that OBB overlap queries account for over 70% of the computation time in both cases for all particles in Figure 4.4, so that the origin of this performance gain likely mostly lies in the latter effect.

We also remark that the asymptotic scaling of our object-based grid algorithm (Grid-ob in Figure 4.4) is super-linear due to the linear increase of the total number of grid cells with N_{vox}, leading to a quadratic worst-case performance in the event that no voxel overlaps are detected after a full grid traversal. Its numerical efficiency however becomes comparable to that of hierarchy-based approaches in the case of highly coarse-grained particles comprised of $N_{\mathrm{vox}} \lesssim 500$ voxels, for which computational costs are dominated by voxel overlap queries rather than

neighbour search [208]. All culling structures are found to vastly outperform our standard cell-list implementation (Grid-st in Figure 4.4) for the particles studied, despite the linear scaling of the latter.

4.2.2 Thread angles and handedness inversion

A further interesting feature of this idealised particle model lies in the continuous threads formed by their uniformly-twisted transverse edges, which constitute a practical realisation of the simplified system of threaded rods first introduced by Straley [82]. In this context, a twisted cuboid of dimensions $L_{\mathbf{u}}$, $L_{\mathbf{v}}$ and $L_{\mathbf{w}}$ may thus also be considered as a threaded rod of length $L_{\mathbf{u}}$ and groove depth Δ,

$$\Delta = \frac{\min\{L_{\mathbf{v}}, L_{\mathbf{w}}\}}{2} \times \left(\sqrt{1+\chi^2} - 1\right), \tag{4.8}$$

where $\chi \equiv \max\{L_{\mathbf{v}}, L_{\mathbf{w}}\}/\min\{L_{\mathbf{v}}, L_{\mathbf{w}}\}$ quantifies the molecular biaxiality of the system.

Intriguingly, the handedness of the cholesteric phase formed by such threaded particles has been previously conjectured to depend on the value of their thread angle ν based on simple geometric arguments [65, 82, 227]. In particular, for $\nu > 45°$ the preferred relative twist of two particles at nearest contact is of the opposite handedness to the particles, whereas for $\nu < 45°$ the twist is of the same handedness, as illustrated in Figure 4.5. At the crossover angle of $\nu = 45°$, the particle long axes are expected to lie at a 90° angle at their point of closest approach.

However, as is well-known, the assumption that the particles adopt such relative inter-axis angles in cholesteric phases leads to the prediction of pitches of the order of just a few particle diameters [9], suggesting that cholesteric behaviour may not be easily described in terms of single-particle geometric features alone [65, 66]. We therefore proceed to investigate the link between cholesteric behaviour and molecular twist to provide a first-hand assessment of the validity of these qualitative assertions.

We reproduce in Figure 4.6 the concentration dependence of the equilibrium cholesteric wavenumbers q_{eq} of HTCs with various thread angles ν and rectangular cross sections χ. Firstly, we note that the results are very insensitive to the surface

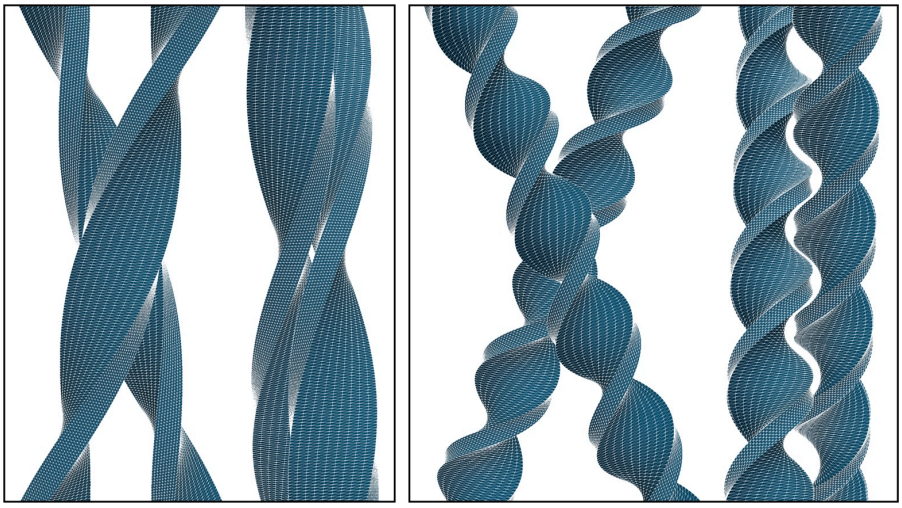

Figure 4.5: Front and side views of two-particle configurations at the relative inclination angle θ_{12} minimising their inter-axis separation distance. The HTCs represented bear a right-handed twist with $L_{\mathbf{u}} = 100$, $L_{\mathbf{v}} = 1$, $L_{\mathbf{w}} = 3$, $\nu = 70°$ (left) and $\nu = 40°$ (right). Note the transition of the arrangements from left- to right-handedness with decreasing particle thread angles.

representation of the particles (c.f. Figure 4.3). Secondly, consistent with the previous geometric arguments, we find that loosely-threaded particles — associated with the larger values of ν — tend to form cholesteric phases with opposite (left) handedness, while increasing microscopic twist progressively stabilises phases with the same (right) handedness. The crossover region over which this handedness inversion occurs is further found to lie in the range $\nu \in [40°, 50°]$, in good apparent agreement with the threshold value $\nu = 45°$ inferred from the dense packing of idealised hard threaded rods [228].

Conversely, we remark that increasing particle twist generally tends to unwind the absolute pitch of the higher-density phases, in stark contrast with intuitive predictions based purely on such geometric considerations. A simple interpretation of this rather puzzling trend may be obtained by considering the chiral components of the angle-dependent two particle excluded volume, formally defined as [95, 96]

$$U_{\pm}(\theta) = -\int_V d\mathbf{r}_{12} \oiint d\mathcal{R}_1 d\mathcal{R}_2 \, f(\mathbf{r}_{12}, \mathcal{R}_1, \mathcal{R}_2) \delta(\mathbf{u}_1 \cdot \mathbf{u}_2 - \cos\theta) \Theta\Big\{ \pm \mathbf{r}_{12} \cdot (\mathbf{u}_1 \times \mathbf{u}_2) \Big\}, \tag{4.9}$$

where U_+ and U_- refer to the excluded volume relative to right- and left-handed pair configurations, respectively. In Eq. (4.9), the Heaviside function Θ mirrors the

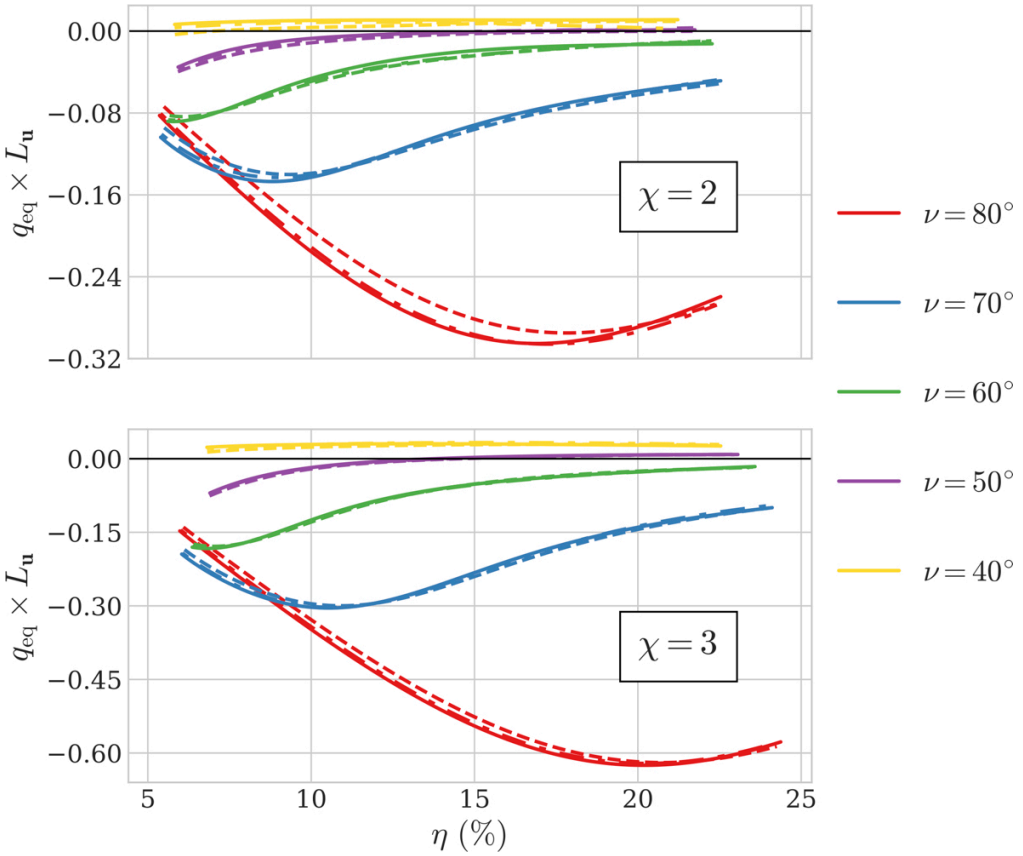

Figure 4.6: Cholesteric wavenumber as a function of particle volume fraction for HTCs with $L_{\mathbf{u}} = 100$, $L_{\mathbf{v}} = 1$, $L_{\mathbf{w}} = \chi L_{\mathbf{v}}$ and various thread angles ν. Positive values of q_{eq} denote a right-handed cholesteric phase. Dashed and dash-dotted lines respectively denote rasterised particle representations with $\xi = 10$ and $\xi = 40$ (Figure 4.3b), while solid lines correspond to tesselated surface meshes with $\xi = 10$ (Figure 4.3c). All particles possess a right-handed microscopic chirality, and the lowest reported densities correspond to their respective nematic binodals, computed as in Chapter 2.

fact that the handedness of an arrangement of two particles with centre-of-mass separation vector $\mathbf{r}_{12} \equiv \mathbf{r}_2 - \mathbf{r}_1$ and respective long axes $\mathbf{u}_i \equiv \mathcal{R}_i \cdot \mathbf{e}_x$ is determined by the sign of $\mathbf{r}_{12} \cdot (\mathbf{u}_1 \times \mathbf{u}_2)$. Using this definition, a system of two particles with inter-axis angle θ_{12} (c.f. Figure 4.3a) will adopt an entropically-stable right-handed configuration if and only if $U_-(\theta_{12}) > U_+(\theta_{12})$. For the sake of normalisation, it is convenient to introduce the dimensionless quantity [96]

$$\Delta_c U^* \equiv \frac{U_+ - U_-}{U_+ + U_-} \equiv \frac{\Delta_c U}{U_+ + U_-} \tag{4.10}$$

with $U_+ + U_-$ the full angle-dependent pair excluded volume.

We reproduce in Figure 4.7 the angle dependence of $\Delta_c U^*$ for the systems

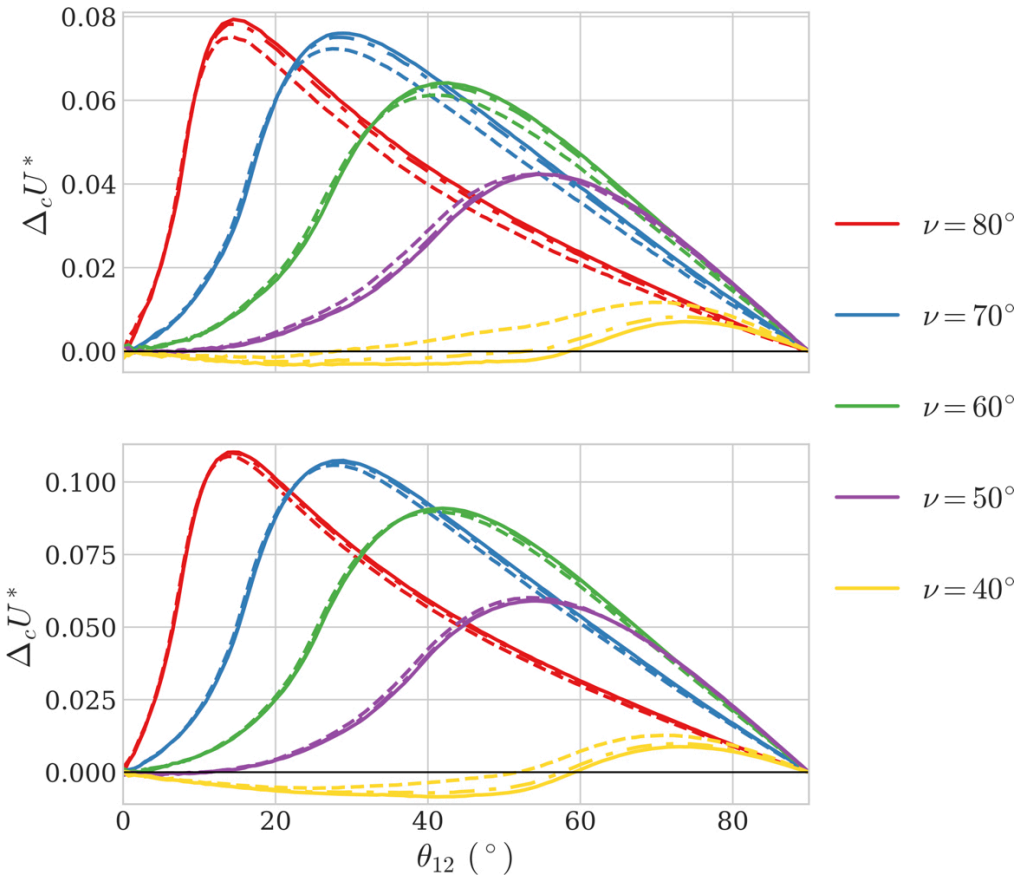

Figure 4.7: Normalised two-particle chiral excluded volume as a function of inter-axis angle (c.f. Figure 4.3a). The x-axis is limited to the range $\theta_{12} \in [0, \pi/2]$ owing to the symmetry relation $\Delta_c U^*(\theta_{12}) = -\Delta_c U^*(\pi - \theta_{12})$ imposed by the apolar nature of the particles. Colours and symbols are defined as in Figure 4.6. The global extrema of $\Delta_c U^*$ for tesselated particles with $\chi = 3$ and $\nu \in \{40°, 70°\}$ correspond to the inter-axis angle of their respective configurations of closest approach as depicted in Figure 4.5.

introduced in Figure 4.6. We note that

$$\Delta_c U^*(\theta_{12}) > 0 \quad \forall \theta_{12} \in [0, \pi/2]$$

for all particles with thread angles $\nu \geq 50°$, ensuring their formation of a stable left-handed phase. Increasing particle twist progressively moves the location of the extremum of $\Delta_c U^*$ to higher values of θ_{12}, mirroring the larger inter-axis angles required by a pair of such particles to reach their distance of minimal approach. Such configurations are however incompatible with the local orientational alignment inherent to a cholesteric structure, and the particles' sampling of their respective excluded volume manifolds is therefore topologically constrained to the region of

small $|\theta_{12}|$, in which $\Delta_c U^*$ progressively vanishes with decreasing thread angles in the range $\nu \in [50°, 80°]$.

This phase-induced restriction of the effective configuration space becomes increasingly stringent at higher particle concentrations and thus prevents the more strongly twisted particles from accommodating their local chirality, thereby accounting for the unwinding of cholesteric pitches observed in this regime (Figure 4.6). Prior to this, there may also be a regime where phase chirality increases with particle concentration as the effects of short-ranged chiral interactions become more important. The resulting minimum in the pitch occurs at higher particle concentrations for the less-twisted particles, consistent with the lesser conflict between the preferred twist of the particles and the local nematic ordering. Finally, cholesteric handedness inversions may be attributed to the appearance of negative local extrema of $\Delta_c U^*$ at low values of θ_{12} for $\nu = 40°$, instigating the gradual stabilisation of a right-handed phase [91].

A simple geometric interpretation of these low-angle extrema may be obtained by closer inspection of Figure 4.5. Indeed, it is apparent from the arrangement of HTCs with thread angle $\nu = 70°$ that the optimal packing of two such particles may be achieved by locally aligning their respective long faces at their point of close contact. Such configurations may however only be reached in the regime where the width $L_{\mathbf{w}}$ of their long faces is shorter than their microscopic pitch, as increasing the twist of the particles progressively precludes the near proximity of these long faces. In this case, a more entropically-favorable arrangement may rather be obtained by locally aligning the short face of one particle with the long face of the other, as illustrated in the right panel of Figure 4.5 for cuboids with $\nu = 40°$, leading to right-handed close-approach configurations with comparatively smaller inter-axis angles between adjacent mesogens.

Lastly, we report in Figure 4.8 the density dependence of the equilibrium cholesteric pitch of HTCs with square cross sections, along with the corresponding angular variations of $\Delta_c U^*$. We note that the shallower grooves of such systems (Eq. (4.8)) significantly reduce the chirality of the resulting phases, and increase

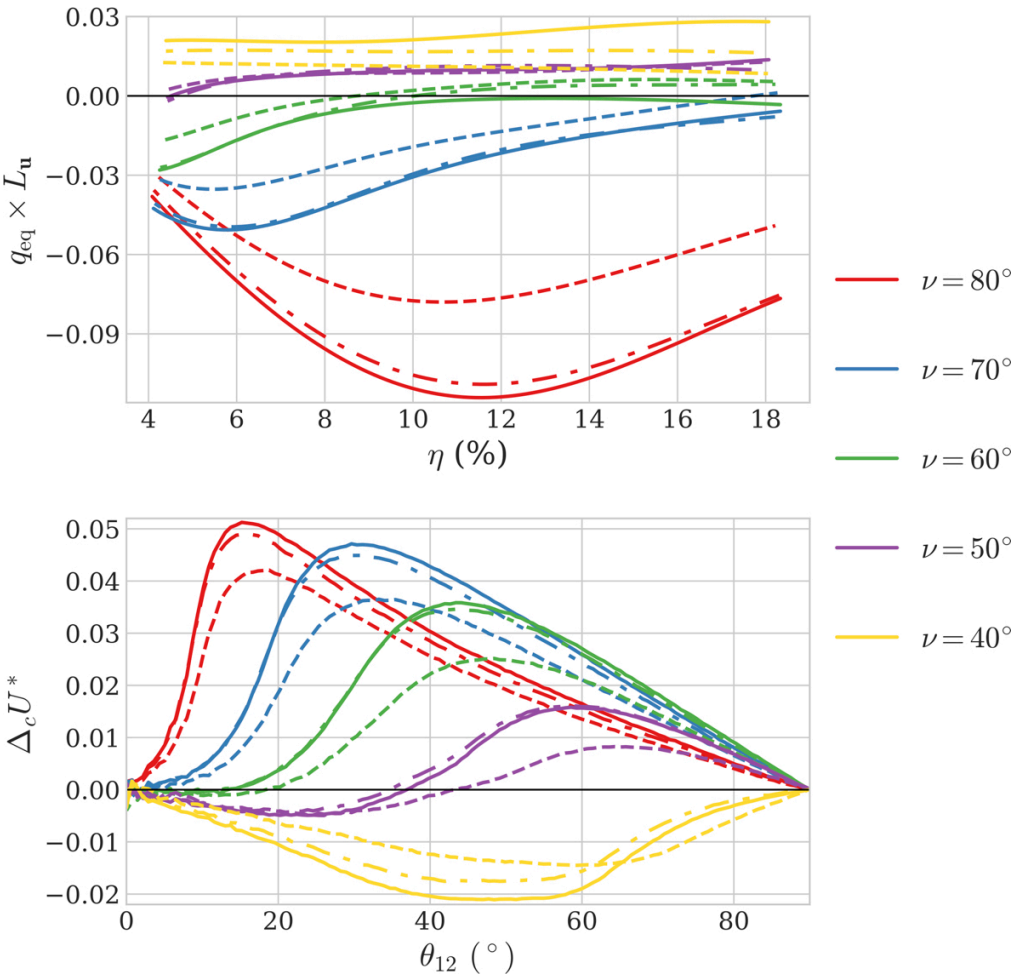

Figure 4.8: Top: cholesteric wavenumber as a function of particle volume fraction for HTCs with $L_{\mathbf{u}} = 100$, $L_{\mathbf{v}} = L_{\mathbf{w}} = 1$ and various thread angles ν. Bottom: normalised two-particle chiral excluded volume as a function of inter-axis angle. Colours and symbols as in Figure 4.6.

the sensitivity of their macroscopic pitch to the microscopic details of their surface structure; the results obtained using rasterised particle models nonetheless converge towards those of their smoother tesselated counterparts with increasing ξ, as all discretisation schemes lead to equivalent particle descriptions in the limit of high voxel resolutions. Furthermore, the onset of handedness inversions is in this case found to depend very finely on both molecular density and local surface representations, with systems in the range $50° \leq \nu \leq 60°$ exhibiting a potential crossover from left- to right-handedness — associated with a weak small-angle minimum of $\Delta_c U^*$ — upon slight variations of their concentration and microscopic features.

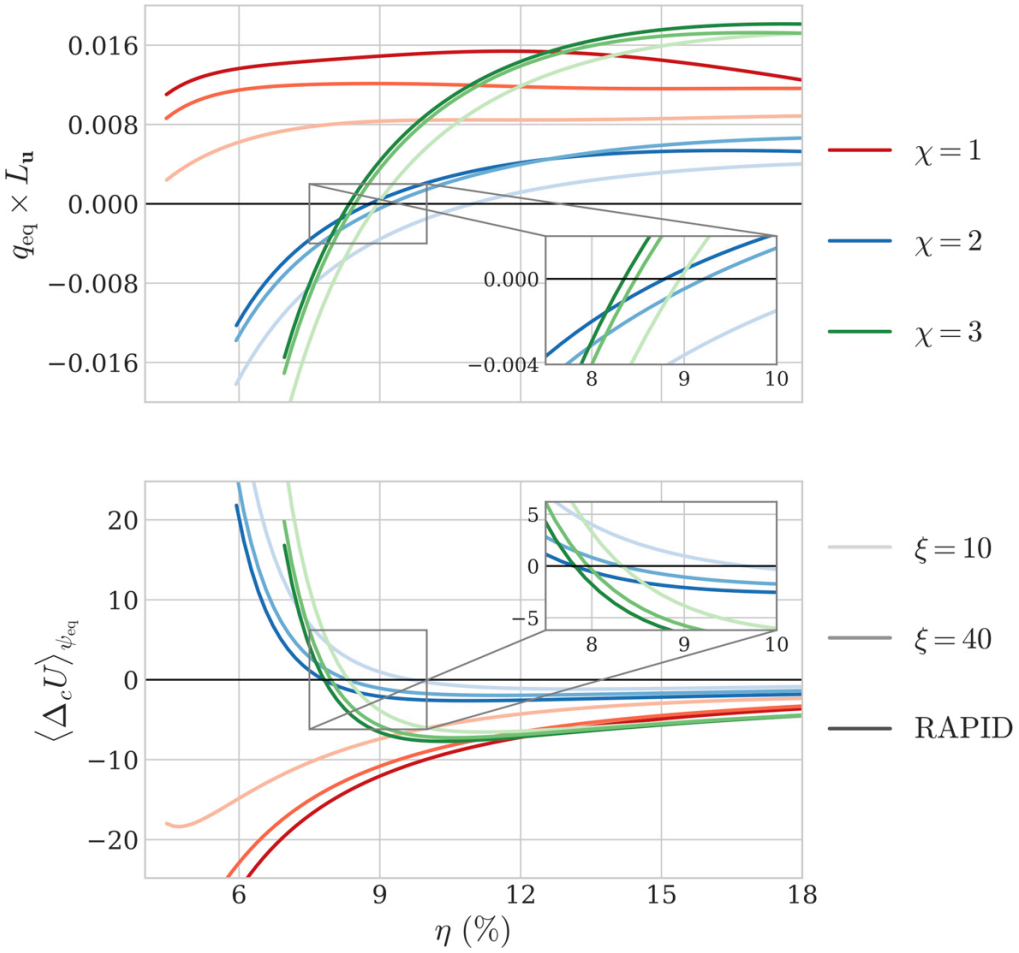

Figure 4.9: Cholesteric wavenumber and angle-averaged chiral excluded volume as a function of particle volume fraction for HTCs with $L_{\mathbf{u}} = 100$, $L_{\mathbf{v}} = 1$, $L_{\mathbf{w}} = \chi L_{\mathbf{v}}$ and $\nu = 45°$. Particle representations are defined as in Figure 4.6, with RAPID denoting tesselated surface meshes with $\xi = 10$.

Keeping the previous discussion in mind, a more rigorous interpretation of these subtle disparities may be achieved by considering the thermodynamic average of the chiral excluded volume (Eq. (2.85)) [95, 96],

$$\langle \Delta_c U \rangle_{\psi_{\mathrm{eq}}} = 8\pi^2 \int_0^{\pi/2} \sin\theta d\theta \, \psi_{\mathrm{eq}}(\cos\theta) \times \Delta_c U(\theta), \tag{4.11}$$

which combines the purely-geometric quantity $\Delta_c U$ with the local nematic correlations underlying the uniaxial approximation of our perturbative approach. In this framework, the handedness of cholesteric phases at equilibrium may then be qualitatively captured by the sign of the density-dependent $\langle \Delta_c U \rangle_{\psi_{\mathrm{eq}}}$, as illustrated in Figure 4.9. The quantitative determination of the magnitude of the corresponding pitches however requires the full evaluation of k_t and K_2, as described in Section 3.2.

4.2.3 Comparison to other model systems

We note that similar handedness inversions were recently reported in cholesteric systems of colloidal hard helices (Section 3.4.2), in which crossovers from left- to right-handedness could be observed upon slight variations of mesogen shape and concentration [94, 96]. A more natural geometric parametrisation for such particles is generally given in terms of their helical pitch p and radius r, related to the microscopic thread angle ν through

$$\nu(r,p) = \arctan\frac{p}{2\pi r}. \tag{4.12}$$

In this case, it was reported in Ref. [94] that helices with $\nu \gtrsim 40°$ preferentially form cholesteric phases with opposite handedness to that of the particles, while lower values of ν gradually stabilise phases of the same handedness. These trends were independently confirmed by the more extensive numerical analysis of Ref. [96], which further uncovered a fine dependence of the crossover region on particle aspect ratio and location in the (r,p) parameter plane. It was thus found that helices with large radii r generally undergo a handedness inversion for thread angles $\nu(r,p) \in [40°, 60°]$, while their shallower-grooved counterparts may exhibit a crossover for values of ν as large as 80° [96] (Figure 4.10).

This qualitative trend seemingly mirrors the shift of the handedness inversion range to higher values of ν observed in Figure 4.8 for HTCs with $\chi = 1$, associated with smaller groove depths. However, the focus of Refs. [94] and [96] on particles with much shorter aspect ratios than considered here precludes the further quantitative comparison of our results with the cholesteric behavior of hard helices. It should nonetheless be noted that the shortest cholesteric pitches observed here, amounting to roughly 1000 particle diameters, are about one order of magnitude larger than those reported in these previous studies, and are comparatively closer to the typical values observed in experimental cholesteric systems [227]. These tighter pitches may be typically obtained for $\nu \sim 65°$ in the case of hard helices and $\nu \in [70°, 80°]$ for HTCs, highlighting the complex relationship between particle twist and phase chirality in both systems.

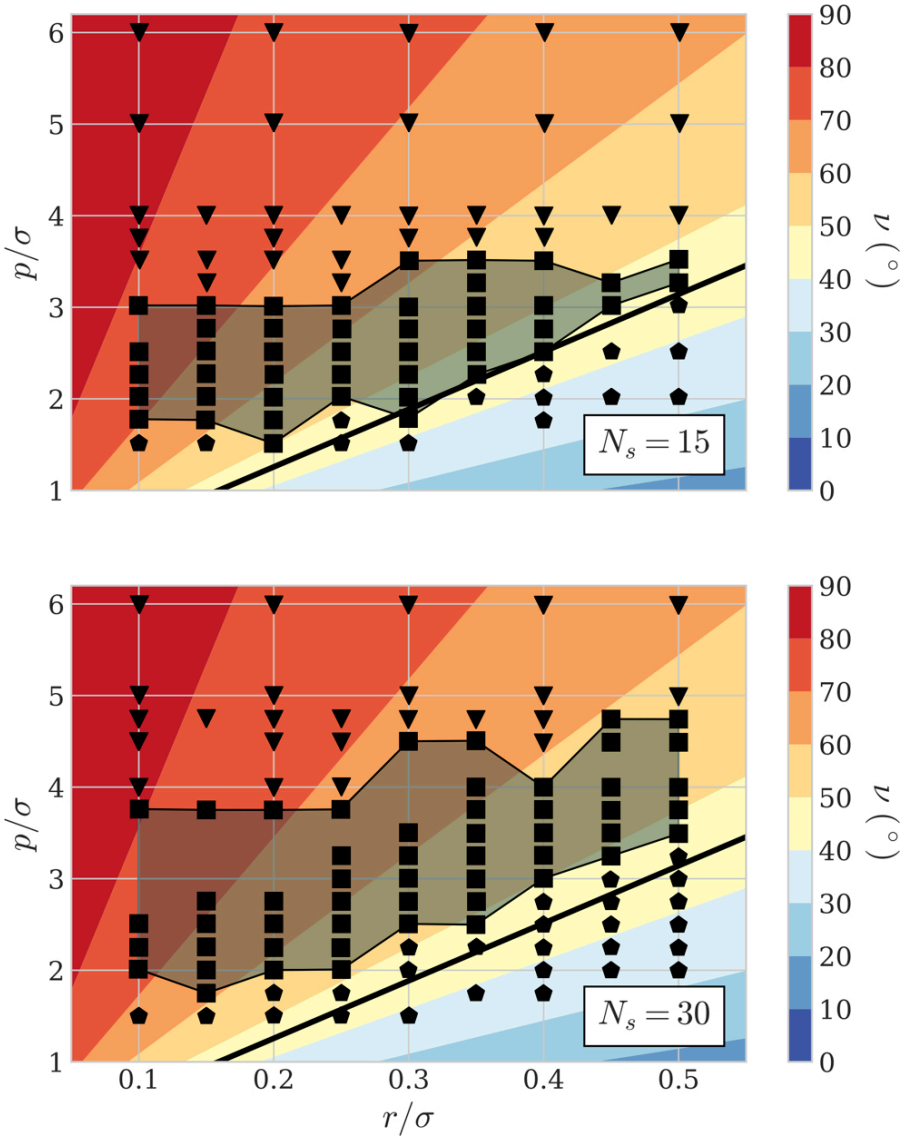

Figure 4.10: Radius-pitch state diagram for hard helices with $l = 10\,\sigma$, $N_s = 15$ (top) and $l = 20\,\sigma$, $N_s = 30$ (bottom). Colours delimit contour lines of constant thread angle ν (Eq. (4.12)), with black solid lines marking the phenomenological threshold value $\nu = 45°$. Symbols are obtained from Ref. [96], with solid pentagons, triangles and squares respectively denoting stable phases with right, left and mixed handedness upon particle density variations.

Finally, it is worth remarking that although the qualitative shape of the different curves at given angle ν does not differ much with varying χ, the pitch of the corresponding phases tends to significantly tighten with increasing cross-section anisotropy. While this effect seemingly concurs with the numerical results of Section 3.4.2 on twisted HTPs, we recall that the assumption of local phase uniaxiality underlying Eqs. (3.31) and (3.32) precludes the treatment of potential long-ranged biaxial correlations in our current framework, and may thus become increasingly inadequate for higher values of χ [112]. This basic symmetry constraint may therefore lead to growing inaccuracies in the description of the corresponding equilibrium cholesteric properties, as discussed in Chapter 3. The relaxation of local cylindrical invariance would allow for a direct investigation of these considerations, and may lead to a more realistic representation of phase structure in these cases.

4.3 Conclusion

In this chapter, we have introduced in detail a novel numerical virial integration scheme for highly anisotropic particles with arbitrarily complex molecular structures. Its implementation within the efficient density-functional framework of Chapters 2 and 3 enables us to probe the cholesteric behaviour of twisted cuboidal mesogens with high surface resolutions, and to provide a quantitative assessment of the intricate link between microscopic twist and cholesteric assembly in the case of hard particles with continuous threads. We thus report that deep-grooved systems undergo a handedness inversion for thread angles in the vicinity of the previously-proposed phenomenological value $\nu = 45°$, while the behaviour of their shallower counterparts depends on the fine details of their surface representation. The relationship between helical twisting power and particle structure is found to be non-trivial in both cases, and may be qualitatively explained in terms of subtle angular variations of the chiral component of their mutual excluded volumes.

The performance of our hierarchy-based approach for the determination of their hard overlaps is shown to be several orders of magnitude faster than traditional cell lists, and nearly three times as fast as dedicated collision detection libraries

in the case of twisted cuboids with high aspect ratios. Even though the polygon mesh support of the latter admittedly provides for a more natural description of such hard faceted particles, the strength of our method lies in its applicability to a much wider variety of finite-ranged force fields and its simple generalisability to poly-molecular systems and multiple interaction potentials — e.g. by constructing one BVH per particle and interaction type [202].

While we have here largely focused on the applications of BVHs to the direct determination of non-bonded energy terms, we note that the procedure described in Section 4.1 may also be more broadly applied to the computation of Verlet lists by introducing a finite Verlet skin as an additional BVH padding parameter [68]. The superior geometric tightness of such object decomposition methods greatly reduces the number of spurious distance calculations ensuing from the use of standard cell lists, which constitute one of the recurrent computational bottlenecks of molecular simulations, and could thus provide sizeable performance gains for the determination of neighbour lists in a number of contexts [73, 207, 208].

However, the top-down construction scheme adopted in Section 4.1.1 may in that case not be ideally suited to modern computing architectures, owing to the limited parallelism of its root-based tree initialisation process. These considerations are largely irrelevant for the virial-type calculations considered here, which are rather parallelised at the level of the MC integrator to process multiple configurations concurrently, but may entail the use of more involved bottom-up algorithms to efficiently build BVHs in the framework of general-purpose molecular simulations [73, 202].

The combined use of BVHs and DFT thus opens up a performant route to investigate the nematic and cholesteric behaviour of vast range of particle models in the experimentally-relevant regime of high mesogen anisotropy and weak phase chirality. The implementation of optimised methods for the evaluation of generalised virial integrals enables us to tackle molecular descriptions with a considerably-higher degree of complexity than previously accessible to existing numerical and analytical approaches [92–96]. For instance, the current framework will be shown in Chapter 6

to be capable of addressing the cholesteric assembly of DNA origamis comprised of ∼15 000 nucleotides [221], using a realistic mechanical model that explicitly represents each individual nucleotide within the origami structure.

5

Introducing particle flexibility in a DFT description of LCLCs

Contents

In the previous chapters, we have so far largely focused on systems of infinitely rigid particles, which may be characterised in terms of their sole centre-of-mass position $\mathbf{r}$ and molecular orientation $\mathcal{R}$. Real polymers, however, generally display a finite flexibility arising from the limited stiffness of their internal chemical bonds, which may lead to substantial deviations from their molecular ground state in typical experimental conditions. In this case, the density function ρ_m describing their microscopic state necessarily depends on the full internal degrees of freedom parametrising the conformations of each constituent molecule, which renders the

derivation of the free energy functional $\mathscr{F}[\rho_m]$ a complex many-body problem even at the second-virial level [229,230]. Considerable efforts have thus been devoted to the generalisation of classical DFT to polyatomic systems of finite rigidity based on various coarse-grained polymer representations and simplified derivations of the corresponding conformational free energy, which provides an additional contribution to the thermodynamical treatment of their phase-ordering transitions [231–245].

The approximate nature of such approaches therefore generally requires their careful preliminary assessment against the results of molecular simulations in order to probe the quantitative effects of their potential shortcomings, independently from the inevitable ambiguities of direct comparisons with experimental results [246]. However, most current formulations of DFT generally rely on a number of system-specific analytical assumptions and numerical approximations, which do not allow for the straightforward application of theory and simulations to identical particle models. Furthermore, theoretical investigations of the nematic behaviour of semi-flexible chains have so far almost exclusively focused on their uniaxial organisation, while the LC phases formed by many biopolymers are commonly observed to rather display a chiral cholesteric arrangement, reflecting the detailed symmetries of their local molecular structures [37].

In this chapter, we describe an efficient implementation of DFT that may be conveniently applied to a wide variety of flexible particle models, taking into account the full details of their microscopic Hamiltonian description. In this hybrid approach, conformational statistics may be introduced through the use of molecular trajectories obtained from direct simulations, thus allowing for a rigorous comparison of theoretical predictions with simulation results. A particular advantage of the method is that it is easily generalisable to Straley's description of the cholesteric phase, and is suitable for the treatment of arbitrary polymer systems with various degrees of molecular complexity.

The structure of the chapter is organised as follows. We first summarise in Section 5.1 the main attempts at the inclusion of particle flexibility in the context of DFT, with a particular emphasis on the physical assumptions underlying the

different theories, and outline the details of our chosen approach and numerical implementation. We then dedicate Section 5.2 to the extensive comparison of our results with molecular simulations of the nematic assembly of coarse-grained semi-flexible chains, and present in Section 5.3 the application of our method to the cholesteric organisation of near-persistence-length DNA duplexes. Finally, we recapitulate in Section 5.4 the main conclusions of these analyses, and highlight some potential directions for future research.

5.1 Classical DFT for polyatomic molecules

5.1.1 The Khokhlov-Semenov approach

The earliest analytical efforts to tackle the effects of conformational statistics on phase ordering can be traced back to the seminal work of Flory [247], based on a discretised lattice representation of polymer solutions with limited degrees of freedom. However, the many approximations underlying such a basic description have largely restricted its applicability to purely qualitative studies in the context of the I/N phase transition [248]. A more sophisticated treatment was subsequently introduced by Khokhlov and Semenov [231–233], and further developed by several authors [235–239], who combined various extensions of the original Onsager excess free energy (Eq. (2.61)) in the limit of hard rigid cylinders with a mean-field description of several flexible chain models [234]. In this framework, internal particle mechanics thus enter the Helmholtz free energy $\mathscr{F}$ purely through the inclusion of a flexibility-dependent orientational entropy term in $\mathscr{F}_{\mathrm{id}}$ (Eq. (2.60)). The resulting expression for $\mathscr{F}$ in the case of continuous worm-like chains may then be minimised through a self-consistent numerical procedure to determine the contour-dependent equilibrium ODF $\psi_{\mathrm{eq}}(s, \mathbf{t})$, quantifying the probability of finding a curvilinear segment $s \in [0, l_c]$ of the chains with fixed contour length l_c pointing in direction $\mathbf{t}$ [239].

Despite its theoretical elegance and reported successes in the description of the uniaxial nematic properties of fairly-stiff and elongated experimental systems [104], a significant shortcoming of this approach lies in its strongly coarse-grained nature.

Indeed, the Khokhlov-Semenov (KS) theory and its extensions effectively reduce the dependence of the phase behaviour of polymers with a given persistence length l_p to a handful of simplified flexibility mechanisms [249] combined with the two ratios l_c/l_p and l_p/d_{eff}, with d_{eff} a somewhat heuristic effective chain diameter subsuming their relevant molecular features [250]. Its generalisation to the treatment of cholesteric order is therefore not straightforward, as the accurate description of phase chirality requires a more detailed account of local microscopic structure [83, 87, 89–91], and has to our knowledge yet to be convincingly carried out beyond the limiting case of long polymer coils [84, 85, 251], for which $d_{\text{eff}} \ll l_p \ll l_c$.

5.1.2 The Fynewever-Yethiraj approach

A somewhat orthogonal treatment was proposed by Fynewever and Yethiraj [241], who conversely suggested that the effects of flexibility should be treated directly through the excess free energy contribution $\mathscr{F}_{\text{exc}}$, while retaining an Onsager-like expression for $\mathscr{F}_{\text{id}}$ (Eq. (2.60)). In this context, the virial integral Eq. (2.61) is instead averaged over a representative ensemble Ω of particle conformations as generated by molecular simulations, while the orientational entropy is simply determined by the chain-averaged ODF $\psi(\mathbf{u}\cdot\mathbf{n}_0)$ describing the molecular ordering of the polymer long axes $\mathbf{u}$ about the uniform director $\mathbf{n}_0$, as depicted in Figure 5.1.

An elegant derivation of this approach in the case of mono-disperse systems may be obtained starting from the microscopic density ρ_m, which generally depends on the discrete set of atom positions $\{\mathbf{r}_i\}_{i\geq 1}$ and bond orientations $\{\mathcal{R}_j\}_{j\geq 1}$ characterising the full microscopic state of each individual constituent particle. The centre-of-mass position $\mathbf{r}$ and molecular orientation $\mathcal{R}$ of a given particle in any conformation are uniquely determined by the specification of all internal degrees of freedom $\{\mathbf{r}_i\}$ and $\{\mathcal{R}_j\}$, so that one may write, without loss of generality,

$$\rho_m\Big(\{\mathbf{r}_i\},\{\mathcal{R}_j\}\Big) = \rho_m\Big(\mathbf{r},\mathcal{R},\{\mathcal{X}\}\Big),$$

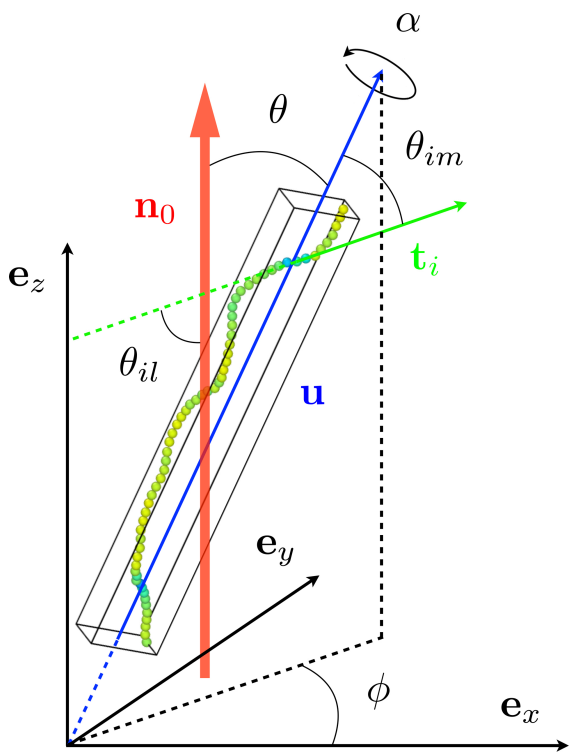

Figure 5.1: Particle long axis $\mathbf{u}$, local bond orientations $\mathbf{t}_i$ and nematic director $\mathbf{n}_0$ for an arbitrary conformation of the coarse-grained persistent chain model described in Ref. [246]. The laboratory frame $\mathcal{R}_{\text{lab}} \equiv [\mathbf{e}_x\ \mathbf{e}_y\ \mathbf{e}_z]$ is chosen such that $\mathbf{e}_z \equiv \mathbf{n}_0$. The black bounding box denotes the eigenvectors of the molecular gyration tensor $\mathcal{G}$ as determined by the numerical procedure of Section 4.1.1, and defines the molecular frame $\mathcal{R}$.

with $\{\mathcal{X}\} \equiv \Big(\{\mathbf{r}_i\}_{i\geq 2}, \{\mathcal{R}_j\}_{j\geq 2}\Big)$. Let $\mathbf{r}'_i$ and $\mathcal{R}'_j$ be the respective projections of $\mathbf{r}_i$ and $\mathcal{R}_j$ in the molecular frame $\mathcal{R}$ centred on $\mathbf{r}$,

$$\mathbf{r}'_i \equiv \mathcal{R}^{\mathsf{T}} \cdot (\mathbf{r}_i - \mathbf{r}), \tag{5.1}$$

$$\mathcal{R}'_j \equiv \mathcal{R}^{\mathsf{T}} \cdot \mathcal{R}_j, \tag{5.2}$$

with $\mathcal{R}^{\mathsf{T}}$ the matrix transpose of $\mathcal{R}$. The Fynewever-Yethiraj (FY) approximation postulates that ρ_m may be cast in the decoupled form [252, 253]

$$\rho_m\Big(\mathbf{r}, \mathcal{R}, \{\mathcal{X}\}\Big) \simeq \rho(\mathbf{r}, \mathcal{R}) \times \Pi\Big(\{\mathcal{X}'\}\Big), \tag{5.3}$$

where $\{\mathcal{X}'\} \equiv \Big(\{\mathbf{r}'_i\}_{i\geq 2}, \{\mathcal{R}'_j\}_{j\geq 2}\Big)$. In Eq. (5.3), ρ corresponds to the *molecular density* describing the global distribution of particle centres of mass $\mathbf{r}$ and orientations $\mathcal{R}$ throughout the sample, while Π quantifies the distribution of the conformational degrees of freedom $\mathbf{r}'_i$ and $\mathcal{R}'_j$ in the local molecular frame, subject to the respective

normalisation constraints [252]

$$\int d\{\mathcal{X}'\}\,\Pi\Big(\{\mathcal{X}'\}\Big) = 1, \tag{5.4}$$

$$\int_V d\mathbf{r} \oint d\mathcal{R}\,\rho(\mathbf{r},\mathcal{R}) = N. \tag{5.5}$$

In the FY theory, Π is assumed to be entirely determined by the intra-molecular interaction potential $U_{\rm int} = U_{\rm int}\Big(\{\mathcal{X}'\}\Big)$, so as to be independent of the overall position $\mathbf{r}$ and orientation $\mathcal{R}$ of the molecule. In the absence of external fields, this approximation amounts to neglecting the effects of many-particle interactions on conformational statistics, as discussed below.

Discarding the effects of extra-molecular interactions, the ideal component $\mathscr{F}_{\rm id}$ of the Helmholtz free energy functional is given by a straightforward generalisation of Eq. (2.17) [242, 252],

$$\beta\mathscr{F}_{\rm id}[\rho_m] = \int_V d\mathbf{r} \oint d\mathcal{R} \int d\{\mathcal{X}\}\,\rho_m\Big(\mathbf{r},\mathcal{R},\{\mathcal{X}\}\Big) \times \Big\{\log\Big[\rho_m\Big(\mathbf{r},\mathcal{R},\{\mathcal{X}\}\Big)\lambda_{\rm th}^3\Big] - 1 + \beta U_{\rm int}\Big(\{\mathcal{X}\}\Big)\Big\},$$

with $\lambda_{\rm th}$ an irrelevant thermal wavelength. Using Eqs. (5.3)–(5.5),

$$\beta\mathscr{F}_{\rm id}[\rho] = \int_V d\mathbf{r} \oint d\mathcal{R}\,\rho(\mathbf{r},\mathcal{R})\Big\{\log\Big[\rho(\mathbf{r},\mathcal{R})\lambda_{\rm FY}^3\Big] - 1\Big\}, \tag{5.6}$$

where the length-scale $\lambda_{\rm FY}$ now reads as

$$\lambda_{\rm FY} = \lambda_{\rm th}\exp\left\{\frac{1}{3}\int d\{\mathcal{X}'\}\,\Pi\Big(\{\mathcal{X}'\}\Big) \times \Big[\log\Pi\Big(\{\mathcal{X}'\}\Big) + \beta U_{\rm int}\Big(\{\mathcal{X}'\}\Big)\Big]\right\},$$

in which we used the change of variables of Eqs. (5.1) and (5.2), with unit Jacobian determinant. Note that $\lambda_{\rm FY}$ generally depends on intra-molecular properties as well as temperature, but is independent of density, so that the functional dependence of Eq. (5.6) on ρ is identical to that of Eq. (2.17).

In the limit of vanishing polymer concentrations, the excess free energy may be similarly expressed as a direct generalisation of the Onsager second-virial functional (Eq. (2.40)) [242],

$$\beta\mathscr{F}_{\rm ex}[\rho_m] = -\frac{1}{2}\iint d\mathbf{1}d\mathbf{2}\,\rho_m(\mathbf{1})\rho_m(\mathbf{2})f(\mathbf{1},\mathbf{2}), \tag{5.7}$$

where the shorthand $\mathbf{i} \equiv \big(\mathbf{r}_i, \mathcal{R}_i, \{\mathcal{X}_i\}\big)$ refers to the full microscopic degrees of freedom of particle i, and f is the Mayer function relative to the extra-molecular interaction energy U_{ext} of particles 1 and 2,

$$f(\mathbf{1},\mathbf{2}) \equiv \exp\Big\{-\beta U_{\text{ext}}(\mathbf{1},\mathbf{2})\Big\} - 1.$$

Using Eq. (5.3), Eq. (5.7) may be recast as [252]

$$\beta\mathscr{F}_{\text{ex}}[\rho] \;=\; -\frac{1}{2}\iint_V d\mathbf{r}_1 d\mathbf{r}_2 \oiint d\mathcal{R}_1 d\mathcal{R}_2\, \rho(\mathbf{r}_1,\mathcal{R}_1)\rho(\mathbf{r}_2,\mathcal{R}_2)\overline{f}(\mathbf{r}_1,\mathbf{r}_2,\mathcal{R}_1,\mathcal{R}_2), \quad (5.8)$$

with $\overline{f}$ the *conformational average* of the f-function,

$$\overline{f}(\mathbf{r}_1,\mathbf{r}_2,\mathcal{R}_1,\mathcal{R}_2) \equiv \iint d\{\mathcal{X}_1'\}d\{\mathcal{X}_2'\}\,\Pi\Big(\{\mathcal{X}_1'\}\Big)\Pi\Big(\{\mathcal{X}_2'\}\Big) f(\mathbf{1},\mathbf{2}). \quad (5.9)$$

In the case of a prolate uniaxial nematic phase of uniform director $\mathbf{n}_0$, the density ansätze of Eqs. (2.57) and (2.58), combined with the discussions of Section 2.2.2, immediately lead to the equilibrium ODF ψ_{eq} as a generalised form of Eq. (2.72),

$$\psi_{\text{eq}}(\cos\theta) = \frac{e^{\beta\mu_\rho}}{\rho\lambda_{\text{FY}}^3}\exp\left\{\frac{\rho G_{\text{ref}}(\eta_{\text{ref}})}{4\pi^2}\int_0^\pi \sin\theta' d\theta'\,\psi_{\text{eq}}(\cos\theta')\overline{\kappa}(\theta,\theta')\right\}, \quad (5.10)$$

with $\overline{\kappa}$ the conformational average of the excluded volume kernel (Eq. (2.73)),

$$\overline{\kappa}(\theta,\theta') = \int_V d\mathbf{r}\iint_0^{2\pi} d\alpha d\alpha' \iint_0^{2\pi} d\phi d\phi'\,\overline{f}(\mathbf{r},\mathcal{R},\mathcal{R}'). \quad (5.11)$$

In this framework, the contributions of conformational statistics to the Helmholtz free energy $\mathscr{F}$ are therefore effectively relegated to the kernel $\overline{\kappa}$, which may be evaluated numerically following the procedure detailed in Section 5.1.3, and thus circumvents the analytical difficulties involved in the explicit functional derivation of $\mathscr{F}$ for non-uniform, flexible polyatomic systems [229]. Its results have been found to compare favourably with direct numerical simulations of various athermal solutions of semi-flexible chains, with quantitative agreement being reported in a number of cases [241, 252–254]. Furthermore, its relatively simple mathematical formulation is largely independent of the specific features of the molecular system studied, and allows for its straightforward application to a wide range of mesogen models.

This hybrid approach, however, is quite numerically expensive, and suffers from two significant drawbacks inherent to the use of the decoupled ansatz in Eq. (5.3). The first lies in its coarse-grained representation of orientational order at the level of the molecular long axes $\mathbf{u}$, as opposed to the more detailed description of local inter-chain correlations between neighbouring monomers through a contour-dependent ODF of the KS-based theories. The second stems from the assumed independence of the conformational distribution Π from the molecular density field ρ, which amounts to neglecting the influence of the variations of the surrounding nematic field on the accessible particle conformational space. In the original FY paper, Π was therefore chosen to describe the conformations of a single chain fluctuating in free space — an assumption we refer to as the *unconfined-chain approximation* (UCA) in the rest of this chapter.

In order to shed some light on the respective effects of these approximations, and their potential consequences on the capability of DFT to describe realistic polymeric systems, we now outline a generic practical implementation of the FY theory applicable to arbitrary flexible particle models.

5.1.3 Numerical procedure

The numerical procedure of Section 3.3.1 may be readily extended to the FY treatment of non-rigid particles as follows.

1. Given an arbitrary polyatomic particle model described by a potential U_{tot} comprising both intra- and extra-molecular interaction forces,

$$U_{\text{tot}} = U_{\text{int}} + U_{\text{ext}},$$

we sample the conformational distribution Π numerically by constructing an ensemble $\Omega = \Omega[U_{\text{int}}]$ of uncorrelated particle conformations by means of a single-chain molecular dynamics (MD) or Monte-Carlo (MC) simulation in the canonical ensemble at fixed temperature T.

2. Using Eqs. (5.9) and (5.11), the conformationally-averaged kernel $\overline{\kappa} = \overline{\kappa}_\Omega$ may then be computed through

$$\overline{\kappa}_\Omega(\theta_1, \theta_2) = \Big\langle \Big\langle \kappa_{\mathcal{C}_1\mathcal{C}_2}(\theta_1, \theta_2) \Big\rangle_\Omega \Big\rangle_\Omega, \tag{5.12}$$

where $\kappa_{\mathcal{C}_1\mathcal{C}_2}$ denotes the excluded volume kernel relative to a given pair of conformations $(\mathcal{C}_1, \mathcal{C}_2) \in \Omega^2$, and $\langle\cdot\rangle_\Omega$ is the conformational average over the ensemble Ω. As in Section 3.3.1, we evaluate Eq. (5.12) by MC sampling, in which every MC step amounts to drawing a random pair of conformations $(\mathcal{C}_1, \mathcal{C}_2)$ from Ω, applying random rigid-body rotations $\mathcal{R}_1$, $\mathcal{R}_2$ and relative translation $\mathbf{r}_{12}$ to each respective conformation, and computing the extra-molecular interaction energy U_{ext} of the obtained configuration.

3. We finally plug the kernel $\overline{\kappa}_\Omega$ into Eq. (5.10), which may be solved iteratively [164] to determine the equilibrium ODF ψ_{eq} at given ρ and T.

In the context of Chapter 4, the extra-molecular energy evaluations at step (2) may be efficiently performed by building a forest of bounding hierarchies, in which a single tree of bounding structures is constructed for every molecular conformation $\mathcal{C} \in \Omega$, and by applying the traversal routines of Section 4.1.2 to a random pair of trees at every MC integration step.

Finally, in the case where the equilibrium phase of the chosen particle model is expected to be cholesteric, rather than uniaxially-symmetric, one may further complement these three steps with the computation of the computation of the associated OF twist elastic modulus K_2 and chiral strength k_t. The application of the considerations of Section 3.2.2 to the FY excess free energy (Eq. (5.8)) immediately yields microscopic expressions for k_t and K_2 as direct generalisations of the PS equations (Eqs. (3.31), (3.32) and (2.69)),

$$\beta k_t(\rho, T) = -\frac{G_{\text{ref}}(\eta_{\text{ref}})\rho^2}{2} \int_V d\mathbf{r}_{12} \iint d\mathcal{R}_1 d\mathcal{R}_2\, \overline{f}(\mathbf{r}_{12}, \mathcal{R}_1, \mathcal{R}_2) \times r_x u_{2y} \times \psi_{\text{eq}}(\cos\theta_1)\dot{\psi}_{\text{eq}}(\cos\theta_2), \tag{5.13}$$

$$\beta K_2(\rho, T) = \frac{G_{\text{ref}}(\eta_{\text{ref}})\rho^2}{2} \int_V d\mathbf{r}_{12} \iint d\mathcal{R}_1 d\mathcal{R}_2\, \overline{f}(\mathbf{r}_{12}, \mathcal{R}_1, \mathcal{R}_2) \times r_x^2 u_{1y} u_{2y} \times \dot{\psi}_{\text{eq}}(\cos\theta_1)\dot{\psi}_{\text{eq}}(\cos\theta_2), \tag{5.14}$$

which may be readily evaluated following the numerical procedure of step (2).

An important prerequisite to the methods above lies in the determination of the long axes $\mathbf{u}$ of the different molecular conformations, with respect to which we choose to quantify orientational nematic order. Several definitions for such axes have been proposed in the literature in the case of arbitrary-shaped particles, based on the spectral decomposition of the molecular polarisability [213, 255], inertia [213, 256] and gyration tensors [257, 258]. As in Chapter 4, we here elect to make use of the latter definition, as we feel the purely-geometric character of the gyration tensor $\mathcal{G}$ (Eq. (4.2)) to be most consistent with the framework of our equilibrium DFT description, for which molecular electronic and inertial properties are largely irrelevant.

The combined use of the UCA at step (1) with the optimised virial integration methods of Chapter 4 for the evaluation of Eqs. (5.12)–(5.14) enables us to greatly reduce the overall computational expense of the procedure, and thus allows us to tackle flexible mesogen models of arbitrary complexity. We now dedicate the next two sections of this chapter to the detailed assessment of its results in systems of both chiral and achiral molecules with various levels of molecular resolution.

5.2 The nematic ordering of coarse-grained polymers

5.2.1 The Kremer-Grest bead-spring chain model

A particularly suitable generic model system for such a quantitative investigation may be provided by the so-called Kremer-Grest (KG) bead-spring chain [259, 260], which constitutes a practical discretised realisation of the original worm-like chain model [261, 262] including the effects of both excluded volume and bond flexibility. The bulk properties of their I/N transition were recently investigated in considerable detail by Egorov *et al.* [246] (Figure 5.2), who combined extensive MD simulations with a simplified implementation of the FY DFT approach to perform a comprehensive mapping of their phase diagram for a wide range of contour lengths, persistence lengths and particle concentrations. The comparison

of simulation results with existing theoretical predictions further confirmed that the FY approach consistently outperforms other formulations of DFT in terms of overall agreement with the MD data, despite increasing discrepancies being reported for all theories in the case of highly-flexible chains [246].

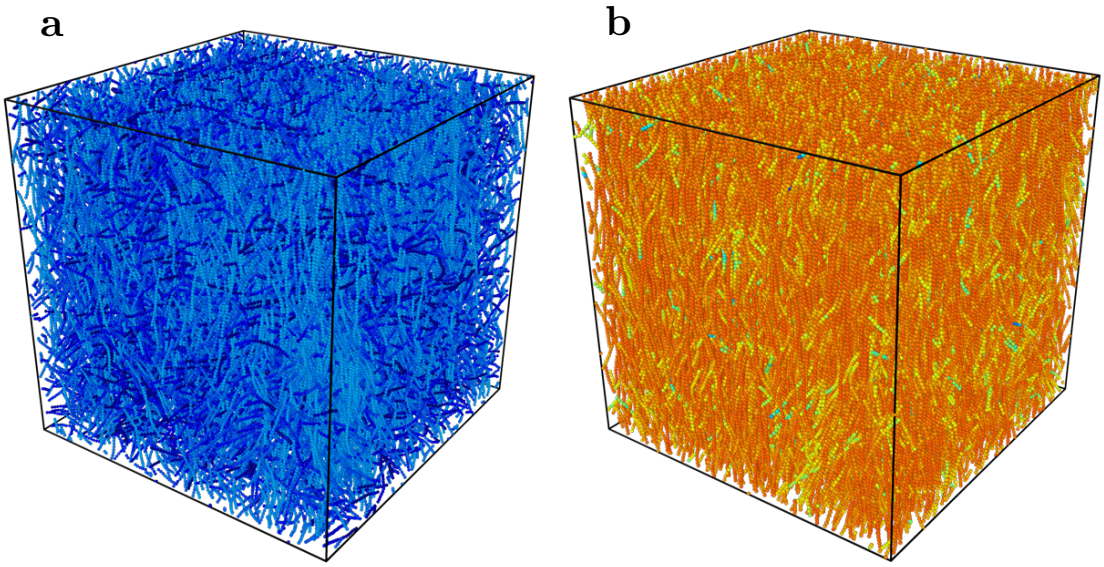

Figure 5.2: I/N ordering of flexible KG chains with persistence length $l_p = 128\,l_b$ and $N_m = 64$ monomers per chain. Simulation data provided by courtesy of A. Milchev (Ref. [246]). a) Snapshot of an equilibrated NVT-MD simulation of $N = 3000$ KG chains taken at volume fraction $\eta = 6.27\,\%$. Particles are coloured according to the projection of each bond vector on the nematic director $\mathbf{n}_0$ rescaled by the bond order parameter S_b, obtained from the KS tensor $\mathcal{Q}_b$ (Eq. (5.21)). b) Same as a) at $\eta = 10.46\,\%$.

In that study, as in previous applications of the FY theory [241, 254], much emphasis was put on the effects of the PL approximation on the accuracy of the DFT predictions, and several forms of the rescaling prefactor G_{ref} were investigated — though no single expression was conclusively found to yield the best results systematically. Such discussions are undoubtedly highly relevant, especially in the context of the shortcomings of the PL rescaling for systems of non-convex particles (c.f. Section 3.3.2). However, we here wish to primarily address the much-less

documented effects of the coarse-grained description of orientational order and of the UCA, as discussed in Section 5.1.2, and thus restrict our focus to the regime of fairly-stiff chains with high aspect ratios, for which the PL approximation is expected to work reasonably well, throughout the rest of this section.

In the implementation of the KG model proposed in Ref. [246], polymers are represented as chains of beads interacting through a repulsive Weeks-Chandler-Andersen (WCA) potential,

$$u_{ij}^{\mathrm{WCA}}(r_{i,j}) = \begin{cases} 4\epsilon\left[\left(\dfrac{\sigma}{r_{i,j}}\right)^{12} - \left(\dfrac{\sigma}{r_{i,j}}\right)^{6} + \dfrac{1}{4}\right] & \text{if } r_{i,j} < r_c \\ 0 & \text{if } r_{i,j} \geq r_c \end{cases},$$

where σ and ϵ define the respective model units of length and energy, $r_c \equiv 2^{1/6}\sigma$ and $r_{i,j} \equiv \|\mathbf{r}_j - \mathbf{r}_i\|$ denotes the separation distance between any two distinct monomers i and j. Particle flexibility is then governed by a simplified bond-bending potential of the form [263]

$$u_i^{\mathrm{bend}}(\theta_i) = \epsilon_b(1 - \cos\theta_i), \tag{5.15}$$

with ϵ_b a bending stiffness parameter and $\theta_i \equiv \arccos(\mathbf{t}_{i-1}\cdot\mathbf{t}_i)$ the angle formed by the two bonds linking the consecutive pairs of monomers indexed by $(i-1, i)$ and $(i, i+1)$, respectively (c.f. Figure 5.1). The equilibrium bond length $l_b \simeq 0.97\,\sigma$ separating two adjacent monomers finally results from the competition between WCA repulsion and an additional freely-extensible nonlinear elastic bonded potential u_i^{FENE} [259,260],

$$u_i^{\mathrm{FENE}}(r_{i,i+1}) = \begin{cases} -0.5k_0r_0^2 \times \log\left\{1 - \left(\dfrac{r_{i,i+1}}{r_0}\right)^2\right\} & \text{if } r_{i,i+1} < r_0 \\ 0 & \text{if } r_{i,i+1} \geq r_0 \end{cases},$$

with $r_0 = 1.5\,\sigma$ and $k_0 = 30\,\epsilon/\sigma^2$ [246]. The persistence length l_p of the chains is then fully determined by ϵ_b, while their contour length l_c is simply related to the number N_m of monomers per chain through $l_c \simeq (N_m - 1)l_b$.

In the framework of Section 5.1.2, the Mayer f-function relative to the pair interaction energy of two arbitrary molecules described by the respective conformations $(\mathcal{C}_1, \mathcal{C}_2) \in \Omega^2$ then reads as

$$f_{\mathcal{C}_1\mathcal{C}_2}(\mathbf{r}_{12}, \mathcal{R}_1, \mathcal{R}_2) = \exp\left(-\beta \sum_{i\in\mathcal{C}_1}\sum_{j\in\mathcal{C}_2} u_{ij}^{\mathrm{WCA}}\right) - 1,$$

where the double sum runs over all pairs of monomers $i \in \mathcal{C}_1$ and $j \in \mathcal{C}_2$, and implicitly depends on the centre-of-mass separation vector $\mathbf{r}_{12}$ and orientations $\mathcal{R}_1$, $\mathcal{R}_2$ of the two chains. Following the procedure of Section 5.1.3, this quantity may then readily be integrated over the two-particle configurational space and conformationally-averaged over the ensemble Ω, where Ω has been preliminarily determined by molecular simulations using a given set of parameters for the above potentials. In the following, we choose the model unit of energy such that $\beta\epsilon = 1$, and parameterise the Hamiltonian in terms of the chain persistence length $l_p \simeq \beta\epsilon_b l_b$ [263]. We further assume the molecular volume fraction η to be such that

$$\eta = \eta_{\text{ref}} = \rho v, \tag{5.16}$$

where we approximate the molecular volume v by that of a linear chain of fused hard spheres with radius σ and separation distance l_b [182]. Note that the latter assumption is somewhat arbitrary; however, these considerations are only relevant to the PL prefactor (Eq. (2.71)), whose effects on the I/N transition of the systems considered here are fairly limited, and are of little consequence in our case.

We here sample the particle conformational space through basic single-chain MC simulations, using random translational moves for individual beads combined with a simple Metropolis acceptance criterion. The maximum step size was adjusted over an equilibration run of 1×10^8 steps to yield an average acceptance rate of about 30% for a given set of l_c and l_p, starting from an initial linear conformation. Production runs of 2.5×10^9 steps were performed, and molecular trajectories were constructed by appending one chain snapshot every 1×10^6 iterations. The resulting set of 2500 uncorrelated conformations was then used to evaluate the conformationally-averaged kernel $\overline{\kappa}$ in the UCA for each chosen chain stiffness and contour length (Eq. (5.12)). This ensemble is henceforth referred to by Ω_0, where the subscript denotes the fact that the UCA represents the particle conformational space in the limit of vanishing polymer concentration.

5.2.2 FY and KS order parameters

We summarise in Figures 5.3 and 5.4 the comparison of our DFT results with the simulation and theory data of Ref. [246] for chains comprised of $N_m = 64$ monomers with $l_p/l_c \simeq 2$ and 1, respectively. We first remark rather generally that the predictions of our approach in the UCA for the I/N transition density appear to be in good agreement with simulations results in both cases, with the increased particle flexibility of the systems in Figure 5.4 deferring the I/N transition to significantly higher volume fractions. However, the further quantitative comparison of nematic properties as described by theory and simulation requires one to carefully distinguish between the different measures of orientational order underlying the FY and KS approaches. In the notation of Section 5.1, the dependence of the former's ODF $\psi_{\rm eq}^{\rm FY}$ on the particle long axes $\mathbf{u}$ allows for the quantification of nematic alignment about the uniform director $\mathbf{n}_0$ through the usual uniaxial order parameter S (c.f. Section 2.3.2),

$$S = 2\pi \oint d\mathbf{u}\, \frac{3(\mathbf{u}\cdot\mathbf{n}_0)^2 - 1}{2} \times \psi_{\rm eq}^{\rm FY}(\mathbf{u}\cdot\mathbf{n}_0), \tag{5.17}$$

while the contour-dependent ODF $\psi_{\rm eq}^{\rm KS}$ of the latter naturally leads to the definition of a generalised uniaxial order parameter S_b,

$$S_b = 2\pi \oint d\mathbf{t}\, \frac{3(\mathbf{t}\cdot\mathbf{n}_0)^2 - 1}{2} \times \left\langle \psi_{\rm eq}^{\rm KS} \right\rangle_c (\mathbf{t}\cdot\mathbf{n}_0), \tag{5.18}$$

with $\langle \psi_{\rm eq}^{\rm KS} \rangle_c$ the contour-averaged equilibrium ODF,

$$\left\langle \psi_{\rm eq}^{\rm KS} \right\rangle_c (\mathbf{t}\cdot\mathbf{n}_0) = \frac{1}{l_c} \int_0^{l_c} ds\, \psi_{\rm eq}^{\rm KS}(s, \mathbf{t}\cdot\mathbf{n}_0).$$

The two order parameters S and S_b therefore generally correspond to rather different physical quantities, as the contour-averaged ODF $\langle \psi_{\rm eq}^{\rm KS} \rangle_c$ appearing in Eq. (5.18) effectively incorporates the intra-molecular dispersion of the chain segment orientations $\mathbf{t}$, which is not directly accounted for by the coarser-grained $\psi_{\rm eq}^{\rm FY}$ of Eq. (5.17). It is proven in Appendix E that under the assumptions of the FY theory, the general relation between S and S_b may be derived in the compact form

$$S_b = S \times S_\Omega, \tag{5.19}$$

with S_Ω an intra-molecular order parameter describing the distribution of chain segments $\mathbf{t}$ about the long axes $\mathbf{u}$ of the polymers as characterised by an arbitrary conformational space Ω,

$$S_\Omega = \left\langle \left\langle \frac{3(\mathbf{t}\cdot\mathbf{u})^2 - 1}{2} \right\rangle_c \right\rangle_\Omega . \tag{5.20}$$

In the following, we assimilate the generic chain segment $\mathbf{t}(s)$ to the normalised bond vector $\mathbf{t}_i$ joining the monomers i and $i+1$ of a discrete KG chain, and thus refer to S and S_b as the *molecular* and *bond order parameters*, respectively.

Note that similarly to S, S_b may then be equivalently worked out from numerical simulations as the largest eigenvalue of the tensor $\mathcal{Q}^b$ [213],

$$\mathcal{Q}^b_{mn} = \left\langle \left\langle \frac{3t_m t_n - \delta_{mn}}{2} \right\rangle_c \right\rangle , \tag{5.21}$$

where $t_m(s) \equiv \mathbf{t}(s)\cdot\mathbf{e}_m$ for $m \in \{x, y, z\}$. The bond nematic director $\mathbf{n}_0^b$, obtained as the corresponding eigenvector of $\mathcal{Q}^b$, may thus *a priori* differ from the molecular director $\mathbf{n}_0$ associated with the largest eigenvalue S of the standard $\mathcal{Q}$ tensor (Eq. (2.87)). However, the relative difference in the coefficients of $\mathbf{n}_0^b$ and $\mathbf{n}_0$, as computed using the simulation data of Ref. [246], was found to be less than 1 % for all systems considered here, and we therefore make no distinction between molecular and bond nematic director in this chapter.

5.2.3 Conformational statistics and nematic assembly

The comparison of simulation results with DFT in the UCA in terms of S reveals that DFT tends to gradually underestimate the level of alignment in the nematic phase with increasing particle flexibilities, contrary to the findings of Ref. [264]. This discrepancy stems from the fact that the authors of that study actually compared the bond order parameter S_b calculated from simulations with the molecular order parameter S of the FY description. Our predicted values for S are however found to be virtually identical to the DFT data reported in Ref. [246], in which a simplified implementation of the FY theory was used based on an empirical expression for $\overline{\kappa}_{\Omega_0}$ reported in Ref. [241] for semi-flexible tangent hard-sphere chains. This

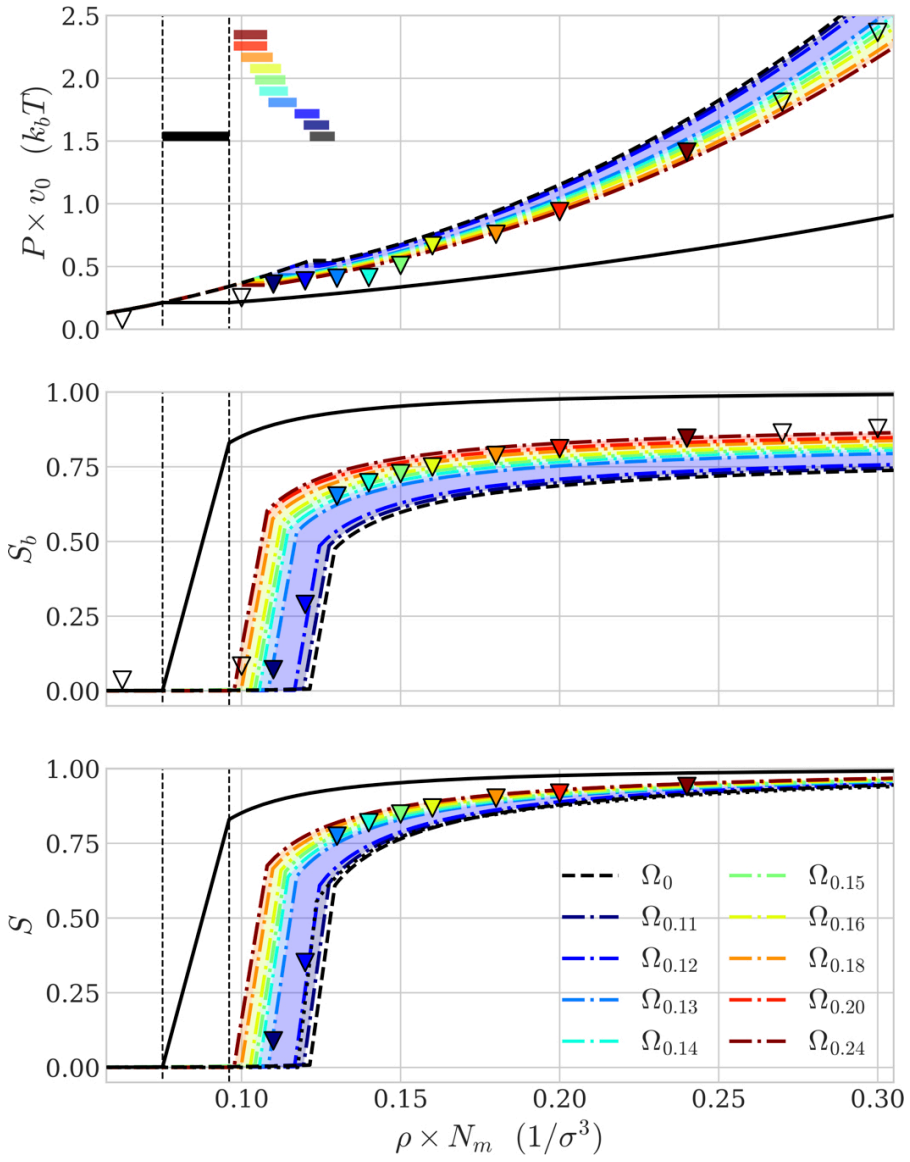

Figure 5.3: Osmotic pressure P, bond order parameter S_b and molecular order parameter S as a function of monomer number density $\rho \times N_m$ for KG chains with persistence length $l_p = 128\,l_b$ and $N_m = 64$ beads (contour length $l_c = 63\,l_b$). Markers denote the simulation results of Ref. [246], from which S and S_b were determined through standard means as the largest eigenvalues of the corresponding Q-tensors (see text). Black solid lines represent our DFT predictions for fully-rigid chains (Ω_∞). Black dashed lines correspond to our DFT results in the UCA (Ω_0), and the black dotted line denotes the DFT data of Ref. [246] (only for S). Dash-dotted lines were computed using the conformational space Ω_ρ obtained from the bulk simulations of Ref. [246] at various fixed densities ρ, as described in the text. The coloured stripes in the upper panel delimit the respective I/N coexistence ranges predicted by the FY theory using the different conformational spaces, in which order parameters were computed through a standard lever-rule interpolation between the isotropic and nematic binodal points.

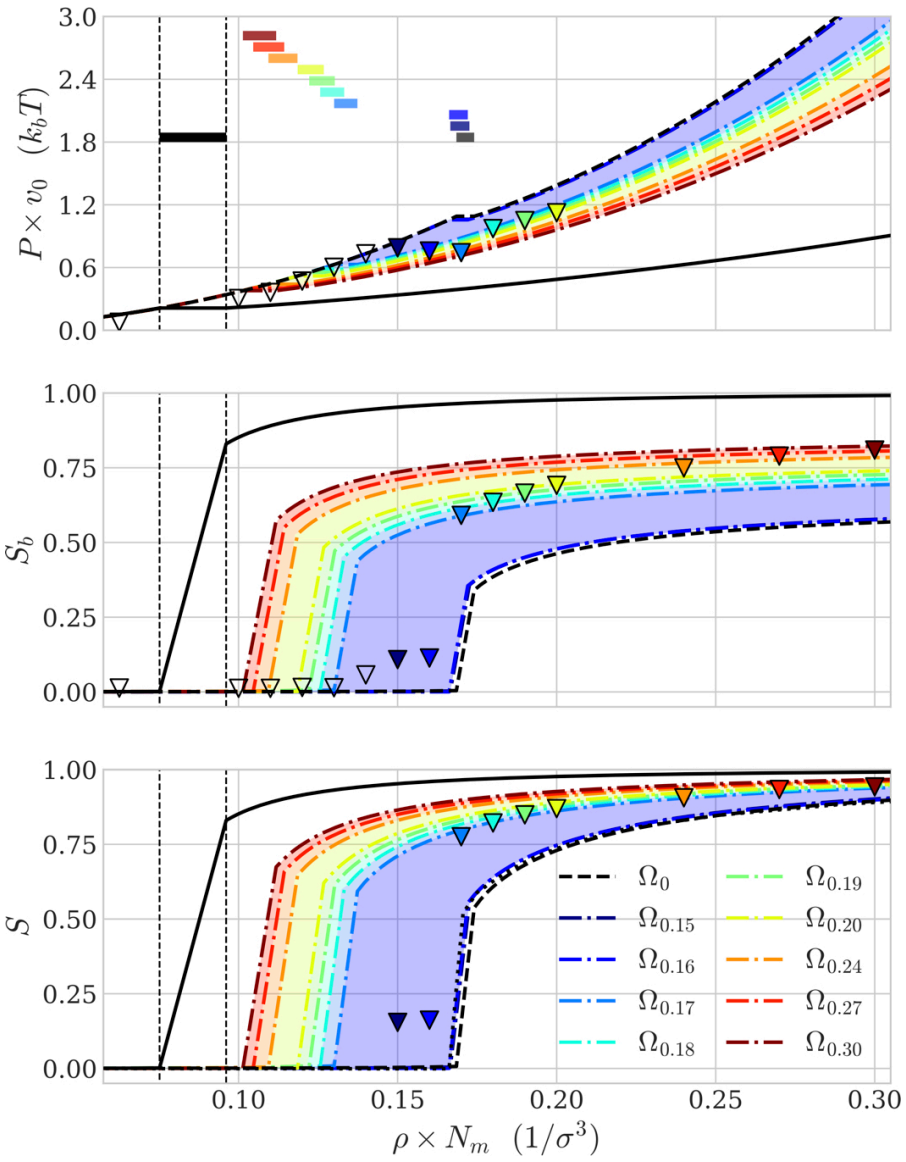

Figure 5.4: Same as in Figure 5.3 for chains with $l_p = 64\, l_b$.

observation demonstrates that the latter system provides a reliable approximation of the KG chains in this context.

The DFT underestimation of nematic order can be easily understood as a direct consequence of the UCA, which does not account for the potential stretching of the chains due to the surrounding nematic field, as the particles gradually forego conformational entropy to optimise their liquid-crystalline packing [235]. It was thus reported in Ref. [246] that while the root-mean-square end-to-end distance $L(\rho)$ generally remains roughly constant in the isotropic phase, the I/N transition

is usually associated with a rather steep jump in L followed by a slower increase towards the saturation value l_c, as the chains progressively straighten along the nematic director. Therefore, the UCA remains quantitatively accurate up to the I/N transition, but increasingly overestimates the effects of particle flexibility as one moves deeper into the nematic range — especially for chains with lower relative stiffnesses l_p/l_c, whose accessible conformations are most affected by these phase-induced restrictions [246].

The effects of this shortcoming of the FY theory may be probed by replacing the previous single-chain conformational space Ω_0 obtained in the limit of infinite dilution with an ensemble Ω_ρ of single-chain conformations obtained from bulk molecular simulations at fixed finite density ρ. We here use for Ω_ρ a set of 30 000 particle conformations obtained from the analysis of the simulation data of Ref. [246] at various monomer densities $\rho \times N_m$, as indicated in Figures 5.3 and 5.4. As expected from the previous discussion, we thus find the DFT results for Ω_ρ taken at simulation state points in the isotropic phase to be in very good agreement with those obtained using Ω_0 in the UCA, which indicates the absence of significant chain stretching prior to the I/N transition for the systems considered here.

While this observation confirms the suitability of the UCA to describe the free energy of the isotropic phase in our case, the use of Ω_0 in the nematic phase leads to an overestimation of the particle conformational entropy associated with an underestimation of their collective packing entropy, resulting in the observed underestimation of local nematic order. The partial compensation of these two effects in the total nematic free energy $\mathscr{F}$ may thus explain the ability of the UCA to correctly capture the rough location of the I/N transition zone, although its detailed predictions in terms of I/N coexistence densities should generally be interpreted with caution, as discussed in the next paragraph. Conversely, the use of simulated ensembles Ω_ρ obtained at nematic state points leads to increasing overestimations of chain stretching in the lower-density regions, and thus gradually pushes the I/N transition predicted by DFT to unrealistically-low concentrations for the more flexible particles.

Hence, it is apparent from Figures 5.3 and 5.4 that while the use of a given ensemble Ω_ρ generally enables DFT to correctly reproduce simulation results at that same density ρ, owing to the state-function character of the underlying free energy $\mathscr{F}$, no single representation of the particle conformational space may yield an accurate description of thermodynamic properties at all concentrations in the framework of the FY description. Such limitations are particularly stringent for the accurate computation of the I/N coexistence range due to the abrupt density variations of the conformational space in this region, illustrated for instance by the wide gap between the DFT predictions relative to the pre-transition $\Omega_{0.16}$ and the post-transition $\Omega_{0.17}$ in Figure 5.4. These effects need to be taken into account for the reliable resolution of the coupled phase-coexistence equations, and may explain the extremely-narrow width of the coexistence domains predicted by DFT in Figures 5.3 and 5.4, delimited by the plateaus in the osmotic pressure P. However, the lack of detailed I/N coexistence analysis in the simulations of Ref. [246] precludes the thorough quantitative investigation of these considerations, whose effects on the comparison of DFT results with experimental observations are further discussed in Section 5.3.

Finally, one may investigate the impact of the coarse-grained treatment of orientational order through the calculation of the DFT-predicted bond order parameters S_b from Eqs. (5.19) and (5.20). Comparison with simulations suggests that the underestimations of S_b using the UCA are more pronounced than for S, which could be partly attributed to the unsuitability of the FY molecular ODF to describe the local ordering of neighbouring chain segments in solution. However, the good quantitative agreement for S_b achieved at given density ρ through the use of Ω_ρ suggests that the main limiting factor may actually lie in the UCA itself. Indeed, it can be seen from Eq. (5.19) that

$$S_b \leq S_\Omega,$$

with the equality being attained in the limit of perfect crystalline order for the particle long axes. It is shown in Appendix E that in the case of stiff unconfined

chains ($l_p \gg l_c$), the intra-molecular order parameter S_{Ω_0} may be approximated as

$$S_{\Omega_0} \simeq 1 - \frac{5l_c}{6l_p}. \tag{5.22}$$

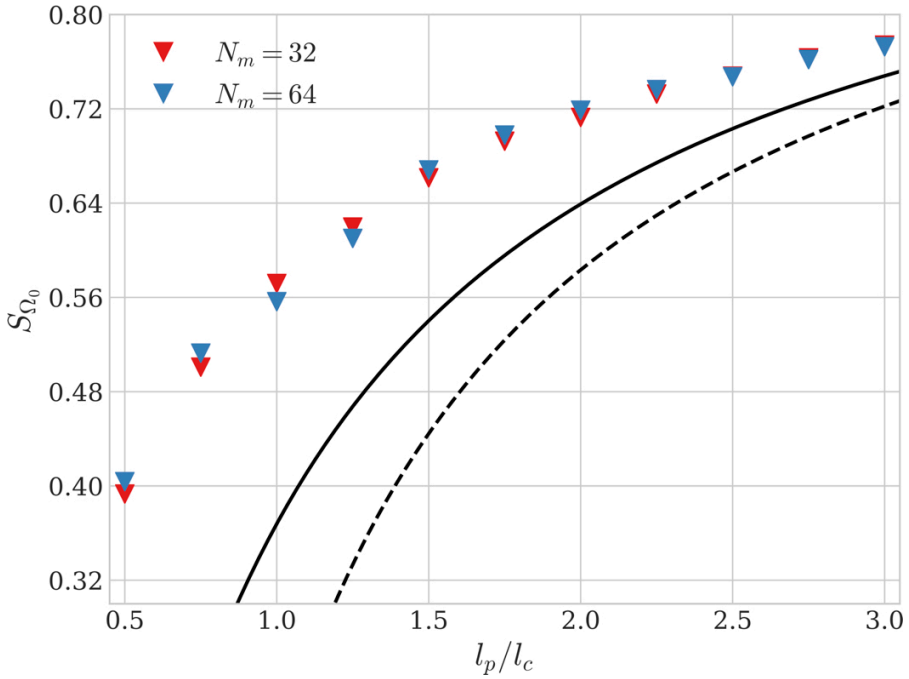

Figure 5.5: Intra-molecular bond order parameter S_{Ω_0} as a function of persistence-to-contour-length ratio for unconfined KG chains. Markers represent the results of single-chain MC simulations with $N_m = 32$ and $N_m = 64$ monomers. The solid line denotes the theoretical values obtained by plugging the full Eqs. (E.24) and (E.26) into Eq. (E.23), and the dashed line those of the truncated asymptotic expansion in Eq. (5.22).

The slow saturation of S_{Ω_0} with increasing persistence lengths (see Figure 5.5), which reflects the presence of small undulations of the free chains about their long axes, therefore imposes an unrealistic upper bound for S_b in the UCA even in the case where l_p is significantly larger than l_c. One thus recovers the important concept of *deflection length* [235], denoted by l_d, which quantifies the average length-scale over which polymers are diverted from their unconfined conformations by the presence of the surrounding nematic field. While our results suggest that the FY molecular order parameter S may be reasonably captured by the UCA for chains such that $l_p \gtrsim 2l_c$, the accurate description of the KS bond order parameter S_b in the UCA thus requires the much more stringent inequalities

$$l_c < l_d \ll l_p,$$

which corresponds to the so-called *rigid-rod limit* where the effects of particle flexibility may be neglected altogether [240]. This limitation therefore imposes the description of the detailed conformational statistics of polymers in a confining nematic field as a necessary prerequisite for any form of DFT based on a finer-grained representation of orientational order. This task may be further complicated by the reported importance of collective deflection fluctuation modes [246,264], which may not be easily captured by the mean-field treatment of KS-based descriptions, and may entail significant further theoretical developments for the reliable implementation of such approaches.

5.3 The cholesteric behaviour of DNA duplexes

As an example application of the techniques introduced here to a more complex and experimentally-realistic system, we now turn our focus to solutions of DNA duplexes. DNA constitutes a well-studied semi-flexible biopolymer with relatively-high stiffness, whose persistence length has been measured to be 130 base pairs (44 nm) at salt concentration $c_{\mathrm{Na}^+} = 0.5\,\mathrm{M}$ [265], although the precise value is somewhat dependent on solution conditions [265,266] and sequence [267]. DNA is also chiral, both in terms of its excluded volume — it is a grooved double helix with the major groove larger than the minor groove — and its electrostatics — it has a double helical pattern of negative charges associated with the phosphate groups along the backbone. Consequently, DNA duplexes in concentrated solutions generally assemble into cholesteric phases, which exhibit a rich structural polymorphism [55, 58, 268, 269]. Highly-oriented dense DNA packings are also relevant to biology, for example, occurring in bacterial nucleoids [270], dinoflagellate chromosomes [271] and sperm cells [272].

Here we will focus on DNA duplexes that are of the order of the persistence length. In particular, we will compare to the results of Refs. [61, 273], which consider DNA duplexes with reported most-probable lengths of about 146 base pairs. As the diameter of DNA duplexes due to excluded volume is about 25 Å, these examples have an aspect ratio of about 20 — although their effective aspect ratio

in solution is expected to be somewhat lower due to the effects of electrostatics [31, 196]. The former study focuses on the phase diagram, in particular the coexisting concentrations of the cholesteric and isotropic phases [273], whereas the latter's emphasis is on the dependence of the cholesteric pitch on DNA concentration and solution conditions [61]. One of the particularly noteworthy results of the latter is that the cholesteric phase is left-handed with a pitch that depends non-monotonically on the DNA concentration.

The left-handed character is intriguing, as the discussions of Sections 4.2.2 and 4.2.3 suggest that right-handed particles with a thread angle less than 45° (it is about 30° for DNA) should generally exhibit an entropically-stabilised right-handed phase. However, the addition of soft extra-molecular interactions may potentially add an additional level of complexity. If one considers the negative charges of the phosphates only, it has been postulated that the electrostatic repulsion would instead be minimised in a left-handed configuration [92, 228], although recent simulation results for coarse-grained particles with helical charge distributions appear to challenge this hypothesis [71, 72, 198]. Conversely, this preference has also been suggested to be reversed if one further considers the possibility of counterion condensation within the grooves of the helix [228].

To try to get a more rigorous insight into these questions, a number of theoretical studies have attempted to explain the observed experimental behaviour. Firstly, Kornyshev *et al.* exclusively considered the potential chirality arising from electrostatic interactions, and although they predicted a dependence of the pitch on concentration that resembled experiment [274], it was later revealed that the corresponding pitches had in fact the wrong handedness [228]. Secondly, Tombolato and Ferrarini applied a Straley-like DFT approach to a simplified representation of the DNA duplexes, and found that when only the steric interactions were considered, a right-handed phase resulted — in agreement with the previous geometric argument. By contrast, when electrostatic interactions were included, this tendency was reversed and a left-handed phase was predicted, whose pitch was further reported to be in reasonable agreement with experiment for the single DNA concentration considered [92].

However, numerous approximations were introduced in this study for the computation of the PS integrals (Eqs. (3.31) and (3.32)), which underpin the determination of the equilibrium pitch $\mathcal{P}_{\text{eq}}$ (Eq. (3.7)). As phase chirality is generally very weak in experimental cholesterics, DFT predictions for the pitch of such systems can be very sensitive to the accuracy of the calculations of such integrals. As discussed in Chapter 3, such results should therefore be generally interpreted with caution, unless a well-defined numerical approach is used that allows for the demonstrable convergence of the procedure to the required accuracy.

Both of the above studies also treated DNA as an infinitely rigid molecule. However, flexibility is likely to have a large impact on the phase behaviour of polymers whose contour lengths are of the order of the persistence length, as is evident from Section 5.2. The potential effects of flexibility on the cholesteric pitch are largely unexplored [72], but should be expected to be equally significant in light of the previous discussions.

Here, we apply the current DFT approach to 146-base pair DNA duplexes. In order to both sample the particle conformational space and to calculate the inter-duplex interactions in the procedure of Section 5.1.3, we make use of the oxDNA model [212, 275], which will be introduced in more detail in Section 6.1.2. For now, we note that the electrostatic interactions in the model are of a simple Debye-Hückel (DH)-like form and have been parameterised to reproduce the salt-concentration dependence of the thermodynamics of hybridisation [212], rather than any specific properties related to inter-duplex interactions.

We generate the UCA ensemble Ω_0 by means of single-duplex MD simulations, using an Andersen-like thermostat at temperature $T = 20\,^{\circ}\text{C}$. Equilibration was performed over 1×10^7 simulation steps, and production runs of 1×10^9 steps were used to generate a set of 2000 uncorrelated configurations. The molecular volume v relative to the PL approximation (Eq. (5.16)) was computed using the average B-DNA nucleotide volumes measured in Ref. [276], and mass concentrations were obtained assuming a molar weight of 650 Da per base pair.

Table 5.1: Isotropic/cholesteric coexistence concentrations for near-persistence-length B-DNA duplexes at $T = 20°$ and various salt concentrations. Ω_0 and Ω_∞ denote the DFT predictions of this work obtained in the UCA and in the limit of infinite duplex stiffness, respectively, and are compared with the experimental results of Refs. [61] and [273]. All values are reported in mg/ml.

	Ref. [273]		Ref. [61]		Ω_∞		Ω_0	
c_{Na^+}	c_i	c_c	c_i	c_c	c_i	c_c	c_i	c_c
0.5 M	n/a	n/a	n/a	218	120	138	242	250
1.0 M	171	270	n/a	257	132	155	268	276

The results for the isotropic-to-cholesteric (I/C) transition densities are presented in Table 6.1. As expected from Section 5.2, the onset of cholesteric order occurs at a much lower concentration when DNA is considered to be rigid. Significantly, the predictions when flexibility is taken into account in the UCA are in much better agreement with the experimental densities c_c reported in Refs. [61,273], although the latter's measurements may not very accurately reflect the true cholesteric binodal point [61]. The dependence of the results on salt concentration is also found to follow the experimental trends, with stronger electrostatic screening generally deferring the I/C transition range to higher densities, as predicted by theory [196].

One notable difference with the results of Ref. [273] lies in the width of the coexistence region, which is found to be strongly underestimated by DFT. This discrepancy may be partially attributable to the shortcomings of the UCA in the vicinity of the I/C transition, as discussed in Section 5.2, and could also reflect potential inaccuracies of the oxDNA model. Furthermore, our theory does not account for the substantial polydispersity reported in the experimental systems [273], which should be expected to significantly widen the phase coexistence range [104, 250].

We now turn our focus to the cholesteric pitch, and first consider rigid straight duplexes in order to compare our results with those previous theoretical investigations. As illustrated in Figure 5.6, we find the predicted pitch to be right-handed when we do not include the electrostatic term in the potential, as expected from the

previous excluded volume argument. Interestingly, the magnitude of the pitch is also found to be much larger than the experimental values, indicating a significant underestimation of phase chirality. However, unlike in Ref. [92], we do not report evidence of a handedness inversion when electrostatic repulsion is taken into account, but rather observe a further reduction of the predicted phase chirality.

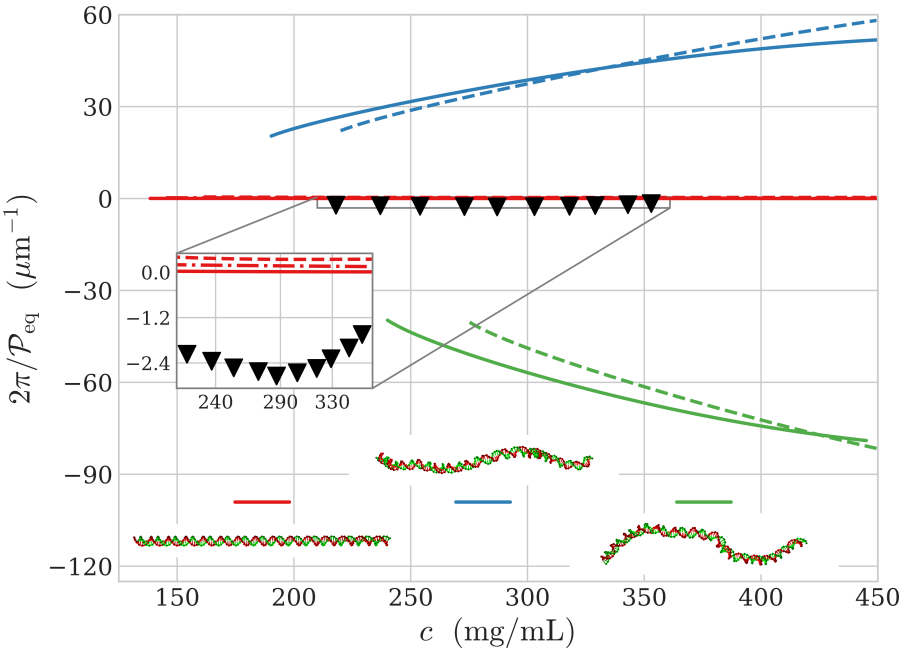

Figure 5.6: Inverse equilibrium cholesteric pitch $2\pi/\mathcal{P}_{\mathrm{eq}}$ as predicted by DFT for 146 base-pair DNA duplexes in the limit of infinite particle stiffness (Ω_∞, in red) and for two instantaneous conformations, respectively observed to possess a strong left- (blue) and right-handed (green) character. Solid lines were computed using the oxDNA-parameterised excluded volume and DH interactions at $T = 20°$ and $c_{\mathrm{Na^+}} = 0.5\,\mathrm{M}$. The dash-dotted line was similarly calculated by replacing the DH contribution with the electrostatic potential of Ref. [92] (only for Ω_∞). Dashed lines were obtained in the limit of pure steric repulsion ($c_{\mathrm{Na^+}} \to \infty$). Markers denote the experimental results of Ref. [61]. The lowest densities reported correspond to the cholesteric binodal points c_c predicted by DFT.

This observation could potentially be explained by the competition between the entropic favourability of right-handed duplex configurations due to excluded-volume contributions and the hypothetical enthalpic preference for left-handed arrangements to minimise electrostatic repulsion, as postulated in Ref. [92]. However, we find a more likely explanation to lie in the fact that electrostatics penalise the close-pair configurations where the chirality of the excluded volume is most relevant, so that longer-range repulsion simply "smears out" the local details of the chiral

surface structure of DNA, as discussed in Section 6.2.2. To verify that this effect is not simply an artefact of our chosen description of electrostatic contributions in the oxDNA model, we repeated the calculations using the electrostatic potential detailed in Ref. [92]. Our results were however found to be very similar in both cases, which leads to the conclusion that the prediction of a left-handed phase in Ref. [92] is most likely due to some of the numerical approximations introduced in the virial calculations therein.

We have also attempted to compute the cholesteric pitch including the effects of flexibility in the UCA. However, we concluded after extensive calculations that the drastic dependence of the predicted pitches on the sampling of the particle conformational space precluded their determination with sufficient statistical accuracy. To illustrate the nature of the problems, we report in Figure 5.6 the equilibrium pitches computed for two example conformations taken from Ω_0, both of which were observed to possess noticeably helicoidal shapes with opposite respective handednesses. Interestingly, the handedness of the equilibrium pitch is then obtained to be opposite to that of the corresponding helicoidal conformation, which mirrors theoretical predictions for hard, weakly-curled coarse-grained helices [94,96]. Furthermore, phase chirality is found to be considerably stronger for these conformations, and the resulting pitches only weakly depend on the inclusion of electrostatics, as the length-scales associated with the shape helicity of the duplexes is in this case considerably larger than that of their screened electrostatic interactions.

The strong variations in the predicted pitches between individual DNA conformations prevented the reliable convergence of the DFT procedure, and the large fluctuations in both their handedness and magnitude obtained using different independent ensembles Ω_0 did not allow for the observation of any meaningful tendencies. Therefore, we could not reliably determine whether such helical conformations may be linked to the underlying intra-molecular chirality of DNA, nor what their net effect on the cholesteric pitch should be, given a large enough statistical sample of the conformational space. Moreover, it is apparent from

Section 5.2 that the UCA should generally be unsuitable for the description of the nematic — and *a fortiori* cholesteric — phases of particles whose contour lengths are of the order of the persistence length, so we made no attempt to pursue this study further.

It nonetheless transpires that the flexibility of DNA duplexes plays a significant role in their LC assembly, which cannot be reasonably neglected in any theoretical investigation of their phase behaviour — especially in the context of the fine determination of their cholesteric pitch. However, the quantitative examination of its effects is an arduous task, as near-persistence-length duplexes are too flexible to be accurately described by the FY DFT in the UCA, while the cholesteric ordering of their shorter counterparts generally entails more involved living polymerisation mechanisms [269], which further complicate their theoretical treatment [277,278].

In the current framework, one possible way to circumvent these issues would of course be to use the oxDNA model to simulate a nematic phase of elongated DNA duplexes at the concentration of interest, in order to generate ensembles of conformations that are more representative of a real cholesteric phase to be input into the FY DFT. However, such simulations may prove to be quite computationally challenging, although they could provide an interesting avenue for future research.

5.4 Conclusion

In this chapter, we have investigated in detail the application of the FY DFT to the description of the nematic self-assembly of various semi-flexible particle models, and showed for the first time how it can be straightforwardly extended to account for the effects of particle flexibility on the cholesteric phase. Extensive comparisons with the results of molecular simulations of persistent KG chains reveal that the I/N transition densities of polymers with $l_p/l_c \gtrsim 1$ appear to be well captured by the theory in the UCA, although the detailed mechanisms underlying these predictions are not fully clear. This limitation stems from the fact that while the FY DFT is found to be quantitatively accurate in the isotropic phase, where no concentration-dependent stretching of the chains is observed for the systems considered here, the reliable

computation of nematic properties beyond the I/N transition generally requires a more involved account of the restrictions of the accessible particle conformational space induced by the confining effects of the surrounding nematic field.

These considerations deserve to be investigated further, and dedicated numerical studies of the I/N coexistence properties of persistent chains, along the lines of the simulations of Ref. [279] for systems of jointed sphero-cylinders, would be desirable. Moreover, the effects of these restrictions should generally depend on the scaled contour length l_c/σ as well as l_p/l_c, while the former ratio was kept fixed in this study. However, the quantitative agreement between FY DFT predictions and simulation results reported in Ref. [246] was found to be relatively unaltered by varying of the contour length in the range $l_c/\sigma \in [15, 63]$ at given l_p/l_c, so it is expected that the previous discussions should quite generally apply to elongated semi-flexible particles.

We additionally demonstrate that the use of a molecular-level representation of orientational order allows the FY theory to circumvent some of these shortcomings by coarse-graining over conformational fluctuations on the scale of the deflection length, which may provide for a satisfactory description of the nematic phase of polymer chains with $l_p/l_c \gtrsim 2$. While this statement may be somewhat limiting in scope, we feel that such a restriction is largely inherent to the underlying formalism of the Onsager DFT, as the complex coupling between conformational statistics and nematic order is further supplemented by the growing inadequacy of the second-virial approximation to describe the higher-density I/N transitions associated with increased particle flexibilities. It is also worth remarking that previous numerical studies have demonstrated the quantitative accuracy of the FY approach to consistently match (and in many cases surpass) that of other DFT implementations across a wide range of chain contour lengths l_c and relative persistence lengths l_p/l_c [241, 242, 246], which points to the rather general unsuitability of existing theoretical frameworks to tackle polymeric systems of intermediate stiffness [104].

Such limitations are particularly stringent for the determination of cholesteric properties, which are especially sensitive to the detailed nature of the conformational fluctuations undergone by flexible particles. It is thus found that while the

combination of the FY DFT and the oxDNA coarse-grained model provides for a satisfactory prediction of the I/C transition of near-persistence-length DNA duplexes, the strong dependence of the predicted pitches on minute structural changes largely precludes their realistic determination in the context of the UCA.

This analysis nonetheless reveals that steric and electrostatic interactions between rigid linear DNA duplexes appear to be unable to account for either the handedness or the magnitude of the phase chirality observed in experiments. This conclusion concurs with the recent findings of Ref. [280], in which extensive all-atom MD simulations of short DNA oligomers demonstrated the absence of a significant chiral contribution attributable to inter-duplex electrostatic interactions — thus suggesting the need for alternative mechanisms to explain their cholesteric behaviour.

The accurate description of the conformational statistics of DNA duplexes in dense phases therefore emerges as a crucial prerequisite to any realistic investigation of their cholesteric assembly, and likely lies beyond the reasonable reach of current theoretical and numerical tools. Perhaps surprisingly given their considerably larger sizes, elongated DNA origamis, whose cholesteric behaviour has been recently explored experimentally [221], may present a more tractable target for the application of the FY DFT due to their much greater relative stiffness. Although the persistence length of the studied 6-helix-bundle origamis is not yet as well-characterised as that of single duplexes, preliminary measurements have indeed suggested that $l_p \geq 5\,l_c$ [281, 282]. Furthermore, their aspect ratio of about 70 [221] leads to their formation of a stable cholesteric phase in a regime approaching the Onsager limit of high dilutions [110]. Such origamis thus provide a much more suitable model system in regard to the fundamental assumptions of the FY DFT, and will be discussed in detail in Chapter 6.

6

The origin of chirality in LCLC phases of DNA origamis

Contents

In light of the previous chapters, we are now in a position to investigate the cholesteric assembly of a wide range of experimentally-relevant, flexible polymeric systems. A particularly interesting first application of the approach is provided by the recent experimental work of Ref. [221], which exploited the synergy between colloidal science and DNA origami technology to tune the micron-scale pitch of the bulk phase via the direct control of single-particle structure at the nanometer level. In this chapter, we describe the combination of our density-functional framework with the well-established oxDNA model [212] to conduct a rigorous theoretical analysis

of these experimental developments, and thus carry out a detailed assessment of the influence of particle mechanical properties and thermodynamic state on their ordering behaviour — without the use of any adjustable parameters.

The structure of the chapter is organised as follows. We first present in Section 6.1 a focused introduction to DNA origami nanotechnology, and provide a brief description of the oxDNA coarse-grained model. We then dedicate Section 6.2 to the cholesteric behaviour of 6-helix-bundle (HB) origamis, examining the respective influence of their molecular ground states and conformational statistics, before discussing the predictions of our approach for the supramolecular assembly of 10-HB origamis in Section 6.3. We finally summarise our main results in Section 6.4, and discuss their potential applicability to other model systems.

6.1 Introduction to DNA nanotechnology

The basic monomeric units of DNA, known as *nucleotides*, are comprised of any one of four *nucleobases* — cytosine (C), guanine (G), adenine (A) and thymine (T) — and of a sugar-phosphate backbone group. The combination of the so-called Watson-Crick pairing of complementary bases (AT, CG) and of π-stacking interactions between adjacent nucleotides gives rise to the famous double-helical structure of DNA. The specific sequence of bases within DNA acts as the vector of genetic information in living organisms and plays a central role in the various nanotechnological applications of DNA, from material science [283] to molecular computing [284] and data storage [285].

6.1.1 The DNA origami technique

The selectivity of Watson-Crick base pairing, combined with a sustained progress in the artificial synthesis of short DNA fragments with addressable sequences, has long been employed for the bottom-up design of a variety of simple DNA-based nanostructures and devices [286–291]. However, a significant breakthrough was achieved in 2006 with the introduction of the DNA origami technique by

Rothemund [292], which considerably expanded the scale and complexity of the nanostructures accessible through the programmable assembly of DNA.

The DNA origami approach is based on the controlled folding of a multi-kilobase *scaffold* DNA strand through the combined action of hundreds of short *staple* strands, each of which being specifically designed to bind with two or more non-consecutive complementary regions of the scaffold strand to force them into close proximity [292]. The versatility, reliability and experimental simplicity of the method have been exploited in a broad range of applications in recent years, spanning the fields of nanomedicine [293,294], nanosensing [295,296] and nanoelectronics [297].

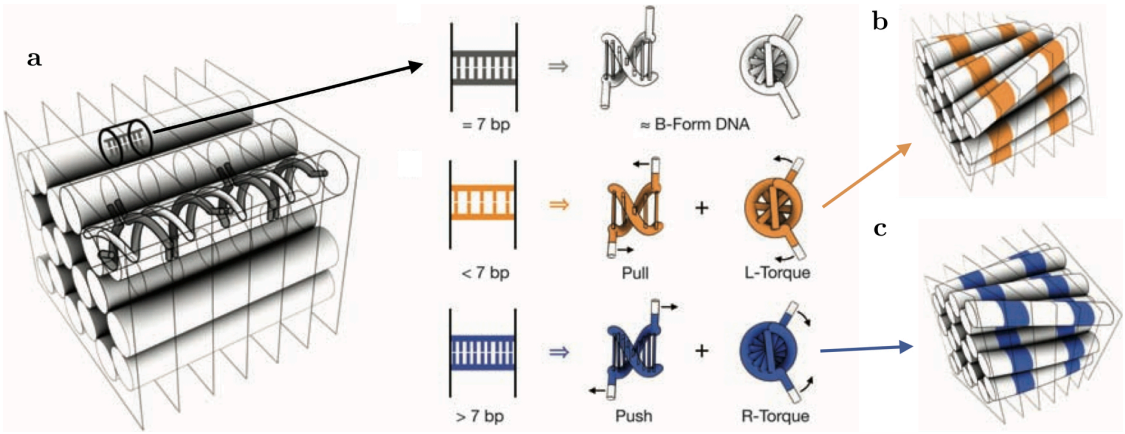

Figure 6.1: Design principles for twisted DNA origami structures. a) The scaffold strand (in white) is folded in a honeycomb arrangement by staple-strand crossovers between neighbouring double helices (in black). The 7 bp spacing between adjacent crossover planes ensures that the relaxed twist density of B-DNA is roughly compatible with the hexagonal lattice topology, and leads to the formation of untwisted bundles. b) and c) A separation distance lesser (resp. greater) than 7 bp conversely leads to overwinding (underwinding) strains within each helix, which may be relieved by a compensatory left-handed (right-handed) twist of the structure. Adapted with permission from Ref. [220].

A particularly interesting origami design in the context of this thesis stems from the seminal work of Dietz *et al.* [220], which extended a general folding strategy for the assembly of lattice-based 3D structures [298] to the fabrication of complex shapes with controllable twist and curvature. In this framework, the target structure may be visualised as an hexagonal array of anti-parallel DNA duplexes, linked by staple-strand crossovers at 7 base-pair (bp) intervals along the axis of each double helix (Figure 6.1a). In this case, assuming the twist density Tw_0 of

ground-state B-DNA to be such that $1/\mathrm{Tw}_0 \simeq 10.5\,\mathrm{bp}$, each helical strand rotates by an angle of 240° between consecutive crossover planes, allowing for the near-optimal alignment of crossover junctions between neighbouring helices on the honeycomb lattice [220]. Conversely, enforcing a separation distance of less (more) than 7 bp between adjacent crossover planes imposes a coherent overwinding (underwinding) of the constituent helices to satisfy the lattice topology, which may be partially relaxed through the propagation of a global left-handed (right-handed) twist of the bundle (Figures 6.1b and c, respectively).

This process remarkably allows for the fabrication of stiff, monodisperse and highly-elongated nanofilaments, whose shape chirality may be directly controlled through the careful choice of crossover locations in the origami design. Such systems therefore provide an ideal experimental benchmark for the application of the theoretical framework developed in this thesis. However, as discussed in Chapter 5, the reliable application of our approach requires the use of a molecular model capable of accurately representing the structure and mechanics of such large DNA assemblies over experimentally-relevant time-scales. A particularly suitable model for this purpose is known as oxDNA, which we now proceed to briefly describe.

6.1.2 The oxDNA model

OxDNA is a nucleotide-level coarse-grained model that represents each DNA nucleotide as a rigid body with three interaction sites, associated with an effective pair potential designed to capture the effects of excluded-volume, Debye-Hückel (DH), π-stacking, hydrogen- and covalent-bonding interactions [212]. The various terms of this interaction potential have been carefully parametrised to accurately reproduce the structural, mechanical and thermodynamic properties of both single- and double-stranded DNA available from detailed experimental measurements [275]. Solvent effects are implicitly incorporated into the inter-nucleotide interactions in an effective fashion, and are further mimicked by the use of an Andersen-like thermostat in MD simulations of the model. OxDNA thus exhibits sensible values for the persistence length and twist modulus of B-DNA [212], has been shown

to capture more subtle phenomena such as twist-bend coupling [299], and has been widely applied to the study of DNA-based systems — both in the context of biophysics and nanotechnology [300, 301].

While the model and its underlying force field have been extensively presented elsewhere [212, 302], it is worth recalling here the explicit expression for the oxDNA extra-molecular interaction potential U_{ext}, which plays a central role in the density-functional treatment of LC assembly in the framework of Section 5.1.3. Neglecting potential coaxial stacking interactions between non-bonded DNA structures, which are only relevant in the case of polymerising systems beyond the scope of this thesis [278], the two salient contributions are in our case simply provided by steric and DH repulsion,

$$U_{\text{ext}} = U_{\text{st}} + U_{\text{DH}}. \tag{6.1}$$

The excluded-volume interaction term U_{st} takes the form

$$U_{\text{st}}^{\mathcal{C}_1\mathcal{C}_2} = \sum_{i\in\mathcal{C}_1^{\text{b}}} \sum_{j\in\mathcal{C}_2^{\text{b}}} u_{\text{bb}}(r_{ij}), \tag{6.2}$$

where the double sum runs over all pairs of backbone interaction sites $i \in \mathcal{C}_1^{\text{b}}$ and $j \in \mathcal{C}_2^{\text{b}}$ of any two molecules described by the respective conformations $\mathcal{C}_1$ and $\mathcal{C}_2$, and the radial backbone-backbone steric contribution u_{bb} is represented by a truncated Lennard-Jones potential with a smooth quadratic long tail [275, 302],

$$u_{\text{bb}}(r) = \begin{cases} 4\epsilon_{\text{bb}}\left[\left(\dfrac{\sigma_{\text{bb}}}{r}\right)^{12} - \left(\dfrac{\sigma_{\text{bb}}}{r}\right)^{6}\right] & \text{if } r < r_{\text{bb}}^{*} \\ k_{\text{bb}}\epsilon_{\text{bb}}\left(r - r_{\text{bb}}^{c}\right)^{2} & \text{if } r_{\text{bb}}^{*} < r < r_{\text{bb}}^{c} \\ 0 & \text{if } r > r_{\text{bb}}^{c} \end{cases}, \tag{6.3}$$

with $\epsilon_{\text{bb}} = 8.284 \times 10^{-20}\,\text{J}$, $\sigma_{\text{bb}} = 5.963\,\text{Å}$ and $r_{\text{bb}}^{*} = 5.750\,\text{Å}$, and where k_{bb} and r_{bb}^{c} are fixed by imposing the continuity and differentiability of u_{bb}. The DH repulsion term U_{DH} consists in a standard linearised Poisson-Boltzmann expression of the form [212]

$$U_{\text{DH}}^{\mathcal{C}_1\mathcal{C}_2} = \sum_{i\in\mathcal{C}_1^{\text{b}}} \sum_{j\in\mathcal{C}_2^{\text{b}}} \frac{(q_{\text{eff}}e)^2}{4\pi\epsilon_0\epsilon_r} \frac{e^{-r_{ij}/\lambda_{\text{DH}}}}{r_{ij}}, \tag{6.4}$$

with e the elementary charge, ϵ_0 the vacuum dielectric permittivity and $\epsilon_r = 80$ the relative permittivity of water. The Debye screening length λ_{DH} is finally given by, at fixed temperature T and monovalent salt concentration c_{Na^+},

$$\lambda_{\mathrm{DH}}\left(T, c_{\mathrm{Na}^+}\right) = \sqrt{\frac{\epsilon_0 \epsilon_r k_b T}{2\mathcal{N}_A e^2 c_{\mathrm{Na}^+}}},$$

with $\mathcal{N}_A$ the Avogadro constant.[1]

In Eq. (6.4), the dimensionless effective charge $q_{\mathrm{eff}} < 1$ accounts for the effects of the negative charge borne by the phosphate group on the DNA backbone combined with the Manning condensation of counterions in the presence of dissolved monovalent electrolytes. Its value is here set to $q_{\mathrm{eff}} = 0.815$, obtained from an optimal fit of the model results to the predictions of SantaLucia [303] for the thermodynamics of duplex melting [212]. This mean-field treatment of electrostatics is obviously highly simplistic, and should generally not be expected to capture the full complexity of the dependence of the local DNA structure and interaction potential on solvent conditions [304]. However, we will show in Section 6.2.3 that the inclusion of soft finite-ranged repulsion is of limited consequence for the predicted LCLC behaviour of DNA origamis once the effects of intra-molecular mechanics are taken into account, so that the main conclusions of this chapter are expected to be largely unaffected by our chosen form of electrostatic interactions at salt concentrations matching experimental conditions [221].

6.2 The cholesteric behaviour of 6-HB origamis

6.2.1 LCLC assembly of ground-state origamis

Following in the footsteps of Ref. [221], we first focus on the case of 6-HB origamis comprised of 15 224 to 15 240 nucleotides, with experimentally-determined contour lengths (l_c) of 420 nm and bundle diameters of 6 nm. A continuum finite-element model based on an elastic rod description of DNA [305] predicts the respective ground states of the different designs to bear negligible (s), 360° right-handed (1x-rh),

[1] Note that a smooth quadratic cutoff similar to that in Eq. (6.3) is also implemented in U_{DH} for $r_{ij} > 3\lambda_{\mathrm{DH}}$, but is here omitted for readability; see Ref. [212] for the full form of the potential.

360° left-handed (1x-lh) and 720° left-handed (2x-lh) twist about the filament long axis, with negligible net curvature (Figure 6.2) [221].

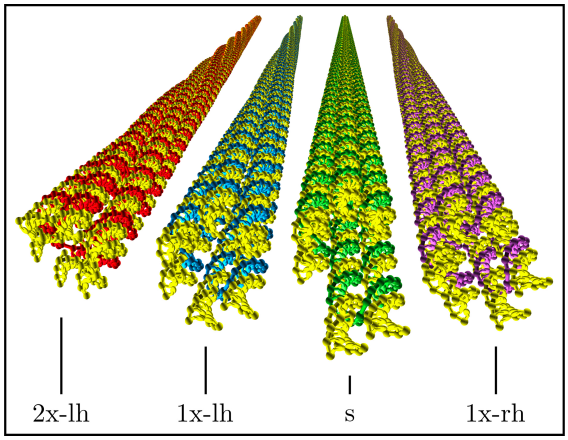

Figure 6.2: Ground-state 6-HB origami conformations. The equilibrium axial twist of the conformations is obtained by elastic energy minimisation using a continuum DNA model [305]. The nucleotide-level depiction corresponds to the finer-grained representation of the oxDNA model [212].

As a first approximation, we neglect the conformational fluctuations of DNA origamis in solution, and assess the cholesteric arrangement of their respective ground states as described by the oxDNA model. In the absence of electrostatic interactions, the entropy-induced ordering of ground-state filaments is governed by their axial twist, which is found to stabilise *anti-chiral* LCLC phases — possessing opposite handedness with respect to the origami twist (Figure 6.3a). This observation is consistent with the results of Chapter 4 for weakly-twisted HTCs, and reflects the handedness of the close-approach arrangement of such filaments (Figure 6.3b). As in the case of HTCs, this entropic preference is found to be reversed in the case of strongly-twisted filaments (Figure 6.3c), which accounts for the weak right-handed phase predicted for the untwisted (s) origamis in terms of the intrinsic right-handed helicity of DNA [92].

However, these predictions are at odds with the experimental measurements of Ref. [221], which instead revealed a general tendency of origami filaments to stabilise *iso-chiral* LCLC phases — bearing the same handedness as their axial twist. These discrepancies persist through the inclusion of electrostatic repulsion, which is simply found to unwind the predicted cholesteric pitches (Figure 6.3a). These effects may

be explained in terms of the longer-ranged character of DH interactions, which indiscriminately penalise all close-pair configurations, in which the local surface chirality of the filaments is most relevant [306], and may be further probed by considering the chiral component of their potential of mean force (PMF).

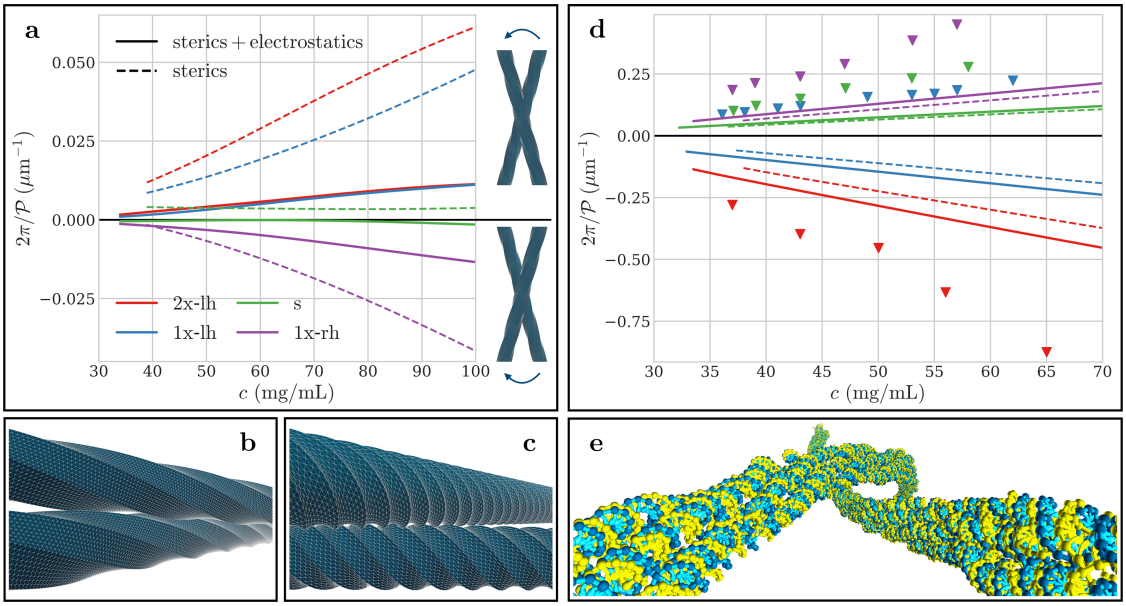

Figure 6.3: Cholesteric behaviour of ground-state and thermalised 6-HB origamis. a) Inverse equilibrium cholesteric pitch $\mathcal{P}$ as a function of particle concentration c for ground-state 6-HB filament conformations. Dashed lines denote values obtained by assuming pure steric interactions, and solid lines by accounting for both steric and Debye-Hückel repulsion. Positive (resp. negative) values of $\mathcal{P}$ correspond to LCLC phases bearing right (resp. left) handedness, as illustrated in the right-hand panel. b) Close-approach configuration of idealised, weakly-twisted right-handed filaments, displaying a left-handed arrangement. c) Same as b) for the case of strongly-twisted right-handed filaments, illustrating their entropic preference for right-handed arrangements. d) Same as a) for the case of thermalised filaments. Markers denote experimental measurements (from Ref. [221]). e) Angular configuration minimising the chiral two-body potential of mean force for thermalised 1x-lh origamis (see Figure 6.4), illustrating the predominance of long-wavelength backbone fluctuations over local axial twist in their LCLC assembly.

6.2.2 Chiral potential of mean force

As in Section 4.2.2, let us now denote the properties relative to right- and left-handed pair configurations by + and − subscripts, respectively. The angular two-body PMF $\overline{U}_{\pm}$ associated with two-particle arrangements of fixed handedness is given by [90, 91]

$$\beta\overline{U}_{\pm}(\theta) \equiv -\log\left\langle e^{-\beta U_{\text{ext}}}\right\rangle_{\pm}^{(\theta)}, \tag{6.5}$$

where the configurational average $\langle\cdot\rangle_{\pm}^{(\theta)}$ is defined as

$$\left\langle e^{-\beta U_{\rm ext}}\right\rangle_{\pm}^{(\theta)} \equiv \frac{1}{V_{\rm int}}\int_V d\mathbf{r}_{12}\oiint d\mathcal{R}_1 d\mathcal{R}_2\, e^{-\beta U_{\rm ext}(\mathbf{r}_{12},\mathcal{R}_1,\mathcal{R}_2)} \times \delta(\mathbf{u}_1\cdot\mathbf{u}_2-\cos\theta)\Theta\Big\{\pm\mathbf{r}_{12}\cdot(\mathbf{u}_1\times\mathbf{u}_2)\Big\}, \quad (6.6)$$

using the notations of Chapter 5. In Eq. (6.6), $V_{\rm int}$ represents the total volume spanned by the spatial and angular integrals,

$$V_{\rm int} = \frac{(8\pi^2)^2}{2}V,$$

where the factor $1/2$ accounts for the equal division of the two-particle configurational space between left- and right-handed arrangements. Note that in the case of flexible particles, Eq. (6.6) may be further averaged over a representative ensemble of molecular conformations using the numerical procedure of Section 5.1.3. In this study, we use for the volume V the smallest cubic box containing all possible interacting configurations of any two origami conformations.

In the context of Eqs. (6.5) and (6.6), a system of two particles with fixed inter-axis angle θ_{12} will adopt a thermodynamically-stable right-handed configuration if their net repulsion is minimised in a right-handed arrangement — i.e., if $\overline{U}_+(\theta_{12}) < \overline{U}_-(\theta_{12})$. Conversely, $\overline{U}_+(\theta_{12}) > \overline{U}_-(\theta_{12})$ indicates a thermodynamic preference for left-handed arrangements. The relative stability of chiral two-particle assemblies is thus quantified by the chiral component of the PMF,

$$\Delta_c\overline{U}(\theta) \equiv \overline{U}_+(\theta) - \overline{U}_-(\theta) = k_bT\log\frac{\left\langle e^{-\beta U_{\rm ext}}\right\rangle_{-}^{(\theta)}}{\left\langle e^{-\beta U_{\rm ext}}\right\rangle_{+}^{(\theta)}}. \quad (6.7)$$

In the case of particles with high aspect ratios interacting through short-ranged repulsive potentials, it is easy to verify that only a small statistical fraction of the configurations sampled in Eq. (6.6) may display a significant interaction energy $U_{\rm ext} > 0$, so that

$$\left\langle e^{-\beta U_{\rm ext}}\right\rangle_{\pm}^{(\theta)} \longrightarrow 1 \qquad \forall\theta\in[-\pi/2,\pi/2].$$

The Taylor expansion of Eq. (6.7) then reads as, to leading order in $1-\left\langle e^{-\beta U_{\rm ext}}\right\rangle_{\pm}$,

$$\Delta_c\overline{U}(\theta) = k_bT\left\{\left\langle e^{-\beta U_{\rm ext}}\right\rangle_{-}^{(\theta)} - \left\langle e^{-\beta U_{\rm ext}}\right\rangle_{+}^{(\theta)}\right\},$$

and one recovers the definition of the chiral pair excluded volume $\Delta_c U$ introduced in Eqs. (4.9) and (4.10) for systems of hard particles, up to a constant multiplicative prefactor.

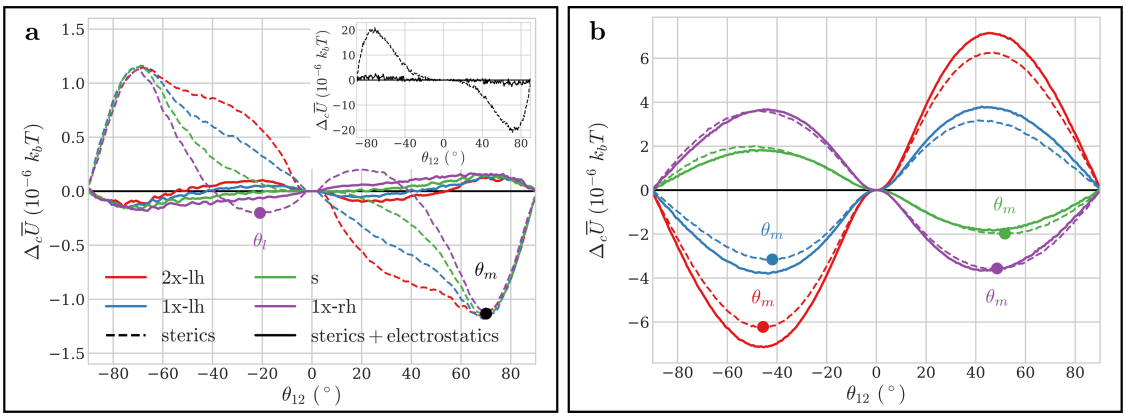

Figure 6.4: Chiral two-body PMF of ground-state and thermalised 6-HB origamis. a) Chiral component of the angular PMF as a function of origami inter-axis angle θ_{12} for ground-state filaments. Positive (resp. negative) values of θ_{12} denote right-handed (resp. left-handed) two-particle arrangements. Solid dots mark the locations of the curve minima, as discussed in the text, and are only displayed in the case of pure steric repulsion for clarity. Inset: chiral PMF of single ground-state 146 bp B-DNA duplexes (c.f. Section 5.3). b) Same as a) for thermalised 6-HB origamis.

It is apparent from Figure 6.4a that the PMFs of ground-state filaments interacting purely through steric repulsion display a shallow global minimum θ_m at large inter-axis angles of $+70°$, corresponding to the close-approach configuration of ground-state duplexes, as the helical threads of B-DNA form a fixed angle of roughly 35° with respect to the normal to the double-helix axis [92]. This large value is obviously incompatible with the local orientational order of LCLCs, but is nonetheless associated with a regime of weakly-negative values of $\Delta_c \overline{U}$ at smaller angles $\theta_{12} > 0$ in the case of the s, 1x-lh and 2x-lh origami variants — and thus leads to their formation of stable right-handed phases. However, the chiral PMF of 1x-rh filaments bears a local secondary minimum θ_l at small inter-axis angles of about $-20°$, arising from their weak right-handed axial twist, which instead stabilises their left-handed LCLC assembly.

Finally, we report that electrostatic interactions greatly reduce the magnitude of the chiral PMFs for all ground-state filaments, indicating that the inclusion of

longer-ranged repulsion results in an effective screening of the chiral nucleotide distribution on the filament surface — and therefore unwinds their equilibrium pitches. This conclusion mirrors the findings of Ref. [306] for LCLC assemblies of bacterial cellulose microcrystals with similar twisted morphologies (Figure 6.5), and is further consistent with the results of extensive all-atom simulations of short DNA oligomers [280], in which the net contribution of electrostatic interactions to the chiral PMF was found to be negligible at comparable monovalent salt concentrations (see also inset in Figure 6.4a). Therefore, it is apparent that simple steric and electrostatic repulsion between ground-state filament conformations cannot account for either the handedness or the magnitude of their experimental LCLC pitches, which reflects the conclusions of Chapter 5 for single B-DNA duplexes.

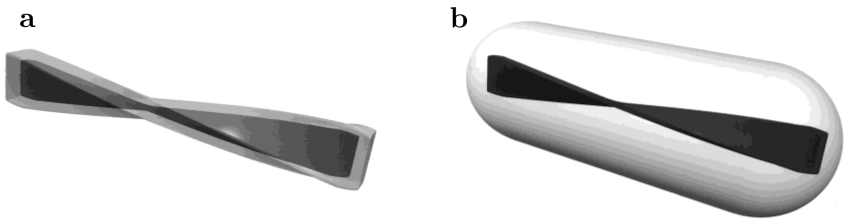

Figure 6.5: Long-ranged repulsion and effective origami shape. a) Schematic representation of a ground-state origami filament, depicted with a repulsive interaction range shorter than the origami groove depth. b) The inclusion of longer-ranged interactions induces a screening of the grooved molecular surface, and leads to an overall reduction of the effective filament shape chirality. Adapted with permission from Ref. [306].

6.2.3 Role of conformational statistics

To assess the influence of conformational statistics on their cholesteric ordering, we make further use of the oxDNA model to probe the detailed thermal fluctuations of the origami filaments. As in Chapter 5, we extend our theoretical framework to flexible particles in the FY approximation through its combination with the numerical sampling of the filament conformational space by single-origami molecular dynamics (MD) simulations. We reiterate that this description is expected to be particularly well-suited for our purposes in light of the discussions of Chapter 5, given the large persistence length (l_p) of the origami structures ($l_p/l_c \gtrsim 5$ [281,282]) and the low packing fractions of their stable LCLC phases [221].

We thus perform single-origami MD simulations on GPUs in the canonical ensemble using the oxDNA model for each of the 6-HB designs in Ref. [221], assuming sequence-averaged DNA thermodynamics, room-temperature conditions ($T = 293\,\mathrm{K}$) and fixed monovalent salt concentration $c_{\mathrm{Na}^+} = 0.5\,\mathrm{M}$. This value was chosen in slight excess of the experimental salt concentration $c_{\mathrm{Na}^+} = 0.26\,\mathrm{M}$ [221], employed in the rest of this chapter, in order to limit the computational cost of the MD simulations. The effects of this approximation on origami conformational statistics are expected to be minimal in the context of the simplified oxDNA treatment of electrostatics [212]. Relaxation was achieved through equilibration runs of $\mathcal{O}(10^6)$ MD steps starting from the origami ground state, and production runs of $\mathcal{O}(10^9)$ steps were conducted to generate $\mathcal{O}(10^3)$ uncorrelated conformations for each origami variant. The statistical independence of the resulting conformations was assessed by ensuring the vanishing autocorrelation of their end-to-end separation distance. Convergence was ensured by verifying the numerical dispersion of the computed pitches to be less than 10 % across the results of 16 DFT/MC runs, using independent bootstrap samples of the ensemble of simulated conformations.

The results of this approach, summarised in Figure 6.3d, display a surprising phase-handedness inversion compared to the LCLC behaviour of the origami ground-states, as well as a considerable tightening of the corresponding equilibrium pitches. The conjunction of these two factors allows for a convincing overall agreement with the experimental measurements of Ref. [221], albeit with a slight offset in the crossover value of the origami twist at which the phase handedness inversion occurs. These effects stem from the emergence of long-wavelength helical deformation modes along the backbone of thermalised origamis, which dominate the chiral component of their PMF over the local surface chirality arising from axial twist (Figure 6.3e).

Indeed, it is apparent from Figure 6.4b that the chiral PMFs of thermalised origamis are significantly larger in magnitude than those of their respective ground states, and are also relatively insensitive to the inclusion of electrostatic repulsion. These two observations evidence the ascendency of long-wavelength backbone

deformations over local axial twist in their LCLC ordering, as the larger length-scales associated with solenoidal writhe render the chiral assembly of thermalised filaments largely independent of the detailed nature of their much shorter-ranged repulsive interactions. The PMFs of thermalised origamis are further found to bear a unique minimum θ_m such that $\theta_m < 0$ for left-twisted filaments and $\theta_m > 0$ for their right-twisted counterparts, thus ensuring their stabilisation of iso-chiral LCLC arrangements (c.f. Section 4.2.2).

This long-ranged, super-helical (or *solenoidal*) writhe may be quantified by Fourier analysis of the filament backbone conformations. We define the *molecular backbone* of each origami by averaging the centre-of-mass locations of its bonded nucleotides over the 6 constituent duplexes of the bundle within each transverse plane along the origami contour (Figure 6.1). Shape fluctuations may then be described by the contour variations of the transverse position vector (Figure 6.6a),

$$\mathbf{r}_\perp(s) = \mathbf{r}(s) - \{\mathbf{r}(s) \cdot \mathbf{u}\}\mathbf{u},$$

with $\mathbf{r}(s)$ the position of the discretised backbone segment with curvilinear abscissa s, assuming the backbone centre of mass to be set to the origin of the frame. Denoting by Δs the curvilinear length of each segment, the Fourier components of $\mathbf{r}_\perp$ read as

$$\widehat{\mathbf{r}}_\perp(k) = \sum_s \Delta s\, \mathbf{r}_\perp(s) \times e^{-2i\pi ks}.$$

Using the convolution theorem, the spectral coherence between the two transverse components of an arbitrary backbone deformation mode may be quantified by their Fourier-transformed cross-correlation function $\widehat{c}_{vw}$,

$$\widehat{c}_{vw}(k) = \widehat{r}_{\perp v}(k) \times \widehat{r}^{\,*}_{\perp w}(k),$$

where $\widehat{r}_{\perp x} = \widehat{\mathbf{r}}_\perp \cdot \mathbf{x}$ for $\mathbf{x} \in \{\mathbf{v}, \mathbf{w}\}$ and $\widehat{r}^{\,*}_{\perp w}$ is the complex conjugate of $\widehat{r}_{\perp w}$. It is shown in Appendix F that an helicity order parameter $\mathcal{H}(k)$ for a deformation mode with arbitrary wavenumber k about the long molecular axis $\mathbf{u}$ may be derived in the form

$$\mathcal{H}(k) = \frac{2 \times \Im\big\{\widehat{c}_{vw}(k)\big\}}{\widehat{c}_{vv}(k) + \widehat{c}_{ww}(k)}, \tag{6.8}$$

with $\Im\{\widehat{c}_{vw}\}$ the imaginary part of $\widehat{c}_{vw}$. One may check that $-1 \leq \mathcal{H}(k) \leq 1$, with $\mathcal{H}(k) = \pm 1$ if and only if the two transverse Fourier components bear equal amplitudes and lie in perfect phase quadrature. In this case, $\widehat{\mathbf{r}}_\perp(k)$ describes an ideal circular helical deformation mode with pitch $1/k$ and handedness determined by the sign of $\mathcal{H}$.

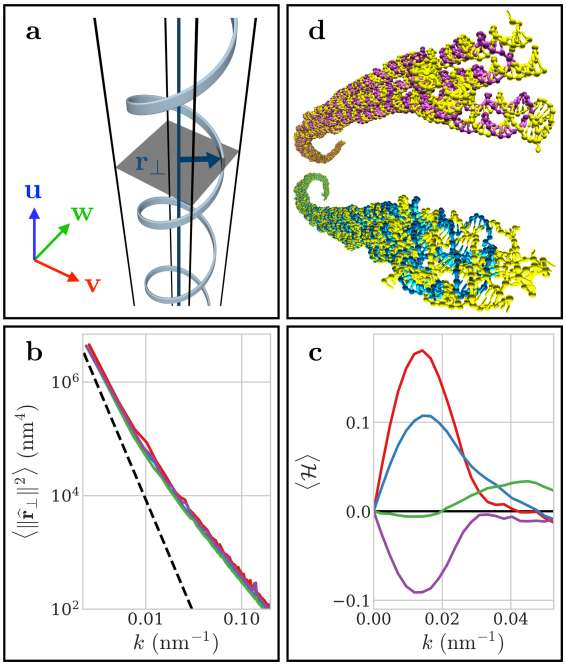

Figure 6.6: Conformational fluctuations and solenoidal writhe of 6-HB origamis. a) Transverse deformation vector $\mathbf{r}_\perp$ for an arbitrary backbone conformation. b) Transverse fluctuation spectrum of each origami variant. The dashed line represents the theoretical scaling behaviour of generic semi-flexible filaments with bending rigidity $l_p/l_c = 8$ at low deformation wavenumbers k (Eq. (F.25)). Colours are as in Figure 6.3. c) Net backbone helicity $\langle \mathcal{H} \rangle$ as a function of k. Positive (resp. negative) values denote a statistical bias towards right-handed (resp. left-handed) deformation modes. Colours are as in Figure 6.3. d) Example simulated conformations of 1x-rh (top) and 1x-lh (bottom) 6-HB origamis, respectively displaying characteristic left- and right-handed backbone helicity.

The fluctuation spectrum of $\mathbf{r}_\perp$ obtained using the oxDNA model is found to be consistent with the asymptotic scaling behaviour of persistent chains in the limit of long-wavelength deformations for typical experimental values of the filament bending rigidity [281,282] (Figure 6.6b). In this regime, the net backbone helicity of each origami variant is found to bear the opposite handedness to the axial twist of its ground state, with left-handed (right-handed) filaments predominantly favouring right-handed (left-handed) helical conformations, respectively (Figures 6.6c and d).

The geometric argument of Figure 6.3b, applied to systems of weakly-curled helices, predicts such conformations to display an entropic preference for opposite-handed arrangements (c.f. Section 4.2.3). In this case, the stabilisation of iso-chiral phases of twisted origami filaments therefore arises from their propensity for long-ranged, anti-chiral deformations under the effects of thermal fluctuations. This original chirality amplification mechanism is further evidenced by the relative insensitivity of our results to the inclusion of electrostatic interactions (Figure 6.3d), as the typical length-scales of the resulting backbone helicities are considerably larger than the experimental Debye screening length ($\lambda_{\mathrm{DH}} \simeq 0.6\,\mathrm{nm}$) [221] (Figures 6.6c and d).

6.2.4 Twist-writhe conversion and helical fluctuations

The origin of this fluctuation-stabilised solenoidal writhe, and of its dependence on filament twist, lies in the geometric constraints imposed by inter-helical crossovers in the origami design. To elucidate its microscopic underpinnings, let us consider a long origami filament whose extremities are firmly clamped to impose the parallel alignment of its backbone end tangents,

$$\left.\frac{d\mathbf{r}}{ds}\right|_{s=0} = \left.\frac{d\mathbf{r}}{ds}\right|_{s=l_c}. \tag{6.9}$$

Following Section 6.2.3, the origami backbone curve $\mathbf{r}$ may be defined as

$$\mathbf{r} \equiv \frac{1}{6}\sum_{i=1}^{6}\mathbf{r}_i,$$

where the continuous centreline $\mathbf{r}_i(s_i)$ of the i-th constituent DNA duplex is obtained by contour interpolation of the centre-of-mass positions of its bonded nucleotides. For simplicity, we neglect the effects of duplex splaying at the origami ends, and thus assume Eq. (6.9) to hold at each of the centre curve extremities,

$$\left.\frac{d\mathbf{r}_i}{ds_i}\right|_{s_i=0} = \left.\frac{d\mathbf{r}_i}{ds_i}\right|_{s_i=l_i}.$$

We further restrict our study to the regime of weak bending deformations of the duplex centrelines about the straight backbone conformation of the origami ground state, and neglect potential fluctuations in their respective contour lengths l_i.

Under these assumptions, the formulation of the Călugăreanu-Fuller-White theorem [307] extended to the treatment of open curves [308] states that the linking number Lk_i of each individual duplex may be decomposed into twist and writhe contributions,

$$\mathrm{Lk}_i = \mathrm{Tw}_i + \mathrm{Wr}_i. \tag{6.10}$$

In this context, Lk_i represents the (signed) number of net right-handed turns per unit contour length by which each strand of the duplex winds around the other. These turns may result in both a local twist of the strands about their common centreline $\mathbf{r}_i$, as quantified by the twist density Tw_i, and/or in a global supercoiling of the centreline itself, as measured by the writhe integral Wr_i. It should be noted that the linking number Lk_i is generally not a topological invariant in the case of non-circular DNA fragments. Within the origami filament architecture, Lk_i is initially constrained by the designed locations of the inter-helical crossovers, but may partially relax towards its preferred unhindered value Lk_0 — thus inducing a global axial twist in the origami ground state (c.f. Section 6.1.1).

Within ground-state B-DNA, the relaxed linking number Lk_0 is entirely absorbed in the form of twist strain,

$$\mathrm{Lk}_0 = \mathrm{Tw}_0 \simeq \frac{1}{10.5}\,\mathrm{bp}^{-1}. \tag{6.11}$$

The axial twist handedness of an origami filament comprised of duplexes with linking number Lk_i is therefore determined by the sign of $\Delta\mathrm{Lk}_i \equiv \mathrm{Lk}_i - \mathrm{Lk}_0$, with $\Delta\mathrm{Lk}_i > 0$ ($\Delta\mathrm{Lk}_i < 0$) respectively denoting a residual over-winding (under-winding) of the duplexes, associated with a global left-handed (right-handed) compensatory twist of the origami. The total elastic energy U_i of a constituent duplex, as defined by an arbitrary centreline curve $\mathbf{r}_i$ and uniform twist density Tw_i, may be obtained as a straightforward generalisation of Eq. (F.22) [309],

$$U_i = \frac{1}{2}\int_0^{l_i} ds_i \left\{ \mathcal{K}_i \left\| \frac{d^2\mathbf{r}_i}{ds_i^2} \right\|^2 + 4\pi^2 C_i \Big(\mathrm{Tw}_i - \mathrm{Tw}_0 \Big)^2 \right\},$$

Table 6.1: Isotropic/cholesteric coexistence concentrations for thermalised untwisted origamis. $c_{\mathrm{st+el}}$ and c_{st} denote the theoretical predictions obtained by taking into account steric inter-particle repulsion with and without electrostatic interactions, respectively. Results are compared with the experimental measurements of Ref. [221].

binodal	c_{st}	$c_{\mathrm{st+el}}$	Ref. [221]
isotropic	31.8 g/L	28.3 g/L	28 g/L
cholesteric	36.7 g/L	32.2 g/L	37 g/L

with $\mathcal{K}_i$ and C_i the respective effective bending and twisting moduli of B-DNA within the origami structure. Eqs. (6.10) and (6.11) immediately yield

$$U_i = \frac{\mathcal{K}_i}{2}\int_0^{l_i} ds_i \left\| \frac{d^2\mathbf{r}_i}{ds_i^2} \right\|^2 + 2\pi^2 C_i l_i \Big(\Delta\mathrm{Lk}_i - \mathrm{Wr}_i\Big)^2 . \tag{6.12}$$

It is evident that the twist elastic contribution in Eq. (6.12) is minimised by conformations in which $\Delta\mathrm{Lk}_i$ and Wr_i bear equal sign and magnitude, leading to a favoured positive (right-handed) supercoiling in the case of left-twisted origamis ($\Delta\mathrm{Lk}_i > 0$, $\mathrm{Wr}_i > 0$), and negative (left-handed) supercoiling for their right-handed counterparts ($\Delta\mathrm{Lk}_i < 0$, $\mathrm{Wr}_i < 0$). However, this twist relaxation mechanism is hindered by the high penalty in bending energy arising from the curvature of the resulting solenoidal centreline deformations. The competition of these two effects, acting constructively on each duplex within the origami structures, leads to the weak anti-chiral backbone fluctuations underpinning their LCLC assembly.

In this framework, the observed offset in the filament phase-handedness inversion behaviour, apparent in Figure 6.3d, could thus be partially explained in terms of a small misestimate of Tw_0, as the equilibrium helical pitch of B-DNA within constrained origami structures may slightly differ from the unconfined value $1/\mathrm{Tw}_0 \simeq 10.5\,\mathrm{bp}$ assumed in both the computation of the origami ground states [305] and the parametrisation of the oxDNA model [212]. Additional possible sources of error include other potential shortcomings of the oxDNA model, such as our use of sequence-averaged mechanics for DNA or the limitation of soft non-bonded interactions to simple DH electrostatics [212]. The overestimations in the magnitude of our cholesteric pitch predictions (Figure 6.3d) are further consistent with the symmetry limitations of the theory, in which long-ranged biaxial correlations

arising from broken local cylindrical invariance are neglected (c.f. Chapter 3). The limited extent of these discrepancies, relative to the vast gap between molecular and cholesteric length-scales, combined with the satisfactory experimental agreement achieved in terms of isotropic/cholesteric binodal concentrations (Table 6.1), nonetheless evidence the ability of the theory to correctly capture the basic physics of LCLC assembly in our case.

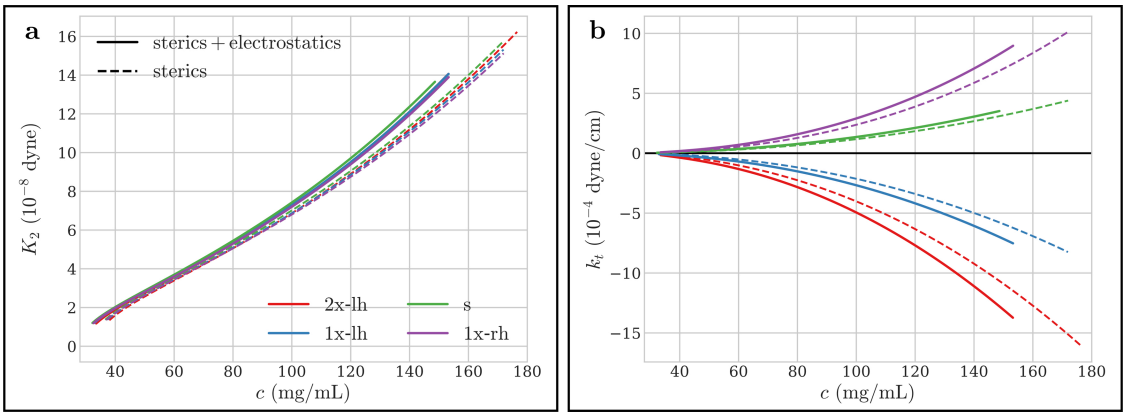

Figure 6.7: Twist elastic modulus and chiral strength of thermalised 6-HB origamis. a) Oseen-Frank twist modulus as a function of particle concentration for the different thermalised origami variants. b) Same as a) for the chiral strength.

We also reproduce in Figure 6.7 the density dependence of the Oseen-Frank twist elastic modulus K_2 and chiral strength k_t in the case of thermalised origami filaments, computed following the procedure of Section 5.1.3. The orders of magnitudes of the obtained values are in very good agreement with experimental measurements performed in filamentous virus solutions [54], whose molecular dimensions, relative flexibility and absolute cholesteric pitches are comparable to those of the origamis [221]. The general tendencies apparent in Figure 6.7 are also consistent with experimental results on virus assemblies, with both K_2 and k_t displaying a marked increase in magnitude with increasing particle concentration [54]. The observed stiffening of twist curvature elasticities upon the inclusion of electrostatic repulsion (Figure 6.7a) further mirrors the experimental variations of K_2 with decreasing salt concentration in such systems [54]. The precise experimental determination of these quantities in LCLC phases of origami filaments would be desirable for the

thorough investigation of these effects, and for further quantitative comparisons with the theoretical predictions of Figure 6.7.

6.3 The cholesteric behaviour of 10-HB origamis

Finally, we briefly discuss the cholesteric assembly of 10-HB origamis comprised of 14 493 to 15 035 nucleotides, with contour lengths of 250 nm and near-rectangular cross sections of dimensions 6 nm × 10 nm [221]. As in Section 6.2, we consider different origami designs engineered to bear various degrees of uniform twist in their respective ground-state structures, ranging from 720° left-handed (2x-lh) to 720° right-handed (2x-rh) axial turns by 360° increments (Figure 6.8). We similarly sample the origami conformational space through single-filament oxDNA simulations, using equilibration runs of $\mathcal{O}(10^6)$ MD steps and production runs of $\mathcal{O}(10^8)$ steps to generate $\mathcal{O}(10^2)$ uncorrelated conformations for each origami variant.

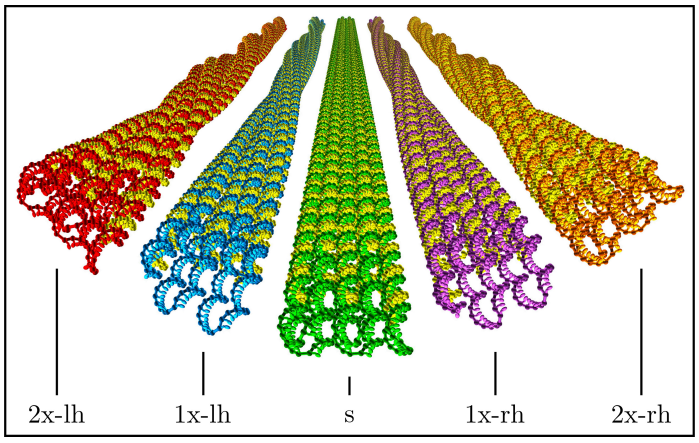

Figure 6.8: Ground-state 10-HB origami conformations (c.f. Figure 6.2).

Note that due to computational constraints, these values are roughly one order of magnitude lower than those employed in Section 6.2.3 for the conformational statistics of 6-HB origamis. The results of this section should therefore be regarded as somewhat preliminary, as a bootstrapping analysis analogous to that in Section 6.2.3 would be necessary to probe the statistical representativity of the simulated ensembles of 10-HB conformations. These issues are however likely to be mitigated by the greater rigidity of the 10-HB filaments, which significantly restricts their

accessible conformational space respective to that of their 6-HB counterparts, as discussed in the next paragraphs.

We reproduce in Figure 6.9 the theoretical cholesteric pitches of thermalised 10-HB origamis. We observe that the shorter aspect ratios of such particles leads to their formation of a stable ordered phase at significantly-higher densities than the previous 6-HB designs (Figure 6.3). Remarkably, we predict 10-HB filaments to favour anti-chiral LCLC assemblies — bearing the opposite handedness to the axial twist of their respective ground states. This tendency is now consistent with the results of Section 4.2.2 for weakly-twisted HTCs, but is in stark contrast with the preferred iso-chiral arrangements reported in Section 6.2 for thermalised 6-HB origamis.

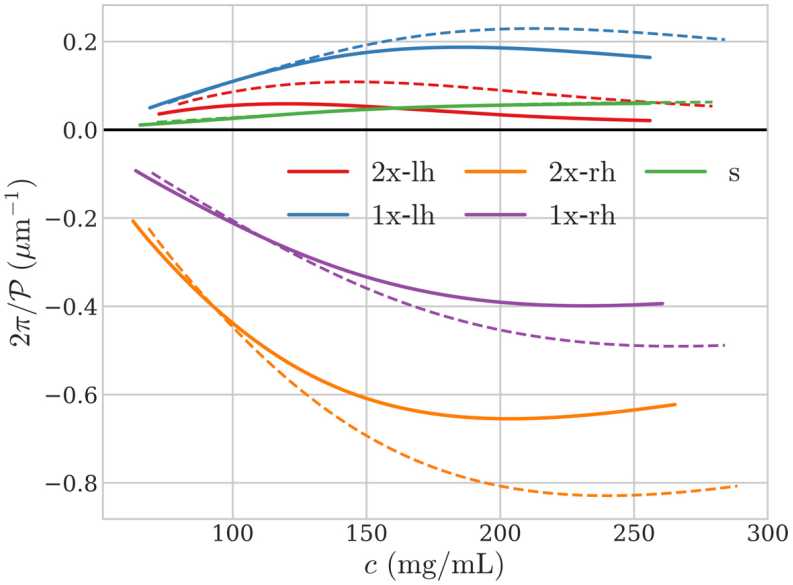

Figure 6.9: Inverse equilibrium cholesteric pitch $\mathcal{P}$ as a function of particle concentration c for thermalised 10-HB filaments.

This surprising result may attributed to the wider cross section of the 10-HB origamis, which leads to a marked increase in both their flexural rigidity and in the effective groove depth associated with their axial twist. Indeed, while their cross-section anisotropy does generally not allow for the description of their bending stiffness in terms a simple persistence length [310], it is apparent from Figures 6.10a–c that the transverse fluctuations of 10-HB filaments are considerably weaker in amplitude than those of their 6-HB counterparts (Figure. 6.6) for all deformation

modes. Therefore, although both origami designs display a similar bias towards long-wavelength, anti-chiral backbone deformations (Figures 6.10d and 6.6c), the mean radius $\langle r_m \rangle$ of the corresponding solenoidal modes (Eq. (F.20)) is of the order of just 1 nm at the smallest accessible wavenumbers for the 10-HB variants (Figure 6.10a).

This value is significantly smaller than the groove depth $\Delta \simeq 3\,\mathrm{nm}$ of their twisted ground-state conformations, obtained from Eq. (4.8) by assimilating their cross section to that of a similarly-dimensioned HTC in the continuum limit, and is in this case too low for conformational fluctuations to dominate over ground-state structure in their LCLC ordering. Furthermore, Δ is also in large excess of the Debye length $\lambda_{\mathrm{DH}} \simeq 0.6\,\mathrm{nm}$ for the 10-HB systems considered here, which now accounts for the limited impact of the inclusion of electrostatics on the magnitude of their predicted cholesteric pitches, consistently with the considerations of Figure 6.5.

In this HTC analogy, the thread angles ν associated with the 360° and 720° twists of ground-state 10-HB filaments may be respectively estimated as 82° and 74° using Eq. (4.4). Therefore, the 2x-lh and 2x-rh origami variants both fall within the geometric regime $\nu \in [70°, 80°]$, for which the tightest cholesteric pitches of HTC assemblies were obtained in Section 4.2. The LCLC behaviour of the 2x-lh origamis is thus rather intriguing, as their loosely-wound phase is found to bear a pitch of comparable magnitude to that of the untwisted (s) filaments (Figure 6.9).

While this observation could be potentially interpreted in terms of the competition between ground-state and fluctuation-induced chirality in their cholesteric organisation, the strong asymmetry visible in the predicted pitches of the 2x-rh and 2x-lh variants cannot be easily explained by such simple mechanical arguments. These effects could be partially attributable to our limited conformational statistics for the 10-HB origamis, and more extensive numerical studies would be required for their further investigation. Experimental measurements of the cholesteric pitch and its density dependence were regrettably not performed in Ref. [221] for 10-HB filaments, and would also be highly desirable for the thorough appraisal of our theoretical predictions for such systems.

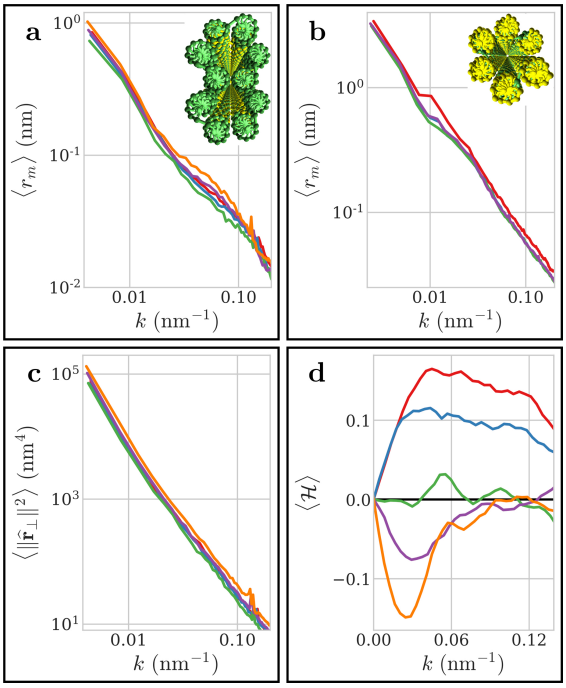

Figure 6.10: Conformational fluctuations and solenoidal writhe of 10-HB origamis. a) Mean solenoidal radius $\langle r_m \rangle$ as a function of deformation wavenumber k for 10-HB origamis. Inset: cross section of a ground-state untwisted (s) 10-HB origami. b) Same as a) for 6-HB origamis. c) Transverse fluctuation spectrum of 10-HB origamis (c.f. Figure 6.6b). d) Net backbone helicity $\langle \mathcal{H} \rangle$ of 10-HB origamis (c.f. Figure 6.6c).

6.4 Conclusion

In this chapter, we have presented the successful application of an extended Onsager theory to the quantitative description of LCLC order in systems of long DNA origami filaments. Its combination with an accurate conformational sampling scheme demonstrates that phase chirality in the case of 6-HB assemblies results from the weak, fluctuation-stabilised solenoidal writhing of the filament backbones, and is therefore largely governed by intra-molecular mechanics. This conclusion represents a marked shift from the prevailing theoretical models, in which the macroscopic breaking of mirror symmetry has generally been attributed to the inter-molecular interactions arising from the chiral structure of the molecular ground state [92, 93, 278]. The link between ground-state and fluctuation-induced chirality is further shown to be non-trivial, as illustrated by the stabilisation of anti-chiral deformation modes through twist-writhe conversion of the filament elastic energy.

This chirality amplification process is grounded in the basic statistical mechanics of the constrained duplexes within each folded origami, and should therefore be quite generally applicable to other supra-molecular assemblies of chiral filament bundles, whose ground-state morphologies have been shown to be widely governed by similar geometric frustration mechanisms [311]. Our findings could thus provide a theoretical basis for the so-called "corkscrew model", previously postulated to explain the puzzling experimental behaviour of filamentous virus suspensions [52] and further discussed in Chapter 7, and more broadly suggest a novel self-assembly paradigm for LCLCs in which subtle, long-wavelength conformational features — rather than local chemical structure — dictate macroscopic chiral organisation.

7 Conclusion

In this thesis, we have introduced an extensive numerical and theoretical framework based on classical DFT to work out the emergent macroscopic properties of uniaxial nematic and cholesteric phases from that of their microscopic constituent mesogens. The Onsager theory is generalised to systems of hard particles with finite shape anisotropy through the use of the decoupling approximation at the level of the direct correlation function. Its combination with the Carnahan-Starling equation of state results in the introduction of a novel corrective prefactor in the self-consistent equation determining the equilibrium density field, although the corresponding free energy reduces to the standard Parsons-Lee expression.

While this prefactor is found to lead to significant gains in accuracy over previous theoretical descriptions for the uniaxial nematic assembly of faceted triangular prisms, further numerical investigations would be desirable to systematically assess the quantitative validity of the different approaches for a greater range of particle models. We also emphasise the general unsuitability of existing theories for the treatment of non-convex mesogens with limited aspect ratios, due to both the inherent ambiguity in the definition of their distance of closest approach and the analytical difficulties involved in the derivation of their geometric excluded volume [118].

The extension of the theory to the cholesteric phase is performed in the Poniewierski-Stecki/Straley formalism, which revolves around the assumptions that

(i) the distribution of particle centres of mass and (ii) the degree of local orientational order both remain unaffected by director fluctuations. The perturbative treatment of phase chirality underlying approximation (ii) is shown to be quantitatively accurate for cholesteric pitches as short as a few dozen particle diameters, and is therefore expected to be appropriate for the description of experimentally-relevant systems. The predictions of the method in terms of the Oseen-Frank elastic moduli are found to be in good quantitative agreement with the results of molecular simulations for calamitic particles with low-to-moderate aspect ratios, although the effects of assumption (i) remain largely untested in the case of highly-elongated molecules [159]. These considerations have been suggested to be less significant for the twist director deformations characteristic of LCLCs [158], but would nonetheless deserve further investigations.

Another interesting avenue for future research lies in the assessment of the role of long-ranged biaxial correlations on cholesteric order [65]. While the generalisation of the methods of Chapter 2 to biaxial nematic phases would be conceptually straightforward, their application to the treatment of non-uniform director fields would require the use of a molecular description of biaxial nematic elasticities [18]. Such theories have been previously derived [312], but have to our knowledge never successfully implemented in practice. The numerical procedure of Chapter 3 could thus provide a convenient framework to directly probe these issues for a broad variety of mesogen models, as discussed further below.

The combination of this density-functional approach with an efficient virial integration scheme based on bounding volume hierarchies enables us to investigate the LCLC assembly of highly-anisotropic particles with a degree of molecular complexity beyond the reach of both pure analytical descriptions and previous numerical studies. The application of the method to systems of hard, structurally-resolved twisted cuboids allows us to provide quantitative evidence of the long-predicted phase handedness inversion with increasing particle thread angles near the phenomenological threshold value of 45°. Our results further highlight the complex relationship between microscopic structure and helical twisting power in

such model systems, which may be attributed to subtle geometric variations of their chiral excluded-volume manifold.

The effects of particle flexibility are accounted for in the DFT framework of Fynewever and Yethiraj [241], which allows for a full account of the microscopic particle Hamiltonian by introducing conformational statistics through the use of single-chain molecular simulations. The location of the isotropic-to-nematic phase transition is found to be in good agreement with numerical results for elongated chains up to relatively high polymer flexibilities, although the predictions of the theory in the nematic regime lead to gradual underestimations of order parameters with decreasing particle stiffness. This shortcoming is attributed to increasing overestimations of the molecular conformational entropy in higher-density phases, which may not be easily addressed in the formalism of DFT for realistic particle models. Practical consequences of these limitations are illustrated through the application of the approach to systems of near-persistence-length DNA duplexes, whose cholesteric behaviour is found to be strongly contingent on their detailed accessible conformational space in concentrated solutions.

We finally apply the method to cholesteric assemblies of DNA origamis, whose large aspect ratios and bending rigidity naturally fall within the regime of applicability of the theory. The use of the well-established oxDNA model to represent the structure and mechanics of DNA within our DFT description enables us to achieve near-quantitative agreement with experimental measurements in terms of equilibrium cholesteric pitches and isotropic-cholesteric coexistence concentrations, while displaying sensible values for the Oseen-Frank elastic moduli and chiral strength. Our results further reveal that the macroscopic cholesteric behaviour is in this case driven by long-wavelength solenoidal fluctuations of the origami backbone, which may be related to the chiral structure of the molecular ground state in a non-trivial fashion.

Although the absence of explicit solvent effects and the coarse-grained treatment of inter-molecular interactions in the oxDNA model are likely somewhat simplistic, especially regarding the limited Debye-Hückel description of electrostatics, our

results are found to be remarkably insensitive to the short-ranged details of the inter-origami repulsive potential once the effects of particle flexibility are included. This observation points to the potential applicability of this original chirality amplification mechanism irrespective of the specific surface chemistry of the mesogens, and would suggest that current microscopic theories based solely on the local chiral interactions between idealised ground-state conformations may be fundamentally ill-suited to resolve the origins of phase chirality in molecular systems of finite stiffness.

The net helicity of these backbone fluctuations is shown to originate from the weak over- or under-winding of the constituent duplexes in the origami ground state, which reflect the geometric frustration governing equilibrium morphology in cohesive bundles of generic chiral filaments [311]. Such aggregates may be found in the molecular structure of a number of flexible cholesteric mesogens, ranging from amyloid fibrils [313] to the protein coat of filamentous viruses [52]. The LCLC assembly of such colloids could therefore be expected to be similarly affected by potential solenoidal deformation modes, thus giving credence to the hypothetical "corkscrew model" proposed in Ref. [52]. However, the quantitative assessment of these considerations and of their effects on the cholesteric pitch of such systems would require the development of mechanical models capable of accurately capturing their respective conformational statistics, and would likely entail significant experimental and theoretical efforts.

More generally, the theoretical framework presented in this thesis, together with the experiments of Ref. [221], opens up a new approach to systematically explore the link between microscopic mesogen properties and macroscopic chiral organisation. The combination of the unique ability of DNA origamis to assemble into programmable shapes of near-arbitrary complexity with the power of our multi-scale description to elucidate their phase behaviour enables us to directly investigate a broad range of liquid-crystalline phenomena. For instance, the juxtaposition of experiments and theory for the LCLC assembly of twisted origami filaments with varying cross-section anisotropy would allow us to quantitatively address the

long-standing question of the causal link between biaxiality and phase chirality, and of its macroscopic implications for the cholesteric pitch.

The inclusion of biaxial order in the theory would also constitute a necessary prerequisite for the treatment of more involved assemblies beyond the cholesteric symmetry, such as the elusive twist-bend phase [199] — and could in turn guide the experimental stabilisation of such structures, in light of the high current costs of bulk origami synthesis. Therefore, we hope that the detailed discussions of this thesis will provide a useful resource to help palliate the highly-scattered nature of the literature on the physics of lyotropic LCs, and will motivate further concerted efforts towards the rational, bottom-up design of complex colloid-based macroscopic materials.

Appendices

A

$SO(3)$ parametrisation and sampling

Contents

A.1 Euler angle conventions

Davenport's rotation theorem [314] states that the orientation of a rigid body in three-dimensional space may be uniquely decomposed into elemental rotations about any three given axes, provided that the second axis is perpendicular to the other two. This loose constraint gives rise to a multitude of definitions for the corresponding Euler (or Tait-Bryan) angles in the literature, between which inter-conversions are generally not straightforward. Here, we assume the molecular frame $\mathcal{R} \equiv \left[\mathbf{v}\ \mathbf{w}\ \mathbf{u}\right]$ to be initially aligned with the laboratory frame $\mathcal{R}_{\text{lab}} \equiv \left[\mathbf{e}_x\ \mathbf{e}_y\ \mathbf{e}_z\right]$, and sample the orientation space $SO(3)$ by rotating the particle by an angle α about $\mathbf{e}_z$, followed by a rotation of angle θ about $\mathbf{e}_y$, and a final rotation of angle ϕ about $\mathbf{e}_z$. In this so-called z-y-z convention, the parametrisation of $\mathcal{R}$ therefore takes the general form

$$\mathcal{R} = \mathcal{R}_z(\phi) \cdot \mathcal{R}_y(\theta) \cdot \mathcal{R}_z(\alpha), \tag{A.1}$$

where we used the associativity of the matrix product, with $\mathcal{R}_k(x)$ the rotation matrix of angle x and axis $\mathbf{e}_k$. Eq. (A.1) then leads to the relation

$$\mathcal{R} = \begin{bmatrix} \cos\alpha\cos\theta\cos\phi - \sin\alpha\sin\phi & -\sin\alpha\cos\theta\cos\phi - \cos\alpha\sin\phi & \sin\theta\cos\phi \\ \cos\alpha\cos\theta\sin\phi + \sin\alpha\cos\phi & -\sin\alpha\cos\theta\sin\phi + \cos\alpha\cos\phi & \sin\theta\sin\phi \\ -\cos\alpha\sin\theta & \sin\alpha\sin\theta & \cos\theta \end{bmatrix}, \tag{A.2}$$

whose column vectors provide explicit expressions for the molecular axes $\mathbf{u}$, $\mathbf{v}$ and $\mathbf{w}$ as a function of α, θ and ϕ. Note that it is easy to check from Eq. (A.2) that

$$\mathcal{R}(\alpha, 2\pi - \theta, \phi) = \mathcal{R}(\alpha + \pi, \theta, \phi + \pi) \qquad \forall(\alpha, \theta, \phi) \in [0, 2\pi]^3, \tag{A.3}$$

so that the polar angle θ must be restricted to the interval $[0, \pi]$ to ensure the uniqueness of this parametrisation on $SO(3)$.

A.2 Uniform sampling of $SO(3)$

For the accurate computation of the configurational integrals underlying much of this thesis, it is essential to enforce a proper sampling of particle orientations so as to avoid any statistical bias in the evaluation of the corresponding integrands. For this purpose, a convenient alternative parametrisation of $SO(3)$ may be obtained by recasting Eq. (A.1) in the form

$$\mathcal{R} = \mathcal{R}_{\mathbf{u}} \cdot \mathcal{R}_z(\alpha), \tag{A.4}$$

with $\mathcal{R}_{\mathbf{u}} \equiv \mathcal{R}_z(\phi) \cdot \mathcal{R}_y(\theta)$ a rotation matrix mapping the laboratory axis $\mathbf{e}_z$ onto the molecular axis $\mathbf{u}$. In this context, let us recall the simple following observation, elicited in Ref. [315]:

> *To generate uniformly-distributed random rotations of a unit sphere, first perform a random rotation about the vertical axis, then rotate the north pole to a random position.*

Using the previous notations, the uniform sampling of angular integrals may thus be achieved by drawing internal rotation angles α uniformly in $[0, 2\pi]$ and ensuring the uniform distribution of molecular polar axes $\mathbf{u}$ on the surface $\mathcal{S}$ of the unit sphere,

$$\oint d\mathcal{R} \cdot = \int_0^{2\pi} d\alpha \oint_{\mathcal{S}} d\mathbf{u} \cdot , \tag{A.5}$$

where $\mathbf{u}$ may be expressed in terms of the Euler angles θ and ϕ through Eq. (A.2),

$$\mathbf{u} \equiv \mathcal{R} \cdot \mathbf{e}_z = \begin{bmatrix} \sin\theta\cos\phi \\ \sin\theta\sin\phi \\ \cos\theta \end{bmatrix}. \tag{A.6}$$

One recognises in Eq. (A.6) the standard Cartesian-to-spherical coordinate transformation for unit vectors, with Jacobian determinant equal to $\sin\theta$. The corresponding change of variable in Eq. (A.5) immediately yields

$$\oint d\mathcal{R} \cdot = \int_0^{2\pi} d\alpha \int_0^{2\pi} d\phi \int_0^{\pi} \sin\theta d\theta \cdot , \tag{A.7}$$

from which we recover the so-called Haar measure on $SO(3)$ [316], which immediately yields the volume $V_{SO(3)}$ of the particle orientational space,

$$V_{SO(3)} = \oint d\mathcal{R} = 8\pi^2. \tag{A.8}$$

B

The Mayer cluster expansion

Contents

B.1 Excess free energy expansion

Let us start from the diagrammatic expansion in Eq. (2.25). Using the homogeneity of space in Eqs. (2.20) and (2.21), one may write

$$\begin{aligned}\langle f_{ij}\rangle &= \frac{1}{(8\pi^2 V)^2}\iint_{V^2} d\mathbf{r}_i d\mathbf{r}_j \oiint d\mathcal{R}_1 d\mathcal{R}_2\, f(\mathbf{r}_1,\mathbf{r}_2,\mathcal{R}_1,\mathcal{R}_2)\\ &= \frac{1}{8\pi^2 V}\int_V d\mathbf{r}_{ij}\oint d\mathcal{R}_{ij}\, f(\mathbf{r}_{ij},\mathcal{R}_{ij}),\end{aligned} \tag{B.1}$$

with $\mathbf{r}_{ij} \equiv \mathbf{r}_j - \mathbf{r}_i$ the centre-of-mass separation vector and $\mathcal{R}_{ij} \equiv \mathcal{R}_i^{\mathsf{T}} \cdot \mathcal{R}_j$ the orientation of particle j relative to the molecular frame of particle i. Before computing the corresponding excess free energy $\mathscr{F}_{\text{ex}}$, it is instructive to investigate

the density dependence of some of the terms in Eq. (2.25). For instance,

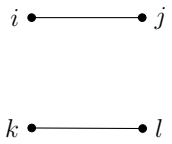

$$
\begin{aligned}
&= \frac{1}{(8\pi^2 V)^2} \sum_{\substack{\{(i,j),(k,l)\} \\ i,j \notin (k,l)}} \sum \iint_{V^2} d\mathbf{r}_{ij} d\mathbf{r}_{kl} \oiint d\mathcal{R}_{ij} d\mathcal{R}_{kl}\, f(\mathbf{r}_{ij}, \mathcal{R}_{ij}) f(\mathbf{r}_{kl}, \mathcal{R}_{kl}) \\
&= \frac{1}{(8\pi^2 V)^2} \times 3 \binom{N}{4} \left\{ \int_V d\mathbf{r}_{12} \oint d\mathcal{R}_{12}\, f(\mathbf{r}_{12}, \mathcal{R}_{12}) \right\}^2 \qquad \text{(B.2)} \\
&\propto N^2,
\end{aligned}
$$

where we used Eq. (B.1), with $\binom{N}{4} \propto N^4$ and $V \propto N$ in the thermodynamic limit. To ensure the extensivity of the free energy,

$$\mathscr{F}_{\text{ex}} \propto N,$$

the contribution of Eq. (B.2) to $\mathscr{F}_{\text{ex}}$ must therefore be cancelled out by other terms in the full expansion of Eq. (2.13) from Eq. (2.25).

More generally, the Goldstone theorem [108] states that on the basis of the classical identity

$$\log(1+x) = \sum_{n=1}^{\infty} (-1)^{n+1} \frac{x^n}{n}, \qquad \text{(B.3)}$$

none of the disconnected diagrams appearing in Eq. (2.25) may survive in the final expression for the excess free energy — i.e., in the diagrammatic representation of $\log Q_N$. A lengthy mathematical analysis of this expansion further reveals that only the so-called *one-particle-irreducible diagrams* — which cannot be separated into disconnected parts by the removal of any single vertex — may physically contribute to $\mathscr{F}_{\text{ex}}$ [103]. Following in the footsteps of van Kampen [317], we outline in the following two sections a more direct derivation of these remarkable properties in the case of particles interacting through short-ranged potentials.

B.2 Second-virial configurational integral

The starting point of the method lies in the following identity, which directly results from Eqs. (B.1) and (B.2),

$$\langle (1+f_{12})(1+f_{13}) \rangle = \langle 1+f_{12} \rangle \langle 1+f_{13} \rangle = \langle 1+f_{12} \rangle^2.$$

This factorisation is generally invalid for products of the f_{ij} involving more than one shared particle, due to the correlations between configurational degrees of freedom arising from the associated pair interactions u_{ij}. However, one may postulate that

$$\langle (1+f_{12})(1+f_{13})(1+f_{23})\rangle \simeq \langle 1+f_{12}\rangle\langle 1+f_{13}\rangle\langle 1+f_{23}\rangle. \tag{B.4}$$

Indeed, the equality in Eq. (B.4) is strict whenever one of the f_{ij} is replaced by 0 — i.e., if one of the three pairs of particles is not interacting. Since the probability for three or more particles to interact simultaneously vanishes at low concentrations for short-ranged potentials, Eq. (B.4) is thus expected to hold reasonably well in the low-density regime in this case. The recursive application of this argument to the full product in Eq.(2.19) yields a first approximation for Q_N,

$$Q_N = \left\langle \prod_{i<j}(1+f_{ij}) \right\rangle \equiv CQ, \tag{B.5}$$

with

$$C \equiv \frac{\left\langle \prod_{i<j}(1+f_{ij})\right\rangle}{\prod_{i<j}\langle 1+f_{ij}\rangle} \simeq 1 \equiv C^{(1)}, \tag{B.6}$$

and Q the *second-virial configurational integral*,

$$\begin{aligned} Q &\equiv \prod_{i<j}\langle 1+f_{ij}\rangle = \langle 1+f_{12}\rangle^{N(N-1)/2} \\ &= \left\{ 1 + \frac{\rho}{N}\int_V d\mathbf{r}_{12} \oint d\mathcal{R}_{12}\, f(\mathbf{r}_{12},\mathcal{R}_{12}) \right\}^{N(N-1)/2}, \end{aligned} \tag{B.7}$$

where we used Eq. (B.1) and $V = N/(8\pi^2\rho)$. Recalling the identity

$$e^x = \lim_{n\to\infty}\left(1+\frac{x}{n}\right)^n, \tag{B.8}$$

Eqs. (B.7) and (B.8) yield, in the thermodynamic limit,

$$\begin{aligned} Q &= \exp\left\{ \frac{N(N-1)}{2}\frac{1}{8\pi^2 V}\int_V d\mathbf{r}_{12}\oint d\mathcal{R}_{12}\, f(\mathbf{r}_{12},\mathcal{R}_{12}) \right\} \\ &= \exp\left(\bullet\!\!-\!\!-\!\!-\!\!-\!\!\bullet \right), \end{aligned} \tag{B.9}$$

where we substituted Eq. (2.23) in the exponential.

B.3 Many-body correction factors

A first correction to Eq. (B.6) may be obtained by accounting for three-particle correlations, previously neglected in the approximation of Eq. (B.4). The application of Eq. (B.4) in Eq. (B.5) requires the introduction of a cumulative correction term $C^{(2)}_{ijk}$,

$$C^{(2)}_{ijk} = \frac{\langle (1+f_{ij})(1+f_{ik})(1+f_{jk})\rangle}{\langle 1+f_{ij}\rangle\langle 1+f_{ik}\rangle\langle 1+f_{jk}\rangle}, \tag{B.10}$$

by which each particle triplet (i,j,k) factored in the right-hand side of Eq. (B.5) needs to be multiplied to compensate the errors underlying this approximation. Using Eq. (B.10),

$$\begin{aligned} C^{(2)}_{ijk} = C^{(2)}_{123} &= \frac{\langle (1+f_{12})(1+f_{13})(1+f_{23})\rangle}{\langle 1+f_{12}\rangle^3} \\ &= \frac{1+3\langle f_{12}\rangle + 3\langle f_{12}\rangle^2 + \langle f_{12}f_{13}f_{23}\rangle}{1+3\langle f_{12}\rangle + 3\langle f_{12}\rangle^2 + \langle f_{12}\rangle^3}, \end{aligned} \tag{B.11}$$

where $\langle f_{12}\rangle \propto 1/V$ and

$$\begin{aligned} \langle f_{12}f_{13}f_{23}\rangle &= \frac{1}{(8\pi^2 V)^2}\iint_{V^2} d\mathbf{r}_{12}d\mathbf{r}_{13}\oiint d\mathcal{R}_{12}d\mathcal{R}_{13}\, f(\mathbf{r}_{12},\mathcal{R}_{12})f(\mathbf{r}_{13},\mathcal{R}_{13})f(\mathbf{r}_{23},\mathcal{R}_{23}) \\ &\propto \frac{1}{V^2}. \end{aligned}$$

Differentiating Eq. (B.3) with respect to x yields the identity

$$\frac{1}{1+x} = \sum_{n=0}^{\infty}(-1)^n x^n, \tag{B.12}$$

which enables us to perform the Taylor expansion of Eq. (B.11) in the thermodynamic limit,

$$\begin{aligned} C^{(2)}_{ijk} &= \Big(1+3\langle f_{12}\rangle + 3\langle f_{12}\rangle^2 + \langle f_{12}f_{13}f_{23}\rangle\Big)\times\Big\{1-3\langle f_{12}\rangle + 6\langle f_{12}\rangle^2 + \mathcal{O}\big(V^{-3}\big)\Big\} \\ &= 1+\langle f_{12}f_{13}f_{23}\rangle + \mathcal{O}\big(V^{-3}\big). \end{aligned}$$

A second approximation for the total correction factor C (Eq. (B.6)) is then given by

$$C^{(2)} = C^{(1)}\prod_{\{i,j,k\}} C^{(2)}_{ijk} = \Big(1+\langle f_{12}f_{13}f_{23}\rangle\Big)^{N(N-1)(N-2)/6},$$

where the factorial runs over the set of $\binom{N}{3}$ distinct particle triplets $\{i, j, k\}$ such that $i < j < k$. Thus, using Eq. (B.8),

$$C^{(2)} = \exp\left\{\frac{N(N-1)(N-2)}{6}\langle f_{12}f_{13}f_{23}\rangle\right\} = \exp\left(\quad\right), \tag{B.13}$$

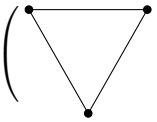

and the partition function Q_N may be obtained from Eqs. (B.5), (B.9) and (B.13),

$$Q_N = CQ = \exp\left[\quad + \quad + \mathcal{O}\left(\left\{\quad\right\}^4\right)\right],$$

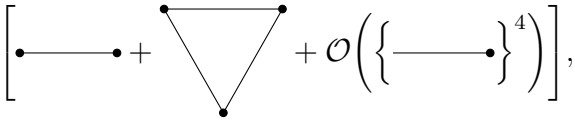

where the $\mathcal{O}(\cdot)$ notation accounts for four-and-more-body terms, which may be determined recursively following a similar procedure to $C^{(2)}$ [317]. Hence, all reducible and disconnected diagrams appearing in Eq. (2.25) vanish in the expansion of $\log Q_N$.

C

The Ornstein-Zernike equation

Contents

C.1 Density-density correlation function

Let us derive the Ornstein-Zernike (OZ) equation in the formalism of Chapter 2. For the purposes of this calculation, it is convenient to introduce a "perturbed" Hamiltonian $\mathscr{H}_N^{(\Phi)}$, in which every particle is coupled to an arbitrary external field $\Phi(\mathbf{r}, \mathcal{R})$, which may eventually be set to $\Phi = 0$ to recover the intrinsic Hamiltonian $\mathscr{H}_N$ of Chapter 2 (Eq. (2.1)). This mathematical artifice is closely related to Bogoliubov's so-called *quasi-average method* for the treatment of spontaneous symmetry breaking transitions [318], and is quite commonly used in statistical field theories of condensed matter systems. Thus,

$$\mathscr{H}_N^{(\Phi)} = \mathscr{H}_N + \sum_{i=1}^{N} \Phi(\mathbf{r}_i, \mathcal{R}_i) = \mathscr{H}_N + \int_V d\mathbf{r} \oint d\mathcal{R}\, \rho_m(\mathbf{r}, \mathcal{R}) \Phi(\mathbf{r}, \mathcal{R}), \tag{C.1}$$

with ρ_m the microscopic density operator (Eq. (2.37)). The canonical partition function of the system may be obtained from Eqs. (2.7)–(2.10),

$$Z_N^{(\Phi)} = \frac{1}{\lambda^{3N} N!} \int d\{\mathcal{X}_i\} \, \exp\Big[- \beta U_N\big(\{\mathcal{X}_i\}\big) - \beta \int d\mathcal{X} \, \rho_m(\mathcal{X}) \Phi(\mathcal{X}) \Big] \tag{C.2}$$

where we used the generalised configurational coordinates $\mathcal{X} \equiv \{\mathbf{r}, \mathcal{R}\}$. The functional differentiation of Eq. (C.2) yields

$$\begin{aligned} \frac{\delta Z_N^{(\Phi)}}{\delta \Phi(\mathcal{X})} &= -\beta \frac{1}{\lambda^{3N} N!} \int d\{\mathcal{X}_i\} \, \rho_m(\mathcal{X}) \exp\Big\{ - \beta \Big[U_N + \int d\mathcal{X} \, \rho_m(\mathcal{X}) \Phi(\mathcal{X}) \Big] \Big\} \\ &= -\beta Z_N^{(\Phi)} \Big\langle \rho_m(\mathcal{X}) \Big\rangle_N^{(\Phi)}, \end{aligned} \tag{C.3}$$

with $\langle \cdot \rangle_N^{(\Phi)}$ the *canonical average* (Eqs. (2.2) and (2.5)),

$$\Big\langle \, \cdot \, \Big\rangle_N^{(\Phi)} \equiv \frac{1}{Z_N^{(\Phi)}} \frac{1}{h^{6N} N!} \int_{-\infty}^{+\infty} d\{\mathbf{p}_i\} \int_{-\infty}^{+\infty} d\{\boldsymbol{\ell}_i\} \int d\{\mathcal{X}_i\} \, e^{-\beta \mathscr{H}_N^{(\Phi)}} \cdot \, . \tag{C.4}$$

The equilibrium density distribution $\rho_{\mathrm{eq}}^{(\Phi)}$ may then be defined as the Boltzmann-weighted microscopic density $\langle \rho_m \rangle_N^{(\Phi)}$ [108],

$$\rho_{\mathrm{eq}}^{(\Phi)}(\mathcal{X}) \equiv \Big\langle \rho_m(\mathcal{X}) \Big\rangle_N^{(\Phi)}. \tag{C.5}$$

Thus, introducing the Helmholtz free energy $F^{(\Phi)}$ associated with $Z_N^{(\Phi)}$ (Eq. (2.6)),

$$\begin{aligned} \frac{\delta F^{(\Phi)}}{\delta \Phi(\mathcal{X})} &= -k_b T \frac{\delta \log Z_N^{(\Phi)}}{\delta \Phi(\mathcal{X})} \\ &= -k_b T \frac{1}{Z_N^{(\Phi)}} \frac{\delta Z_N^{(\Phi)}}{\delta \Phi(\mathcal{X})} \qquad \text{(C.6)} \\ &= \rho_{\mathrm{eq}}^{(\Phi)}(\mathcal{X}), \qquad \text{(C.7)} \end{aligned}$$

where we used Eq. (C.3), and the further functional differentiation of Eq. (C.6) yields

$$\begin{aligned} \frac{\delta^2 F^{(\Phi)}}{\delta \Phi(\mathcal{X}) \delta \Phi(\mathcal{X}')} &= -k_b T \frac{1}{Z_N^{(\Phi)}} \frac{\delta^2 Z_N^{(\Phi)}}{\delta \Phi(\mathcal{X}) \delta \Phi(\mathcal{X}')} + k_b T \frac{1}{\big(Z_N^{(\Phi)}\big)^2} \frac{\delta Z_N^{(\Phi)}}{\delta \Phi(\mathcal{X})} \frac{\delta Z_N^{(\Phi)}}{\delta \Phi(\mathcal{X}')} \\ &= \beta \Big\{ - \Big\langle \rho_m(\mathcal{X}) \rho_m(\mathcal{X}') \Big\rangle_N^{(\Phi)} + \Big\langle \rho_m(\mathcal{X}) \Big\rangle_N^{(\Phi)} \Big\langle \rho_m(\mathcal{X}') \Big\rangle_N^{(\Phi)} \Big\} \qquad \text{(C.8)} \\ &\equiv -\beta H(\mathcal{X}, \mathcal{X}'), \qquad \text{(C.9)} \end{aligned}$$

with H the so-called *density-density correlation function*, related to the equilibrium density distribution $\rho_{\mathrm{eq}}^{(\Phi)}$ through

$$H(\mathcal{X}, \mathcal{X}') = -k_b T \frac{\delta \rho_{\mathrm{eq}}^{(\Phi)}(\mathcal{X})}{\delta \Phi(\mathcal{X}')}, \tag{C.10}$$

where we used Eqs. (C.7) and (C.9).

C.2 Direct correlation function and OZ equation

Let us now consider the HKM free energy functional F associated with Eq. (C.1) [105],

$$F[\rho] = \mathscr{F}[\rho] + \int d\mathcal{X}\, \rho(\mathcal{X})\Phi(\mathcal{X}) - \mu_N\Big\{\int d\mathcal{X}\, \rho(\mathcal{X}) - N\Big\}, \tag{C.11}$$

where $\mathscr{F}[\rho]$ is the *a priori* unknown functional form of the intrinsic Helmholtz free energy (Eq. (2.11)), whose independence from the external potential Φ is a further consequence of the HKM theorem [106, 107]. In Eq. (C.11), μ_N plays the role of a Lagrange multiplier which ensures the proper normalisation of ρ by guaranteeing the cancellation of the term inside the brackets. The HKM variational principle states that $F[\rho_{\text{eq}}^{(\Phi)}] = F^{(\Phi)}$ constitutes a global minimum of the functional $F[\rho]$,

$$\left.\frac{\delta F}{\delta \rho}\right|_{\rho=\rho_{\text{eq}}^{(\Phi)}} = 0. \tag{C.12}$$

Eqs. (C.11) and (C.12) immediately yield

$$\begin{aligned}
\left.\frac{\delta \mathscr{F}[\rho]}{\delta\rho(\mathcal{X})}\right|_{\rho_{\text{eq}}^{(\Phi)}} &= \mu_N - \Phi(\mathcal{X}),\\
\left.\frac{\delta^2 \mathscr{F}[\rho]}{\delta\rho(\mathcal{X})\delta\rho(\mathcal{X}')}\right|_{\rho_{\text{eq}}^{(\Phi)}} &= -\left.\frac{\delta\Phi(\mathcal{X})}{\delta\rho(\mathcal{X}')}\right|_{\rho_{\text{eq}}^{(\Phi)}}\\
&= k_bT\, H^{-1}(\mathcal{X},\mathcal{X}'),
\end{aligned} \tag{C.13}$$

in which the last equality follows from the functional identity

$$\begin{aligned}
\left.\frac{\delta\rho(\mathcal{X})}{\delta\rho(\mathcal{X}')}\right|_{\rho_{\text{eq}}^{(\Phi)}} = \delta(\mathcal{X}-\mathcal{X}') &= \int d\mathcal{X}''\, k_bT \frac{\delta\rho_{\text{eq}}^{(\Phi)}(\mathcal{X})}{\delta\Phi(\mathcal{X}'')} \times \beta\left.\frac{\delta\Phi(\mathcal{X}'')}{\delta\rho(\mathcal{X}')}\right|_{\rho_{\text{eq}}^{(\Phi)}}\\
&\equiv \int d\mathcal{X}''\, H(\mathcal{X},\mathcal{X}'')H^{-1}(\mathcal{X}'',\mathcal{X}'),
\end{aligned} \tag{C.14}$$

where we used the mathematical definition of the functional inverse, substituting Eq. (C.10) for H. Based on the decomposition of the Helmholtz free energy $\mathscr{F}$ into ideal and excess contributions (Eq. (2.11)), it is straightforward to show that

$$\beta\left.\frac{\delta^2\mathscr{F}[\rho]}{\delta\rho(\mathcal{X})\delta\rho(\mathcal{X}')}\right|_{\rho_{\text{eq}}^{(\Phi)}} = \frac{\delta(\mathcal{X}-\mathcal{X}')}{\rho_{\text{eq}}^{(\Phi)}(\mathcal{X})} - c_{\text{eq}}^{(2)(\Phi)}(\mathcal{X},\mathcal{X}'), \tag{C.15}$$

in which we differentiated Eq. (2.44) and introduced the equilibrium direct correlation function,

$$c_{\text{eq}}^{(2)(\Phi)}(\mathcal{X},\mathcal{X}') \equiv -\beta\left.\frac{\delta^2\mathscr{F}_{\text{ex}}[\rho]}{\delta\rho(\mathcal{X})\delta\rho(\mathcal{X}')}\right|_{\rho_{\text{eq}}^{(\Phi)}}.$$

For readability, let us henceforth omit all (Φ) superscripts. Eq. (2.37) directly leads to

$$\begin{aligned}\Big\langle \rho_m(\mathcal{X})\rho_m(\mathcal{X}')\Big\rangle_N &= \sum_{i,j}\Big\langle \delta(\mathcal{X}-\mathcal{X}_i)\delta(\mathcal{X}'-\mathcal{X}_j)\Big\rangle_N \\ &= \rho^{(2)}_{\rm eq}(\mathcal{X},\mathcal{X}') + \delta(\mathcal{X}-\mathcal{X}')\Big\langle \rho_m(\mathcal{X})\Big\rangle_N, \end{aligned} \tag{C.16}$$

where $\delta(\mathcal{X}-\mathcal{X}_i) \equiv \delta(\mathbf{r}-\mathbf{r}_i)\delta(\mathcal{R}-\mathcal{R}_i)$, and we used the relation

$$\sum_{i=1}^{N}\Big\langle \delta(\mathcal{X}-\mathcal{X}_i)\delta(\mathcal{X}'-\mathcal{X}_i)\Big\rangle_N = \delta(\mathcal{X}-\mathcal{X}')\Big\langle \rho_m(\mathcal{X})\Big\rangle_N,$$

based on Eqs. (2.37) and (C.4). In Eq. (C.17), $\rho^{(2)}_{\rm eq}(\mathcal{X}_1,\mathcal{X}_2)$ is known as the *two-particle density*, formally defined as

$$\rho^{(2)}_{\rm eq}(\mathcal{X},\mathcal{X}') \equiv \sum_{i\neq j}\Big\langle \delta(\mathcal{X}-\mathcal{X}_i)\delta(\mathcal{X}'-\mathcal{X}_j)\Big\rangle_N. \tag{C.17}$$

Plugging Eqs. (C.5) and (C.17) into Eq. (C.8) yields

$$\begin{aligned}\beta H(\mathcal{X},\mathcal{X}') &= \rho^{(2)}_{\rm eq}(\mathcal{X},\mathcal{X}') - \rho_{\rm eq}(\mathcal{X})\rho_{\rm eq}(\mathcal{X}') + \rho_{\rm eq}(\mathcal{X})\delta(\mathcal{X}-\mathcal{X}') \\ &\equiv h^{(2)}_{\rm eq}(\mathcal{X},\mathcal{X}')\rho_{\rm eq}(\mathcal{X})\rho_{\rm eq}(\mathcal{X}') + \rho_{\rm eq}(\mathcal{X})\delta(\mathcal{X}-\mathcal{X}'), \end{aligned} \tag{C.18}$$

with $h^{(2)}_{\rm eq}$ the *total correlation function* (TCF),

$$h^{(2)}_{\rm eq}(\mathcal{X},\mathcal{X}') \equiv \frac{\rho^{(2)}_{\rm eq}(\mathcal{X},\mathcal{X}')}{\rho_{\rm eq}(\mathcal{X})\rho_{\rm eq}(\mathcal{X}')} - 1.$$

Finally, substituting Eqs. (C.13), (C.15) and (C.18) for H^{-1} and H in Eq. (C.14),

$$\begin{aligned}\delta(\mathcal{X}-\mathcal{X}') = h^{(2)}_{\rm eq}(\mathcal{X},\mathcal{X}')\rho_{\rm eq}(\mathcal{X}) + \delta(\mathcal{X}-\mathcal{X}') - c^{(2)}_{\rm eq}(\mathcal{X},\mathcal{X}')\rho_{\rm eq}(\mathcal{X}) \\ - \rho_{\rm eq}(\mathcal{X})\int d\mathcal{X}''\,\rho_{\rm eq}(\mathcal{X}'')h^{(2)}_{\rm eq}(\mathcal{X},\mathcal{X}'')c^{(2)}_{\rm eq}(\mathcal{X}'',\mathcal{X}'),\end{aligned}$$

which reduces to the general formulation of the OZ equation,

$$h^{(2)}_{\rm eq}(\mathcal{X},\mathcal{X}') = c^{(2)}_{\rm eq}(\mathcal{X},\mathcal{X}') + \int d\mathcal{X}''\,\rho_{\rm eq}(\mathcal{X}'')h^{(2)}_{\rm eq}(\mathcal{X},\mathcal{X}'')c^{(2)}_{\rm eq}(\mathcal{X}'',\mathcal{X}'). \tag{C.19}$$

In the limit where the external field vanishes ($\Phi \to 0$), all quantities in Eq. (C.19) converge toward their respective unperturbed equilibrium distributions, and one recovers Eq. (2.48).

C.3 Low-density asymptotic correlations

To assess the behaviour of correlation functions in the low-density limit, it is convenient to reformulate these quantities in the grand-canonical ensemble. We thus now allow the number of particles N of the system to freely fluctuate via exchanges with the surrounding medium, while instead fixing its chemical potential μ. The corresponding grand-canonical potential $\mathcal{F}$ is then related to the Helmholtz free energy $\mathscr{F}$ through

$$\mathcal{F} = \mathscr{F} - \mu N \equiv -k_b T \log \Xi, \tag{C.20}$$

with Ξ the grand partition function,

$$\begin{aligned}\Xi &\equiv \sum_{N=0}^{\infty} \frac{e^{\beta\mu N}}{h^{6N} N!} \int_{-\infty}^{+\infty} d\{\mathbf{p}_i\} \int_{-\infty}^{+\infty} d\{\boldsymbol{\ell}_i\} \int d\{\mathcal{X}_i\}\, e^{-\beta \mathscr{H}_N} \\ &= \sum_{N=0}^{\infty} \frac{z^N}{N!} \int d\{\mathcal{X}_i\}\, e^{-\beta U_N},\end{aligned} \tag{C.21}$$

where we introduced the so-called *fugacity* z,

$$z \equiv \frac{e^{\beta\mu}}{\lambda^3}. \tag{C.22}$$

It follows from Eq. (2.44) that in the case of an ideal gas with uniform density $\rho_0 \equiv \langle N \rangle / V$,

$$\mu_{\mathrm{id}} \equiv \left.\frac{\delta \mathscr{F}_{\mathrm{id}}}{\delta \rho}\right|_{\rho=\rho_0} = k_b T \log\left(\rho_0 \lambda^3\right) \implies z_{\mathrm{id}} = \rho_0, \tag{C.23}$$

$$\Xi_{\mathrm{id}} = \sum_{N=0}^{\infty} \frac{z_{\mathrm{id}}^N}{N!} (8\pi^2 V)^N = \exp(\rho_0 8\pi^2 V). \tag{C.24}$$

Using Eqs. (C.4), (C.5) and (C.17), the canonical definitions of ρ_{eq} and $\rho_{\mathrm{eq}}^{(2)}$ may be recast in the form of marginal integrals,

$$\begin{aligned}\rho_{\mathrm{eq}}(\mathcal{X}) &= \frac{1}{Q_N} \frac{N}{(8\pi^2 V)^N} \int d\{\mathcal{X}_i\}_{i\in[\![2,N]\!]} \exp\Big[-\beta U_N\Big(\mathcal{X}, \{\mathcal{X}_i\}_{i\in[\![2,N]\!]}\Big)\Big] \\ &\equiv \rho_N^{(1)}(\mathcal{X}), \\ \rho_{\mathrm{eq}}^{(2)}(\mathcal{X}, \mathcal{X}') &= \frac{1}{Q_N} \frac{N(N-1)}{(8\pi^2 V)^N} \int d\{\mathcal{X}_i\}_{i\in[\![3,N]\!]} \exp\Big[-\beta U_N\Big(\mathcal{X}, \mathcal{X}', \{\mathcal{X}_i\}_{i\in[\![3,N]\!]}\Big)\Big] \\ &\equiv \rho_N^{(2)}(\mathcal{X}, \mathcal{X}').\end{aligned}$$

Their grand-canonical counterparts $\rho^{(1)}$ and $\rho^{(2)}$ respectively read as [108]

$$\begin{aligned}\rho^{(1)}(\mathcal{X}) &\equiv \sum_{N=1}^{\infty} \Pi_\mu(N)\rho_N^{(1)}(\mathcal{X}) \\ &= \frac{z}{\Xi} + \frac{1}{\Xi}\sum_{N=2}^{\infty}\frac{z^N}{(N-1)!}\int d\{\mathcal{X}_i\}_{i\in[\![2,N]\!]}\,\exp\Big[-\beta U_N\Big(\mathcal{X},\{\mathcal{X}_i\}_{i\in[\![2,N]\!]}\Big)\Big],\end{aligned} \tag{C.25}$$

$$\begin{aligned}\rho^{(2)}(\mathcal{X},\mathcal{X}') &\equiv \sum_{N=2}^{\infty} \Pi_\mu(N)\rho_N^{(2)}(\mathcal{X},\mathcal{X}') \\ &= \frac{z^2}{\Xi}\exp\Big[-\beta U_2(\mathcal{X},\mathcal{X}')\Big] \\ &\quad + \frac{1}{\Xi}\sum_{N=3}^{\infty}\frac{z^N}{(N-2)!}\int d\{\mathcal{X}_i\}_{i\in[\![3,N]\!]}\,\exp\Big[-\beta U_N\Big(\mathcal{X},\mathcal{X}',\{\mathcal{X}_i\}_{i\in[\![3,N]\!]}\Big)\Big],\end{aligned} \tag{C.26}$$

where we introduced the equilibrium probability $\Pi_\mu(N)$ to find the grand-canonical system in a state comprising exactly N particles,

$$\Pi_\mu(N) = \frac{1}{\Xi}\frac{z^N}{N!}\int d\{\mathcal{X}_i\}\,e^{-\beta U_N} = \frac{1}{\Xi}\frac{z^N}{N!}\times(8\pi^2 V)^N Q_N. \tag{C.27}$$

Using Eqs. (B.12), (C.25) and (C.26), we may perform the series expansion

$$\frac{\rho^{(2)}(\mathcal{X},\mathcal{X}')}{\rho^{(1)}(\mathcal{X})\rho^{(1)}(\mathcal{X}')} = \Xi\exp\Big\{-\beta U_2(\mathcal{X},\mathcal{X}')\Big\} + \mathcal{O}(z).$$

At vanishing particle densities, one must recover the ideal gas behaviour, and Eqs. (C.23) and (C.24) lead to, at fixed volume V,

$$\begin{aligned} z &\xrightarrow[\frac{\langle N\rangle}{V}\to 0]{} 0, \\ \Xi &\xrightarrow[\frac{\langle N\rangle}{V}\to 0]{} 1,\end{aligned}$$

which finally yields the asymptotic behaviour of the grand-canonical TCF,

$$h^{(2)}(\mathcal{X},\mathcal{X}') \equiv \frac{\rho^{(2)}(\mathcal{X},\mathcal{X}')}{\rho^{(1)}(\mathcal{X})\rho^{(1)}(\mathcal{X}')} - 1 \xrightarrow[\frac{\langle N\rangle}{V}\to 0]{} \exp\Big\{-\beta U_2(\mathcal{X},\mathcal{X}')\Big\} - 1. \tag{C.28}$$

D

The Parsons-Lee correction

Contents

D.1 Decoupling approximation

Let us assume that the DCF $c^{(2)}$ of the system may be written in the form of Eq. (2.68). In this case, Eq. (2.66) may be recast as

$$\overline{c^{(2)}}(\mathbf{r}_{12},\mathcal{R}_1,\mathcal{R}_2;\overline{\rho}) = 2\int_0^1 d\gamma \int_0^\gamma d\gamma'\, c_{\text{ref}}^{(2)}\left\{\frac{r_{12}}{\sigma(\mathbf{u}_{12},\mathcal{R}_1,\mathcal{R}_2)};\gamma'\overline{\rho}\right\}, \tag{D.1}$$

where $r_{12} \equiv \|\mathbf{r}_{12}\|$. Due to the translational invariance of the ODF ψ, we may directly perform the integration over the positional degrees of freedom in Eq. (D.1) for the computation of the corresponding excess free energy functional (Eq. (2.65)). Thus, in the thermodynamic limit,

$$\int_V d\mathbf{r}_{12}\,\overline{c^{(2)}}(\mathbf{r}_{12},\mathcal{R}_1,\mathcal{R}_2;\overline{\rho}) = \oint_{\mathcal{S}} d\mathbf{u}_{12}\int_0^\infty r_{12}^2 dr_{12}\,\overline{c^{(2)}}(\mathbf{r}_{12},\mathcal{R}_1,\mathcal{R}_2;\overline{\rho}) \tag{D.2}$$

$$= \oint_{\mathcal{S}} d\mathbf{u}_{12}\,\sigma(\mathbf{u}_{12},\mathcal{R}_1,\mathcal{R}_2)^3 \times 2\int_0^1 d\gamma\int_0^\gamma d\gamma'\int_0^\infty y^2 dy\, c_{\text{ref}}^{(2)}(y;\gamma'\overline{\rho}), \tag{D.3}$$

where we used the notation of Appendix A, along with the change of variable $y \equiv r_{12}/\sigma(\mathbf{u}_{12}, \mathcal{R}_1, \mathcal{R}_2)$ in the innermost integral. Hence, it is apparent from Eq. (D.3) that the angular and radial contributions to the integral in Eq. (2.65) may be independently factorised in the calculation of $\mathscr{F}_{\text{ex}}$, and have thus been effectively *decoupled* by the use of the ansatz in Eq. (2.68).

It follows from the definition of the distance of closest approach $\sigma(\mathbf{u}_{12}, \mathcal{R}_1, \mathcal{R}_2)$ that two convex particles overlap if and only if their separation distance r_{12} is such that $r_{12} < \sigma(\mathbf{u}_{12}, \mathcal{R}_1, \mathcal{R}_2)$. Therefore, in the case of pure hard-body repulsion,

$$f(\mathbf{r}_{12}, \mathcal{R}_1, \mathcal{R}_2) = \begin{cases} -1 & \text{if } r_{12} < \sigma(\mathbf{u}_{12}, \mathcal{R}_1, \mathcal{R}_2) \\ \\ 0 & \text{if } r_{12} > \sigma(\mathbf{u}_{12}, \mathcal{R}_1, \mathcal{R}_2) \end{cases}.$$

Thus, at fixed particle orientations $\mathcal{R}_1$ and $\mathcal{R}_2$,

$$\int_V d\mathbf{r}_{12}\, f(\mathbf{r}_{12}, \mathcal{R}_1, \mathcal{R}_2) = \oint_{\mathcal{S}} d\mathbf{u}_{12} \int_{\sigma(\mathbf{u}_{12}, \mathcal{R}_1, \mathcal{R}_2)}^{0} r_{12}^2 dr_{12} = -\frac{1}{3} \oint_{\mathcal{S}} d\mathbf{u}_{12}\, \sigma(\mathbf{u}_{12}, \mathcal{R}_1, \mathcal{R}_2)^3. \tag{D.4}$$

Plugging Eqs. (D.3) and (D.4) back into Eq. (2.65) leads to

$$\frac{\beta \mathscr{F}_{\text{ex}}[\psi]}{V} = -G_{\text{ref}}(\overline{\rho}) \frac{\rho^2}{2} \int_V d\mathbf{r}_{12} \oiint d\mathcal{R}_1 d\mathcal{R}_2\, \psi(\cos\theta_1)\psi(\cos\theta_2) f(\mathbf{r}_{12}, \mathcal{R}_1, \mathcal{R}_2), \tag{D.5}$$

which yields the Onsager functional (Eq. (2.61)), up to the multiplicative prefactor

$$G_{\text{ref}}(\overline{\rho}) = -6 \int_0^1 d\gamma \int_0^{\gamma} d\gamma' \int_0^{\infty} y^2 dy\, c_{\text{ref}}^{(2)}(y; \gamma' \overline{\rho}). \tag{D.6}$$

To evaluate the density-dependent correction G_{ref} for a chosen reference equation of state, it is convenient to exploit the general thermodynamic relation between DCF and isothermal compressibility, which we proceed to derive in the next section.

D.2 Compressibility equation

Let us start from the grand-canonical density distributions $\rho^{(1)}$ and $\rho^{(2)}$, respectively defined in Eqs. (C.25) and (C.26). In the notations of Appendix C, it is easy to verify that

$$\int d\mathcal{X}_1\, \rho^{(1)}(\mathcal{X}_1) = \sum_{N=1}^{\infty} \Pi_\mu(N) \int d\mathcal{X}_1\, \rho_N^{(1)}(\mathcal{X}_1) = \langle N \rangle_\mu,$$

$$\iint d\mathcal{X}_1 d\mathcal{X}_2\, \rho^{(2)}(\mathcal{X}_1, \mathcal{X}_2) = \sum_{N=2}^{\infty} \Pi_\mu(N) \iint d\mathcal{X}_1 d\mathcal{X}_2\, \rho_N^{(2)}(\mathcal{X}_1, \mathcal{X}_2) = \langle N(N-1) \rangle_\mu,$$

where $\Pi_\mu(N)$ is the probability distribution in Eq. (C.27) and $\langle\cdot\rangle_\mu$ is the grand-canonical average [108]. Thus, it immediately follows that

$$\iint d\mathcal{X}_1 d\mathcal{X}_2\, \rho^{(1)}(\mathcal{X}_1)\rho^{(1)}(\mathcal{X}_2)h^{(2)}(\mathcal{X}_1,\mathcal{X}_2) = \langle N(N-1)\rangle_\mu - \langle N\rangle_\mu^2, \tag{D.7}$$

with h the TCF (Eq. (C.28)). For simplicity, let us henceforth consider an homogeneous system of spherically-symmetric particles with uniform density $\rho^{(1)}(\mathcal{X}) = \rho$. In this case, translational and rotational invariance impose that

$$h^{(2)}(\mathcal{X}_1,\mathcal{X}_2) = h^{(2)}(r_{12}),$$

and Eq. (D.7) reduces to

$$\overline{\rho}\langle N\rangle_\mu \int_V d\mathbf{r}_{12}\, h^{(2)}(r_{12}) = \langle N^2\rangle_\mu - \langle N\rangle_\mu - \langle N\rangle_\mu^2, \tag{D.8}$$

where $\overline{\rho} \equiv 8\pi^2\rho = \langle N\rangle_\mu/V$ is the angle-integrated number density.

The average number of particles $\langle N\rangle_\mu$ of the system may be computed from Eqs. (C.21) and (C.27),

$$\langle N\rangle_\mu = \sum_{N=0}^{\infty} N\Pi_\mu(N) = \frac{1}{\Xi}\sum_{N=0}^{\infty} N\frac{z^N}{N!}\int d\{\mathcal{X}_i\}\, e^{-\beta U_N} = \frac{1}{\Xi}\frac{\partial\Xi}{\partial z}\times z,$$

which may be recast in the form

$$\langle N\rangle_\mu = \frac{\partial\log\Xi}{\partial\log z} = k_b T\frac{\partial\log\Xi}{\partial\mu}, \tag{D.9}$$

where we used Eq. (C.22). Further differentiation of Eq. (D.9) yields

$$\begin{aligned}\frac{\partial\langle N\rangle_\mu}{\partial\mu} &= \frac{\beta}{\Xi}\frac{\partial^2\Xi}{(\partial\log z)^2} - \frac{\beta}{\Xi^2}\left(\frac{\partial\Xi}{\partial\log z}\right)^2 \\ &= \beta\Big(\langle N^2\rangle_\mu - \langle N\rangle_\mu^2\Big).\end{aligned} \tag{D.10}$$

Let us introduce the isothermal compressibility χ_T,

$$\chi_T \equiv -\frac{1}{V}\frac{\partial V}{\partial P}\bigg|_{N,T} = -\frac{1}{V}\frac{dV}{d\overline{\rho}}\frac{\partial\overline{\rho}}{dP}\bigg|_T = \frac{1}{\overline{\rho}}\frac{\partial\overline{\rho}}{\partial P}\bigg|_T. \tag{D.11}$$

The Gibbs-Duhem relation leads to

$$\frac{\partial P}{\partial\mu}\bigg|_T = \overline{\rho},$$

which may be plugged into Eq. (D.11),

$$\chi_T = \frac{1}{\overline{\rho}}\frac{\partial\overline{\rho}}{\partial\mu}\bigg|_T \frac{\partial\mu}{\partial P}\bigg|_T = \frac{1}{\overline{\rho}^2 V}\frac{\partial\langle N\rangle_\mu}{\partial\mu}\bigg|_T. \tag{D.12}$$

Thus, it follows from Eqs. (D.10) and (D.12) that

$$\overline{\rho}k_bT\chi_T = \frac{\langle N^2\rangle_\mu - \langle N\rangle_\mu^2}{\langle N\rangle_\mu},$$

which may be substituted in Eq. (D.8) to yield the so-called *compressibility equation*,

$$\overline{\rho}\int_V d\mathbf{r}_{12}\, h^{(2)}(r_{12}) = \overline{\rho}k_bT\chi_T - 1. \tag{D.13}$$

Eq. (D.13) may be conveniently rewritten in terms of the DCF $c^{(2)}$ using the OZ equation (Eq. (2.48)), which in this case takes the simple form

$$h^{(2)}(\mathbf{r}_{12}) = c^{(2)}(\mathbf{r}_{12}) + \overline{\rho}\int_V d\mathbf{r}_3\, h^{(2)}(\mathbf{r}_{13})c^{(2)}(\mathbf{r}_{32}) = c^{(2)}(\mathbf{r}_{12}) + \overline{\rho}\Big(c^{(2)} * h^{(2)}\Big)(\mathbf{r}_{12}), \tag{D.14}$$

where we used the homogeneity of space along with the basic symmetries of uniform simple fluids, with $*$ the spatial convolution product,

$$(\zeta * \xi)(\mathbf{x}) \equiv \int_V d\mathbf{x}'\, \zeta(\mathbf{x}-\mathbf{x}')\xi(\mathbf{x}').$$

Using the convolution theorem, Eq. (D.14) may be expediently recast in Fourier space,

$$\widehat{h^{(2)}}(\mathbf{k}) = \widehat{c^{(2)}}(\mathbf{k}) + \overline{\rho}\widehat{c^{(2)}}(\mathbf{k})\widehat{h^{(2)}}(\mathbf{k}),$$

where $\widehat{f}$ denotes the Fourier transform of f, and irrelevant boundary terms are discarded in the thermodynamic limit. It directly follows that

$$1 - \overline{\rho}\widehat{c^{(2)}}(\mathbf{k}) = \frac{\widehat{c^{(2)}}(\mathbf{k})}{\widehat{h^{(2)}}(\mathbf{k})} = \frac{1}{1+\overline{\rho}\widehat{h^{(2)}}(\mathbf{k})}. \tag{D.15}$$

Thus, for $\mathbf{k} = \mathbf{0}$, Eq. (D.15) yields

$$1 - \overline{\rho}\int_V d\mathbf{r}_{12}\, c^{(2)}(\mathbf{r}_{12}) = \left\{1 + \overline{\rho}\int_V d\mathbf{r}_{12}\, h^{(2)}(\mathbf{r}_{12})\right\}^{-1},$$

which may finally be plugged into Eq. (D.13) to yield

$$1 - \overline{\rho}\int_V d\mathbf{r}_{12}\, c^{(2)}(r_{12}) = \frac{1}{\overline{\rho}k_bT\chi_T} = \beta\frac{\partial P}{\partial\overline{\rho}}\bigg|_T. \tag{D.16}$$

D.3 Parsons-Lee prefactor

In the case of a hard-sphere system, scale invariance imposes that the DCF $c_{\rm ref}^{(2)}$ may be written in terms of the reduced quantities

$$c_{\rm ref}^{(2)}(r;\overline{\rho}) = c_{\rm ref}^{(2)}(r/\sigma_{\rm ref};\overline{\rho}\sigma_{\rm ref}^3),$$

where $\sigma_{\rm ref}$ is the hard-sphere diameter. One may then write

$$\begin{aligned}\overline{\rho}\int_V d\mathbf{r}\, c_{\rm ref}^{(2)}(r;\overline{\rho}) &= \overline{\rho}\sigma_{\rm ref}^3\frac{4\pi}{\sigma_{\rm ref}^3}\int_V r^2 dr\, c_{\rm ref}^{(2)}(r/\sigma_{\rm ref};\overline{\rho}\sigma_{\rm ref}^3)\\ &= 4\pi\overline{\rho}\sigma_{\rm ref}^3\int_0^\infty y^2 dy\, c_{\rm ref}^{(2)}(y;\overline{\rho}\sigma_{\rm ref}^3),\end{aligned} \tag{D.17}$$

with $y = r/\sigma_{\rm ref}$. Thus, using Eqs. (D.16) and (D.17) we may conveniently reformulate the scaled radial integral in Eq. (D.6) in terms of the isothermal compressibility,

$$\begin{aligned}\int_0^\infty y^2 dy\, c_{\rm ref}^{(2)}(y;\gamma'\overline{\rho}) &= \frac{1}{4\pi\gamma'\overline{\rho}\sigma_{\rm ref}^3}\left\{1-\beta\frac{\partial P}{\partial\overline{\rho}}\bigg|_T(\gamma'\overline{\rho}\sigma_{\rm ref}^3)\right\}\\ &= \frac{1}{24\gamma'\eta_{\rm ref}}\left\{1-\beta\frac{\partial P}{\partial\overline{\rho}}\bigg|_T(\gamma'\eta_{\rm ref})\right\},\end{aligned} \tag{D.18}$$

where we introduced the dimensionless volume fraction $\eta_{\rm ref} = \overline{\rho}\pi\sigma_{\rm ref}^3/6$. .

Using the CS EOS, one obtains [319]

$$1-\beta\frac{\partial P}{\partial\overline{\rho}}\bigg|_T(\eta) = \frac{2\eta^2-8\eta}{(1-\eta)^4}. \tag{D.19}$$

The double integration of Eqs. (D.18) and (D.19) leads to

$$\begin{aligned}\int_0^\gamma d\gamma'\int_0^\infty y^2 dy\, c_{\rm ref}^{(2)}(y;\gamma'\overline{\rho}) &= \frac{1}{12}\int_0^\gamma d\gamma'\,\frac{\gamma'\eta_{\rm ref}-4}{(1-\gamma'\eta_{\rm ref})^4}\\ &= \frac{1}{12\eta_{\rm ref}}\left[\frac{x-3}{2(1-x)^3}\right]_0^{\gamma\eta_{\rm ref}}\\ &= \frac{1}{24\eta_{\rm ref}}\left\{\frac{\gamma\eta_{\rm ref}-3}{(1-\gamma\eta_{\rm ref})^3}+3\right\},\end{aligned} \tag{D.20}$$

$$\begin{aligned}\int_0^1 d\gamma\int_0^\gamma d\gamma'\int_0^\infty y^2 dy\, c_{\rm ref}^{(2)}(y;\gamma'\overline{\rho}) &= \frac{1}{24\eta_{\rm ref}^2}\left[\frac{x-2}{(1-x)^2}\right]_0^{\eta_{\rm ref}}+\frac{1}{8\eta_{\rm ref}}\\ &= \frac{1}{24\eta_{\rm ref}^2}\frac{\eta_{\rm ref}-2+2(1-\eta_{\rm ref})^2+3\eta_{\rm ref}(1-\eta_{\rm ref})^2}{(1-\eta_{\rm ref})^2}\\ &= \frac{3\eta_{\rm ref}-4}{24(1-\eta_{\rm ref})^2}.\end{aligned} \tag{D.21}$$

Plugging Eq. (D.21) back into Eq. (D.6) then yields

$$G_{\text{ref}}(\overline{\rho}) = \frac{1 - 3\eta_{\text{ref}}/4}{(1-\eta_{\text{ref}})^2} \equiv G_{\text{PL}}(\eta_{\text{ref}}). \tag{D.22}$$

Finally, it is easy to verify that substituting Eq. (2.68) in Eq. (2.54) similarly leads to

$$\begin{aligned} c^{(1)}(\mathcal{R}_1;\overline{\rho}) &= \overline{\rho}\int_0^1 d\gamma \int_V d\mathbf{r}_{12} \oint d\mathcal{R}_2\, \psi(\mathcal{R}_2) c^{(2)}_{\text{ref}}\left\{ \frac{r_{12}}{\sigma(\mathbf{u}_{12},\mathcal{R}_1,\mathcal{R}_2)}; \gamma\overline{\rho}\right\} \\ &= \overline{\rho} G^{(1)}_{\text{ref}}(\overline{\rho}) \int_V d\mathbf{r}_{12} \oint d\mathcal{R}_2\, \psi(\mathcal{R}_2) f(\mathbf{r}_{12},\mathcal{R}_1,\mathcal{R}_2), \end{aligned} \tag{D.23}$$

with a different density-dependent correction $G^{(1)}_{\text{ref}}$,

$$G^{(1)}_{\text{ref}}(\overline{\rho}) = -3\int_0^1 d\gamma \int_0^\infty y^2 dy\, c^{(2)}_{\text{ref}}(y;\gamma\overline{\rho}).$$

The corresponding prefactor in the case of the CS EOS may thus be directly obtained by setting γ to 1 in Eq. (D.20),

$$G^{(1)}_{\text{ref}}(\overline{\rho}) = \frac{1}{8\eta_{\text{ref}}}\left\{ \frac{3-\eta_{\text{ref}}}{(1-\eta_{\text{ref}})^3} - 3\right\} \equiv G^{(1)}_{\text{PL}}(\eta_{\text{ref}}). \tag{D.24}$$

The equilibrium ODF ψ_{eq} may then be determined by plugging Eqs. (D.23) and (D.24) into Eq. (2.46),

$$\psi_{\text{eq}}(\mathcal{R}) = \frac{e^{\beta\mu_N}}{\overline{\rho}\lambda^3} \exp\left\{ \overline{\rho} G^{(1)}_{\text{PL}}(\eta_{\text{ref}}) \oint d\mathcal{R}'\, \psi_{\text{eq}}(\mathcal{R}') \int_V d\mathbf{r}\, f(\mathbf{r},\mathcal{R},\mathcal{R}')\right\}. \tag{D.25}$$

Note that in the case of the PL prefactor, the detour through the compressibility equation (Eq. (D.16)) was made necessary by the current lack of an exact analytical DCF for the CS EOS. However, in the case where a closed-form expression for the DCF is known, G_{ref} may be more straightforwardly computed by solving Eq. (D.6) directly. This simple procedure leads to the Pynn-Wulf prefactor G_{PW} in the case of the Percus-Yevick DCF, and is outlined in Ref. [104].

E

Molecular and bond order parameters

Contents

E.1 KS, FY and intra-molecular order parameters

In the case of a discretised KG polymer chain, the formal definition of the KS nematic order parameter (Eq. (5.18)) may be recast in the form

$$S_b \equiv \left\langle \frac{3(\mathbf{t}_i \cdot \mathbf{n}_0)^2 - 1}{2} \right\rangle_{\{\psi_i\}} \equiv \left\langle \frac{3\cos^2\theta_{il} - 1}{2} \right\rangle_{\{\psi_i\}}, \tag{E.1}$$

where we used the notation of Figure 5.1, denoting by the brackets an average over all bond orientations $\mathbf{t}_i$ about the uniform director $\mathbf{n}_0$. Such orientations may be fully characterised by a set of contour-dependent ODFs $\{\psi_i\}$ for all bonds i comprising the chain. In this case, the FY decoupling approximation (Eq. (5.3)) reads as [252, 253]

$$\psi_i(\mathbf{t}_i) = \psi(\mathcal{R}) \times \Pi_i(\mathcal{R}^{\mathsf{T}} \cdot \mathbf{t}_i), \tag{E.2}$$

with ψ the molecular (FY) ODF quantifying the probability of finding a chain with orientation $\mathcal{R}$ as defined in Figure 5.1, and Π_i the probability of finding the

i-th bond vector pointing along $\mathbf{t}_i$ in the molecular frame $\mathcal{R}$ of an arbitrary chain. Under these assumptions, one readily obtains

$$\Big\langle \cdot \Big\rangle_{\{\psi_i\}} = \Big\langle \Big\langle \cdot \Big\rangle_{\psi} \Big\rangle_{\{\Pi_i\}}, \tag{E.3}$$

where the inner brackets denote a thermodynamic average over all molecular orientations $\mathcal{R}$, and the outer brackets a conformational average over all accessible bond orientations $\mathbf{t}_i$ as expressed in the molecular frame. In the FY approximation (Eq. (E.2)), these two averages may thus be computed independently by projecting the normalised bond vectors $\mathbf{t}_i$ onto $\mathcal{R}$,

$$\mathcal{R}^{\mathsf{T}} \cdot \mathbf{t}_i = \mathcal{R}^{\mathsf{T}} \cdot \begin{bmatrix} \sin\theta_{il}\cos\phi_{il} \\ \sin\theta_{il}\sin\phi_{il} \\ \cos\theta_{il} \end{bmatrix}_{\mathcal{R}_{\text{lab}}} \equiv \begin{bmatrix} \sin\theta_{im}\cos\phi_{im} \\ \sin\theta_{im}\sin\phi_{im} \\ \cos\theta_{im} \end{bmatrix}_{\mathcal{R}}, \tag{E.4}$$

with ϕ_{il} and ϕ_{im} the respective azimuthal bond angles in the laboratory and molecular frame. Hence,

$$\begin{bmatrix} \sin\theta_{il}\cos\phi_{il} \\ \sin\theta_{il}\sin\phi_{il} \\ \cos\theta_{il} \end{bmatrix}_{\mathcal{R}_{\text{lab}}} = \mathcal{R} \cdot \begin{bmatrix} \sin\theta_{im}\cos\phi_{im} \\ \sin\theta_{im}\sin\phi_{im} \\ \cos\theta_{im} \end{bmatrix}_{\mathcal{R}}, \tag{E.5}$$

with $\mathcal{R}$ being represented in $\mathcal{R}_{\text{lab}}$ by the Euler angle triad (α, θ, ϕ) in the z-y-z convention (see Appendix A). Plugging Eq. (A.2) into Eq. (E.5) and projecting the result onto $\mathbf{e}_z$ leads to

$$\cos\theta_{il} = \cos\theta_{im}\cos\theta + \sin\theta_{im}\sin\theta \times (\sin\phi_{im}\sin\alpha - \cos\phi_{im}\cos\alpha),$$

which yields, after some rearrangements,

$$\begin{aligned}\cos^2\theta_{il} = {} & \cos^2\theta_{im}\cos^2\theta + \sin^2\theta_{im}\sin^2\phi_{im}\sin^2\theta\sin^2\alpha + \sin^2\theta_{im}\cos^2\phi_{im}\sin^2\theta\cos^2\alpha \\ & + \frac{\sin 2\theta_{im}\sin 2\theta}{2}(\sin\phi_{im}\sin\alpha - \cos\phi_{im}\cos\alpha) - \frac{\sin 2\phi_{im}\sin 2\alpha}{2}\sin^2\theta_{im}\sin^2\theta.\end{aligned} \tag{E.6}$$

Let us first perform the average of Eq. (E.6) over the molecular ODF ψ, which respect to which the angles θ_{im} and ϕ_{im} are taken to be invariant following the previous discussion. One must therefore have, for any functions $\zeta(\theta_{im}, \phi_{im})$ and $\xi(\mathcal{R})$,

$$\Big\langle \zeta(\theta_{im},\phi_{im})\xi(\mathcal{R}) \Big\rangle_{\psi} = \zeta(\theta_{im},\phi_{im})\Big\langle \xi(\mathcal{R}) \Big\rangle_{\psi} \equiv \zeta(\theta_{im},\phi_{im}) \oint d\mathcal{R}\, \psi(\mathcal{R})\xi(\mathcal{R}). \tag{E.7}$$

Let us further assume the molecular ODF ψ to be cylindrically-symmetric about $\mathbf{n}_0$,

$$\psi(\mathcal{R}) = \psi(\cos\theta),$$

so that for any function $\xi(\theta, \alpha)$,

$$\Big\langle \xi(\theta,\alpha) \Big\rangle_{\psi} = 2\pi \int_0^{\pi} \sin\theta d\theta \, \psi(\cos\theta) \int_0^{2\pi} d\alpha \, \xi(\theta,\alpha). \tag{E.8}$$

Using Eqs. (E.7) and (E.8), one obtains

$$\Big\langle \sin^2\theta_{im} \sin^2\phi_{im} \sin^2\theta \sin^2\alpha \Big\rangle_{\psi} = \frac{\sin^2\theta_{im} \sin^2\phi_{im} \Big\langle \sin^2\theta \Big\rangle_{\psi}}{2},$$
$$\Big\langle \sin^2\theta_{im} \cos^2\phi_{im} \sin^2\theta \cos^2\alpha \Big\rangle_{\psi} = \frac{\sin^2\theta_{im} \cos^2\phi_{im} \Big\langle \sin^2\theta \Big\rangle_{\psi}}{2},$$

and it is easy to show that all the terms in the second line of Eq. (E.6), involving only odd powers of $\cos\alpha$ and $\sin\alpha$, average out to zero. Thus,

$$\Big\langle \cos^2\theta_{il} \Big\rangle_{\psi} = \cos^2\theta_{im} \Big\langle \cos^2\theta \Big\rangle_{\psi} + \frac{\sin^2\theta_{im} \Big\langle \sin^2\theta \Big\rangle_{\psi}}{2}.$$

Finally, using the shorthand

$$\Big\langle \cdot \Big\rangle_{\Pi} \equiv \Big\langle \cdot \Big\rangle_{\{\Pi_i\}} \tag{E.9}$$

for the conformational average, the KS order parameter S_b may be written as

$$\begin{aligned}
S_b &= \frac{3\Big\langle \Big\langle \cos^2\theta_{il} \Big\rangle_{\psi} \Big\rangle_{\Pi} - 1}{2} \\
&= \frac{3\Big\langle \cos^2\theta_{im} \Big\rangle_{\Pi} \Big\langle \cos^2\theta \Big\rangle_{\psi}}{2} + \frac{3\Big\langle \sin^2\theta_{im} \Big\rangle_{\Pi} \Big\langle \sin^2\theta \Big\rangle_{\psi}}{4} - \frac{1}{2} \\
&= \frac{3\Big\langle \cos^2\theta_{im} \Big\rangle_{\Pi} \Big\langle \cos^2\theta \Big\rangle_{\psi}}{2} + \frac{3\Big(\Big\langle \sin^2\theta_{im} \Big\rangle_{\Pi} - 1\Big)\Big(\Big\langle \sin^2\theta \Big\rangle_{\psi} - 1\Big)}{4} \\
&\quad + \frac{3\Big(\Big\langle \sin^2\theta_{im} \Big\rangle_{\Pi} + \Big\langle \sin^2\theta \Big\rangle_{\psi}\Big)}{4} - \frac{5}{4} \\
&= \frac{9\Big\langle \cos^2\theta_{im} \Big\rangle_{\Pi} \Big\langle \cos^2\theta \Big\rangle_{\psi}}{4} - \frac{3\Big(\Big\langle \cos^2\theta_{im} \Big\rangle_{\Pi} + \Big\langle \cos^2\theta \Big\rangle_{\psi}\Big)}{4} + \frac{1}{4} \\
&= \left(\frac{3\Big\langle \cos^2\theta_{im} \Big\rangle_{\Pi} - 1}{2}\right) \times \left(\frac{3\Big\langle \cos^2\theta \Big\rangle_{\psi} - 1}{2}\right).
\end{aligned}$$

Thus,

$$S_b = S \times S_\Omega, \tag{E.10}$$

with S the FY nematic order parameter quantifying the angular distribution of the molecular long axes,

$$S = \frac{3\Big\langle \cos^2\theta \Big\rangle_\psi - 1}{2}, \tag{E.11}$$

and S_Ω an intra-molecular order parameter describing the distribution of bond orientations about the long axis of each chain conformation,

$$S_\Omega = \frac{3\Big\langle \cos^2\theta_{im} \Big\rangle_\Pi - 1}{2}, \tag{E.12}$$

which yield the discretised versions of Eqs. (5.17)–(5.20).

E.2 Intra-molecular OP for unconfined persistent chains

Let us now work out the scaling behaviour of the order parameter S_{Ω_0} for unconfined chains as a function of their contour and persistence length l_c and l_p. In the KG bead-spring model, chain stiffness is governed by the bond bending potential in Eq. (5.15),

$$U_{\text{bend}} = \sum_{i=1}^{N-2} \epsilon_b\Big(1 - \mathbf{t}_{i+1}\cdot\mathbf{t}_i\Big) = \frac{\epsilon_b}{2}\sum_{i=1}^{N-2}\Big(\mathbf{t}_{i+1} - \mathbf{t}_i\Big)^2, \tag{E.13}$$

with $\mathbf{t}_i$ the normalised bond vector linking the monomers i and $i+1$, respectively located in $\mathbf{r}_i$ and $\mathbf{r}_{i+1}$,

$$\mathbf{t}_i \equiv \frac{\mathbf{r}_{i+1} - \mathbf{r}_i}{\|\mathbf{r}_{i+1} - \mathbf{r}_i\|}, \tag{E.14}$$

where $\|\cdot\|$ is the Euclidean norm. Let us denote by l_b the bond length separating any two adjacent monomers, taken to be a constant, and define $s \equiv l_b \times i$ as the curvilinear abscissa of the i-th monomer. In the continuum limit ($l_c \gg l_b$), one may assume $\{\mathbf{r}(s), \mathbf{t}(s)\} \equiv \{\mathbf{r}_i, \mathbf{t}_i\}$ to be differentiable functions of the continuous variable s, so that Eq. (E.13) converges towards the Riemann integral

$$U_{\text{bend}} = \frac{\epsilon_b l_b}{2}\int_0^{l_c} ds \left(\frac{d\mathbf{t}}{ds}\right)^2, \tag{E.15}$$

and Eq. (E.14) takes the form of the simple differential

$$\mathbf{t} = \frac{d\mathbf{r}}{ds}, \tag{E.16}$$

with $\mathbf{r}(s)$ the continuous curve describing the chain conformation in space. One thus recovers the standard worm-like chain model, with bending modulus $\mathcal{K} = \epsilon_b l_b \equiv l_p k_b T$.

Let us denote by $\mathcal{R} \equiv \left[\mathbf{v} \times \mathbf{u}\ \mathbf{v}\ \mathbf{u}\right]$ the three unit vectors defining the molecular frame $\mathcal{R}$. In the framework of PCA (c.f. Section 4.1.1), $\mathbf{v}$ and $\mathbf{u}$ respectively correspond to the molecular short and long axes, and are defined such that the following inequalities are always verified,

$$\lambda^2_{\mathbf{u}} > \lambda^2_{\mathbf{v}\times\mathbf{u}} > \lambda^2_{\mathbf{v}}, \tag{E.17}$$

where the $\lambda^2_{\mathbf{x}}$ represent the principal moments of the gyration tensor, and quantify the extent of the chain along axis $\mathbf{x}$. Their expression reads, in our notation,

$$\lambda^2_{\mathbf{x}} \equiv \left\langle (\mathbf{r}\cdot\mathbf{x})^2 \right\rangle_c \qquad \forall\, \mathbf{x} \in \{\mathbf{v}\times\mathbf{u}, \mathbf{v}, \mathbf{u}\}, \tag{E.18}$$

with $\langle\cdot\rangle_c$ the contour average,

$$\left\langle\ \cdot\ \right\rangle_c \equiv \frac{1}{l_c}\int_0^{l_c} ds\ \cdot\ , \tag{E.19}$$

assuming the particle centre of mass to be set to the origin of the frame, i.e., $\langle\mathbf{r}\rangle_c = \mathbf{0}$. The dimensionless molecular anisotropy parameter $\mathcal{A}$ is then defined as [258]

$$\mathcal{A} \equiv \frac{3}{2}\frac{\lambda^4_{\mathbf{u}} + \lambda^4_{\mathbf{v}} + \lambda^4_{\mathbf{v}\times\mathbf{u}}}{(\lambda^2_{\mathbf{u}} + \lambda^2_{\mathbf{v}} + \lambda^2_{\mathbf{v}\times\mathbf{u}})^2} - \frac{1}{2},$$

which verifies $0 \leq \mathcal{A} \leq 1$, $\mathcal{A} = 0$ being reached in the limit of a spherically-symmetric monomer distribution and $\mathcal{A} = 1$ in the case of an ideal linear chain.

In the following, we restrict our study to systems of stiff linear polymers such that $l_p \gg l_c$, for which $\mathcal{A} \sim 1$. In this case, the first inequality in Eq. (E.17) becomes wide, so that

$$\lambda^2_{\mathbf{u}} \gg \lambda^2_{\mathbf{v}\times\mathbf{u}}, \lambda^2_{\mathbf{v}}.$$

One may then approximate the end-to-end separation vector by its projection onto $\mathbf{u}$,

$$[\mathbf{r}(l_c) - \mathbf{r}(0)] \cdot \mathbf{u} = \int_0^{l_c} ds\, \mathbf{t}(s) \cdot \mathbf{u} = \int_0^{l_c} ds\, \cos\theta_m(s),$$

where we used Eq.(E.16), denoting by $\theta_m(s)$ the continuous limit of the bond angle θ_{im} as defined in Figure 5.1. The squared end-to-end distance L^2 thus reads as

$$L^2 \simeq \iint_0^{l_c} ds ds'\, \cos\theta_m(s) \cos\theta_m(s'). \tag{E.20}$$

Assuming θ_m to be a slowly-varying function of s for stiff polymers, one may write

$$\cos\theta_m(s') \simeq \cos\theta_m(s) + (s'-s)\frac{d\cos\theta_m(s)}{ds},$$

so that Eq. (E.20) may be recast in the form

$$L^2 \simeq l_c^2 \big\langle \cos^2\theta_m \big\rangle_c + \iint_0^{l_c} ds ds'\, \frac{s'-s}{2} \frac{d\cos^2\theta_m(s)}{ds}. \tag{E.21}$$

The integration by parts of the last term in Eq. (E.21) leads to, after rearrangements,

$$L^2 \simeq \frac{l_c^2}{2}\left\{ 3\big\langle \cos^2\theta_m \big\rangle_c - \frac{\cos^2\theta_m(0) + \cos^2\theta_m(l_c)}{2} \right\},$$

which yields the mean squared end-to-end distance $\langle L^2 \rangle_\Omega$,

$$\frac{\big\langle L^2 \big\rangle_\Omega}{l_c^2} \simeq \frac{3\Big\langle \big\langle \cos^2\theta_m \big\rangle_c \Big\rangle_\Omega - \big\langle \cos^2\theta_m(0) \big\rangle_\Omega}{2}, \tag{E.22}$$

where we used the equivalence of the two chain extremities. Eqs. (5.20) and (E.22) thus provide a first expression for S_Ω,

$$S_\Omega \simeq \frac{\big\langle L^2 \big\rangle_\Omega}{l_c^2} + \frac{\big\langle \cos^2\theta_m(0) \big\rangle_\Omega - 1}{2}. \tag{E.23}$$

For inextensible and unconfined worm-like chains as described by Eqs. (E.15) and (E.16), the algebraic expression for $\langle L^2 \rangle_{\Omega_0}$ reads as [320]

$$\frac{\big\langle L^2 \big\rangle_{\Omega_0}}{l_c^2} = 2\left(\frac{l_p}{l_c}\right)^2 \times \left\{ \frac{l_c}{l_p} - 1 + \exp\left(-\frac{l_c}{l_p} \right) \right\} \tag{E.24}$$

$$= 1 - \frac{l_c}{3l_p} + \mathcal{O}\left\{ \left(\frac{l_c}{l_p}\right)^2 \right\}. \tag{E.25}$$

Let us now assimilate the long axis $\mathbf{u}$ of a stiff chain to the contour-averaged local tangent vector $\mathbf{t}(s)$, so that

$$\cos\theta_m(0) \equiv \mathbf{t}(0)\cdot\mathbf{u} \cong \mathbf{t}(0)\cdot\Big\langle\mathbf{t}\Big\rangle_c.$$

It follows from the usual definition of the persistence length that

$$\begin{aligned}\Big\langle\cos\theta_m(0)\Big\rangle_{\Omega_0} &= \frac{1}{l_c}\int_0^{l_c} ds\,\Big\langle\mathbf{t}(0)\cdot\mathbf{t}(s)\Big\rangle_{\Omega_0}\\ &= \frac{1}{l_c}\int_0^{l_c} ds\,\exp\left(-\frac{s}{l_p}\right)\\ &= 1-\frac{\Big\langle\theta_m(0)^2\Big\rangle_{\Omega_0}}{2}+\mathcal{O}\Big\{\Big\langle\theta_m(0)^4\Big\rangle_{\Omega_0}\Big\}.\end{aligned}$$

Thus, for $\theta_m(0) \ll 1$,

$$\begin{aligned}\frac{\Big\langle\cos^2\theta_m(0)\Big\rangle_{\Omega_0}-1}{2} &= -\frac{\Big\langle\theta_m(0)^2\Big\rangle_{\Omega_0}}{2}\\ &= \frac{l_p}{l_c}\left\{1-\exp\left(-\frac{l_c}{l_p}\right)\right\}-1 \qquad \text{(E.26)}\\ &= -\frac{l_c}{2l_p}+\mathcal{O}\left\{\left(\frac{l_c}{l_p}\right)^2\right\}. \qquad \text{(E.27)}\end{aligned}$$

Plugging Eqs. (E.25) and (E.27) into Eq. (E.23) finally yields a simple scaling law for the intra-molecular order parameter of stiff, unconfined persistent chains,

$$S_{\Omega_0} \simeq 1-\frac{5l_c}{6l_p}.$$

F

Backbone helicity and conformational fluctuations

Contents

F.1 Derivation of an helicity order parameter

Let us parametrise an arbitrary backbone conformation of an origami with contour length l_c by a continuous curve $\mathbf{r}(s)$, where $s \in [0, l_c]$ is the curvilinear abscissa. The local unit tangent to the curve reads as

$$\mathbf{t}(s) = \frac{d\mathbf{r}}{ds} \equiv t_{\parallel}(s)\mathbf{u} + \mathbf{t}_{\perp}(s), \tag{F.1}$$

with $\mathbf{u}$ the long axis of the conformation as defined in Section 5.1.3 and $\mathbf{t}_{\perp} \cdot \mathbf{u} = 0$. Due to the large bending rigidity of the filaments, we assume the transverse fluctuations of $\mathbf{r}$ to be small,

$$\|\mathbf{t}_{\perp}(s)\| = \left\| \frac{d\mathbf{r}_{\perp}}{ds} \right\| \ll 1,$$

where we used the notation of Figure 6.6a, with $\|\cdot\|$ the Euclidean norm. Thus,

$$t_{\parallel}(s) = \sqrt{1 - \|\mathbf{t}_{\perp}(s)\|^2} = 1 + \mathcal{O}\Big(\|\mathbf{t}_{\perp}\|^2\Big),$$

and integrating Eq. (F.1) yields, to leading order in $\mathbf{t}_{\perp}$,

$$\mathbf{r}(s) = \mathbf{r}_0 + s\mathbf{u} + \mathbf{r}_{\perp}(s), \tag{F.2}$$

where $\mathbf{r}_0 = \mathbf{r}(0) - \mathbf{r}_{\perp}(0)$. Consistently with the previous approximations, we further assimilate the filament long axis $\mathbf{u}$ with the normalised end-to-end separation vector,

$$\mathbf{u} \cong \frac{\mathbf{r}(l_c) - \mathbf{r}(0)}{\|\mathbf{r}(l_c) - \mathbf{r}(0)\|},$$

so that Eq. (F.2) imposes simple periodic boundary conditions for $\mathbf{r}_{\perp}$,

$$\mathbf{r}_{\perp}(0) = \mathbf{r}_{\perp}(l_c).$$

$\mathbf{r}_{\perp}$ may then be expressed in the form of an inverse Fourier transform,

$$\mathbf{r}_{\perp}(s) = \frac{1}{l_c} \sum_k \widehat{\mathbf{r}}_{\perp}(k) \times e^{2i\pi k s}, \tag{F.3}$$

with discrete wavenumbers $k = n/l_c$ for any non-zero integer n and coefficients

$$\widehat{\mathbf{r}}_{\perp}(k) = \int_0^{l_c} ds\, \mathbf{r}_{\perp}(s) \times e^{-2i\pi k s} \equiv \widehat{r}_{\perp v}(k)\mathbf{v} + \widehat{r}_{\perp w}(k)\mathbf{w}. \tag{F.4}$$

Let $|\cdot|$ be the complex modulus, and

$$e^{i\phi_v(k)} \equiv \frac{\widehat{r}_{\perp v}(k)}{|\widehat{r}_{\perp v}(k)|}, \tag{F.5}$$

$$e^{i\phi_w(k)} \equiv \frac{\widehat{r}_{\perp w}(k)}{|\widehat{r}_{\perp w}(k)|}. \tag{F.6}$$

Using Eqs. (F.2)–(F.4), the backbone conformation $\mathbf{r}_k$ associated with a transverse deformation mode of arbitrary wavenumber k is given by the parametric equation

$$\mathbf{r}_k(s) = s\mathbf{u} + \frac{2}{l_c}\Big\{|\widehat{r}_{\perp v}(k)| \cos[2\pi k s + \phi_v(k)]\mathbf{v} + |\widehat{r}_{\perp w}(k)| \cos[2\pi k s + \phi_w(k)]\mathbf{w}\Big\}. \tag{F.7}$$

In the most general case, Eq. (F.7) describes an elliptical helix of axis $\mathbf{u}$ and pitch $p = 1/k$. The shape chirality associated with a deformation mode $\mathbf{r}_k$ is thus quantified by the anisotropy of its elliptical cross section, which we now proceed

to analyse. In the following, we omit some of the explicit k dependences in order to alleviate the notations when no confusion can arise. Let us denote by

$$\|\widehat{\mathbf{r}}_\perp\| \equiv \sqrt{\widehat{\mathbf{r}}_\perp \cdot \widehat{\mathbf{r}}_\perp^*} = \sqrt{|\widehat{r}_{\perp v}|^2 + |\widehat{r}_{\perp w}|^2} \tag{F.8}$$

the Euclidean modulus of $\widehat{\mathbf{r}}_\perp$, and define

$$\theta \equiv \arccos \frac{|\widehat{r}_{\perp v}|}{\|\widehat{\mathbf{r}}_\perp\|}, \tag{F.9}$$

$$A \equiv \frac{2\|\widehat{\mathbf{r}}_\perp\|}{l_c}. \tag{F.10}$$

Using Eqs. (F.7)–(F.10), the transverse components of $\mathbf{r}_k$ may be rewritten as

$$r_{kv}(s) \equiv \mathbf{r}_k(s) \cdot \mathbf{v} = A\cos\theta \times \cos(\omega s + \phi_v), \tag{F.11}$$

$$r_{kw}(s) \equiv \mathbf{r}_k(s) \cdot \mathbf{w} = A\sin\theta \times \cos(\omega s + \phi_w), \tag{F.12}$$

with $\omega \equiv 2\pi k$. Eq. (F.12) then yields

$$\frac{r_{kw}(s)}{A\sin\theta} = \cos(\omega s + \phi_v)\cos\phi + \sin(\omega s + \phi_v)\sin\phi,$$

where

$$\phi \equiv \phi_v - \phi_w. \tag{F.13}$$

Thus, using Eq. (F.11),

$$\frac{r_{kw}(s)}{A\sin\theta} - \frac{r_{kv}(s)}{A\cos\theta}\cos\phi = \sin(\omega s + \phi_v)\sin\phi, \tag{F.14}$$

and Eq. (F.11) immediately yields the further relation

$$\sin(\omega s + \phi_v) = \pm\sqrt{1 - \left\{\frac{r_{kv}(s)}{A\cos\theta}\right\}^2}. \tag{F.15}$$

Plugging Eq. (F.15) into Eq. (F.14) leads to a quadratic equation for r_{kv} and r_{kw},

$$\left(\frac{r_{kv}}{A\cos\theta}\right)^2 + \left(\frac{r_{kw}}{A\sin\theta}\right)^2 - 2\cos\phi\frac{r_{kv}r_{kw}}{A^2\cos\theta\sin\theta} = \sin^2\phi. \tag{F.16}$$

Denoting by $\mathbf{r}_{k\perp}$ the total transverse component of $\mathbf{r}_k$,

$$\mathbf{r}_{k\perp}(s) \equiv r_{kv}(s)\mathbf{v} + r_{kw}(s)\mathbf{w},$$

Eq. (F.16) may be recast in the compact form

$$\mathbf{r}_{k\perp}^{\mathsf{T}} \cdot \mathcal{Q} \cdot \mathbf{r}_{k\perp} = 1,$$

with $\mathbf{r}_{k\perp}^{\mathsf{T}}$ the matrix transpose of $\mathbf{r}_{k\perp}$ and $\mathcal{Q}$ the matrix representation of the quadratic form in Eq. (F.16),

$$\mathcal{Q} = \frac{1}{\sin^2\phi}\begin{bmatrix} \dfrac{1}{(A\cos\theta)^2} & -\dfrac{\cos\phi}{A^2\cos\theta\sin\theta} \\ -\dfrac{\cos\phi}{A^2\cos\theta\sin\theta} & \dfrac{1}{(A\sin\theta)^2} \end{bmatrix}.$$

The respective lengths $r_\pm$ of the semi-major and semi-minor elliptical axes are then related to the respective largest and smallest eigenvalues $\lambda_\pm$ of $\mathcal{Q}$ through [321]

$$r_\pm = 1/\sqrt{\lambda_\mp},$$

which yields, after rearrangements,

$$r_\pm = A\sqrt{\frac{1 \pm \sqrt{1-\sin^2\phi\sin^2 2\theta}}{2}}. \tag{F.17}$$

Interestingly, Eq. (F.17) bears a strong resemblance to the Jones vector parametrisation of the polarisation ellipse in classical electrodynamics [322], which stems from the similarity between Eq. (F.7) and the field equation of a polarised electromagnetic wave propagating along the direction $\mathbf{u}$.

Let us define

$$\mathcal{H} \equiv \sin\phi\sin 2\theta. \tag{F.18}$$

An explicit expression for $\mathcal{H}$ in terms of the Fourier components $\widehat{\mathbf{r}}_\perp(k)$ may be obtained by substituting Eqs. (F.8) and (F.9) for θ,

$$\sin 2\theta = 2\cos\theta\sin\theta = \frac{2|\widehat{r}_{\perp v}||\widehat{r}_{\perp w}|}{|\widehat{r}_{\perp v}|^2 + |\widehat{r}_{\perp w}|^2},$$

and substituting Eqs. (F.13), (F.5) and (F.6) for ϕ,

$$e^{i\phi} = e^{i\phi_v}e^{-i\phi_w} = \frac{\widehat{r}_{\perp v} \times \widehat{r}^{\,*}_{\perp w}}{|\widehat{r}_{\perp v}||\widehat{r}_{\perp w}|}.$$

Eq. (F.18) may thus be rewritten in the form

$$\mathcal{H} = 2 \times \frac{\Im\left\{\widehat{r}_{\perp v} \times \widehat{r}^{\,*}_{\perp w}\right\}}{\left|\widehat{r}_{\perp v}\right|^2 + \left|\widehat{r}_{\perp w}\right|^2} = 2 \times \frac{\Im\left\{\widehat{c}_{vw}\right\}}{\widehat{c}_{vv} + \widehat{c}_{ww}}, \tag{F.19}$$

and one recovers the definition of Eq. (6.8), with $\widehat{c}_{vw}(k)$ the Fourier components of the cross-correlation function of $r_{\perp v}$ and $r_{\perp w}$ as given by the convolution theorem,

$$\widehat{c}_{vw}(k) = \widehat{r}_{\perp v}(k) \times \widehat{r}^{\,*}_{\perp w}(k).$$

Using Eqs. (F.17) and (F.18), the transverse eccentricity of the elliptical cross section reads as

$$e^2 \equiv \frac{r_+^2 - r_-^2}{r_+^2} = \frac{2\sqrt{1-\mathcal{H}^2}}{1+\sqrt{1-\mathcal{H}^2}}.$$

A necessary and sufficient condition for the deformation mode $\mathbf{r}_k$ to describe an ideal circular helix is given by

$$e(k) = 0 \iff \mathcal{H}(k) = \pm 1.$$

Conversely,

$$e(k) = 1 \iff \mathcal{H}(k) = 0$$

describes the degenerate case in which the elliptical cross section collapses to a flat line segment, leading to an achiral deformation mode. The mean solenoidal radius r_m of an arbitrary deformation mode may finally be obtained in the compact form

$$r_m \equiv \sqrt{r_+ \times r_-} = A\sqrt{\frac{|\mathcal{H}|}{2}}. \tag{F.20}$$

F.2 Determination of helical handedness

The magnitude of $\mathcal{H}(k)$ may thus be understood as a measure of the degree of circular helicity of the deformation mode $\mathbf{r}_k$. The link between the sign of $\mathcal{H}(k)$ and the corresponding helical handedness may be elucidated by considering the case of an ideal circular helical conformation of axis $\mathbf{u}$, radius $r_h > 0$ and inverse

pitch $q = 1/p_h$. The general parametric equation of such a conformation reads as, in the limit of weak helical curvature ($qr_h \ll 1$),

$$\mathbf{r}_q^h(s) = s\mathbf{u} + r_h \cos(2\pi q s + \phi_h)\mathbf{v} + r_h \sin(2\pi q s + \phi_h)\mathbf{w}, \tag{F.21}$$

with $\phi_h \in [0, 2\pi]$. In the convention of Eq. (F.21), the handedness of the helix is quantified by the sign of q, with $q > 0$ (resp. $q < 0$) corresponding to a right-handed (resp. left-handed) helicity. Using the previous notations, the Fourier components of the transverse vector $\mathbf{r}_{q\perp}^h$ associated with Eq. (F.21) read as

$$\widehat{\mathbf{r}}_{q\perp}^{\,h}(k) = \begin{cases} l_c \times \dfrac{r_h e^{\pm i\phi_h}}{2}\left(\mathbf{v} \pm e^{-i\pi/2}\mathbf{w}\right) & \text{if} \quad k = \pm q \\ \mathbf{0} & \text{if } |k| \neq |q| \end{cases}.$$

In this case, for any wavenumber $k > 0$, Eq. (F.19) reduces to

$$\mathcal{H}(k) = \delta_{k,|q|} \times \operatorname{sgn} q,$$

and it is easy to check that Eqs. (F.17), (F.8) and (F.10) yield

$$r_+(k) = r_-(k) = \delta_{k,|q|} \times r_h,$$

with δ the Kronecker delta and sgn the sign function. Therefore, the handedness of a deformation mode with arbitrary wavenumber $k > 0$ may be determined by the sign of $\mathcal{H}(k)$, with $\mathcal{H}(k) > 0$ and $\mathcal{H}(k) < 0$ respectively describing a right- and left-handed helicity.

F.3 Fluctuation spectrum and the equipartition theorem

Using the notations of Section F.1, the enthalpic penalty U_{bend} associated with the bending response of a single origami to thermal fluctuations may be readily obtained from Eqs. (E.15), (F.1) and (F.2)) in the case of weak curvature deformations,

$$U_{\text{bend}} = \frac{\mathcal{K}}{2}\int_0^{l_c} ds \left\| \frac{d^2\mathbf{r}_\perp}{ds^2} \right\|^2, \tag{F.22}$$

where the bending modulus $\mathcal{K}$ is related to the origami persistence length l_p through

$$\mathcal{K} = l_p k_b T. \tag{F.23}$$

Substituting Eqs. (F.3) and (F.4) for $\mathbf{r}_\perp$ in Eq. (F.22) yields

$$U_{\text{bend}} = \frac{\mathcal{K}}{2l_c} \times \sum_k (2\pi k)^4 \Big\{ |\widehat{r}_{\perp v}(k)|^2 + |\widehat{r}_{\perp w}(k)|^2 \Big\}. \tag{F.24}$$

Assimilating the different transverse deformation modes in Eq. (F.24) to decoupled degrees of freedom, the equipartition theorem imposes for $\widehat{r}_{\perp v}$ and $\widehat{r}_{\perp w}$ [235]

$$\left\langle |\widehat{r}_{\perp v}(k)|^2 \right\rangle = \left\langle |\widehat{r}_{\perp w}(k)|^2 \right\rangle = \frac{k_b T l_c}{\mathcal{K}} \times \frac{1}{(2\pi k)^4}.$$

Thus, using Eqs. (F.8) and (F.23),

$$\left\langle \|\widehat{\mathbf{r}}_\perp(k)\|^2 \right\rangle = \frac{l_c}{l_p} \times \frac{1}{8\pi^4 k^4}, \tag{F.25}$$

valid in the limit of long-wavelength fluctuations ($k \to 0$).

Bibliography

[1] J. W. Goodby, *J. Mater. Chem.* **1**, 307 (1991).

[2] T. Graham, *Phil. Trans. R. Soc. London* **151**, 183 (1861).

[3] A. D. McNaught, *Compendium of Chemical Terminology*, vol. 1669 (Blackwell Science, Oxford, 1997).

[4] S. C. Glotzer, M. J. Solomon, *Nat. Mater.* **6**, 557 (2007).

[5] G. M. Whitesides, B. Grzybowski, *Science* **295**, 2418 (2002).

[6] M. A. Boles, M. Engel, D. V. Talapin, *Chem. Rev.* **116**, 11220 (2016).

[7] F. Li, D. P. Josephson, A. Stein, *Angew. Chem. Int. Edit.* **50**, 360 (2011).

[8] D. F. Evans, H. Wennerström, *The Colloidal Domain: Where Physics, Chemistry, Biology, and Technology Meet* (VCH, New York, NY, 1999).

[9] P.-G. de Gennes, J. Prost, *The Physics of Liquid Crystals* (Clarendon Press, Oxford, 1993).

[10] J. W. Goodby, G. W. Gray, *Handbook of Liquid Crystals*, D. Demus, J. Goodby, G. W. Gray, H.-W. Spiess, V. Vill, eds. (Wiley-VCH Verlag GmbH, Weinheim, 2008), pp. 17–23.

[11] R. Goetz, R. Lipowsky, *J. Chem. Phys.* **108**, 7397 (1998).

[12] C. M. Coppin, P. C. Leavis, *Biophys. J.* **63**, 794 (1992).

[13] J. W. Harris, *P. Soc. Exp. Biol. Med.* **75**, 197 (1950).

[14] A. M. Figueiredo Neto, S. R. A. Salinas, *The Physics of Lyotropic Liquid Crystals* (Oxford University Press, Oxford, 2005).

[15] S.-T. Wu, *Phys. Rev. A* **33**, 1270 (1986).

[16] V. Fréedericksz, V. Zolina, *T. Faraday Soc.* **29**, 919 (1933).

[17] M. Doi, *J. Polym. Sci. Polym. Phys. Ed.* **19**, 243 (1981).

[18] G. R. Luckhurst, T. J. Sluckin, *Biaxial Nematic Liquid Crystals: Theory, Simulation and Experiment* (John Wiley & Sons, New York, NY, 2015).

[19] J. P. F. Lagerwall, G. Scalia, *Curr. Appl. Phys.* **12**, 1387 (2012).

[20] G. Singhvi, S. Banerjee, A. Khosa, *Organic Materials as Smart Nanocarriers for Drug Delivery*, A. M. Grumezescu, ed. (William Andrew Publishing, Norwich, NY, 2018), chap. 11, pp. 471—517.

[21] F. Vollrath, D. P. Knight, *Nature* **410**, 541 (2001).

[22] J. Uffink, *Philosophy of Physics*, J. Butterfield, J. Earman, eds., Handbook of the Philosophy of Science (North-Holland, Amsterdam, 2007), pp. 923 – 1074.

[23] V. N. Manoharan, *Science* **349**, 1253751 (2015).

[24] M. E. Cates, V. N. Manoharan, *Soft Matter* **11**, 6538 (2015).

[25] H. N. W. Lekkerkerker, R. Tuinier, *Colloids and the Depletion Interaction*, vol. 833 of *Lecture Notes in Physics* (Springer Netherlands, Dordrecht, 2011).

[26] C. E. Shannon, *Bell Syst. Tech. J.* **27**, 379 (1948).

[27] D. Frenkel, *Physica A* **263**, 26 (1999).

[28] D. Frenkel, *Nat. Mater.* **14**, 9 (2014).

[29] B. J. Alder, T. E. Wainwright, *J. Chem. Phys.* **27**, 1208 (1957).

[30] P. N. Pusey, W. van Megen, *Nature* **320**, 340 (1986).

[31] L. Onsager, *Ann. N.Y. Acad. Sci.* **51**, 627 (1949).

[32] W. Thomson, *Baltimore Lectures on Molecular Dynamics and the Wave Theory of Light* (Cambridge Library Collection, Cambridge, 1904).

[33] J. E. McMurry, *Organic Chemistry* (Brooks/Cole, Pacific Grove, CA, 1992).

[34] L. Pasteur, *C. R. Acad. Sci.* **26**, 535 (1848).

[35] E. J. Ariens, *Eur. J. Clin. Pharmacol.* **26**, 663 (1984).

[36] G. H. Brown, J. J. Wolken, *Liquid Crystals and Biological Structures* (Academic Press, New York, NY, 1979).

[37] M. Mitov, *Soft Matter* **13**, 4176 (2017).

[38] F. Reinitzer, *Monatsh. Chem.* **9**, 421 (1888).

[39] D. A. Dunmur, T. J. Sluckin, *Soap, Science, and Flat-screen TVs: A History of Liquid Crystals* (Oxford University Press, Oxford, 2011).

[40] Y. Bouligand, *Tissue Cell* **4**, 189 (1972).

[41] E. Belamie, G. Mosser, F. Gobeaux, M.-M. Giraud-Guille, *J. Phys.: Condens. Matter* **18**, S115 (2006).

[42] M. H. Chow, K. T. Yan, M. J. Bennett, J. T. Y. Wong, *Eukaryot. cell* **9**, 1577 (2010).

[43] G. Friedel, *Ann. Phys.* **9**, 273 (1922).

[44] L. M. Blinov, *Structure and Properties of Liquid Crystals* (Springer Science & Business Media, Heidelberg, 2011).

[45] J. C. Weaver, *et al.*, *Science* **336**, 1275 (2012).

[46] S. Vignolini, *et al.*, *Proc. Natl. Acad. Sci. USA* **109**, 15712 (2012).

[47] A. G. Dumanli, *et al.*, *Adv. Opt. Mater.* **2**, 646 (2014).

[48] L. Wang, A. M. Urbas, Q. Li, *Adv. Mater.* **0**, 1801335 (2018).

[49] J. P. F. Lagerwall, *et al.*, *NPG Asia Mater.* **6**, e80 (2014).

[50] A. P. Almeida, *et al.*, *Adv. Mater.* **30**, 1703655 (2018).

[51] E. Barry, D. Beller, Z. Dogic, *Soft Matter* **5**, 2563 (2009).

[52] E. Grelet, S. Fraden, *Phys. Rev. Lett.* **90**, 198302 (2003).

[53] F. C. Bawden, N. W. Pirie, J. D. Bernal, I. Fankuchen, *Nature* **138**, 1051 (1936).

[54] Z. Dogic, S. Fraden, *Langmuir* **16**, 7820 (2000).

[55] G. Zanchetta, *et al.*, *Proc. Natl. Acad. Sci. USA* **107**, 17497 (2010).

[56] D. B. DuPré, R. W. Duke, *J. Chem. Phys.* **63**, 143 (1975).

[57] Y. M. Yevdokimov, S. G. Skuridin, V. I. Salyanov, *Liq. Cryst.* **3**, 1443 (1988).

[58] D. H. van Winkle, M. W. Davidson, W. X. Chen, R. L. Rill, *Macromolecules* **23**, 4140 (1990).

[59] X. M. Dong, D. G. Gray, *Langmuir* **13**, 2404 (1997).

[60] A. F. Miller, A. M. Donald, *Biomacromolecules* **4**, 510 (2003).

[61] C. B. Stanley, H. Hong, H. H. Strey, *Biophys. J.* **89**, 2552 (2005).

[62] P. De Sa Peixoto, A. Deniset-Besseau, M.-C. Schanne-Klein, G. Mosser, *Soft Matter* **7**, 11203 (2011).

[63] M. F. Moreira, *et al.*, *Appl. Phys. Lett.* **85**, 2691 (2004).

[64] A. Mujahid, H. Stathopulos, P. A. Lieberzeit, F. L. Dickert, *Sensors* **10**, 4887 (2010).

[65] A. B. Harris, R. D. Kamien, T. C. Lubensky, *Rev. Mod. Phys.* **71**, 1745 (1999).

[66] A. B. Harris, R. D. Kamien, T. C. Lubensky, *Phys. Rev. Lett.* **78**, 1476 (1997).

[67] N. Metropolis, A. W. Rosenbluth, M. N. Rosenbluth, A. H. Teller, E. Teller, *J. Chem. Phys.* **21**, 1087 (1953).

[68] M. P. Allen, D. J. Tildesley, *Computer Simulation of Liquids* (Clarendon Press, New York, NY, 1989).

[69] D. Frenkel, B. Smit, *Understanding Molecular Simulation* (Academic Press, San Diego, CA, 2002), second edn.

[70] M. R. Wilson, *Int. Rev. Phys. Chem.* **24**, 421 (2005).

[71] S. Ruzicka, H. H. Wensink, *Soft Matter* **12**, 5205 (2016).

[72] L. Wu, H. Sun, *Soft Matter* **14**, 344 (2018).

[73] J. A. Anderson, M. E. Irrgang, S. C. Glotzer, *Comput. Phys. Commun.* **204**, 21 (2016).

[74] S. Dussi, M. Dijkstra, *Nat. Commun.* **7**, 11175 (2016).

[75] D. Frenkel, *Eur. Phys. J. Plus* **128**, 10 (2013).

[76] M. P. Allen, A. J. Masters, *Mol. Phys.* **79**, 277 (1993).

[77] M. P. Allen, *Phys. Rev. E* **47**, 4611 (1993).

[78] P. J. Camp, *Mol. Phys.* **91**, 381 (1997).

[79] M. J. Cook, M. R. Wilson, *J. Chem. Phys.* **112**, 1560 (2000).

[80] M. P. Allen, A. J. Masters, *J. Mater. Chem.* **11**, 2678 (2001).

[81] G. Germano, M. P. Allen, A. J. Masters, *J. Chem. Phys.* **116**, 9422 (2002).

[82] J. P. Straley, *Phys. Rev. A* **14**, 1835 (1976).

[83] M. A. Osipov, *Chem. Phys.* **96**, 259 (1985).

[84] T. Odijk, *J. Phys. Chem.* **91**, 6060 (1987).

[85] R. A. Pelcovits, *Liq. Cryst.* **21**, 361 (1996).

[86] G. T. Evans, *Mol. Phys.* **77**, 969 (1992).

[87] S. Varga, G. Jackson, *Mol. Phys.* **104**, 3681 (2006).

[88] S. Varga, G. Jackson, *Mol. Phys.* **109**, 1313 (2011).

[89] H. H. Wensink, G. Jackson, *J. Chem. Phys.* **130**, 234911 (2009).

[90] H. H. Wensink, G. Jackson, *J. Phys.: Condens. Matter* **23**, 194107 (2011).

[91] H. H. Wensink, *Europhys. Lett.* **107**, 36001 (2014).

[92] F. Tombolato, A. Ferrarini, *J. Chem. Phys.* **122**, 054908 (2005).

[93] F. Tombolato, A. Ferrarini, E. Grelet, *Phys. Rev. Lett.* **96**, 258302 (2006).

[94] E. Frezza, A. Ferrarini, H. B. Kolli, A. Giacometti, G. Cinacchi, *Phys. Chem. Chem. Phys.* **16**, 16225 (2014).

[95] S. Belli, S. Dussi, M. Dijkstra, R. van Roij, *Phys. Rev. E* **90**, 020503 (2014).

[96] S. Dussi, S. Belli, R. van Roij, M. Dijkstra, *J. Chem. Phys.* **142**, 074905 (2015).

[97] M. M. C. Tortora, J. P. K. Doye, *J. Chem. Phys.* **146**, 184504 (2017).

[98] M. M. C. Tortora, J. P. K. Doye, *J. Chem. Phys.* **147**, 224504 (2017).

[99] M. M. C. Tortora, J. P. K. Doye, *Mol. Phys.* **116**, 2773 (2018).

[100] M. M. C. Tortora, G. Mishra, D. Prešern, J. P. K. Doye, *Sci. Adv.* (in review.).

[101] C. Kittel, *Thermal Physics* (John Wiley & Sons, Inc., New York, NY, 1969).

[102] K. Lucas, *Molecular Models for Fluids* (Cambridge University Press, Cambridge, 2007).

[103] J. E. Mayer, *J. Chem. Phys.* **5**, 67 (1937).

[104] G. J. Vroege, H. N. W. Lekkerkerker, *Rep. Prog. Phys.* **55**, 1241 (1992).

[105] R. Evans, *Adv. Phys.* **28**, 143 (1979).

[106] P. Hohenberg, W. Kohn, *Phys. Rev.* **136**, B864 (1964).

[107] N. D. Mermin, *Phys. Rev.* **137**, A1441 (1965).

[108] J.-P. Hansen, I. R. McDonald, *Theory of Simple Liquids* (Academic Press, London, 1976).

[109] D. Frenkel, *J. Phys. Chem.* **91**, 4912 (1987).

[110] J. P. Straley, *Mol. Cryst. Liq. Cryst.* **24**, 7 (1973).

[111] H. B. Kolli, *et al.*, *Soft Matter* **10**, 8171 (2014).

[112] S. Dussi, N. Tasios, T. Drwenski, R. van Roij, M. Dijkstra, *Phys. Rev. Lett.* **120**, 177801 (2018).

[113] A. J. Masters, *J. Phys.: Condens. Matter* **20**, 283102 (2008).

[114] X.-M. You, A. Y. Vlasov, A. J. Masters, *J. Chem. Phys.* **123**, 034510 (2005).

[115] X.-M. You, A. Y. Vlasov, L. Anton, A. J. Masters, *Phys. Rev. E* **85**, 061706 (2012).

[116] M. S. Wertheim, *Phys. Rev. Lett.* **10**, 321 (1963).

[117] T. Morita, K. Hiroike, *Prog. Theor. Phys.* **23**, 385 (1960).

[118] Y. Rosenfeld, *J. Chem. Phys.* **89**, 4272 (1988).

[119] R. Wittmann, M. Marechal, K. Mecke, *J. Phys.: Condens. Matter* **28**, 244003 (2016).

[120] M. Schmidt, *Phys. Rev. E* **60**, R6291 (1999).

[121] R. Pynn, *Solid State Commun.* **14**, 29 (1974).

[122] A. Wulf, *J. Chem. Phys.* **67**, 2254 (1977).

[123] J. D. Parsons, *Phys. Rev. A* **19**, 1225 (1979).

[124] S.-D. Lee, *J. Chem. Phys.* **87**, 4972 (1987).

[125] S. Boyd, L. Vandenberghe, *Convex Optimization* (Cambridge University Press, Cambridge, 2004).

[126] J. K. Percus, G. J. Yevick, *Phys. Rev.* **110**, 1 (1958).

[127] N. F. Carnahan, K. E. Starling, *J. Chem. Phys.* **51**, 635 (1969).

[128] P. J. Camp, C. P. Mason, M. P. Allen, A. A. Khare, D. A. Kofke, *J. Chem. Phys.* **105**, 2837 (1996).

[129] A. Cuetos, B. Martínez-Haya, S. Lago, L. F. Rull, *Phys. Rev. E* **75**, 061701 (2007).

[130] A. Cuetos, B. Martínez-Haya, S. Lago, L. F. Rull, *J. Phys. Chem. B* **109**, 13729 (2005).

[131] C. Vega, S. Lago, *Comput. Chem.* **18**, 55 (1994).

[132] D. Frenkel, H. N. W. Lekkerkerker, A. Stroobants, *Nature* **332**, 822 (1988).

[133] P. Bolhuis, D. Frenkel, *J. Chem. Phys.* **106**, 666 (1997).

[134] S. C. McGrother, D. C. Williamson, G. Jackson, *J. Chem. Phys.* **104**, 6755 (1996).

[135] M. Dijkstra, R. van Roij, R. Evans, *Phys. Rev. E* **63**, 051703 (2001).

[136] A. Cuetos, M. Dijkstra, *Phys. Rev. Lett.* **98**, 095701 (2007).

[137] R. Ni, S. Belli, R. van Roij, M. Dijkstra, *Phys. Rev. Lett.* **105**, 088302 (2010).

[138] A. Patti, D. El Masri, R. van Roij, M. Dijkstra, *J. Chem. Phys.* **132**, 224907 (2010).

[139] J. M. Haile, C. G. Gray, *Chem. Phys. Lett.* **76**, 583 (1980).

[140] S. V. Savenko, M. Dijkstra, *Phys. Rev. E* **72**, 021202 (2005).

[141] M. P. Allen, C. P. Mason, E. De Miguel, J. Stelzer, *Phys. Rev. E* **52**, R25 (1995).

[142] N. H. Phuong, G. Germano, F. Schmid, *J. Chem. Phys.* **115**, 7227 (2001).

[143] N. H. Phuong, G. Germano, F. Schmid, *Comput. Phys. Commun.* **147**, 350 (2002).

[144] N. H. Phuong, F. Schmid, *J. Chem. Phys.* **119**, 1214 (2003).

[145] M. Dennison, A. J. Masters, D. L. Cheung, M. P. Allen, *Mol. Phys.* **107**, 375 (2009).

[146] C. Ebner, W. F. Saam, D. Stroud, *Phys. Rev. A* **14**, 2264 (1976).

[147] W. F. Saam, C. Ebner, *Phys. Rev. A* **15**, 2566 (1977).

[148] S.-D. Lee, *Phys. Rev. A* **39**, 3631 (1989).

[149] W. B. Streett, D. J. Tildesley, *Proc. R. Soc. Lond. A* **348**, 485 (1976).

[150] W. R. Gibbs, *Computation in Modern Physics* (World Scientific Publishing Company, Singapore, 2006).

[151] J. A. Anderson, C. D. Lorenz, A. Travesset, *J. Comput. Phys.* **227**, 5342 (2008).

[152] J. Glaser, *et al.*, *Comput. Phys. Commun.* **192**, 97 (2015).

[153] C.-E. Froberg, *Introduction to Numerical Analysis* (Addison-Wesley, Reading, MA, 1969).

[154] M. Kardar, *Statistical Physics of Fields* (Cambridge University Press, Cambridge, 2007).

[155] M. J. Stephen, J. P. Straley, *Rev. Mod. Phys.* **46**, 617 (1974).

[156] D. Andrienko, *J. Mol. Liq.* **267**, 520 (2018).

[157] A. M. Somoza, P. Tarazona, *Mol. Phys.* **72**, 911 (1991).

[158] R. B. Meyer, *Polymer Liquid Crystals*, A. Ciferri, W. Krigbaum, R. B. Meyer, eds. (Academic Press, Cambridge, MA, 1982), chap. 6, pp. 133 – 163.

[159] A. Milchev, S. A. Egorov, K. Binder, A. Nikoubashman, *J. Chem. Phys.* **149**, 174909 (2018).

[160] K. E. Gubbins, *Chem. Phys. Lett.* **76**, 329 (1980).

[161] A. Poniewierski, J. Stecki, *Mol. Phys.* **38**, 1931 (1979).

[162] J. P. Straley, *Phys. Rev. A* **8**, 2181 (1973).

[163] A. M. Somoza, P. Tarazona, *Phys. Rev. A* **40**, 6069 (1989).

[164] J. Herzfeld, A. E. Berger, J. W. Wingate, *Macromolecules* **17**, 1718 (1984).

[165] F. James, *Rep. Prog. Phys.* **43**, 1145 (1980).

[166] S. Lang, *Algebra* (Springer-Verlag, New York, NY, 2002), third edn.

[167] R. F. Kayser Jr, H. J. Raveché, *Phys. Rev. A* **17**, 2067 (1978).

[168] X. Xiao, P. Sheng, *Phys. Rev. E* **88**, 062501 (2013).

[169] E. van den Pol, A. Petukhov, D. Thies-Weesie, D. Byelov, G. Vroege, *Phys. Rev. Lett.* **103**, 258301 (2009).

[170] S. Belli, A. Patti, M. Dijkstra, R. van Roij, *Phys. Rev. Lett.* **107**, 148303 (2011).

[171] S. D. Peroukidis, A. G. Vanakaras, *Soft Matter* **9**, 7419 (2013).

[172] K. Severing, K. Saalwächter, *Phys. Rev. Lett.* **92**, 125501 (2004).

[173] L. A. Madsen, T. J. Dingemans, M. Nakata, E. T. Samulski, *Phys. Rev. Lett.* **92**, 145505 (2004).

[174] G. R. Luckhurst, *Nature* **430**, 413 (2004).

[175] B. R. Acharya, A. Primak, S. Kumar, *Phys. Rev. Lett.* **92**, 145506 (2004).

[176] R. Berardi, L. Muccioli, S. Orlandi, M. Ricci, C. Zannoni, *J. Phys.: Condens. Matt.* **20**, 463101 (2008).

[177] A. Cuetos, M. Dennison, A. J. Masters, A. Patti, *Soft Matter* **13**, 4720 (2017).

[178] E. Frezza, A. Ferrarini, H. B. Kolli, A. Giacometti, G. Cinacchi, *J. Chem. Phys.* **138**, 164906 (2013).

[179] H. B. Kolli, *et al.*, *J. Chem. Phys.* **140**, 081101 (2014).

[180] D. C. Williamson, G. Jackson, *J. Chem. Phys.* **108**, 10294 (1998).

[181] J. L. F. Abascal, S. Lago, *J. Mol. Liq.* **30**, 133 (1985).

[182] S. Varga, I. Szalai, *Mol. Phys.* **98**, 693 (2000).

[183] M. Marechal, S. Dussi, M. Dijkstra, *J. Chem. Phys.* **146**, 124905 (2017).

[184] S. Gottschalk, M. C. Lin, D. Manocha, *Proceedings of the 23rd Annual Conference on Computer Graphics and Interactive Techniques* (ACM, 1996), pp. 171–180.

[185] E. Fischermeier, D. Bartuschat, T. Preclik, M. Marechal, K. Mecke, *Comput. Phys. Commun.* **185**, 3156 (2014).

[186] M. P. Allen, D. Frenkel, *Phys. Rev. A* **37**, 1813 (1988).

[187] R. Wittmann, M. Marechal, K. Mecke, *Phys. Rev. E* **91**, 052501 (2015).

[188] M. Kröger, P. Ilg, *J. Chem. Phys.* **127**, 034903 (2007).

[189] A. M. Somoza, P. Tarazona, *J. Chem. Phys.* **91**, 517 (1989).

[190] A. Poniewierski, R. Hołyst, *Phys. Rev. A* **41**, 6871 (1990).

[191] L. Mederos, E. Velasco, Y. Martínez-Ratón, *J. Phys.: Condens. Matter* **26**, 463101 (2014).

[192] M. P. Allen, *Mol. Phys.* **114**, 2574 (2016).

[193] R. G. Priest, T. C. Lubensky, *Phys. Rev. A* **9**, 893 (1974).

[194] S. Dhakal, J. V. Selinger, *Phys. Rev. E* **83**, 020702 (2011).

[195] M. Kleman, O. D. Lavrentovich, *Soft Matter Physics: An Introduction* (Springer Science & Business Media, New York, NY, 2007).

[196] A. Stroobants, H. N. W. Lekkerkerker, T. Odijk, *Macromolecules* **19**, 2232 (1986).

[197] C. Honorato-Rios, *et al.*, *Front. Mater.* **3**, 21 (2016).

[198] A. Kuhnhold, T. Schilling, *J. Chem. Phys.* **145**, 194904 (2016).

[199] I. Dozov, *Europhys. Lett.* **56**, 247 (2001).

[200] P. De Gregorio, E. Frezza, C. Greco, A. Ferrarini, *Soft Matter* **12**, 5188 (2016).

[201] L. Rovigatti, P. Šulc, I. Z. Reguly, F. Romano, *J. Comput. Chem.* **36**, 1 (2015).

[202] M. P. Howard, J. A. Anderson, A. Nikoubashman, S. C. Glotzer, A. Z. Panagiotopoulos, *Comput. Phys. Commun.* **203**, 45 (2016).

[203] D. Hsu, R. Kindel, J.-C. Latombe, S. Rock, *Int. J. Robot. Res.* **21**, 233 (2002).

[204] I. Wald, S. Boulos, P. Shirley, *ACM T. Graphic.* **26**, 6 (2007).

[205] D. H. Eberly, *3D Game Engine Design, Second Edition: A Practical Approach to Real-Time Computer Graphics* (Morgan Kaufmann Publishers Inc., San Francisco, CA, USA, 2006).

[206] S. Ding, M. A. Mannan, A. N. Poo, *Comput. Aided Design* **36**, 1281 (2004).

[207] S. Grudinin, S. Redon, *J. Comput. Chem.* **31**, 1799 (2010).

[208] S. Artemova, S. Grudinin, S. Redon, *J. Comput. Chem.* **32**, 2865 (2011).

[209] I. Lotan, F. Schwarzer, D. Halperin, J.-C. Latombe, *J. Comput. Biol.* **11**, 902 (2004).

[210] C. Ericson, *Real-Time Collision Detection*, C. Ericson, ed., The Morgan Kaufmann Series in Interactive 3D Technology (Morgan Kaufmann, San Francisco, 2005), chap. 4, pp. 75 – 123.

[211] J. T. Klosowski, M. Held, J. S. B. Mitchell, H. Sowizral, K. Zikan, *IEEE T. Vis. Comput. Gr.* **4**, 21 (1998).

[212] B. E. K. Snodin, *et al.*, *J. Chem. Phys.* **142**, 234901 (2015).

[213] M. R. Wilson, *J. Mol. Liq.* **68**, 23 (1996).

[214] M. E. Wall, A. Rechtsteiner, L. M. Rocha, *A Practical Approach to Microarray Data Analysis*, D. P. Berrar, W. Dubitzky, M. Granzow, eds. (Springer US, Boston, MA, 2003), pp. 91–109.

[215] T. F. Chan, *ACM T. Math. Software* **8**, 72 (1982).

[216] G. Barequet, B. Chazelle, L. J. Guibas, J. S. B. Mitchell, A. Tal, *Comput. Graph. Forum* **15**, 387 (1996).

[217] J. Goldsmith, J. Salmon, *IEEE Comput. Graph.* **7**, 14 (1987).

[218] J. L. Bentley, *Commun. ACM* **18**, 509 (1975).

[219] P. W. K. Rothemund, *Nature* **440**, 297 (2006).

[220] H. Dietz, S. M. Douglas, W. M. Shih, *Science* **325**, 725 (2009).

[221] M. Siavashpouri, *et al.*, *Nat. Mater.* **16**, 849 (2017).

[222] F. Cherhal, F. Cousin, I. Capron, *Langmuir* **31**, 5596 (2015).

[223] I. Usov, *et al.*, *Nat. Commun.* **6** (2015).

[224] C. Honorato-Rios, *et al.*, *Front. Mater.* **3**, 21 (2016).

[225] H. M. Farkas, I. Kra, *Riemann Surfaces* (Springer US, New York, NY, 1992), pp. 9–31.

[226] M. Reggiani, M. Mazzoli, S. Caselli, *IEEE/RSJ International Conference on Intelligent Robots and Systems* (2002), vol. 3, pp. 2329–2334.

[227] N. Katsonis, E. Lacaze, A. Ferrarini, *J. Mater. Chem.* **22**, 7088 (2012).

[228] A. G. Cherstvy, *J. Phys. Chem. B* **112**, 12585 (2008).

[229] D. Chandler, J. D. McCoy, S. J. Singer, *J. Chem. Phys.* **85**, 5971 (1986).

[230] D. Chandler, J. D. McCoy, S. J. Singer, *J. Chem. Phys.* **85**, 5977 (1986).

[231] A. R. Khokhlov, *Phys. Lett. A* **68**, 135 (1978).

[232] A. R. Khokhlov, A. N. Semenov, *Physica A* **108**, 546 (1981).

[233] A. R. Khokhlov, A. N. Semenov, *Physica A* **112**, 605 (1982).

[234] A. R. Khokhlov, A. N. Semenov, *Macromolecules* **17**, 2678 (1984).

[235] T. Odijk, *Macromolecules* **19**, 2313 (1986).

[236] R. Hentschke, *Macromolecules* **23**, 1192 (1990).

[237] T. Sato, A. Teramoto, *Mol. Cryst. Liq. Cryst.* **178**, 143 (1990).

[238] D. B. DuPré, S.-J. Yang, *J. Chem. Phys.* **94**, 7466 (1991).

[239] Z. Y. Chen, *Macromolecules* **26**, 3419 (1993).

[240] P. van der Schoot, M. E. Cates, *Europhys. Lett.* **25**, 515 (1994).

[241] H. Fynewever, A. Yethiraj, *J. Chem. Phys.* **108**, 1636 (1998).

[242] K. M. Jaffer, S. B. Opps, D. E. Sullivan, B. G. Nickel, L. Mederos, *J. Chem. Phys.* **114**, 3314 (2001).

[243] R. Diplock, D. E. Sullivan, K. M. Jaffer, S. B. Opps, *Phys. Rev. E* **69**, 062701 (2004).

[244] M. Dennison, M. Dijkstra, R. van Roij, *Phys. Rev. Lett.* **106**, 208302 (2011).

[245] W. Zhang, E. D. Gomez, S. T. Milner, *Macromolecules* **48**, 1454 (2015).

[246] S. A. Egorov, A. Milchev, P. Virnau, K. Binder, *Soft Matter* **12**, 4944 (2016).

[247] P. J. Flory, *Macromolecules* **11**, 1141 (1978).

[248] P. J. Flory, *Liquid Crystal Polymers I*, N. A. Platé, ed. (Springer-Verlag, Berlin, Heidelberg, 1984), pp. 1–36.

[249] A. R. Khokhlov, A. N. Semenov, *J. Stat. Phys.* **38**, 161 (1985).

[250] T. Sato, A. Teramoto, *Concentrated Solutions of Liquid-crystalline Polymers* (Springer-Verlag, Berlin, Heidelberg, 1996), pp. 85–161.

[251] M. A. Osipov, *Liquid Crystalline and Mesomorphic Polymers*, V. P. Shibaev, L. Lam, eds. (Springer US, New York, NY, 1994), pp. 1–25.

[252] T. van Westen, T. J. Vlugt, J. Gross, *J. Chem. Phys.* **137**, 044906 (2012).

[253] T. van Westen, B. Oyarzún, T. J. Vlugt, J. Gross, *J. Chem. Phys.* **139**, 034505 (2013).

[254] T. Jiang, J. Wu, *J. Chem. Phys.* **127**, 034902 (2007).

[255] A. M. Sonnet, E. G. Virga, G. E. Durand, *Phys. Rev. E* **67**, 061701 (2003).

[256] A. V. Komolkin, A. Laaksonen, A. Maliniak, *J. Chem. Phys.* **101**, 4103 (1994).

[257] K. Šolc, *J. Chem. Phys.* **55**, 335 (1971).

[258] D. N. Theodorou, U. W. Suter, *Macromolecules* **18**, 1206 (1985).

[259] G. S. Grest, K. Kremer, *Phys. Rev. A* **33**, 3628 (1986).

[260] K. Kremer, G. S. Grest, *J. Chem. Phys.* **92**, 5057 (1990).

[261] O. Kratky, G. Porod, *J. Colloid Sci.* **4**, 35 (1949).

[262] O. Kratky, G. Porod, *Recl. Trav. Chim. Pays-Bas* **68**, 1106 (1949).

[263] K. G. Honnell, J. G. Curro, K. S. Schweizer, *Macromolecules* **23**, 3496 (1990).

[264] S. A. Egorov, A. Milchev, K. Binder, *Phys. Rev. Lett.* **116**, 187801 (2016).

[265] E. Herrero-Galán, *et al.*, *J. Am. Chem. Soc.* **135**, 122 (2013).

[266] J. R. Wenner, M. C. Williams, I. Rouzina, V. A. Bloomfield, *Biophys. J.* **82**, 3160 (2002).

[267] S. Geggier, A. Vologodskii, *Proc. Natl. Acad. Sci. USA* **107**, 15421 (2010).

[268] F. Livolant, A. Leforestier, *Prog. Polym. Sci.* **21**, 1115 (1996).

[269] M. Nakata, *et al.*, *Science* **318**, 1276 (2007).

[270] J. P. Gourret, *Biol. Cell.* **32**, 299 (1978).

[271] F. Livolant, M. F. Maestre, *Biochemistry* **19**, 3056 (1988).

[272] N. S. Blanc, A. Senn, A. Leforestier, F. Livolant, J. Dubochet, *J. Struct. Biol.* **134**, 76 (2001).

[273] T. E. Strzelecka, R. L. Rill, *Macromolecules* **24**, 5124 (1991).

[274] A. A. Kornyshev, S. Leikin, S. V. Malinin, *Eur. Phys. J. E* **7**, 83 (2002).

[275] T. E. Ouldridge, A. A. Louis, J. P. K. Doye, *J. Chem. Phys.* **134**, 085101 (2011).

[276] K. Nadassy, I. Tomás-Oliveira, I. Alberts, J. Janin, S. J. Wodak, *Nucleic Acids Res.* **29**, 3362 (2001).

[277] C. De Michele, L. Rovigatti, T. Bellini, F. Sciortino, *Soft Matter* **8**, 8388 (2012).

[278] C. De Michele, G. Zanchetta, T. Bellini, E. Frezza, A. Ferrarini, *ACS Macro Lett.* **5**, 208 (2016).

[279] M. Dijkstra, D. Frenkel, *Phys. Rev. E* **51**, 5891 (1995).

[280] R. Cortini, X. Cheng, J. C. Smith, *J. Phys.: Condens. Matter* **29**, 084002 (2017).

[281] D. J. Kauert, T. Kurth, T. Liedl, R. Seidel, *Nano Lett.* **11**, 5558 (2011).

[282] D. Schiffels, T. Liedl, D. K. Fygenson, *ACS Nano* **7**, 6700 (2013).

[283] N. C. Seeman, *Nature* **421**, 427 (2003).

[284] L. M. Adleman, *Science* **266**, 1021 (1994).

[285] G. M. Church, Y. Gao, S. Kosuri, *Science* **337**, 1628 (2012).

[286] N. C. Seeman, *J. Theor. Biol.* **99**, 237 (1982).

[287] J. Chen, N. C. Seeman, *Nature* **350**, 631 (1991).

[288] E. Winfree, F. Liu, L. A. Wenzler, N. C. Seeman, *Nature* **394**, 539 (1998).

[289] B. Yurke, A. J. Turberfield, A. P. Mills Jr, F. C. Simmel, J. L. Neumann, *Nature* **406**, 605 (2000).

[290] H. Yan, S. H. Park, G. Finkelstein, J. H. Reif, T. H. LaBean, *Science* **301**, 1882 (2003).

[291] W. M. Shih, J. D. Quispe, G. F. Joyce, *Nature* **427**, 618 (2004).

[292] P. W. K. Rothemund, *Nature* **440**, 297 (2006).

[293] E. S. Andersen, *et al.*, *Nature* **459**, 73 (2009).

[294] S. Li, *et al.*, *Nat. Biotechnol.* **36**, 258 (2018).

[295] N. A. W. Bell, *et al.*, *Nano Lett.* **12**, 512 (2012).

[296] D. Koirala, *et al.*, *Angew. Chem. Int. Ed.* **53**, 8137 (2014).

[297] A. V. Pinheiro, D. Han, W. M. Shih, H. Yan, *Nat. Nanotechnol.* **6**, 763 (2011).

[298] S. M. Douglas, *et al.*, *Nature* **459**, 414 (2009).

[299] E. Skorupppa, M. Laleman, S. K. Nomidis, E. Carlon, *J. Chem. Phys.* **146**, 214902 (2017).

[300] J. P. K. Doye, *et al.*, *Phys. Chem. Chem. Phys.* **15**, 20395 (2013).

[301] M. C. Engel, *et al.*, *ACS Nano* **12**, 6734 (2018).

[302] T. E. Ouldridge, *Coarse-grained modelling of DNA and DNA self-assembly*, Springer Theses (Springer-Verlag, Berlin, Heidelberg, 2012).

[303] J. SantaLucia, Jr., D. Hicks, *Annu. Rev. Biophys. Biomol. Struct.* **33**, 415 (2004).

[304] D. Potoyan, A. Savelyev, G. A. Papoian, *WIRES: Comp. Mol. Sci.* **3**, 69 (2013).

[305] D.-N. Kim, F. Kilchherr, H. Dietz, M. Bathe, *Nucleic Acids Res.* **40**, 2862 (2012).

[306] J. Araki, S. Kuga, *Langmuir* **17**, 4493 (2001).

[307] F. B. Fuller, *Proc. Natl. Acad. Sci. USA* **68**, 815 (1971).

[308] J. C. Alexander, S. S. Antman, *Q. Appl. Math.* **40**, 83 (1982).

[309] J. F. Marko, E. D. Siggia, *Phys. Rev. E* **52**, 2912 (1995).

[310] M. L. Gardel, K. E. Kasza, C. P. Brangwynne, J. Liu, D. A. Weitz, *Method. Cell Biol.* **89**, 487 (2008).

[311] D. M. Hall, I. R. Bruss, J. R. Barone, G. M. Grason, *Nat. Mater.* **15**, 727 (2016).

[312] A. Kapanowski, *Z. Naturforsch. A* **57**, 105 (2002).

[313] J. Adamcik, *et al.*, *Nat. Nanotechnol.* **5**, 423 (2010).

[314] P. B. Davenport, *AIAA J.* **11**, 853 (1973).

[315] J. Arvo, *Graphics Gems III (IBM Version)*, D. Kirk, ed. (Morgan Kaufmann, San Francisco, CA, 1992), pp. 117 – 120.

[316] M. E. Munroe, *Introduction to Measure and Integration* (Addison-Wesley, Reading, MA, 1953).

[317] N. G. van Kampen, *Physica* **27**, 783 (1961).

[318] N. N. Bogoliubov, *Quasi-averages in Problems of Statistical Mechanics* (Gordon and Breach Sci. Pub., Philadelphia, PA, 1970), vol. 2, pp. 1–45.

[319] L. L. Lee, *J. Chem. Phys.* **103**, 9388 (1995).

[320] I. Teraoka, *Models of Polymer Chains* (John Wiley & Sons, Inc., Hoboken, NJ, 2002), pp. 1–67.

[321] G. Salmon, *A Treatise on Conic Sections* (AMS Chelsea Publishing, Providence, RI, 2000), 6th edn.

[322] R. C. Jones, *J. Opt. Soc. Am.* **31**, 488 (1941).